STRUCTURAL LOAD PATHS IN LOW-RISE, WOOD-FRAMED STRUCTURES

By

PETER LEROY DATIN

A DISSERTATION PRESENTED TO THE GRADUATE SCHOOL
OF THE UNIVERSITY OF FLORIDA IN PARTIAL FULFILLMENT
OF THE REQUIREMENTS FOR THE DEGREE OF
DOCTOR OF PHILOSOPHY

UNIVERSITY OF FLORIDA

2010

To Angie, Joshua, Emily, and Jessica

ACKNOWLEDGMENTS

First and foremost, I would like to thank my advisor, Dr. David O. Prevatt, for his guidance, support, and friendship. This work would not have been accomplished without his mentoring. I would also like to thank my committee members – Dr. Forrest Masters, Dr. Gary Consolazio, Dr. Rakesh Gupta, and Dr. Louis Cattafesta – for their help and support during various aspects of my research and graduate studies. Additionally, I would like to thank Akwasi Mensah, Jim Austin, Jimmy Jesteadt, Scott Bolton, and Jason Smith for their help in various aspects of my research. I would most like to thank my wife, Angie. She has always been my biggest supporter and is always willing to listen to me talk about the exciting things I do even though she does not share the same attitude and passion for structural and wind engineering. Finally, I wish to thank my parents for providing the constant support and encouragement to do my best and to pursue my dreams.

The financial support for this research is gratefully acknowledged from the National Science Foundation under grant number 0800023 – Performance Based Wind Engineering (PBWE): Interaction of Hurricanes with Residential Structures. I am also grateful for the Alumni Fellowship from the University of Florida which provided additional financial support during my graduate studies.

TABLE OF CONTENTS

page

LIST OF TABLES

LIST OF FIGURES

ABSTRACT OF DISSERTATION PRESENTED TO THE GRADUATE SCHOOL OF THE UNIVERSITY OF FLORIDA IN PARTIAL FULFILLMENT OF THE REQUIREMENTS FOR THE DEGREE OF DOCTOR OF PHILOSOPHY

STRUCTURAL LOAD PATHS IN LOW-RISE, WOOD-FRAMED STRUCTURES

By

Peter Leroy Datin

December 2010

Chair: David O. Prevatt
Major: Civil Engineering

Light-framed wood residential buildings continue to suffer damage from extreme wind events, even at wind speeds below design levels. One of the major findings in post-hurricane damage investigations is that a continuous load path to transfer the wind uplifts loads acting on the roof into the foundations was missing. The roof-to-wall connections are major components in this load path that have inadequate capacity during extreme wind events causing catastrophic failure. The objective of this dissertation is the evaluation of the vertical structural load paths due to wind loading on the roof of a low-rise, light-framed wood building. Through the use of static influence coefficients developed on a 1/3rd-scale wood building instrumented at twenty (20) roof-to-wall and wall-to-foundation connections, the vertical structural load paths were determined. Using a database-assisted design (DAD) methodology combining the structural influence coefficients with wind tunnel-derived pressure coefficients, estimated peak structural connection loads were determined. These peak loads were compared with loads estimated from two other previously established methods, namely the covariance integration (CI) and load-response-correlation (LRC) methods.

Generally, the CI and LRC methods estimated the mean connection loads well but underestimated the peak loads.

The hypothesis of the research is that a wood-framed roof is sufficiently flexible to be excited by dynamic wind loads. An analytical finite element model of a 21-truss roof was developed to investigate the effects of dynamic loads on the roof. A fundamental frequency analysis was performed on the roof and various roof components to determine the first vertical mode of vibration. The analysis showed that the roof is sufficiently stiff with fundamental frequencies well above the low frequencies that dominate natural wind flows. This finding discredits the hypothesis and shows that the static influence coefficients are valid for light-frame wood structures.

The DAD-derived peak reactions were also compared with design loads determined using the ASCE 7-05 wind load provisions and the prescriptive loads provided by the *Wood Frame Construction Manual* (WFCM). The roof-to-wall connection design loads determined using the ASCE 7-05 main wind force resisting system (MWFRS) procedures (both the low-rise and all heights provisions) underestimate significantly the peak loads developed using the DAD methodology. However, the design loads determined using the ASCE 7-05 components and cladding (C&C) provisions provide a better estimation of the peak loads, but still underestimate the DAD-derived peak loads at some roof-to-wall connections. This significant and unanticipated finding is due to the fact that the influence coefficients used to develop the MWFRS were for steel portal frames, which are not applicable to light-frame wood construction.

CHAPTER 1
INTRODUCTION AND BACKGROUND

Introduction

Approximately one-third of the United States population now lives within 100 miles of a hurricane-prone coastline, such as the Atlantic and Gulf coasts (US Census Bureau 2007), and most of these (>90%) live in single-family, light-frame wood structures (LFWS) (van de Lindt and Dao 2009). LFWS are susceptible to wind damage, and in particular, older homes have suffered more damage in recent storms (Gurley et al. 2006). More than 80% of homes in the US were built before improved building codes were introduced in 1994 as a result of Hurricane Andrew in South Florida in 1992 (US Census Bureau 2003) and as a result constitute the majority of wind damage. Extreme wind events (i.e., hurricanes and tornadoes) continue to cause extensive structural and non-structural damage in hurricane- and tornado-prone communities causing billions of dollars of damage annually. Davenport (2002) found that these losses continue to increase and double approximately every 5-10 years. Adjusting to 2006 dollars, the estimated annual total losses from hurricanes in the US is shown in Figure 1-1 (NSB 2007). The majority of these monetary losses occur to residential LFWS (e.g., nearly 60% of total insured losses from Hurricane Hugo, the majority of which was roof damage (Sparks 1991)). While some improvements to hurricane resistance have been made with more recent code changes (Gurley et al. 2006), of greater concern is that even hurricanes that do not produce winds exceeding design wind speeds cause extensive damage to residential LFWS (van de Lindt et al. 2007). It is becoming clear that the damage may be due to inadequate understanding of structural load paths and the behavior of these systems. Additionally, this continued failure could be partially

attributed to lack of proper inspections during construction leading to poor workmanship and buildings that in fact are not actually built to the building code standards to which they profess to adhere. However, the existing, older housing stock is still more vulnerable to failures in extreme winds due to the insufficient building codes used before 1994. The need to understand the load paths in these older LFWS is then necessary to enable the application of proper mitigation techniques.

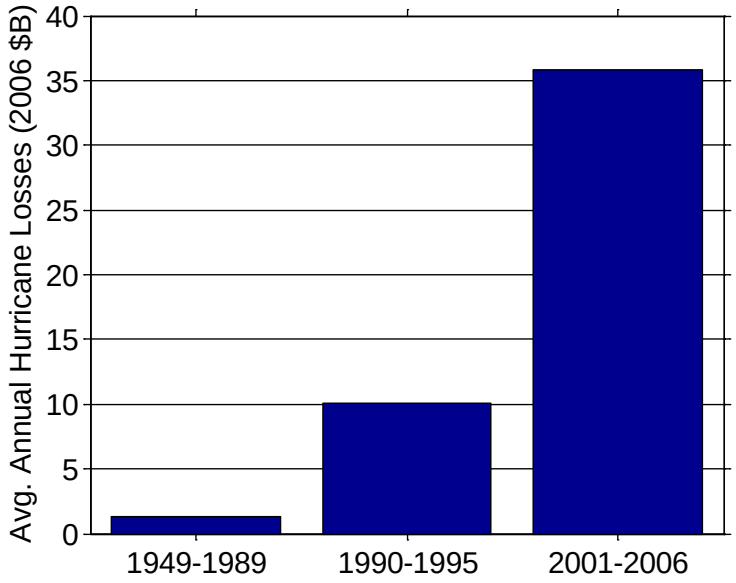

Figure 1-1. Average annual hurricane losses in the US adjusted to 2006 dollars (adapted from NSB 2007)

With $1.9 trillion worth of existing structures in the state of Florida alone (Pinelli et al. 2008), there is an urgent need for better understanding of the reasons for such continued damage, especially to residential LFWS. Structural research on residential LFWS has mainly focused on gravity loads (e.g., Wolfe and McCarthy 1989; Cramer et al. 2000) and lateral (e.g., seismic) load resistance (e.g., Paevere et al. 2003; Collins et al. 2005a; Collins et al. 2005b). However, limited research has been conducted on the actual structural performance of wood-frame roof systems in extreme wind events, with the primary focus on the performance of wood components (i.e., roof sheathing and

roof-to-wall connections) (e.g., Cunningham 1993; Mizzell 1994; Reed et al. 1997; Riley and Sadek 2003). All of this work has used either uniform static loads or ramp loads to model the wind loads, which realistically are highly dynamic (or unsteady) in nature.

Researchers have used full-scale instrumented buildings to measure wind pressures and structural forces due to natural wind loadings (Levitan and Mehta 1992a; Porterfield and Jones 2001; Doudak et al. 2005; Zisis and Stathopoulos 2009), but their results were limited by vagaries of the natural winds and environmental conditions at the site, and except for the Texas Tech (TTU) building (Levitan and Mehta 1992a) none of these buildings experienced major extreme wind events. Additionally, all but the TTU building had no control on the direction of the wind in relation to the orientation of the building. Still, the structural system of the TTU building itself, which is a steel, portal-framed building, differs from the wood structural systems found in typical residential construction.

The University of Western Ontario has undertaken a full-scale testing facility to apply realistic wind pressures to the roof and walls of residential LFWS called the "Three Little Pigs" project (Kopp et al. 2008). However, to date wind tunnel derived pressure traces have been applied to the roof of a two-story house, but structural loads were not monitored (Morrison and Kopp 2009). Another ongoing project to record wind pressures on residential LFWS during land falling hurricanes is the Florida Coastal Monitoring Program (FCMP). The FCMP has instrumented various occupied homes along the coasts of Florida and the Carolinas and captured real-time hurricane roof pressures (Liu et al. 2009).

Another tool used to understand how structural loads are transferred and the reasons for failure in LFWS is analytical structural modeling. Finite element (FE) analyses of 3D building models have been conducted in various studies (Kasal et al. 1994; Gupta and Limkatanyoo 2008; Martin 2010; Thampi et al. 2010) with connections generally modeled as either pinned or rigid with nails and wall hold downs simulated with either linear or non-linear springs. Dao and van de Lindt (2008) proposed a FE model for nailed roof sheathing failure in uplift based on experimental research that accounts for eccentric loading and nail bending as it is pulled from the framing member. A major problem with predicting performance of residential LWFS is that they are constructed according to prescriptive building codes, developed with limited research and relying on engineering judgment (Crandell and Kochkin 2003; Crandell et al. 2006). Recently, there has been a more concerted effort to develop performance based design methodologies for LFWS that will provide more risk consistency and better reliability of LFWS (Crandell et al. 2006; Ellingwood et al. 2006; van de Lindt and Dao 2009). Ellingwood et al. (2006) defined performance based engineering as “an engineering approach that is based on (1) specific performance objectives and safety goals of building occupants, owners, and the public, (2) probabilistic or deterministic evaluation of hazards, and (3) quantitative evaluation of design alternatives against performance objectives; but does not prescribe specific technical solutions.” This move towards performance based design criteria will require both a greater understanding of various components in residential LFWS construction, and more importantly, a greater understanding of system performance (i.e., all of the individual components and connections working together as a whole).

Knowledge Gap in Performance of Residential Light-Frame Wood Structures (LFWS)

The previous section outlined the severity of continued poor performance of residential LFWS. The tremendous costs associated with damage to LFWS subjected to extreme winds will continue to persist without further knowledge and understanding of the reasons for structural failure so that proper mitigation strategies can be implemented. The large gap in the research is that no available studies have experimentally investigated the structural load paths in a complete residential LFWS, thus ensuring that any system effects (not just isolated components) are included. A few analytical FE studies have been conducted, but proper experimental validation is needed. Additionally, most of the analytical models have not focused on wind uplift forces on the roof assembly.

Construction of Residential Light-Frame Wood Structures

This section describes the development of residential construction in the US in the 20th century. The introduction of mass produced steel nails in the 1830s led to a revolutionary change in the wood construction industry. Prior to the 1830s, wood construction consisted of heavy timbers connected by mortise and tenon joints (Wolfe and McCarthy 1989), but after the invention of nails, light-framed wood construction led to the use of smaller, standardized lumber sections (typically 2×4, 2×6, etc.) that are still in use today. From the 1830s through the 1940s little changed in construction practices for wood-frame roof assemblies with wood planking (typically with a nominal 1 in. thickness) fastened with two or three nails per framing member (Wolfe and McCarthy 1989). During World War II, there was a far greater demand for housing and construction of war-related infrastructure by the United States military, which propelled

the development of more efficient and faster construction methods. As a result, plywood sheathing was developed to replace wood planking in the construction of roof structures. Plywood sheets manufactured in 4 ft by 8 ft panels were lighter than planking and could be installed more quickly due to fewer nails and a larger coverage area.

Another significant change occurred in the mid-1950s when metal plate connected trusses were introduced. This system rapidly replaced the lumber rafters and board sheathing construction. The combination of plywood sheathing and metal plate connected trusses led to a substantial increase in the production and use of light-frame wood trusses and plywood due to the ease of constructability and resultant economic savings.

Contemporary residential light-frame wood structures (LFWS) are constructed of components built using dimensional lumber – nominal 2×4 and 2×6 members are typical. The exterior walls are “stick-built” on site and fastened together using nails. The majority of residential roof structures today are framed with trusses composed of several lumber pieces connected using metal plate connectors. The roof trusses are typically factory-built and delivered to the site. Sheathing is then attached to the walls and roof trusses or rafters, creating a diaphragm to resist in-plane loads. The wall framing members or studs are typically spaced at 16 inches on center. Wood rafters (typically nominal 2×6 or 2×8 lumber) are still used in some instances today. Figure 1-2 provides a visual representation of the construction of typical residential LFWS, often called “stick-built” or platform construction.

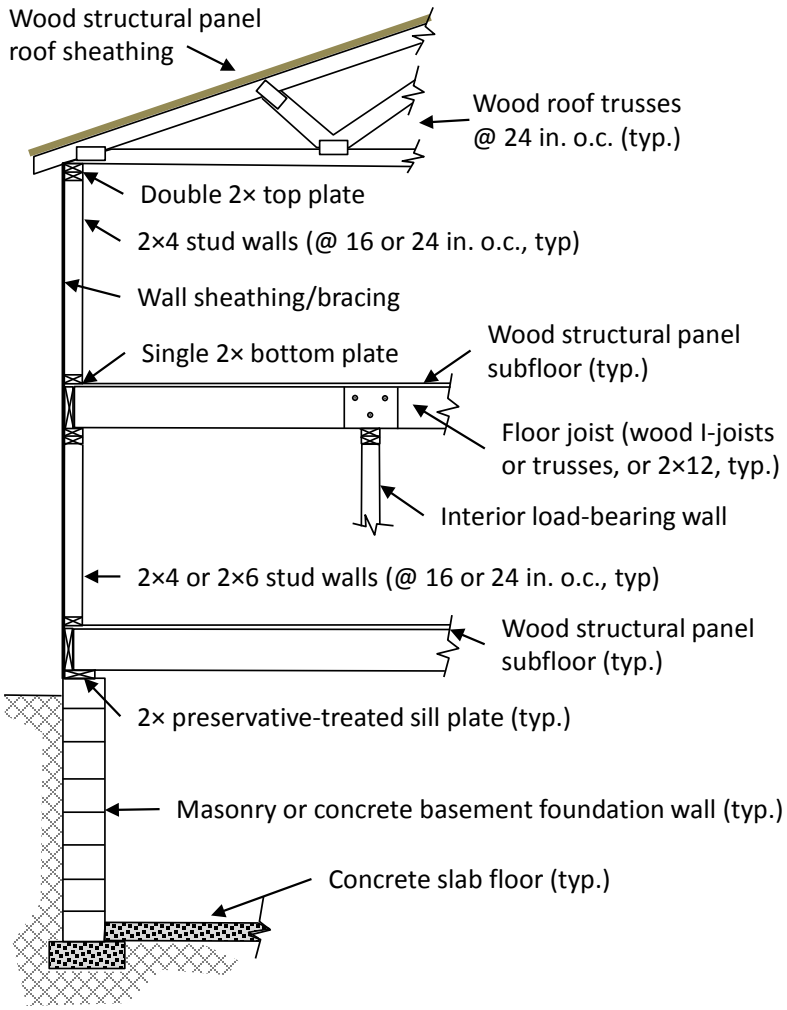

Figure 1-2. Typical modern light-frame wood construction (adapted from HUD 2000)

In summary, wide changes in conventional light-frame construction practices occurred approximately 60 year ago with the introduction of metal plate connected trusses and plywood. The weight of roofs was reduced by using plywood instead of planks and the number of nails used was reduced with an increase in nail spacing (typically 6d common nails spaced at 6 in. o.c. on panel edges and 12 in. o.c. everywhere else). Additionally, houses were constructed not as frames but as an assemblage of multiple 2D components. This provided for a rapid expansion in housing construction in the US. From 1950 to 1990, about 69 million homes were constructed, which still account for approximately 65% of the existing building stock in the US (US

Census Bureau 2003). The development of these construction practices hint at the fact that no clearly defined structural load paths existed in residential housing.

Structural Load Paths

Figure 1-3 depicts the basic components in a continuous vertical structural load path (SLP) to resist wind uplift forces on a roof. The SLP is the "path" that an applied load is transferred, or "moved," through a structure. The wind load acting upwards on the roof sheathing is resisted by nailed connections between the sheathing and truss. The trusses are held in place by roof-to-wall connections which transfers load into the wall system (e.g., a combination of studs and sheathing). The walls are fastened to the foundation using anchors which transfer the load to the foundation and finally to the ground, thus completing the load path. The connections between structural elements are the most important part of the load path, and they must be designed to adequately transfer the applied loads from one component to the next. Many failures in wind

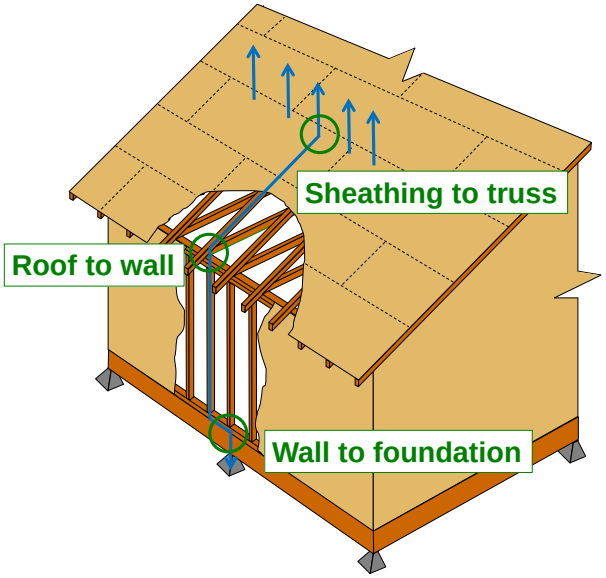

Figure 1-3. Vertical load paths in low-rise, wood-frame structures

storms occur due to brittle failures of connections which failed at loads well below the capacity of the structural members. Therefore, a structurally continuous load path is essential.

Background

The pressing need to understand how loads are distributed through a wood-framed residential building is evident in damage assessments after hurricanes. Post hurricane damage investigations have shown that wood structures tend to suffer little structural damage when the roof system remains intact under extreme wind loading, while major structural damage occurs when the roof system is partially or completely damaged (Reed et al. 1997). van de Lindt et al. (2007), and others (e.g., FEMA 2005c; FEMA 2006), documented extensive damage which occurred to wood-framed buildings because of inadequacies in their vertical load paths (Figure 1-4). Unfortunately the inadequacy of structural load paths in LFWS is not a new concern. In their report on Hurricane Camille which struck the Louisiana and Mississippi Gulf Coasts in 1969 (in nearly the same path as Hurricane Katrina in 2005), Dikkers et al. (1970) stated the following:

> "As demonstrated in Hurricane Camille as well as in previous hurricanes, it is essential that wood-frame buildings be properly anchored to their foundations, and walls, floors and roofs adequately tied together."

Similar observations were made by the Federal Emergency Management Agency (FEMA) disaster assessment teams and by others after various hurricanes, summarized in Table 1-1.

Since most wood-frame residential structures are not engineered, relying instead on prescriptive design codes, the result is a highly complex structural system due to its construction method as explained previously and shown in Figure 1-2. There is little

Table 1-1. Major findings and recommendations of post-hurricane investigations for specific hurricanes (1969-2008)

Hurricane (Year)	Damage[a] ($Billion)	Hurricane Category	Main Finding/Recommendation	Reference
Camille (1969)	21.2-24.0	5	• Most common failures were roofs • "…proper anchorage…"	Dikkers et al. (1970)
Alicia (1983)	7.2-7.5	3	• Most structural damage due to loss of roof sheathing • "Total collapse of timber-framed houses was a common scene."	Kareem (1985)
Gilbert (1988)	0.2	4	• Most of the damage due to anchorage deficiencies • Continuous load path is needed	Adams(1989); Allen (1989)
Hugo (1989)	15.3-17.5	4	• Roof loss with subsequent collapse of walls • Most damage was roof and wall cladding failures resulting in extensive rain damage	Sparks (1990)
Andrew (1992)	54.3-57.7	5	• Excessive negative pressure and/or induced internal pressure • Correct methods for load transfer are needed	FEMA (1992)
Iniki (1992)	1.8[b]	4	• Overload on roof systems due to uplift forces • Load path must be continuous from the roof to the foundation	FEMA (1993)
Charley (2004)	16.3	4	• High internal pressure due to window failure was the major cause of roof loss • Load path needs to be continuous	FEMA (2005c; 2005a)
Ivan (2004)	15.5	3	• Structural damage was due to sheathing loss • Ensure a complete load path for uplift loads	FEMA (2005c; 2005b)
Katrina (2005)	81.0	3	• Structural failures limited to roof sheathing loss and roof-to-wall connection failure • A continuous load path must be present	FEMA (2006)

Notes: (a) Normalized damage accounting for inflation, growth in wealth, and population or housing increases referenced to 2005 (Pielke et al. 2008). (b) Raw 1992 dollars (not adjusted by Pielke et al. 2008).

Figure 1-4. Examples of failures in residential LFWS due to inadequacies in the vertical load path (from van de Lindt 2007)

knowledge available of how loads are actually transferred through the complex 3D system from the roof sheathing into the foundation. While there are multiple load paths available, little is known as to which are the most critical and important load paths. It is hypothesized that this lack of understanding the load paths has contributed, at least in part, to the continued premature failures of roof systems in high wind events below design wind speeds. It is the consensus of most investigations that a continuous load path was missing resulting in premature failures in hurricanes. FEMA (1999) observed that the major structural failures in residential homes due to tornados were also due to the lack of a continuous load path.

Residential roof geometries have been changing from simple rectangular gable or hipped configurations to highly complex folded roofs that have intersecting gables, valleys, dormers, etc. (Figure 1-5). As trussed roof configurations become more complex there is a greater need to investigate and understand the structural load path behavior (i.e., how loads are resisted, transferred, and distributed) of the complete roof system (Gupta 2005). Understanding the structural load paths and load transfer mechanisms in LFWS systems is critical to improving the prediction of structural failures

in extreme wind events. It is also fundamental to developing performance-based wind design of these structures (as discussed previously) and thereby reducing future damage and economic losses to the inventory of LFWS.

Typically once the design pressures and loads have been determined, a basic tributary area analysis is performed to design the individual components of the structure (i.e., roof sheathing thickness and fastener schedule, roof trusses, roof-to-wall connections, etc.). The tributary area method is a 2D analysis technique that assigns a geometric area to a particular building component with the loads acting on that area used for design of that component. For example, if roof trusses are spaced at 2 ft on center, then the tributary width of a single truss is 2 ft – one foot on either side – and the pressures that act on that 2 ft wide strip along the entire length of the truss provide the design pressures for that truss. The truss member forces and reactions are determined through standard structural analysis techniques by applying these pressures to the 2D truss. While this traditional 2D tributary area method is easily used in design, its validity to actual spatio-temporal wind loads experienced by the structure is questioned, since it does not account for 3D structural behavior, which is well documented (discussed in detail in Chapter 2).

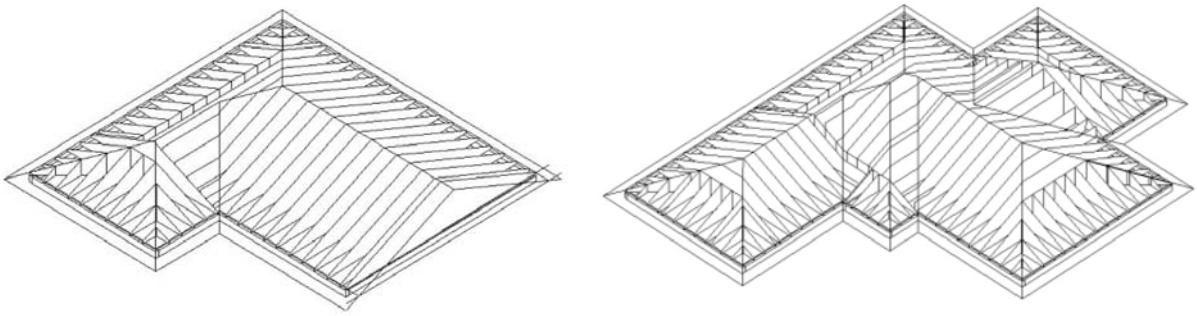

Figure 1-5. Example of trussed roof configurations (from Limkatanyoo 2003)

Research Objective

The overarching objective of this experimental and analytical research is to develop a fundamental understanding of the structural load paths in simple, gable-roofed residential LFWS, subjected to wind uplift loads. There is limited understanding of how the entire 3D system works together in residential LFWS, including the important links in the load paths (e.g., sheathing and truss/rafter-to-wall connections). Previous attempts to identify the load paths have been made using static influence functions, both experimentally and analytically (Wolfe and LaBissoniere 1991; Mani 1997; Datin and Prevatt 2007). However, wind loads (pressures) on a roof vary significantly in time and space, and wood roof structures (specifically individual components, e.g., roof sheathing) are believed to be more flexible than the entire structure which is considered a rigid, non-flexible structure for wind load design purposes. The dynamic characteristics of the individual components of the roof (i.e., sheathing and trusses/rafters) and how they affect wind load transfer into the structure are not well understood. Static influence functions may have the disadvantage of not realistically representing the structural response of the roof to fluctuating wind loads. It is believed our understanding of the wind/structure interaction in residential LFWS can be improved by a detailed study of the dynamic wind forces interacting directly with the structure, including the structural and dynamic properties of the building.

Hypothesis

The hypothesis of this research is that static influence functions do not accurately reflect the true wind load/structure interaction because they do not consider the correlations of the spatio-temporal wind fluctuations or the dynamic properties of the system including the natural frequencies of the components as well as the damping

effects. Therefore, a “dynamic influence function” is needed to capture the structural dynamics characteristics of the structure to provide a better understanding of the load paths in these complex, non-engineered buildings, including the damping in the structure. The dynamic influence functions will be defined as the impulse and frequency response functions relating the response of the structure excited by temporally varying loads at specific locations (i.e., reactions at roof-to-wall connections). By applying a dynamic load systematically to the roof of a residential LFWS and measuring structural forces at key locations within the structure, impulse and frequency response functions can be generated that inherently account for the structural damping, natural frequencies, and modes of the components and load paths. These impulse and frequency response functions essentially are “dynamic influence functions” because they will be calculated at specific key locations in the structure for loads applied at various locations.

The hypothesis will be evaluated by developing and comparing static influence functions against the dynamic influence functions and determine which best predicts the structural response in a LFWS at the roof-to-wall and wall-to-foundation connections when the structure is subjected to spatio-temporal wind loads. In order to accomplish this, a one-third scale residential LFWS has been constructed and instrumented with 20 load cells at critical connections within the structure (i.e., 11 roof-to-wall connections and 9 wall-to-foundation connections) to experimentally measure static influence functions as well as the impulse and frequency response functions at these specific locations.

Layout of Dissertation

This dissertation consists of seven chapters. Chapter 1 contains the introduction and background for the research and the research objectives and hypothesis. A review of pertinent literature is presented in Chapter 2, and Chapter 3 describes the methods and materials used. The experimental results for the static analysis are provided in Chapter 4 with the analytical dynamic analysis results in Chapter 5. A discussion of the results is found in Chapter 6, with conclusions and recommendations included in Chapter 7.

CHAPTER 2
LITERATURE REVIEW

Development of Tropical Cyclones

Hurricanes, also known as tropical cyclones, are large storms with diameters on the order of 200 miles or more with sustained wind speeds (peak 1-min wind speed at an elevation of 33 ft over unobstructed exposure) of at least 74 mph. In the Atlantic Basin (comprising the Atlantic Ocean, Caribbean Sea, and the Gulf of Mexico), hurricanes generally originate in the tropics between latitudes 5 and 20 and are fueled by vast amounts of latent heat released from condensing water vapor (Simiu and Scanlan 1996). The peak time for occurrence of hurricanes in the Atlantic Basin is generally August and September with varying intensity levels. To quantify the strength of hurricanes, the Saffir-Simpson Hurricane Scale (SSHS) was developed, which includes measures of central atmospheric pressure and sustained wind speed (Saffir 1971) and storm surge (Simpson 1974).

Measurements made during multiple landfalling hurricanes showed that the storm surges did not correlate well with the wind speeds in the SSHS (NHC/NOAA 2010). To address this deficiency, the National Hurricane Center recently revised this scale by removing storm surge and atmospheric pressure ranges and renamed the scale the Saffir-Simpson Hurricane Wind Scale (SSHWS) (NHC/NOAA 2010). Table 2-1 provides a description of the SSHWS with associated damage levels pertaining to wood-framed houses and representative storms.

Wind Forces on Low-Rise Buildings

Extreme wind flows around structures create damaging wind pressures that fluctuate in time and space. Turbulence associated with natural winds is due to

Table 2-1. Saffir-Simpson hurricane wind scale[a]

Cat.	Wind Speeds[b] (mph)	Expected Damage to Wood-Frame Houses	Example
1	74-95	• Loss of roof covering and gable end damage to poorly constructed houses • Damage to roof shingles, vinyl siding, soffit panels, and gutters in well-constructed houses.	Hurricane Dolly (2008) – South Padre Island, TX
2	96-110	• High chance of full-roof removal in poorly constructed houses, especially without proper roof-to-wall anchorage • Major roof and siding damage possible in well-constructed houses	Hurricane Frances (2004) – Port St. Lucie, FL
3	111-130	• Possibility of total destruction of poorly constructed houses • Removal of roof decking and gable end failures in well-constructed houses	Hurricane Ivan (2004) – Gulf Shores, AL
4	131-155	• Complete collapse of poorly constructed houses • Loss of most of the roof structure and/or exterior walls in well-constructed houses possible	Hurricane Charley (2004) – Punta Gorda, FL
5	>155	• High percentage of wood-framed homes completely destroyed	Hurricane Andrew (1992) – Cutler Ridge, FL

Notes: (a) Adapted from NHC/NOAA (2010) and (b) Peak 1-min. wind speed at an elevation of 33 ft over unobstructed exposure

mechanical disturbances (or mixing) of the flow near the ground due to buildings, trees, and rough terrain upstream (Simiu and Scanlan 1996). For buildings, most of the pressure variability occurs near roof corners, edges, and along roof ridges where wind flow separates at sharp building edges creating either a 2D separation bubble or 3D conical vortices (Banks and Meroney 2001). These separation regions create large pressure fluctuations that produce the high (suction). The spatial variability and dynamic nature of wind pressure fluctuations on residential roofs are well established in the literature.

Wind design provisions in ASCE 7-05 (ASCE 2006) include methodologies to determine minimum design wind pressures for buildings. The design wind pressure coefficients for roof and wall pressure zones are determined using look-up tables based on data from boundary layer wind tunnel tests on small-scale building models (e.g., Stathopoulos 1979; Ho et al. 1991; Ho et al. 1992) (see the commentary in ASCE 7-05 for a comprehensive list). The wind loading standards make use of quasi-steady, or "pseudo," loading conditions. The quasi-steady wind load theory relies on two assumptions (Uematsu and Isyumov 1999; Banks and Meroney 2001): (1) the wind field is steady, inviscid, irrotational, and incompressible so that the surface pressure coefficient is directly related to the velocity of the flow immediately above that surface; and (2) the entire flow field velocity changes simultaneously (i.e., the correlation of the velocity at any point to a reference velocity measured somewhere else within the flow field is unity). It follows from these two assumptions that the cross-correlation between wind velocity and surface pressure is also 1.0. Subsequently, all pressure fluctuations are the direct result of velocity fluctuations, and therefore, the maximum velocity on the structure produces the peak pressures or loads (Uematsu and Isyumov 1999).

Full-Scale Wind Pressure Measurements on Low-Rise Structures

One of the earliest experiments to measure pressures on full-scale, low-rise buildings is the Aylesbury study (Eaton and Mayne 1975) at the Building Research Station in the United Kingdom. The Aylesbury experimental building measured 23 ft by 43 ft in plan with a gable roof that could change roof slope from 5° to 45°. This structure provided a first look at the wind-structure interaction in the lowest 10 m (33 ft) of the atmosphere. One interesting observation made by Eaton and Mayne (1975) is that the frequency content of the pressures measured on the roof (especially near the ridge)

were shifted substantially to higher frequencies (from approximately 0.4 to 1.4 Hz) than the wind speed power spectrum.

Another important full-scale instrumented low-rise structure is the Wind Engineering Research Field Laboratory (WERFL) at Texas Tech University (TTU) in Lubbock, Texas. The WERFL building is a steel, portal-frame building measuring 30 ft by 45 ft with a 13 ft eave height and a nearly flat roof (Levitan and Mehta 1992a; Levitan and Mehta 1992b). Instrumented with more than 100 pressure transducers on all four walls and the roof, the building is capable of being rotated providing control of the wind angle of attack. Numerous studies have been published based on data collected for over 20 years on the WERFL building, and it is still used as a benchmark for validating wind tunnel characteristics.

The Florida Coastal Monitoring Program (FCMP) is a full-scale, low-rise building wind pressure monitoring program started in 1997 and is a joint venture between the University of Florida, Clemson University, Florida International University, the Institute for Business and Home Safety, and the Florida Institute of Technology (Gurley et al. 2005). The FCMP has approximately 36 residential structures concentrated mostly along the Florida panhandle and Atlantic coast as well as a handful in the Carolinas. The houses are prewired to allow pressure transducers to be mounted to the roof and walls immediately before a land-falling hurricane enabling real-time pressure measurements on actual occupied homes as hurricanes make landfall (Masters 2004; Liu 2006). Many of the instrumented homes have complicated roof geometries located in homogeneous suburban terrains. Liu et al. (2009) compared wind tunnel results with full-scale pressures monitored on a FCMP house during Hurricane Ivan in 2004. They

found that (1) although the mean and standard deviations of the pressure coefficients at full and model scale are similar, the peak negative pressure coefficients were consistently underestimated by the wind tunnel study and (2) the peak uplift loads prescribed by ASCE 7-05 may be non-conservative for homes situated in suburban terrain.

Influence Functions

Influence functions, or influence coefficients, provide a quantitative measure of a specific reaction (i.e., shear, moment, force, etc.) due to an applied load at a certain point on the structure. Figure 2-1 shows graphically how an influence coefficient is calculated for a simple beam. To calculate influence coefficients, a known load (*P*) is applied at a certain point on the structure (i.e., a point load on a roof). Then a specific reaction (*R*) to that applied load is measured (i.e., a roof-to-wall connection). The influence coefficient for that reaction to the load applied at that location is calculated by dividing the measured reaction load by the applied load. Therefore, an influence coefficient is the fraction (or percentage) of the applied load that is transferred through the given reaction.

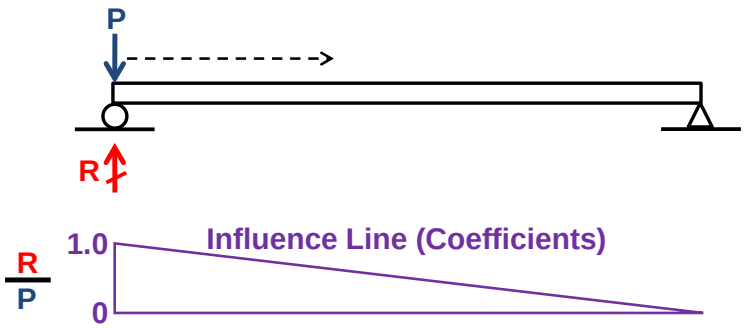

Figure 2-1. Influence line (coefficient) sample calculation

Influence coefficients are commonly used in structural analysis in design of bridges and other structures that have moving loads (Hibbeler 2002). This concept has

also been used in wind engineering to calculate structural responses due to wind loading. Davenport (1995) showed how this is accomplished in Eqn. 2-1.

$$R = q \int_A \left[C_p \beta_R(z)\right] dA \tag{2-1}$$

where: q is the dynamic velocity pressure; C_p is the pressure coefficient time history; β_R is the influence coefficient (or surface) for connection R; A is the reference area over which the pressures act: and z is a point within the area. The important point for using influence coefficients is that they enable the dynamic response of a given reaction to be determined (Davenport 1995) using Eqn. 2-1.

Influence coefficients have also been used in developing the design pressures for wind loading included in ASCE 7-05 standard (ASCE 2006). The ASCE 7-05 standard contains wind loading provisions for main wind-force resisting systems (MWFRS) that represent fictitious loading conditions that envelope the desired structural responses (e.g., bending moments, shear, or thrust at the knee or foot of a steel portal frame) independent of wind direction for a given building (see Commentary C6.5.11 in ASCE 7-05). The fictitious loading conditions were based on rigid, portal-framed, steel structures with frames spaced 25 ft apart and a span of 80 ft (Figure 2-2). Influence coefficients were derived based on a 2D analysis of the frames, although it appears that the effect of cladding (and thus load-sharing) was not included in the analysis, nor were the calculated values verified experimentally. The derived influence coefficients for rigid frames were spatially and time averaged with the wind tunnel pressures to develop the maximum applied forces needed for design.

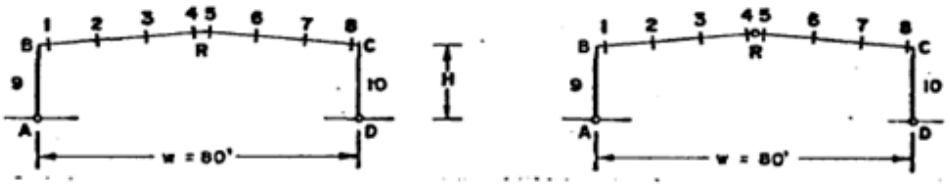

Two-pinned Frame Three-pinned Frame

The influence factors are given in a matrix form v_{ij} where i signifies the generalized bay load coefficient (i = 1 to 7) and j gives the particular directly measured (through manifolds) pressure load coefficients for the secondary structural elements (j = 1 to 8 for purlins, j = 9, 10 for wall sections).

i	Bay Load Coefficient	
1	Vertical uplift force	V.F
2	Horizontal thrust	H.T
3	Bending moment at B (two-pinned frame)	MB2
4	Bending moment at R (two-pinned frame)	MR2
5	Bending moment at C (two-pinned frame)	MC2
6	Bending moment at B (three-pinned frame)	MB3
7	Bending moment at C (three-pinned frame)	MC3

MATRIX OF INFLUENCE FACTORS (Assuming a Horizontal Roof)

i \ j	1	2	3	4	5	6	7	8	9	10
1	.10065	.14922	.14922	.10065	.10065	.14922	.14922	.10065	.0	.0
2	.0	.0	.0	.0	.0	.0	.0	.0	1.0	-1.0
3	-.00076	-.00647	-.00980	-.00752	-.00752	-.00980	-.00647	-.00076	.00850	-.01150
4	.00056	.00662	.01442	.01634	.01634	.01442	.00662	.00056	-.00150	-.00150
5	-.00076	-.00647	-.00980	-.00752	-.00752	-.00980	-.00647	-.00076	-.01150	.00850
6	-.00013	-.01309	-.02422	-.02384	-.02384	-.02422	-.01309	-.00013	.01000	-.01000
7	-.00013	-.01309	-.02422	-.02384	-.02384	-0.2422	-.01309	-.00013	-.01000	.01000

MATRIX IF2412

i \ j	1	2	3	4	5	6	7	8	9	10
1	.06292	.11312	.11312	.06434	.06434	.11312	.11312	.06292	0.	0.
2	.11156	.20000	.20000	.11343	-.11343	-.20000	-.20000	-.11156	.37500	-.37500
3	.01857	.02354	.01681	.00800	-.01923	-.03120	-.02449	-.00821	.03047	-.01453
4	-.00768	-.01416	-.00653	.00673	.00673	-.00653	-.01416	-.00768	-.01624	-.01624
5	-.00821	-.02449	-.03120	-.01923	.00800	.01681	.02354	.01857	-.01453	.03047
6	.02145	.02885	.01925	.00547	-.02176	-.02876	-.01916	-.00533	.03656	-.00844
7	-.00533	-.01916	-.02876	-.02176	.00547	.01925	.02885	.02145	-.00844	.03656

Figure 2-2. Development of influence coefficients in ASCE 7 (from Stathopoulos 1979)

Comparing the structural system in Figure 2-2 with that shown in Figure 1-2 for typical light-frame construction, it is obvious that they are completely different. It is not certain whether influence coefficients for a framed system developing moments will be applicable to a structure transferring loads by direct nail withdrawal and shear with little to no moment transfer. The validity of using the same "pseudo" loading conditions for light-framed, wood roofs with metal-plate-connected trusses spaced at 2 ft o.c. has not been confirmed. In fact Coffman et al. (2010) found that using similar buildings to those used by Stathopoulos (1979), the ASCE 7-05 analytical procedure underestimated the maximum bending moment at the knee by as much as 90% when only external pressures were used (i.e., neglected internal pressures).

The ASCE 7-05 provisions result in design values that are not risk consistent, particularly when applied to other structural systems (Simiu and Stathopoulos 1997). Further, the wind load standards offer no information on wind loading so that influence-function-dependent wind effects can be calculated for structural systems that differ from that assumed in the original wind tunnel tests (Simiu and Stathopoulos 1997).

Load Sharing in Wood-Frame Roofs

Load sharing occurs by two different component interactions: partial composite action (also known as T-beam action) and two-way action (sometimes directly referred to as load sharing) (Wolfe and LaBissoniere 1991; Bulleit and Liu 1995). Partial composite action is the interaction between the roof sheathing and rafter or top chord of the truss where the sheathing shares the load with the rafter or truss along the lengthwise axis of the wood member increasing member stiffness and reducing member deflections. The partial composite action (as opposed to fully composite where the sheathing and wood members would act completely together as if one solid piece) is

due to the fact that the connections between the joists and sheathing are not completely rigid and do not ensure complete shear transfer across the connection. Two-way action of the roof sheathing acting as a thin, wide continuous beam spanning the trusses or joist members reduces the vertical displacement among members. The two-way action of the sheathing is the main contributor to the load sharing and redistribution of loads in a sheathed lumber system (Wolfe and LaBissoniere 1991). Load sharing does not occur until one truss deflects relative to adjacent trusses (Wolfe and LaBissoniere 1991). The two-way action can also redistribute load from members that have yielded or ruptured to members that have not failed (Bulleit and Liu 1995).

The National Design Specification for Wood Construction (NDS) (AF&PA 2005a) provides for a 15% increase in the allowable bending stress if three or more parallel members (i.e., studs, rafters, truss chords, joists, and decking) spaced no more than 24 inches apart are connected via load distributing elements that force them to act together. Wolfe (1990) and Gupta et al. (2004) report this multiplier was developed by the ASTM D7 Committee in the 1960s using a simple analysis of three parallel bending members, and subsequently shown to be a conservative value for wood truss roofs (Wolfe 1990; Wolfe and LaBissoniere 1991).

Experimental and Analytical Studies of Full-Scale Wood Roof Assemblies

Forest Products Laboratory testing. The Forest Products Laboratory (FPL) performed several full-scale tests of residential wood-framed structural systems (McCutcheon 1977; Wolfe and McCarthy 1989; Wolfe and LaBissoniere 1991). McCutcheon (1977) experimentally investigated partial composite action and load sharing behavior in wood-joist floor systems. He developed a simplified analytical procedure for determining the stiffness and deflections of partial composite wood floor

systems, validated with experimental testing, and showed that partial composite action reduces deflections of individual joist members. Thus, load sharing is a result of increased stiffness in the overall system.

Some of the first experimental work on load sharing between adjacent trusses was carried out by Wolfe and McCarthy (1989) and Wolfe and LaBissoniere (1991) resulting in the creation of an experimental database of test results for 3D roof truss assemblies. The researchers tested 9-truss assembles using Fink and scissors trusses to provide a benchmark database for use to validate/calibrate 3D finite element models. Wolfe and McCarthy investigated the effects of different truss stiffness on the ability of the overall roof system to distribute loads. They constructed two nine-truss roofs (using Fink style trusses, Figure 2-3) with slopes of 3 in 12 and 6 in 12. The lumber used to construct the trusses was sorted by the individual lumber member's modulus of elasticity (MOE) into three categories: low, medium, and high. Each truss was constructed from lumber members from only one category resulting in trusses with low, medium, and high MOE values. The trusses were tested individually first to determine the stiffness properties and develop load-deflection curves. Each roof assembly consisted of three trusses from each of the MOE categories. A load influence matrix was developed for the entire roof assembly.

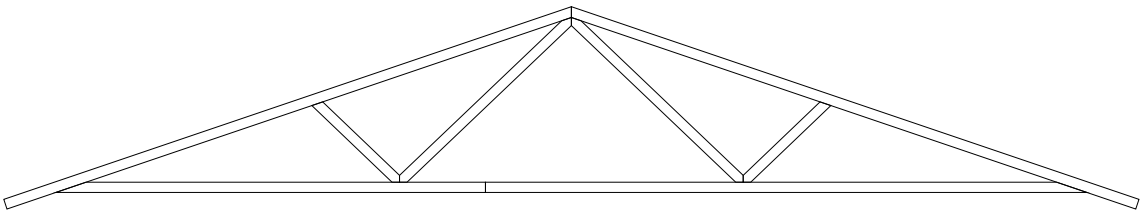

Figure 2-3. Typical Fink truss

Several interesting and important conclusions resulted from this testing (Wolfe and McCarthy 1989):

- The influence matrix did not change much with different applied loads until the roof assembly began to experience damage. Therefore, in the linear elastic range, the influence functions remain constant regardless of the load but change when the system becomes nonlinear due to damage.

- The effect of material variability (i.e., MOE) was not as significant in the full assembly as in individual performance, meaning that stiffer trusses with higher MOE values carry more load than less stiff trusses with lower MOE values due to the entire system deflecting together.

- The principle of superposition can be used to predict overall truss reactions and deflections. Therefore in the linear elastic range, summing the reactions from individual point loads on the roof results in the same reaction as if all of the points were loaded at the same time.

- Individual truss stiffness and apparent strength increased in the roof assembly due to the system interaction. Measured vertical deflections at two top chord nodes were as much as 50% less in the roof assembly than for individual trusses, and the failure loads increased by as much as 20% in the 3:12 slope roof and 40% in the 6:12 slope roof.

Wolfe and LaBissionere (1991) constructed two additional nine truss roof assemblies of the same slope and size as those tested by Wolfe and McCarthy (1989) as well as a scissors truss roof with a 6:12 slope. The major difference in the trusses used here from the previous study by Wolfe and McCarthy is that these new assemblies were constructed in a typical manner without selecting certain MOE categories or heavier truss plates to provide a realistic truss roof. Additionally, these roofs included a gable end truss (Figure 2-4) which has sheathing nailed to the vertical members. It was observed that individually loaded trusses within the assembly produced positive (downward) reactions on trusses up to five trusses away from the loaded truss. The stiffer gable end truss carried more load than the immediately adjacent and interior trusses, and that 40-70% of the load applied to a single truss is distributed to adjacent trusses by the sheathing. The significance of this is that load redistribution is not trivial in wood-frame roof assemblies, which could result in significant over-design of trusses

in some instances if a 2D analysis is used where the entire load applied to the truss is carried by the truss end connections.

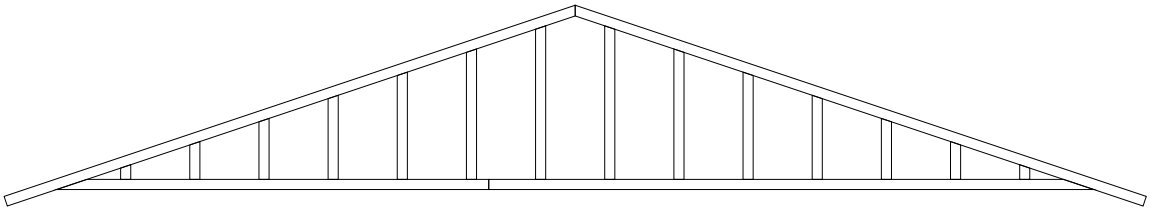

Figure 2-4. Typical gable end truss (vertical members typically spaced at 24 in. o.c.)

Wolfe and LaBissionere (1991) showed that composite action increases apparent truss stiffness, which is controlled by connection stiffness (i.e., nail spacing). However, near the capacity of the assembly, joint-slip (between the sheathing and truss top chord) caused a decrease in the composite action resulting in no apparent strength increase. They also showed that load redistribution will increase with relative displacement, an increase in relative stiffness of the sheathing, and a decrease in truss spacing. Trusses located near the gable end had the most significant stiffness increase due to the much stiffer gable-end truss. Wolfe and LaBissionere reported load sharing contributed to an increase in assembly load capacity of 13-29% and 30-49% for the 3 in 12 and 6 in 12 Fink truss roof systems, respectively. Additionally, they found that the repetitive member factor of 1.15 used in the NDS (AF&PA 2005a) for bending is conservative.

Limitations of FPL tests. The results from tests conducted at the FPL (McCutcheon 1977; Wolfe and McCarthy 1989; Wolfe and LaBissoniere 1991) have several limitations. First, the studies only focused on gravity (downward) loads. Second, the loads applied were uniform and are not applicable for simulating effects of varying wind loads. Further, the studies did not investigate upward (suction) forces, casting doubt on whether the influence coefficients developed for gravity loads are appropriate for predicting connection forces to uplift loads.

Cramer and Wolfe (1989) study. Cramer and Wolfe (1989) used the results of full-scale experimental roof tests (Wolfe and McCarthy 1989) to develop and calibrate a three-dimensional, matrix based, stiffness-method frame analysis computer model to investigate load-sharing behavior in wood-truss roof assemblies. This program was limited in its scope to predicting load distribution among trusses of varying stiffnesses. One interesting finding from this study is that when the "average" trusses were used, fabrication characteristics, such as truss alignment or truss-plate placement, are more important in load distribution than truss-stiffness variability. The authors suggest that for the "average" roof, use of the tributary area methodology (described in Chapter 1 in the Background section) is "entirely appropriate" for design purposes. For the roof assemblies where the truss stiffness was carefully selected, load sharing effects were significant, and thus the tributary area methodology was inappropriate.

Liu and Bulleit (1995) study. To investigate the overload behavior of sheathed lumber systems (i.e., floors and roofs), Liu and Bulleit (1995) performed a Monte Carlo simulation varying different material and physical properties of wood members (i.e., number of members, sheathing thickness, nail stiffness, lumber member spans, and the coefficient of variation of the modulus of elasticity and modulus of rupture) using a structural analysis program. The system, consisting of No. 2 grade nominal 2×8 Douglas fir lumber spaced at 16 inches on center and plywood, was subjected to a uniform gravity load until failure to identify system-failure criteria. The authors included the effects of component interactions (i.e., partial composite action and two-way action) by using the partial composite analytical model developed by McCutcheon (1977). They showed that once a member of the system (i.e., a beam) fails, the sheathing

redistributes the loads once carried by the failed (i.e., yielded or ruptured) member to other members and helps to generate a post-yield behavior of the partially composite members (i.e., higher system failure load than individual first member yield load). In addition, it was found that increasing the sheathing thickness increases the overall capacity of the system, but this was not an effective means of achieving a stronger system. They also found that the stiffness of the nailed sheathing to wood connection had little to no effect on load sharing and load redistribution within the system because (1) the connector stiffness does not directly contribute to the strength of the wood members and (2) the sheathing and nail stiffness is much less than the stiffness of the structural lumber members so even if the connector stiffness was increased, the stiffness of the wood members would not increase significantly or at all. If the sheathing was much stiffer in relation to the wood members, then an increase in nail stiffness (i.e., closer spacing) could increase significantly the load sharing ability of the system due an increase in partial composite action.

Limitations of Liu and Bulleit (1995) study. Several limitations of this study are evident in attempting to apply these results to a wood-frame roof subjected to wind loads. The analysis was carried out only using a uniformly distributed load which is not realistic for a roof experiencing an extreme wind load. Also, the study was limited to a floor system not representative of a roof system using sloping trusses.

Reed et al. (1997) and Rosowsky et al. (1998) studies. Reed et al. (1997) and Rosowsky et al. (1998) tested toe-nailed and metal-strap-connected roof-to-wall connections both individually and in repetitive member systems. The roof framing members were No. 2 or better spruce-pine-fir nominal 2×6 rafters (not trusses) nailed to

a nominal 2×4 Southern yellow pine top plate. For the repetitive member system tests, ½-inch thick oriented strand board (OSB) was fastened to rafters spaced at 16 in. on center using 6d common nails. The system tests comprised a total of seven rafters each with a load tree applying equal uplift loads to the underside of the rafters. Reed et al. (1997) and Rosowsky et al. (1998) found that significant load sharing takes place in repetitive toe-nailed connections of wood rafter systems. However, when the connections used metal hurricane clips there was no evidence of load sharing. For the repetitive toe-nailed connections, the load sharing created an increase in average uplift capacity of approximately 55% over individual connections. The load capacity increase was attributed to the large variability in ultimate uplift capacity of toe-nailed connections. The coefficient of variation (COV) of the toe-nailed connections and metal hurricane straps was 0.23 and 0.10, respectively. They found that stiffer connections attract a larger proportion of the loads; therefore, the load was redistributed more in the toe-nailed connections than in using the much less variable metal clips. However, the metal hurricane clips provided an average uplift resistance of 1900-3000 lbs (depending on the type of clip) versus the toe-nailed connections at 430 lbs. Thus the metal clips are far superior to toe-nailed connections at providing uplift resistance.

Cramer et al. (2000) study. Cramer et al. (2000) used a finite element structural analysis program developed to model 3D wood truss assemblies using a nonlinear, matrix-displacement method to determine the load-sharing effects on members in metal-plate-connected wood truss assemblies. The assemblies were analyzed with and without sheathing to determine the effects of sheathing on load sharing and distribution. They defined ultimate capacities of each truss member was based on a combined

stress index (CSI) relating stress interactions for both combined compression and bending (Eqn. 2-2) and combined tension and bending (Eqn. 2-3). If the CSI values exceed 1.0, failure is expected.

$$CSI = \left(\frac{f_c}{F_c'}\right)^2 + \frac{f_b}{F_b'} \leq 1.0 \quad (2\text{-}2)$$

$$CSI = \frac{f_t}{F_t} + \frac{f_b}{F_b'} \leq 1.0 \quad (2\text{-}3)$$

where: f_c is the compressive stress, F_c' is the compressive strength including buckling reduction, f_b is the bending stress, F_b' is the bending strength, f_t is the tensile stress, and F_t' is the tensile strength.

Several wood material properties were simulated (e.g., modulus of elasticity, modulus of rupture, ultimate compressive strength, and ultimate tensile strength), and roof assemblies consisting of seven and 21 trusses were analyzed. The load-sharing ratios were computed as the ratio of the CSI of the sheathed assembly over the unsheathed assembly. 200 simulations were conducted for four different roof truss configurations with the mean load-sharing ratios ranging from 1.06-1.22 (with a mean of 1.12) for systems loaded to the design load (42 psf) and 1.07-1.24 (with a mean of 1.17) at two times the design load (84 psf). The slight increase at two times the design load was attributed to the connections becoming nonlinear under increased displacements and thus amplifying the load-sharing. The mean load sharing ratios were considered to be conservative since the wood member strengths provided by the NDS (AF&PA 2005a) use a lower 5% lower exclusion value. Cramer et al. (2000) concluded that the repetitive member factor of 1.15 for bending in the NDS is conservative for wood design

and should be extended to tension and compression in truss chords as well. They also showed that partial composite action and gaps in the modeled sheathing did not affect the load sharing significantly.

Limitations of Cramer et al (2000) study. The major weakness of this study is the use of a uniform load on the roof assembly applied in the direction of gravity. The uniformity of the load is completely unrealistic for wind loading. Additionally, there is no guarantee that the load sharing behavior would be the same for uplift loads.

Li (1996) and Li et al. (1998) studies. Li (1996) and Li et al. (1998) developed a computer model of a wood truss roof assembly using a common structural engineering design program (ETABS by Computers and Structures, Inc.). Their main focus was to investigate the system effects of a complete wood roof assembly, including load sharing effects. Metal plate connected wood Fink trusses were modeled with beam and spring elements to represent semi-rigid behavior at the truss joints with the sheathing modeled as beam elements. The loads applied to the model were uniform downward (gravity) loads with model validation achieved by comparing the results to previously published literature (Wolfe and McCarthy 1989; Wolfe and LaBissoniere 1991). The model predicted the vertical deflections of individual trusses loaded uniformly within 7% of full-scale results as well as the internal axial loads in truss members within 10% of full-scale results. The individual truss strength (ultimate load) was predicted within 9%. For load sharing behavior, the model predicted the experimental behavior within 2%. Therefore, the authors proposed that trussed-roof system design may be improved by using system behavior directly instead of just using the system effects modification factor of 1.15 to design a single truss.

Limkatanyoo (2003) and Gupta and Limkatanyoo (2008) studies. Limkatanyoo (2003) and Gupta and Limkatanyoo (2008) investigated overall system effects that are not accounted for in conventional design. In a conventional design procedure (CDP) of a roof truss, the trusses are designed individually as 2D systems with the truss designed to resist just the loads in its tributary area usually involving proprietary software developed by metal truss plate manufacturers. The CDP was compared with a system design procedure (SDP) that can account for system behaviors (e.g., load sharing and boundary conditions). Three different roof models were modeled and investigated and shown in Figure 2-5: T-shaped, L-shaped, and complex, containing 4, 17, and 27 different types of trusses, respectively.

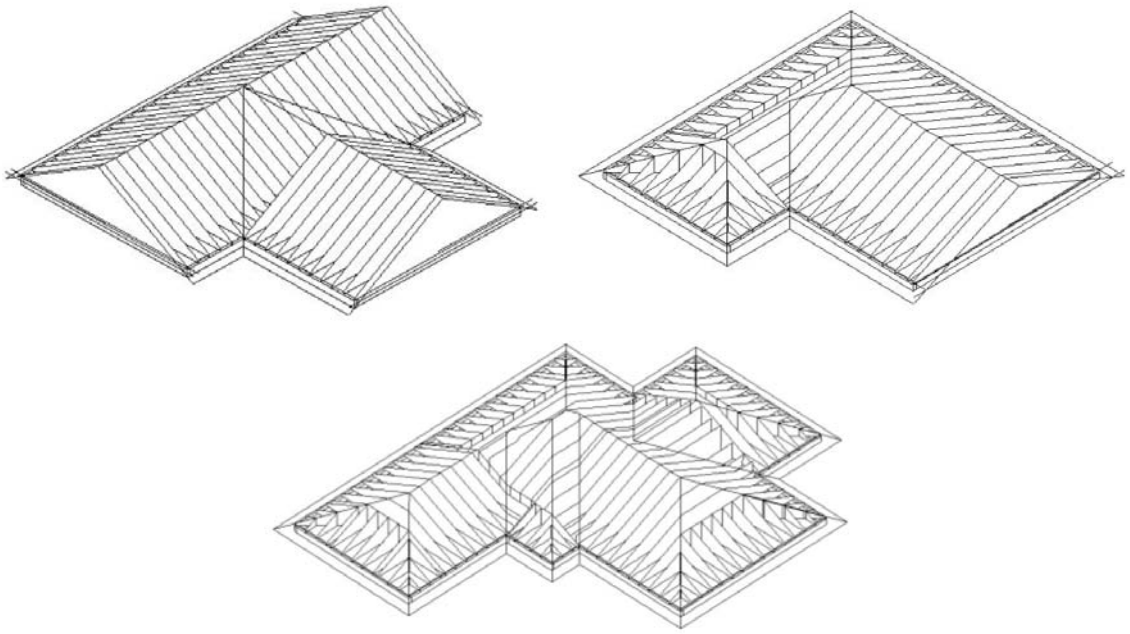

Figure 2-5. Three complex roof models studied by Limkatanyoo (2003)

Limkatanyoo (2003) reported three system effects observed by using the SDP that are not accounted for in the CDP:

- The applied load on the trusses was up to 10% less in the SDP than the CDP since the SDP accounts for the actual tributary area of each individual truss representing a more realistic applied load. In the CDP, two-foot truss spacing and

subsequently a two-foot tributary width for each truss is always assumed. Since trusses are not always spaced at two feet on center, the SDP accounts for this effect, effectively reducing the actual applied load to the trusses.

- The CDP assumes that each truss reaction support has no deflection (e.g., sits on a wall). However, many trusses have elastic (or spring) supports as they are supported by other trusses or wood girders. These displacements are not accounted for in the CDP, but the SDP does include these effects.

- Stiffer trusses (e.g., gable end trusses and 2-ply trusses, meaning two trusses set side-by-side and fastened together) attract more load and thus reduce the combined stress index (CSI) in the adjacent trusses. In general, maximum CSI values were reduced up to 60% in the SDP over the CDP. However, CSI values can increase in the SDP as well, typically in the gable end truss since they have a larger tributary area due to the roof overhang.

Limitations of Limkatanyoo (2003) and Gupta and Limkatanyoo (2008) studies. One of the limitations of these studies is that the sheathing was modeled using frame elements instead of shell or plate elements. Another limitation is that the roofs modeled were not supported on walls. Walls provide support conditions that are neither pins nor rollers but rather something in between. Since changing the support conditions can have a significant effect on the load distribution (Gupta et al. 2004), accounting for the walls is important.

Gupta et al. (2004) study. Gupta et al. (2004) further extended the analysis of a complex 3D roof system using the SDP. Using commercially available 3D structural analysis program (SAP2000 by Computers and Structures, Inc.), they modeled a T-shaped roof with fourteen different truss types typical of this type of residential LFWS. Their analysis included comparing CSI values for the truss members. Several important conclusions resulted from this study by Gupta et al. (2004):

- CSI values decreased by as much as 43% when the trusses were analyzed using the SDP as compared with the CDP. While most trusses saw a decrease in CSI values, a few select trusses experienced an increase in CSI to greater than 1.0, indicating that truss failure would occur. Therefore, one of the values of the SDP

method is to identify assembly weak points (i.e., inadequately designed) that need to be strengthened.

- The interaction between different trusses, including truss support conditions, significantly affected the load sharing in the assembly and the reaction forces. The SDP can more accurately model the actual support conditions than the CDP (which always assumes a pin-roller support condition).

- It is feasible to use a simple 3D structural analysis software package to design wood truss roof assemblies, while accounting for several additional parameters (e.g., roof geometry, interaction of different types of trusses, and support conditions) that are not included in the conventional design procedure. However, one observation made is that the placement of sheathing beam elements may significantly affect the behavior (results) of the 3D roof model.

Limitations of Gupta et al. (2004) study. One of the limitations of this model is that the sheathing was modeled as beam strips instead of shell elements. It is unclear how this modeling issue (of using beam strips for sheathing which is common in many FE models in the literature) affects load sharing in the roof assembly. Another drawback to this model is that the truss heel and peak joints were not simple pin or rigid connections but rather semi-rigid consisting of small trusses themselves with cross bracing using different MOE and cross-sectional area values. These types of connections are time consuming to develop and input into a FE model. In fact, Gupta (2005) believes that the variation in member properties is much less important in overall system behavior than the system geometry and types of trusses used in the system.

Model-Scale Studies on Load Sharing in Wood Roof Assemblies

Mani (1997) study. Mani (1997) conducted a load sharing study for a simple gable wood truss roof to investigate load distribution for uplift loads by utilizing a $1/8^{th}$-scale structural roof model of a LFWS building (Figure 2-6). The main objective of this experiment was to develop influence functions for evaluating design wind loads at roof-to-wall connections in low-rise, wood-framed structures. These influence functions were

to be used in future research by combining them with wind tunnel generated pressures to produce time histories of wind loads on roof-to-wall connections to quantify the magnitudes of uplift loads at these connections during extreme wind events. The model roof trusses were constructed with basswood and scaled geometrically to 1/8th of the dimensions of a standard nominal 2×4 with a roof slope of 5:14 (20°). The truss plates were made of 1/32nd-inch thick sheets of 3-ply model aircraft plywood and glued to the truss members. Two roof assembles were constructed consisting of 9 and 21 trusses spaced at three inches on center with 1/16th-inch thick sheets of 3-ply model aircraft plywood attached to the top chords of the trusses. The truss reactions (i.e., roof-to-wall connections) were all instrumented with a specially designed load cell designed to mimic the vertical stiffness of a typical wood-framed wall.

Figure 2-6. 1/8th scale roof model used by Mani (1997)

Mani then determined structural influence coefficients for each truss reaction by applying gravity (vertically downward) loads at various locations on the roof. Mani found reasonable agreement between the influence coefficients for gravity loading from the 1/8th scale model (Figure 2-7) and those of Wolfe and McCarthy (1989) on the full-scale roof assembly. He then determined influence functions for the roof-to-wall connections for uplift loads by pulling on the roof at multiple locations. Next, using the design wind pressures determined for the roof with the main wind force resisting system (MWFRS)

provisions in ASCE 7-95, Mani used the experimental influence functions to develop full-scale reaction loads. He found that using influence functions produced higher loads (40% higher) on the end truss compared to the load produced using tributary area, but comparable loads for most of the interior trusses. This implies that the tributary area methodology is not conservative for end truss reaction points.

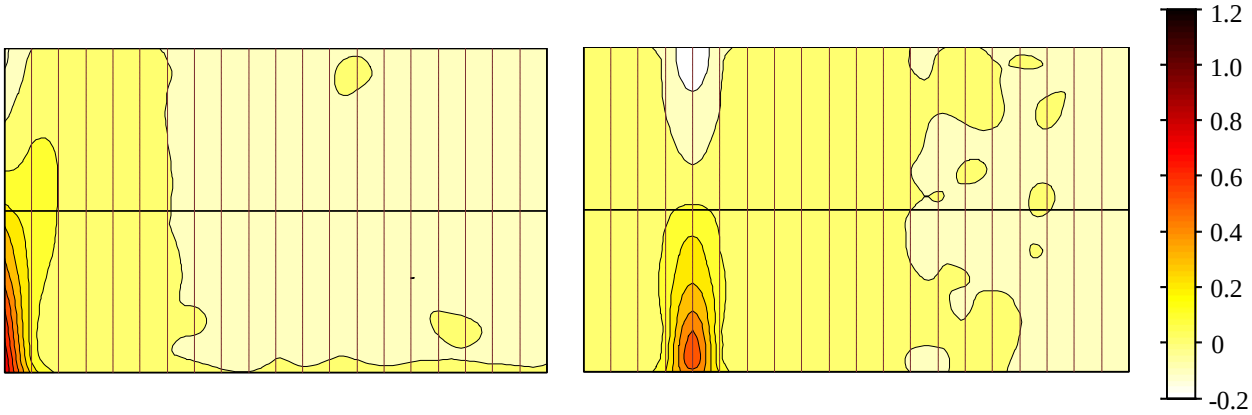

Figure 2-7. Influence surfaces for gable end and interior connections

Limitations of Mani (1997) study. The experimental model used by Mani was unable to create complete proper similitude requirements at the 1/8th scale model used. Although truss members were scaled appropriately, the wood gusset plates at the joints were overly stiff (modeled as rigid connections) for them to represent metal-plate-connections (which are semi-rigid connections). Mani's study was important as a first step in showing that there is a difference, at least to some degree for some trusses, that using influence functions produces higher loads than the widely accepted and used tributary area methodology. However, another limitation to Mani's study was that the influence functions were combined with design pressures and not actual fluctuating pressures.

Datin and Prevatt (2007) study. Datin and Prevatt (2007) conducted a study to experimentally determine load-transfer (or influence) functions for a typical wood-

framed, gable roof residential structure and then combine them with wind-tunnel derived pressure coefficients to determine wind uplift reactions at roof-to-wall connections. They constructed a 1/3-scale roof model (Figure 2-8a) using trusses developed by Gupta et al. (2005), which is reviewed in detail later. For construction of this roof model, proper structural scaling laws were used (Harris and Sabnis 1999) and will be elaborated on in a later section. The 1/3rd scale trusses were constructed of southern yellow pine (SYP) with each truss joint modeled using scaled metal plate connectors constructed of 30 gage sheet metal with between 24 and 40 staples 0.25 in. in length. The trusses were supported on a rigid steel angle (Figure 2-8b), and only three end trusses were instrumented with load cells on both ends. Beam strips were used to model the sheathing that provided a scaled flexural stiffness of 15/32 in. thick oriented strand board (OSB). Influence coefficients were determined at the three end truss reactions by applying point loads to the roof at the intersection of the beam strips and trusses. Figure 2-9 provides the influence function matrix developed for reactions A2 and C2 (Figure 2-9a), which shows that loaded trusses more than two trusses away from the reaction of interest had little to no effect on the reaction.

Datin and Prevatt (2007) then combined wind tunnel data recorded for a simple gable roof structure with the influence functions to determine the reaction time histories. The same procedure was also repeated using tributary areas of the roof trusses to determine the reaction time histories. Figure 2-10 provides an example of the dynamic reaction loads developed using these two methods. As can be seen, when using the influence functions, the magnitude of the dynamic load is much higher.

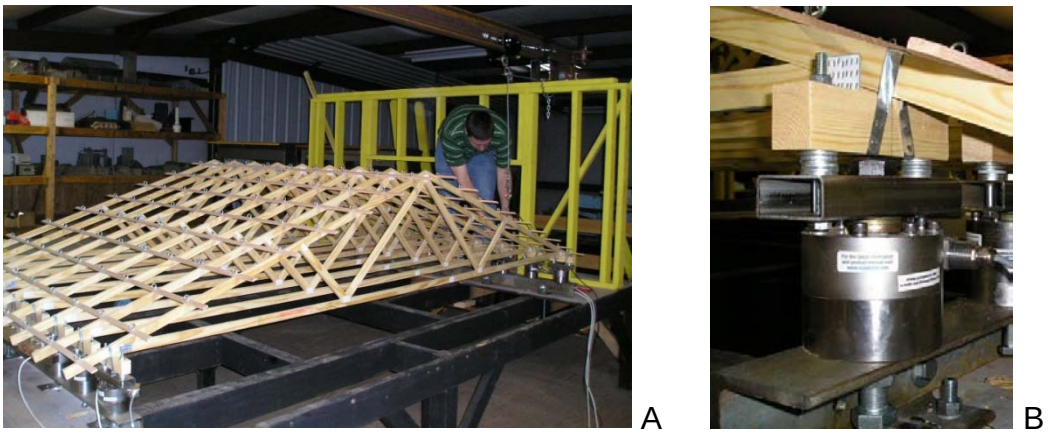

Figure 2-8. A) 1/3-scale roof assembly and B) Roof-to-wall connection detail with load cell (from Datin and Prevatt 2007)

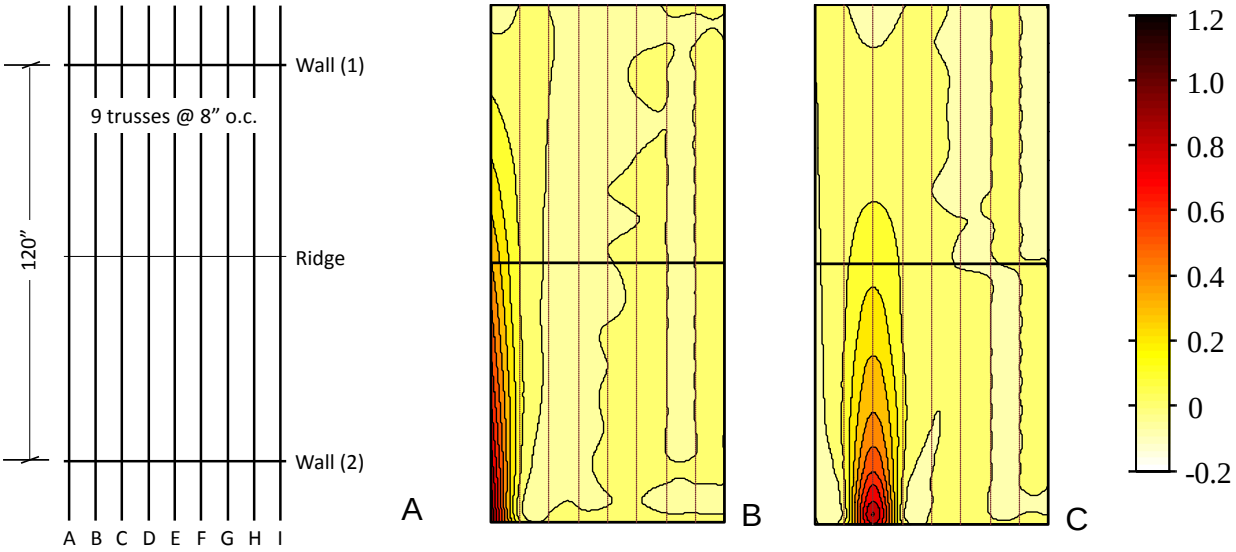

Figure 2-9. A) Roof layout and influence surface plots for B) A2 and C) C2 (after Datin and Prevatt 2007)

Limitations of the Datin and Prevatt (2007) study. A shortcoming of this study is the modeling of the sheathing with beam strips having an equivalent out-of-plane stiffness of the sheathing. In retrospect, it was determined this reduces the effect of partial composite action due to nailed sheathing connections. The anchorage of the truss reactions was also not realistic. The trusses were supported on discontinuous “top plates” that were then attached to a rigid steel channel. To be more realistic, a

continuous top plate on a wood wall is needed so that the effects of the less stiff (than the 3x3x3/8 steel angle) wall can be realized.

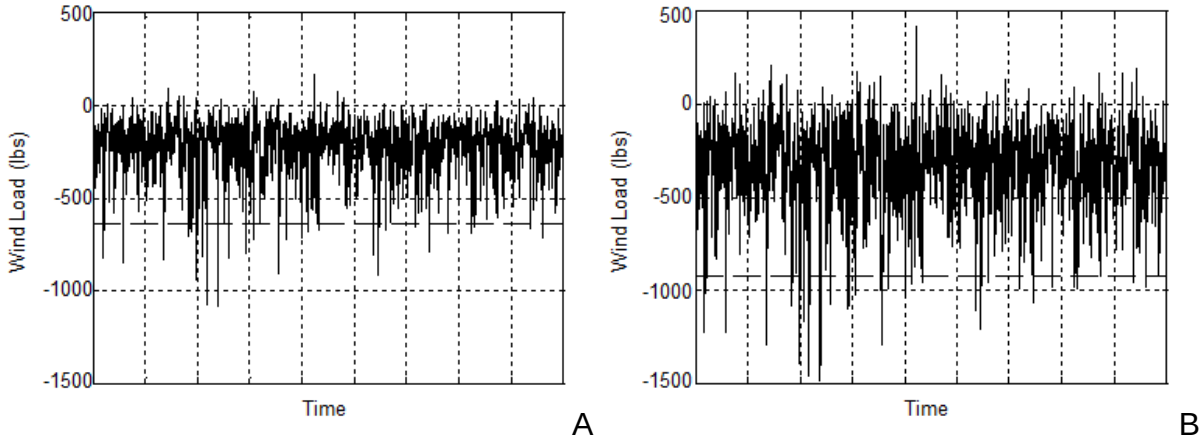

Figure 2-10. Wind load time history for reaction B1 with a 45° wind angle using A) Tributary area methodology and B) Influence function methodology. (The dashed line is the 99th percentile value.) (from Datin and Prevatt 2007)

Recent Full-Scale Studies of Wood Building Behavior

Doudak et al. (2005) study. Doudak et al. (2005) monitored a LFWS subjected to environmental loading (e.g., snow and wind) to prove the feasibility of monitoring the structural response of LFWS to snow and wind loads for extended periods. The LFWS was an industrial shed measuring 49 ft by 26 ft with a flat roof 16.7 ft high that is attached to another LFWS along one of the short walls. The walls consisted of nominal 2×6 spruce-pine-fir (SPF) lumber spaced at 16 in. on center and 0.5 in. thick 4 ft by 8 ft plywood wall sheathing. The roof consisted of 18 in. deep wood I-joists spaced 16 in. on center and sheathed with plywood. Displacements of three adjacent sets of parallel studs and roof joists were monitored. Wind pressures were measured along one of the short walls. The roof was subjected to both a uniform load (applied by flooding the roof) and point loads applied near the instrumented joists. Point loads were also applied normal to the walls at the top and mid-height.

Doudak et al. (2005) found that when a point load (675 lbs) was applied at midspan of a roof joist, 73% of that load was redistributed to adjacent joists based on displacement readings. Limited conclusions can be made about the wind loading due to the variability in wind speeds and directions, and the pressure coefficients used in the calculations were simplified.

Limitations of Doudak et al. (2005) study. The conclusions of this study are limited since only deflections were measured resulting in limited knowledge of the actual load behavior of the system. This study was also conducted on a large industrial wood building with wood I-joists supporting the roof. Therefore, the behavior of a residential LFWS with shorter walls and trusses might be different.

Zisis et al. (2009) study. Zisis et al. (2009) conducted an interesting study investigating structural load paths in a residential LFWS subjected to natural wind loads. The building, located in Fredericton, New Brunswick, Canada, is a rectangular single story gable LFWS measuring 28 ft by 56 ft in plan with a mean roof height of 18 ft and a 4 in 12 roof slope. The building contains 40 pressure sensors, including 28 on the roof that are concentrated near three “main frames” (interpreted to mean three trusses). The house is supported entirely on 27 3D load cells with an additional six load cells located at the roof-to-wall connections of the three “main frames” with the concentration of pressure sensors. The objective of the experiment is to determine the structural attenuation (i.e., load dissipation due to the dynamic response of the building by energy absorption) of the wind loads as they are transferred from the roof to the roof-to-wall connections and eventually through the wall-to-foundation connections. The data presented are for a frame located at the center of the building. A simplified 2D

structural analysis was performed of the frame consisting of the roof truss and a wall stud supporting each end of the truss. The tributary areas of the pressure taps located near the frame were used along with recorded wind pressures to determine the predicted structural reaction loads at the roof-to-wall and wall-to-foundation connections. The simplified structural analysis results were compared with the actual recorded loads for the same wind records. They found that the loads predicted by the structural analysis were 26-46% higher than the measured loads for the roof-to-wall connections and 21-42% higher than the measured loads for the wall-to-foundation connections. This reduction is attributed to structural attenuation of the building system.

Limitations of Zisis et al. (2009) study. One of the major limitations of this study is the over-simplified structural analysis model used to determine the amount of structural dissipation in the building. As has been shown by the various studies by Gupta (2005), system effects can have a major effect on load distribution. The complexity of residential LFWS makes such simplifications questionable. Another possible limitation is that the maximum wind speeds measured at the structure were only 21 mph with a mean of 12 mph. Additionally, neither displacements nor accelerations were measured to quantify any dynamic effects of the roof or walls. A quantitative measure of structural attenuation (i.e., energy loss) in the system is needed before making the conclusion that up to 46% of the applied wind loads are "disappearing" in the structure.

Roof Sheathing

Datin et al. (2010) provide a detailed review of all known pressure testing of wood roof sheathing panels. Two main observations are drawn from this review: (1) all roof sheathing tests conducted used a uniform static load – either a stepping function or a

monotonically increasing uniform load and (2) there is also no consensus or standard wood roof sheathing test procedure. Datin et al. proposed a standardized test method for testing of wood roof sheathing panels (called UF-WRSUT) and conducted multiple tests of sheathing panels with various nails and nail spacings using the proposed test. The results are generally within the magnitude of the previous tests on wood roof sheathing.

Hill et al. (2009a; 2009b) investigated the effects of dynamic loads on wood roof sheathing compared to the traditional uniform, static testing. They tested 4 ft by 8 ft by 0.5 in. thick oriented strand board (OSB) roof sheathing panels fastened to southern yellow pine (SYP) 2×4s using various nail sizes and spacings. The panels were installed in a pressure chamber and loaded with both a uniform static load in a step sequence (i.e., load in 15 psf increments and hold at each pressure step for 10 seconds) and a uniform dynamic loading sequence developed from wind tunnel pressure traces. They found that with the dynamic loads, the average ultimate capacity of the sheathing was reduced by about 20% from the average ultimate capacity using static loads. This result implies that the current static pressure testing procedures may not be appropriate for estimating the wind uplift resistance of wood roof panels and likely overestimates the failure capacities of the panels. The continued failure of sheathing panels in extreme wind events may partially be due to this misunderstanding of the failure capacities of roof sheathing by overestimating them. Additionally, during the dynamic testing of the panels, the sheathing panels deflected substantially between the framing members and appeared to be “bouncing” as the pressures fluctuations were applied, implying that the sheathing is not rigid and is indeed a flexible membrane.

Dixon and Prevatt (2010) revisited the dynamic testing of wood roof sheathing panels performed by Hill et al. (2009a; 2009b) using a modified dynamic trace developed by Datin and Prevatt (2009) that contained fewer “peaks” than that used by Hill et al. Dixon and Prevatt found that there was no statistical difference in loading the roof panels with a static pressure versus the dynamic pressure. This is in contrast to the findings of Hill et al. where a 20% decrease in panel failure pressures was observed for the dynamic loading compared to static loading. Continuing studies are underway at the University of Florida to evaluate the effect of dynamic fluctuations on wood roof sheathing panel failures.

Roof-to-Wall Connections

Riley and Sadek (2003) tested two types of roof-to-wall connections (toe-nailed connections and hurricane clips) in order to determine overall behavior and performance including failure mechanisms under uplift loads, in-situ behavior of the connections, and displacements and forces that occur in the connections. For the toe-nailed connections, a constant uplift load was applied at a rate of 0.25 in./min for approximately 360 seconds. The maximum load achieved in the connection was approximately 3,900 lbs. After about 125 seconds of load, the connection lost almost all capacity to transfer load. The hurricane clip was tested to a maximum load of approximately 6,000 lbs. The first hurricane clip failure was actually the top plate pulling off of the studs with the hurricane clip still firmly attached. After repairing the connection, the hurricane clip performed much better and the failure mode was still the top plate splitting down the middle and separating.

Cheng (2004) conducted experiments on over 300 individual toe-nailed connections using ASTM D1761 (ASTM 2006a) to determine and compare the uplift

capacities with current building code defined wind loads. The main conclusion of Cheng's work was that most toe-nailed connections will fail in a 90 mph design wind speed provided in ASCE 7. He found that most of the connection failures were due to nail withdrawal from the wall plate and confirmed that toe-nailed connections are not safe in hurricane and tornado prone areas.

Ellingwood et al. (2004) performed a fragility analysis comparing the capacity of toe-nailed connections and a metal hurricane clip. The probability of connection failure is greatly reduced when a metal clip is used instead of just a toe-nailed connection. Ellingwood et al. also conducted a sensitivity analysis to determine which factors are the most dominant in the failure of roof-to-wall connections and found that wind speed was the predominant factor.

Shanmugam et al. (2009) tested in-situ roof-to-wall connections in 50-60 year old residential LFWS consisting of two or three toe nails per connection. Four roof-to-wall connections were tested simultaneously by loading the four connections with a spreader beam and measuring load and displacement of the connection. A cyclic loading sequence was selected based on ASTM D1761 (ASTM 2006a) to quantify the hysteretic behavior (i.e., energy dissipation) in the connections due to dynamic loading. An analytical model for use in finite element analysis of the response of the toe-nailed roof-to-wall connections was proposed that includes strength and stiffness degradation (i.e., nonlinear behavior) of the connections. This model was shown to predict the energy dissipation of the connections within 7% of the actual measured energy dissipation.

Morrison and Kopp (2010) tested toe-nailed roof-to-wall connections using both ramp loads and realistic wind load time histories using a pressure load actuator. For the

three ramp rates used (225, 1800, and 7200 lbs/min), the average failure capacities were nearly identical with an average value of 630 lbs and a range of 270 to 1050 lbs indicating that the toe-nailed connection strength is independent of the loading rate. For the wind load time history, the failure capacities were in the same range as the ramp loading. Additionally, Morrison and Kopp (2010) found that the realistic wind loads failed the toe-nailed connections incrementally and at loads less than the maximum applied load. They concluded that the number of peaks experienced by the connection has a higher significance than the magnitude of the peaks.

Estimation of Structural Forces using Wind Tunnel Data

Several methods have been developed to estimate the mean and peak structural responses (e.g., moments, shears, reactions, etc.) of low-rise structures subjected to varying wind loads. Three of these methods are discussed in this section: (1) covariance integration method (Holmes and Best 1981), (2) load-response correlation method (Kasperski 1992; Kasperski and Niemann 1992), and (3) database-assisted design (Simiu and Stathopoulos 1997).

Covariance Integration (CI) Method

The covariance integration method was developed by Holmes and Best (1981) for determining the fluctuating overall structural loads due to wind on a low-rise building. Assuming a Gaussian distribution for the structural loads, the peak loads are also determined. Wind tunnel data is used along with static influence coefficients to predict these effects.

The root-mean-square (RMS) of the fluctuating value of any structural effect, η, is related to the loads on N individual panels (or areas) exposed to wind pressures by Eqn. 2-4.

$$\left(\overline{\eta'^2}\right)^{1/2} = \left(\sum_{i=1}^{N}\sum_{j=1}^{N}\overline{p_i'p_j'}\,\beta_i\beta_j A_i A_j\right)^{1/2} \tag{2-4}$$

where: $\overline{p_i'p_j'}$ is the covariance between the fluctuating wind pressures $p_i(t)$ and $p_j(t)$ acting on panels i and j. β_i and β_j are the influence coefficients associated with the panels i and j of areas A_i and A_j, respectively.

The covariance term can also be written in the form of Eqn. 2-5.

$$\overline{p_i'p_j'} = \left(\frac{1}{2}\rho\bar{V}^2\right)^2 C_{pi}'C_{pj}'r_{ij} \tag{2-5}$$

where: C_{pi}' and C_{pj}' are the RMS values of the fluctuating pressure coefficients, r_{ij} is the cross-correlation coefficient, and $\frac{1}{2}\rho\bar{V}^2$ is the dynamic pressure. Substituting Eqn. 2-5 into Eqn. 2-4, the RMS value of the structural effect yields Eqn. 2-6.

$$\left(\overline{\eta'^2}\right)^{1/2} = \frac{1}{2}\rho\bar{V}^2\left(\sum_{i=1}^{N}\sum_{j=1}^{N}r_{ij}C_{pi}'C_{pj}'\,\beta_i\beta_j A_i A_j\right)^{1/2} \tag{2-6}$$

In order to determine the peak structural response over a specified time period, T, a Gaussian distribution is assumed for the structural load, η. While this assumption of normality needs to be further investigated, Holmes and Best state that since the structural effects are influenced by pressure over large areas with corresponding influence coefficients with varying sign, the central-limit theorem will tend to make the probability distribution of the structural effect close to Gaussian.

Following the developments by Cartwright and Longuet-Higgins (1956) and Davenport (1964), the average peak value over a time period, T, is given by Eqn. 2-7 (assuming a Gaussian distribution for the structural load).

$$\hat{\bar{\eta}} = \bar{\eta} \pm \left(\overline{\eta'^2}\right)^{1/2} \left(\sqrt{2ln(\upsilon T)} + \frac{\gamma}{\sqrt{2ln(\upsilon T)}} \right) \tag{2-7}$$

where: γ is Euler's constant (0.5772), and υ is the cycling rate for the response, $\eta(t)$, shown in Eqn. 2-8.

$$\upsilon = \frac{\left(\overline{\dot{\eta}'^2}\right)^{1/2}}{2\pi\left(\overline{\eta'^2}\right)^{1/2}} \tag{2-8}$$

where: $\left(\overline{\dot{\eta}'^2}\right)^{1/2}$ is the RMS of the derivative of $\eta(t)$ given in Eqn. 2-9.

$$\left(\overline{\dot{\eta}'^2}\right)^{1/2} = \frac{1}{2}\rho\bar{V}^2 \left(\sum_{i=1}^{N}\sum_{j=1}^{N} \dot{r}_{ij}\dot{C}'_{pi}\dot{C}'_{pj}\,\beta_i\beta_j A_i A_j \right)^{1/2} \tag{2-9}$$

where: $\dot{C}'_{pi}$ and $\dot{C}'_{pj}$ are the RMS values of dC_{pi}/dt and dC_{pj}/dt, respectively, where dC_p/dt is the time derivative of the pressure coefficient time history, and $\dot{r}_{ij}$ is the cross-correlation matrix of the derivative of the pressure fluctuations.In order to calculate the derivatives of the pressure coefficient time histories, a numerical differentiation technique is used called backward difference. This technique is implemented by using Eqn. 2-10:

$$\dot{C}_{pi}(t) = \frac{dC_{pi}(t)}{dt} \approx \frac{C_p(t_i) - C_p(t_{i-1})}{t_i - t_{i-1}} \tag{2-10}$$

where: the time steps, t_i, were calculated based on the reduced frequency scaling for a given full-scale wind speed.

The mean value of the structural response is given by Eqn. 2-11.

$$\bar{\eta} = \frac{1}{2}\rho\bar{V}^2 \sum_{i=1}^{N} \overline{C_{pi}}\beta_i A_i \tag{2-11}$$

Load-Response Correlation (LRC) Method

The load-response-correlation (LRC) method is a method developed by Kasperski and Niemann (1992) and also described in Kasperski (1992) for determining the peak overall structural loads due to wind on a low-rise building. The LRC method assumes a Gaussian distribution for the structural effect. Wind tunnel data is used along with static influence functions to predict these effects. The LRC method is described in the following paragraphs.

The maximum response of a structural effect, r_i, is given by Eqn. 2-12.

$$\eta_{i,max} = \sum_{k=1}^{m} \beta_{ik}\overline{p_k} \pm g_\eta \left(\sum_{k=1}^{m}\sum_{l=1}^{m} \beta_{ik}\beta_{il}\sigma_{p_{kl}}^2 \right)^{1/2} \quad (2\text{-}12)$$

where: β_k is the influence function of load k to response i, $\overline{p_k}$ is the mean value of load *k*, g_η is the peak factor, and $\sigma_{p_{kl}}^2$ is the covariance of load *k* and *l*.

Eqn. 2-12 can also be written in the form of Eqn. 2-13.

$$\eta_{i,max} = \sum_{k=1}^{m} \beta_{ik}\overline{p_k} \pm g_\eta \frac{\sum_{k=1}^{m}\beta_{ik}\sum_{l=1}^{m}\beta_{il}\sigma_{p_{kl}}^2}{\sigma_{\eta_i}} \quad (2\text{-}13)$$

where:

$$\sigma_{\eta_i p_k}^2 = \sum_{l=1}^{m} \beta_{il}\,\sigma_{p_k}^2 = \rho_{\eta_i p_k}\sigma_{\eta_i}\sigma_{p_k} \quad (2\text{-}14)$$

where: $\rho_{\eta_i p_k}$ is the load-response-correlation, σ_{η_i} is the standard deviation of response i, and σ_{p_k} is the standard deviation of load k.

Substituting Eqn. 2-14 into Eqn. 2-13 yields Eqn. 2-15.

$$\eta_{i,max} = \sum_{k=1}^{m} \beta_{ik}\overline{p_k} \pm g_\eta \sum_{k=1}^{m} \beta_{ik}\,\rho_{\eta_i p_k}\sigma_{p_k} \quad (2\text{-}15)$$

The load-response-correlation, $\rho_{\eta_i p_k}$, is the correlation of the response, η_i, and the load, p_k, and is given by Eqn. 2-16:

$$\rho_{\eta_i p_k} = \frac{\sum_{l=1}^{n} \beta_{il} \sigma_{p_{kl}}^2}{\left[\sum_{l=1}^{n} \beta_{il} \sum_{m=1}^{n} \beta_{im} \sigma_{p_{lm}}^2\right]^{1/2} \sigma_{p_k}} \tag{2-16}$$

Since, our data is in terms of pressure coefficients, the load-response-correlation is given by Eqn. 2-17 and the maximum response, $\eta_{i,max}$, is given by Eqn. 2-18.

$$\rho_{\eta_i p_k} = \frac{\sum_{l=1}^{n} \beta_{il} A_l \sigma_{Cp_{kl}}^2}{\left[\sum_{l=1}^{n} \beta_{il} A_l \sum_{m=1}^{n} \beta_{im} A_m \sigma_{Cp_{lm}}^2\right]^{1/2} \sigma_{Cp_k}} \tag{2-17}$$

$$\eta_{i,max} = \frac{1}{2} \rho \bar{V}^2 \sum_{k=1}^{m} \beta_{ik} A_k \left[\overline{C_{pi}} \pm g_\eta \rho_{\eta_i p_k} \sigma_{Cp_k}\right] \tag{2-18}$$

Kasperski (2007) presented a methodology, using the LRC method, for determining design wind loads on gable roof buildings that was adopted in a draft of ISO 4354, an international code on wind actions. This new approach uses fractiles of the pressure coefficient distributions with an extreme value Type I (Gumbel) distribution assumed for the peak pressure coefficients. Then, the design pressure coefficient, $C_{p,des}$, is the 80%-fractile of the peak pressure coefficient distribution, given in Eqn. 2-19.

$$C_{p,des} = \hat{C}_{p,80\%} = \mu_{\hat{C}_p} \left(1 + 0.7 \frac{\sigma_{\hat{C}_p}}{\mu_{\hat{C}_p}}\right) \tag{2-19}$$

where: $\hat{C}_{p,80\%}$ is the 80%-fractile of the extreme pressure coefficients; $\mu_{\hat{C}_p}$ is the mean value of the extreme pressure coefficients; and $\sigma_{\hat{C}_p}$ is the standard deviation of the extreme pressure coefficients. With this in mind, the LRC method provides an effective

pressure distribution, $C_{p,eff}$, for design purposes by combining the mean pressure distribution and a weighted standard deviation component (Eqn. 2-20).

$$C_{p_i,eff} = \mu_{C_{p_i}} + g_\eta \rho_{\eta p_i} \sigma_{C_{p_i}} \tag{2-20}$$

where: $\mu_{C_{p_i}}$ is the mean pressure coefficient; g_η is the peak factor for the response considered; $\rho_{\eta p_i}$ is the load-response-correlation between pressure at i and the response considered; and $\sigma_{C_{p_i}}$ is the standard deviation of the pressure coefficient at i. The peak factor is obtained from the fractile value of the extreme value distribution of the response shown in Eqn. 2-21 using the 80%-fractile (Kasperski 2007).

$$g_\eta = \frac{\hat{\eta}_{mean}\left(1 + 0.7\frac{\hat{\eta}_{sdev}}{\hat{\eta}_{mean}}\right) - \eta_{mean}}{\eta_{sdev}} \tag{2-21}$$

where: $\hat{\eta}_{mean}$ is the mean value of the extreme response; $\hat{\eta}_{sdev}$ is the standard deviation of the extreme response; $\eta_{mean}$is the mean value of the response (Eqn. 2-11); and η_{sdev} is the standard deviation of the response (Eqn. 2-22).

$$\eta_{sdev} = \frac{1}{2}\rho \bar{V}^2 \left(\sum_{i=1}^{N} \sum_{j=1}^{N} \rho_{p_i p_j} \sigma_{C_{p_i}} \sigma_{C_{p_j}} \beta_i \beta_j A_i A_j \right)^{1/2} \tag{2-22}$$

where: $\sigma_{C_{p_i}}$ is the standard deviation of the pressure coefficient; and $\rho_{p_i p_j}$ is the correlation coefficient between pressures p_i and p_j.

Database-Assisted Design (DAD) Methodology

The need for a database-assisted design (DAD) methodology for design of low-rise buildings was first proposed by Simiu and Stathopoulos (1997). They pointed out that current wind load provisions were based on “simplified aerodynamics and

climatological models and on summary information supplied in reductive tables." They noted several instances in the ASCE 7 Standard (ASCE 2006) where the provisions are not risk-consistent, meaning that the level of risk or probability of failure are not consistent across different building types, building materials, or loading conditions. Additionally, ASCE 7 does not allow the designer to "account realistically and comprehensively for spatio-temporal wind load effects on either linear or nonlinear structural behavior," including gust factors, wind load factors, wind directionality effects, and pressure coefficient dependence on building geometry. They also mention that improving the building standards and codes has a practical limit since modification upon modification would result in bulky and complex provisions. They proposed a DAD philosophy, which would allow a designer to consider a site specific design rather than using the conventional provisions.

Wind tunnel data used to develop the wind load provisions in the ASCE 7 Standard were greatly simplified for codification purposes and use with slide-rule calculations. Simiu et al. (2003) showed using DAD software that these simplified procedures can lead to errors up to 50% in the estimation of wind effects.

The first DAD software development conducted by the National Institute of Standards and Technology (NIST) was reported by Whalen et al. (1998). Utilizing wind tunnel studies of various buildings having similar shapes but different sizes, the DAD software interpolates between the wind tunnel time histories to arrive at an estimate of the structural response in question (i.e., moment at a knee joint in a frame, shear at a support, etc.). The strength of this design philosophy is that it is able to analyze a building for wind and estimate the maximum structural responses for any wind direction

without having to perform an actual wind tunnel study specific to that structure. The DAD software developed at NIST accounts for wind speeds at or near the given site (Batts et al. 1980) including directionality effects and wind speed probability distributions for a given wind direction at the site. The DAD methodology provides a more risk-consistent design leading to safer and more economical structures better able to withstand extreme wind forces.

One of the earliest versions of the DAD software was called WiLDE-LRS (Wind Load Design Environment for Low-Rise Structures) (Whalen et al. 2000). The purpose of this software was to show that a DAD approach was realistic and indeed necessary to improve wind resistant design of low-rise structures and focused on steel portal-framed buildings. After undergoing several iterations and modifications, an improved version of WiLDE was developed called windPRESSURE (**wind P**eak **R**esponse **E**stimation for **S**tatic **S**tructures **U**sing **R**ecorded **E**xperiments) (Main and Fritz 2006), which is an open-source MATLAB-based program.

There are four main components of the DAD software (Main and Fritz 2006):

- *Aerodynamic databases* – These databases are wind tunnel pressure time histories and are saved into a data format called Hierarchical Data Format (HDF) developed at the National Center for Supercomputing Applications (NCSA) at the University of Illinois at Urbana-Champaign (see http://hdfgroup.org for more information on the HDF format) allowing for much smaller size data files. Utilizing the pressure time histories in this way, no preprocessing of the data is needed as in previous versions of the software (Whalen et al. 1998; Whalen et al. 2000).
- *Climatological databases* – These databases include probability distributions for extreme wind speeds for various locations along the Gulf and Atlantic Coasts of the US. The extreme wind speeds were developed by Batts et al. (1980) using a Monte Carlo simulation for 999 hurricanes for various mileposts along the coast.
- *Specified return period* – The DAD software can look at wind speeds with a mean recurrence interval of 50, 100, 250, 500, 750, and 1000 years corresponding to the simulated wind speeds developed by Batts et al. (1980).

- *Structural influence coefficients* – The current DAD software utilizes structural influence coefficients developed analytically with computer models. At present, the only type of influence coefficients included in the software (available from NIST) are for a steel, portal-frame building.

To determine a given response time history using the aerodynamic databases, the pressure coefficient time histories are combined with structural influence coefficients as shown in Eqn. 2-23 (Main and Fritz 2006).

$$\eta_{\theta j}(t) = \frac{1}{2}\rho V_H^2 \sum_{i=1}^{n} \beta_{ij} A_i \left[C_{p,\theta}(t)\right]_i \tag{2-23}$$

where: η_θ is the response time history at reaction point j for a given wind direction θ; ρ is the density of air; V_H is the mean wind speed at roof height H; β_i is the influence coefficient at location i for reaction point j; A_i is the tributary area at location i; and $\left[C_{p,\theta}(t)\right]_i$ is measured pressure coefficient time history for a given wind direction θ at location i. Eqn. 2-23 does not directly account for the climatological information or a specified return period, however, by selecting the appropriate V_H and θ, this information is included.

Several important issues have been raised with the help of the DAD software. Whalen et al. (2002) found a large inconsistency in the current building code standards (including ASCE 7) with respect to mean recurrence interval for directional wind effects. They found that directionality has a large influence on the peak responses of a building subjected to wind loads. The current ASCE 7 design standard (ASCE 2006) uses a directionality reduction factor of 0.85, but Whalen et al. (2002) found that, while this may be appropriate for a 50-year mean recurrence interval, it is not conservative for many directions when the recurrence interval is larger corresponding to ultimate limit states. In these cases, the directionality factor should be closer to unity. Rigato et al. (2001)

also found similar results for the directionality factor. They concluded that using a directionality factor of 0.85 may result in 10-15% of buildings designed according to ASCE 7 underestimating the extreme wind effects. Whalen et al. (2002) also found that steel, portal-frames designed according to ASCE 7 standards have widely varying capacities for different cross-sections. Another important finding using the DAD approach is that time histories of wind-induced load effects in low-rise buildings are non-Gaussian, meaning that other methods for estimating peak responses due to wind-induced loads are needed other than typical (and easier) Gaussian distribution properties.

Jang et al. (2002) discuss in detail the analysis and comparison of a low-rise, steel, portal-frame building using the DAD methodology and ASCE 7. They again show the lack of risk consistency in the current building standard provisions. Simiu et al. (2003) found that by using the DAD approach, pressure coefficients for low-rise buildings are dependent on the terrain roughness, a fact for which ASCE 7 does not account.

Ultimately, the DAD procedure would be best incorporated with a system design procedure (SDP) as outlined by Gupta and Limkatanyoo (2008) for the most efficient and reliable design methodology for low-rise, wood-framed buildings. This combined approach would provide risk consistency and result in more robust and economical designs capable of resisting extreme winds, thus reducing the damage and economic losses associated with these disasters.

Small-Scale Structural Modeling

The use of physical structural models (as opposed to analytical models) is arguably the best way for engineers and scientists to establish performance, since

analytical models use assumptions that do not capture the entire effect of what actually happens. However, full-scale models tend to be costly and occupy valuable laboratory space. Small-scale structural models offer a less costly option for experiments, and in some instances they can be easier to work with. This cost reduction includes less material costs, smaller test frames, and less robust loading equipment and measurement devices (e.g., load cells, linear variable displacement transducers or LVDTs, etc.). One of the benefits to using scaled models is the significant reduction in loading that is needed, since the required load to failure is reduced by the square of the geometric scale factor (e.g., a 1,000 lb prototype load on a 1:4 scale is reduced to 62.5 lb). Along with the reduced cost of full-scale structures is the ability of a physical model to represent the actual behavior of a complete structure loaded to the collapse stage. Analytical models using computer software packages still do not accurately predict the failure capacity of the more complex three-dimensional structural systems (Harris and Sabnis 1999).

Non-Dimensional Scaling Parameters

For any experiment that is performed on a scale model, similitude requirements have to be met. In other words, certain parameters have to be kept constant between the prototype and the model. There is a whole area of study devoted to scaling laws and parameters (Harris and Sabnis 1999). The most commonly used method for determining the appropriate scaling parameter is known as the Buckingham Pi Theorem (Buckingham 1914). This method utilizes the concept of dimensional analysis to determine what parameters are of importance in modeling.

Dimensions are the basic units of measure. These fundamental measures are length (L), force (F), time (T), temperature (θ), and electric charge (Q). All other

measures can be expressed in these basic forms. For static structural modeling, the two important fundamental measures are length and force, while time is also necessary for dynamic modeling. All other units of measure can be described by these fundamental units. Table 2-2 shows the dimensions of some of the important physical characteristics for structures. Murphy (1950) lists two axioms that are the basis for dimensional analysis:

> *Axiom 1* – Absolute numerical equality of quantities may exist only when the quantities are similar qualitatively.
>
> *Axiom 2* – The ratio of the magnitudes of two like quantities is independent of the units used in their measurement, provided that the same units are used for evaluating each.

The first axiom simply means that in order to compare two things or measurements, the quantities have to have the same dimensions. For example, something measured in terms of pressure can only be equated to another quantity measured in terms of pressure. If the second quantity has units of length, force, or any units other than pressure, it cannot be equated with the first quantity. The second axiom simply means that it does not matter what units are used in defining a ratio as long as the units are the same. For example, the ratio of height to width of a window is the same whether units of inches, feet, or meters are used. These two axioms provide the basis for all dimensional analysis.

The Buckingham Pi Theorem uses dimensional analysis to determine the necessary similitude requirements. This theorem states that "any dimensionally homogeneous equation involving certain physical quantities can be reduced to an equivalent equation involving a complete set of dimensionless products" (Harris and Sabnis 1999). In other words, an equation used for a physical quantity $F(X_1, X_2,...,X_n) =$

0 can be expressed in the form $G(\Pi_1, \Pi_2, ..., \Pi_n) = 0$, where the pi terms are dimensionless products of the physical quantities $X_1, X_2, ..., X_n$. The number of pi terms, m, is determined by $m = n - r$, where n is the number of physical variables, and *r* is the number of fundamental dimensions used. Harris and Sabnis (1999) describe in detail how to actually formulate the pi terms. Wind tunnel modeling is a good example of the application of similitude requirements.

Static-elastic modeling

One of the common pi terms used in static elastic modeling is given in Eqn. 2-24.

$$\Pi = \frac{P}{EL^2} \tag{2-24}$$

where: P is the load, E is the modulus of elasticity, and L is the geometric length.

The scaling factors, S, are obtained by setting the pi terms equal for model and full-scale as shown in Eqn. 2-25, which is then rearranged, yielding Eqn. 2-26.

$$\left(\frac{P}{EL^2}\right)_p = \left(\frac{P}{EL^2}\right)_m \tag{2-25}$$

$$\frac{P_p}{P_m} = \frac{E_p L_p^2}{E_m L_m^2} = S_E S_L^2 \tag{2-26}$$

where: S_E and S_L are the scale factors of the full-scale (prototype) MOE and geometric length to model scale, respectively. Table 2-2 shows the different scaling quantities of interest in static elastic modeling and the appropriate scale factors.

Dynamic similitude

For scale models loaded with dynamic loads (i.e., time varying) dynamic similarity governs. The most common dynamic similitude requirement is given in Eqn. 2-27

(Harris and Sabnis 1999). By rearranging Eqn. 2-27, Eqn. 2-28 is presented in terms of scale factors.

$$\left(\frac{Pt^2}{mL}\right)_p = \left(\frac{Pt^2}{mL}\right)_m \tag{2-27}$$

$$\frac{P_p}{P_m} = \frac{t_m^2 m_p L_p}{t_p^2 m_m L_m} = \frac{S_L S_m}{S_t^2} \tag{2-28}$$

where: S_L, S_m, and S_t are the ratios of the full-scale (prototype) geometric length, mass, and time to model scale, respectively. Table 2-3 shows the different scaling quantities of interest in dynamic modeling and the appropriate scale factors.

Table 2-2. Similitude requirements for static elastic modeling

Quantities	Dimensions	Scale Factor
Material-Related Properties		
Stress	FL^{-2}	S_E
Modulus of Elasticity	FL^{-2}	S_E
Poisson's Ratio	—	1
Specific Weight	FL^{-3}	S_E/S_L
Strain	—	1
Geometry		
Linear Dimension	L	S_L
Linear Displacement	L	S_L
Angular Displacement	—	1
Area	L^2	$S_L^{\ 2}$
Moment of Inertia	L^4	$S_L^{\ 4}$
Loading		
Concentrated Load, *P*	F	$S_E S_L^{\ 2}$
Uniformly Distributed Line Load, *w*	FL^{-1}	$S_E S_L$
Pressure or Uniformly Distributed Surface Load, *q*	FL^{-2}	S_E
Moment, *M*, or Torque, *T*	FL	$S_E S_L^{\ 3}$
Shear Force, *V*	F	$S_E S_L^{\ 2}$

Note: Adapted from Harris and Sabnis (1999)

Previous Small-Scale Wood Modeling

After a review of the available literature, few small-scale modeling studies of structural wood have been performed. Harris and Sabnis discuss several small-scale wood projects conducted at Drexel University by students as part of term projects in a

modeling course. Parts of these studies are published in Harris and Sabnis (1999), but the actual project reports are not available. The following discussions of the previous published studies are the only known published scale studies of structural wood systems.

Table 2-3. Similitude requirements for dynamic modeling

Quantities	Dimensions	Scale Factor
Loading		
Force, P	F	$S_E S_L^2$
Gravitational acceleration, g	LT^{-2}	1
Time, t	T	$S_L^{1/2}$
Geometry		
Linear dimension, L	L	S_L
Displacement, δ	L	S_L
Frequency, f	T^{-1}	$S_L^{-1/2}$
Material properties		
Modulus of elasticity, E	FL^{-2}	S_E
Stress, σ	FL^{-2}	S_E
Poisson's ratio, ν	—	1
Specific Weight, γ	—	S_E/S_L

Note: Adapted from Harris and Sabnis (1999)

Small-scale truss modeling

Gupta et al. (2005) developed a one-third scale metal-plate-connected wood truss. The main thrust of this research was in modeling the metal-plate-connected wood truss joints. Two truss joints were investigated thoroughly: a tension splice joint (TSJ) and a heel joint (HJ). The other joint models were based on these two model joints. Figure 2-11 shows the locations of the different joints in a typical Fink style wood truss.

The study conducted by Gupta et al. (2005) utilized nominal 2×4 Douglas-Fir lumber. The model scale boards were cut and planed from these full-size members into the one-third model size of 0.5 in. by 1.17 in. A modulus of elasticity (MOE) test was conducted on the full-size boards and then on the model boards. The goal was to ensure that the model boards had the same MOE as the full-scale boards to make the

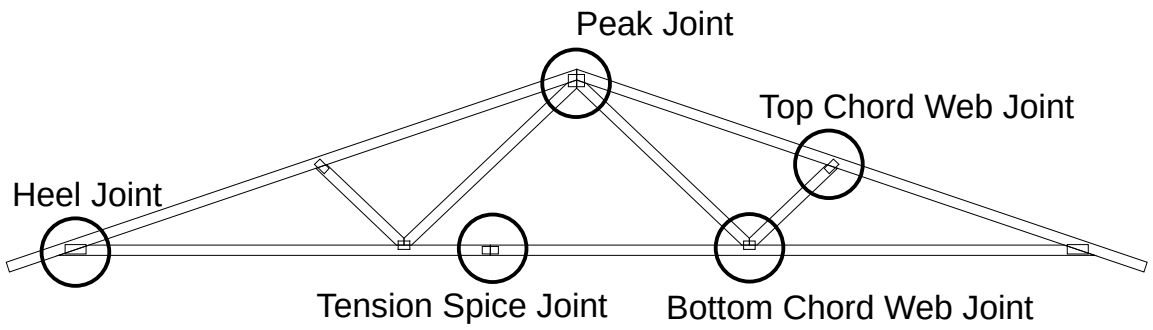

Figure 2-11. Fink truss joint labels

similitude scaling easier. The joint plates were constructed of 30-gage sheet metal which is a little thinner than the similitude requirement of 0.036 mm thick sheet metal. The 30-gage metal was selected because the staples used consistently penetrated through the material. The staples were 0.25 in. long which is twice as long as the similitude requirement, but shorter staples did not penetrate the wood far enough to hold. Therefore, the staples used corresponded to a ratio of approximately one model tooth for every two prototype truss-plate teeth.

The largest obstacle in determining the modeled truss plates was the size of the model plates and the number of staples needed in each joint. After testing various arrangements and comparing the data with full-scale joints, conclusions were reached as to which modeled connections best represented the full-scale connections. Once the dimensions and staple arrangements were selected for the TSJ and the HJ, the other truss joint configurations were extrapolated.

Gupta et al. (2005) then constructed full one-third scale trusses. The trusses were then tested by loading them at the peak joint and the two top chord web joints simultaneously with the same load. Deflections were measured at several locations on the truss and the stiffnesses of the trusses were determined. After scaling the model

truss stiffness to full scale, the average stiffnesses compared favorably with stiffnesses reported in other literature as well as the overall average truss strength.

Small-scale sheathing modeling

Lee and Hong (2002) developed a half-scale model of a light-frame wood shear wall in order to quantify the racking behavior of full-scale shear walls. The half-scale model was selected to minimize effects from defects in the wood and splitting due to connections. The authors used commercially available materials for the model sheathing, lumber, and nails. The model sizes that performed well compared to full-scale tests were selected based on having the smallest similarity errors of the materials and sizes considered. The similarity error (*SE*) can be evaluated by Eqn. 2-29:

$$SE = \frac{(value\ of\ model\ \times scale\ ratio) - (value\ of\ prototype)}{value\ of\ prototype} \times 100\% \qquad (2\text{-}29)$$

Lee and Hong (2002) concluded that the half-scale models could be used to predict the maximum load, initial shear stress, and the failure mode of the full-scale shear walls. They also found that the modeled walls could not be used to obtain the entire load-deformation curves from the racking tests. This study was limited to the investigation of sheathing subjected to shear loading in the plane of the sheathing.

Another study also focused on racking performance of light-frame shear walls using scale models (Patton-Mallory et al. 1984). This study, conducted at the Forest Products Laboratory, investigated shear walls constructed with four different aspect ratios. However, the authors did not correlate the small-scale walls with full-scale and used full-sized members in the scaled walls. Therefore, no modeling considerations can be determined from this study.

Small-scale whole house modeling

Leicester and Hawkins (1983) study. Leicester and Hawkins (1983) built sixteen (16) 1/3-scale square gable roof buildings measuring 8 ft by 8ft in plan with an eave height of 3.28 ft and a roof slope of 14°. On one of the buildings, a 7.9 in. wide centerline strip perpendicular to the ridge was instrumented with load cells and eight load sensing panels to capture the influence of wind pressures acting on a single frame (i.e., roof truss and wall stud). The purpose of this study was to validate the use of large models as a means of investigating the effects of natural wind pressures and load effects. They showed that the 1/3-scale building was appropriate for determining gust factor effects for horizontal and vertical forces as well as overturning moment.

Limitations of Leicester and Hawkins (1983) study. The models used by Leicester and Hawkins (1983) were limited in their structural response behavior to a single isolated frame. The effects of load sharing were not investigated, nor could they be, with the experimental setup used.

Garcia (2008) study. Garcia (2008) developed a $1/6^{th}$-scale model of a two-story residential LFWS to determine forces in the structure when subjected to wave loading along a coast (i.e., tsunami wave). The main objective in the similitude scaling, was to produce displacements in the model equal to $1/6^{th}$ of the displacements in the prototype structure. The major contributors to lateral strength and stability in residential LFWS are shear walls. Therefore, the goal was to model shear wall behavior. Several connectors were tested to determine their hysteretic behavior under dynamic loading. A 19 gage nail (1/2 in. long) was selected since it modeled best the behavior of an 8d common nail. The wall sheathing was modeled with 0.23 in. thick OSB created by cutting 15/32 in. thick OSB in half. The computer program SAPWood was used to design the shear

walls using this scaled nail. After several iterations, a nailing pattern was developed to best imitate the full-scale behavior of a shear wall (Figure 2-12 for an example). The horizontal diaphragms (i.e., roof and floor) were designed to be rigid so as to focus on the lateral capacity of the structure and therefore used 0.25 in. thick plywood.

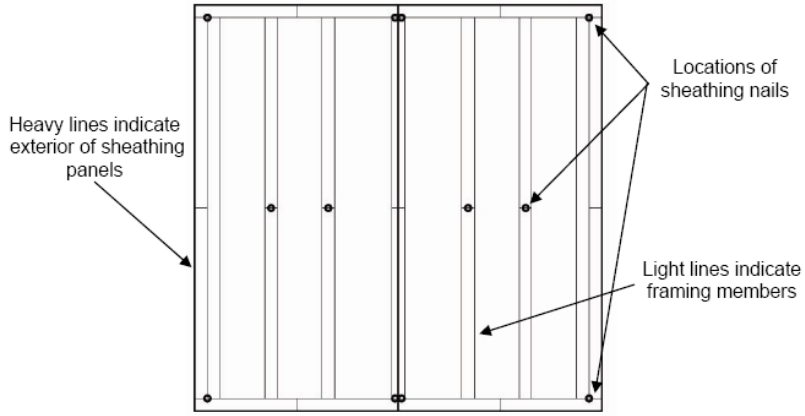

Figure 2-12. 1/6th-scale wood shear wall nailing pattern (from Garcia 2008)

Limitations of Garcia (2008) study. The focus of the structural scaling was shear wall performance (i.e., resistance to in-plane loads by the sheathing), with nail size and nailing schedule driving the design. For wind loads, the loading acts normal to the sheathing surface, and for this reason, the same procedure to determine the nail size and nailing pattern would undoubtedly be different. In order to resist out-of-plane loads, the sheathing would most likely need more fasteners. There were also no tests performed on the scaled sheathing itself. The scaled sheathing seemed to be arbitrarily selected and based on the thickness three times thicker than geometric similitude requires.

Analytical Models of Wood-Frame Buildings

Various studies have used finite element (FE) models of wood-frame buildings to investigate the effects of wind loading. Many of these have focused on lateral loading only. Additionally, most of the analytical models used experimental data for validation.

A few of these studies were presented previously in the section on load-sharing (Cramer and Wolfe 1989; Li 1996; Cramer et al. 2000).

Lateral force resisting systems. Kasal et al. (1994) developed a FE model of a complete one-story, rectangular, wood-framed residential structure, that was validated by a full-scale experiment. The focus of the experiment was to predict lateral displacement of the walls due to lateral wind loading and investigate the effects of various shear walls in the entire system. Using this FE model as a basis, Kasal et al. (2004) improved its capabilities including more complex roof shapes to be modeled (including L- and T-shapes). They validated the model based on full-scale research by Paevere et al. (2003) and found that the tributary area method used in design of the lateral force resisting system was highly inaccurate in predicting the distribution of the lateral wind forces through the walls. Collins et al. (2005a; 2005b) also constructed and validated a FE model of a light-frame, wood building using a full-scale experiment. The model has the capacity to predict well the displacements and force distribution once the system has yielded and entered the inelastic range. The capability of applying realistic dynamic loading was also incorporated but was not validated.

Limitations lateral force resisting systems. The major drawback to most of the FE models found in the literature is that the focus has been on lateral loading and how the walls distribute this load. In all of these studies, there was no mention of any roof loading of any kind. In fact in a couple of the models (Kasal et al. 1994; Kasal et al. 2004), the roof model was greatly simplified and individual roof trusses were not modeled.

Scoville (2005) study. Scoville (2005) studied the interaction of roof-to-wall connections (using both monotonic and cyclic tests) under combined uplift and shear loading and developed interaction diagrams for different load combinations. She also developed a FE model of an individual roof-to-wall metal connector incorporating the combined effects and found good agreement with the experimental results. The addition of this interaction into FE models could provide better models for investigating the overall behavior of light-frame roof systems.

Martin (2010) study. Martin (2010) developed an analytical model of a rectangular, gable roof LFWS using SAP2000. He modeled the roof trusses, sheathing, wall framing, and wall sheathing with all joints in the model either pinned or rigid. One of the primary objectives of his study was to develop a practical method to integrate the effect of edge nailing into the model without having to model individual nails, which is a tedious process. The novelty of this modeling method is that the sheathing was modeled as passing through the centerline of the framing members with the sheathing mesh corresponding to the meshing of the beam (or frame) elements used for the framing members. Martin then used a correlation procedure to model the nail schedule for the sheathing to frame connections using an equation provided in a supplement to the NDS (AF&PA 2005b). Instead of modeling individual nails, he developed a relationship between the shear modulus (G_{12}) of the sheathing (using an elastic, orthotropic material) and the nail spacing for racking loads in shear walls. By increasing the shear modulus, Martin was able to simulate the effect of edge nails at a decreased spacing.

Martin also validated his model using experimental data provided by the FPL (Wolfe et al. 1986; Wolfe and McCarthy 1989). Additionally, static influence surfaces were compared with those generated in this study on the 1/3-scale LFWS. Good agreement was observed with the trends although the magnitudes showed some discrepancies. One interesting finding Martin made pertains to the gable end wall. When the sheathing is continuous between the gable end truss and the end wall, a significant portion of the applied roof load is transferred through the end wall into the foundation instead of passing through the truss reactions at the heel joints.

Limitations of Martin (2010) study. The major drawback is that the sheathing was modeled as passing through the centerline of the framing members instead of being offset from the centerline in actuality. For shear wall behavior when the sheathing is loaded in plane, this might not be a major issue. However, for roof sheathing, when out-of-plane loads are investigated, the effect of this offset might be more pronounced, especially if dynamic loading is investigated. More studies would need to be performed to see what effect this might have on the behavior of the roof system.

Modal Testing of Residential Buildings

The application of dynamic loads is vital to understand a structure's response to those types of loads. One common method for investigating the dynamic characteristics of structural components is modal testing. Modal testing is defined as "the process involved in testing components or structures with the objective of obtaining a mathematical description of their dynamic or vibration behaviour" (Ewins 1984). The basic process involves providing an excitation (input) to the structure (usually a force or acceleration) and measuring the response (output) of the structure at a specific location. The analysis involves creating a transfer function that relates the response (output) to

the excitation (input). From the transfer function and the Fast Fourier Transform (FFT), the frequency response function (FRF) can be determined (Bendat and Piersol 2000). The FRF and its manipulation can provide much insight into the dynamic characteristics of the structure or structural component.

Fundamental frequencies of light-frame, wood structures. Foliente and Zacher (1994) and Foliente (1994; 1997) provide a range of natural frequencies for wood buildings in North America. For one- through three-story buildings, the range of natural frequencies is 3.0 to 18.0 Hz based on actual experiments and estimates. Figure 2-13 (adapted from Ferry Borges and Castanheta 1971; Foliente 1994) shows the distribution of fundamental frequencies for various structures along with the typical frequencies of wind and earthquake events. As can be seen, the fundamental frequencies of low-rise (normal) buildings lie within the range of earthquake natural frequencies whereas wind tends to have much lower frequency content. However, it should be noted that this is for lateral loading (both wind and seismic) and for lateral frequencies in the structures. Therefore, the application of these natural frequencies to wind loading on a roof (vertical loading) is unknown.

Foliente and Zacher (1994) also discuss testing performed by Touliatos et al. (1991) on a two-story wood building using a six-degree-of-freedom earthquake simulator. The structure was built according to the Canadian building code and was subjected to the three components (lateral, longitudinal, and vertical) of the 1986 Kalamata earthquake. The fundamental frequencies of the structure were 5.56 Hz in the lateral and longitudinal directions and 6.25 Hz in the vertical direction at the center of the roof. No details are provided on what the “center of the roof” means or whether

the roof included shingles. However, this is about the only reference to a vertical natural frequency found in the literature.

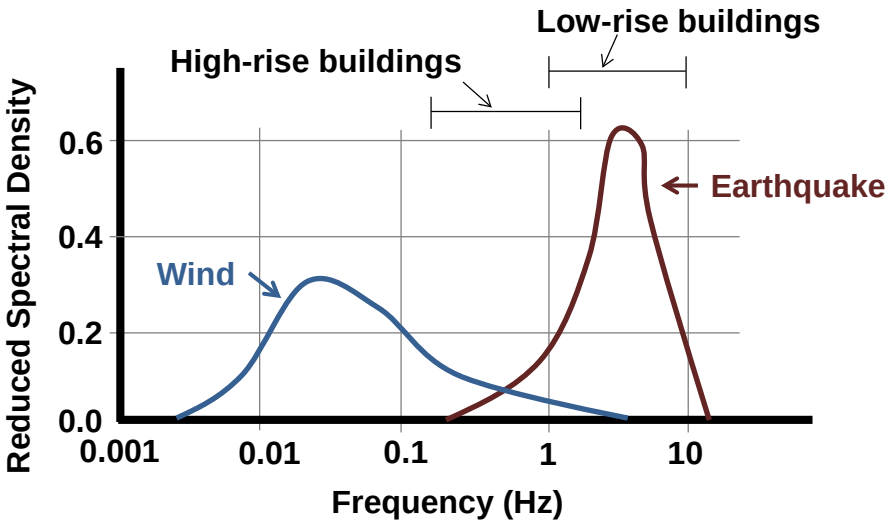

Figure 2-13. Fundamental frequencies of various structures with spectral densities of wind velocity and earthquake acceleration (adapted from Ferry Borges and Castanheta 1971)

Suzuki et al. (1996) study. Suzuki et al. (1996) tested three full-scale, two-story residential houses constructed with a glued laminated timber frame to determine the natural frequencies, damping factors, and mode shapes. Using an impact hammer weighing approximately 12 lbs, they measured accelerations at 12 different locations in the house and then calculated the frequency response functions. The impact hammer was used near the center of the second story, and hammering was conducted in two directions corresponding to the orientation of the building. The calculated frequency response functions provided the mode shapes and natural frequencies of the three structures tested. The natural frequencies of the first mode ranged from 2.5 Hz to 5.4 Hz for the three houses tested, and the damping ratios ranged from 0.7-5.0%. Additionally, Suzuki et al. used an electric exciter mounted at the same location as the impact hammer load points and repeated the experiment. The exciter used a 22 lb

weight to provide a sinusoidal excitation function with varying frequencies ranging from 2-25 Hz. The frequency response functions calculated using the accelerations produced by the sinusoidal forcing function were nearly identical to those determined using the impact hammer. They concluded that both methods – impact hammer and electric exciter – can be used to determine the dynamic properties of full-scale wood houses.

Gad et al. (2001) study. Gad et al. (2001) conducted tests on three parts of cold-formed, steel-framed residential structures to assess their performance and characteristics under lateral loads. The individual parts tested include an isolated, unclad wall panel, a one room test house, and a full-scale house. The first two were tested on a shake table where they were able to determine the overall characteristics (i.e., natural frequencies, damping ratios, and mode shapes) using modal analysis using transfer functions (output divided by input). Specifically, they calculated the transfer functions using the input acceleration and the output displacements measured at various locations. For the one room test house, the testing was performed in stages corresponding to different phases of the construction. The natural frequencies increased from 3.85 Hz with unclad wall frames to 4.45 Hz with walls that included strapping for bracing and plasterboard. The damping ratios increased from 4.2 to 10.3 for the same construction phases. When the walls were clad on the outside with brick veneer, the first mode corresponded to a frequency of 4.0 Hz with 10% damping.

Limitations of Suzuki et al. (1996) and Gad et al. (2001) studies. The major drawback to these studies is that the loading was in the lateral direction of the structure. Therefore, the natural frequencies of the structure in the vertical direction were not

measured. Wind loads acting on the roof of the structure would cause the structure to vibrate primarily in the vertical direction. Additionally, no inferences can be made about the load paths from these studies, since specific connections were not instrumented. Only the global dynamic characteristics of the structures were measured. However, if a connection were to be instrumented, characteristics of the load paths could be determined. No one is known to have applied modal testing to wood frame structures with the purpose of determining load paths and load transfer mechanisms for vertical wind loads.

Camelo (2003) study. Camelo (2003) tested multiple wood-framed buildings to determine the fundamental frequencies at low-amplitude shaking as part of the CUREE-Caltech Woodframe Project. The buildings were one to three stories in height. The measured natural frequencies ranged from 1.8 to 8.7 Hz. A regression analysis was performed on the collected data and a formula presented for determining the median value of the fundamental period based on building height. The observed damping ratios varied from 2.6-17.3% with an average of 7.2%.

Limitations of Camelo (2003) study. Although fairly comprehensive, the major drawback to the Camelo (2003) study is that the focus was on the lateral system. The fundamental frequencies were for the transverse and longitudinal directions of the buildings. Since the focus of this study is on vertical wind loading, the vertical frequencies of vibration are of interest and may not be similar to the horizontal frequencies reported in the literature.

CHAPTER 3
METHODS AND MATERIALS

1/3rd-Scale Wood Building

To further extend the work performed by Datin and Prevatt (2007), an entire 1/3-scale residential LFWS was built to further investigate load paths from wind induced pressures. The construction of the 1/3-scale model followed proper structural scaling laws (Harris and Sabnis 1999). The prototype house modeled has floor plan dimensions of 30 ft wide by 40 ft long. The roof has a slope of 4 in 12 (18.4°) and an overhang of 18 in. all around. The walls are built of standard studs and measure just over 8 ft in height. The sheathing modeled on both the roof and walls is ½ in. thick OSB. The roof trusses are constructed after the manner of Gupta et al. (2005) and consist of southern yellow pine (SYP) wood members. The walls use the same procedure as the roof trusses to properly scale the members and are made of spruce-pine-fir (SPF) lumber.

Roof Truss Construction

A one-third scale wood-truss roof using trusses previously developed by Gupta et al. (2005) was constructed out of No. 1 Grade Southern Yellow Pine (SYP) 2×4 dimensional lumber. A total of 21 trusses were constructed for the roof. The 1:3 scale model boards were fabricated from 2×4s with scale dimensions of 0.5 in. and 1.17 in. These dimensions were achieved by first ripping the 2×4s into four pieces with a table saw and then using a planer to shave the excess wood until the desired thicknesses were achieved.

Truss framing members

In order to simplify the similitude requirements between the full-scale and model-scale trusses, the modulus of elasticity (MOE) of the model boards needs to be equal (or nearly equal) to that of the full-scale boards. As discussed in Kittel (1997), the reason for using the same MOE values between model and prototype boards is that if different materials are used, it might not properly counteract model behavior differences even if similitude requirements are met. For example, if the model is deflection sensitive and if the MOE of the model boards is less than the prototype, larger deflections of the truss members are possible. This can result in larger bending moments at the truss joints which might have a negative effect on the model joint strength and stiffness (Kittel 1997). In order to accomplish this, a simple bending test was conducted on both the full-scale boards and then the subsequent scale boards, described in ASTM D4761-02a (ASTM 2004b). The premise behind this method is that if the mid-span deflection is measured with a known applied load, then the MOE can be determined by the following equation for the mid-span deflection of a simply-supported beam loaded at its mid-point:

$$\delta = \frac{PL^3}{48EI} \tag{3-1}$$

where: δ is the deflection; *P* is the load; *L* is the length of the span; *E* is the modulus of elasticity; and *I* is the moment of inertia.

Since an environmental chamber was not available for conditioning the wood members, the 2×4s were stacked loosely and allowed to air dry to reach an equilibrium condition. A Delmhorst BD-2100 digital moisture meter was used to take moisture content (MC) samples from all of the boards every two to three days until the MC

remained nearly constant. The moisture content was also measured at the time of the MOE testing and is provided in Table 3-1.

A support structure was constructed to provide a roller support at both ends (Figure 3-1). A dial gauge was situated at the mid-span of the boards. For the full-scale 2×4s, the span length used in the test was 118 in. For the 1/3-scale boards, the length used was 39.5 in. The boards were tested in flatwise bending (i.e., along their weak axis). For the full-scale boards, a weight of approximately 7 lbs was applied (hung) at the mid-span to take away any twist effects in the board to ensure that the board rested firmly on both supports. The model-scale boards had an initial weight of approximately 4 lbs. Each of the boards was then loaded in increments of approximately 13.5 lbs for the full-scale boards (three increments) and 4.4 lbs (three increments) for the model boards. After each additional load was applied, the mid-span deflection was measured. This allowed for a load-deflection slope to be calculated giving a better estimate of the beam deflection. After manipulating Eqn. 3-1 and replacing the P/δ term with the calculated slope, the MOE of the beam is calculated by Eqn. 3-2.

$$E = \frac{slope(P/\delta) \cdot L^3}{48I} \tag{3-2}$$

Figure 3-1. Test setup for determining modulus of elasticity of framing members

Table 3-1 provides the results from testing for MOE in SYP. A student's *t*-test was performed and found that the two sample means are statistically equal (*p*-value = 0.129). Therefore, there are no scaling effects due to different MOE values between full-scale and model scale. As presented in Table 3-1, the coefficient of variation of the scaled framing members is higher than the prototype due to larger variability in the model boards. For example, a scaled framing member with a smaller cross-section compared to full-scale could contain only a few annual growth rings which could result in one model board containing more latewood or earlywood than another board (Gupta et al. 2005). (Latewood is more dense and therefore stronger than earlywood (Breyer et al. 2007)). Gupta et al. reported a similar observation between the variability in full-scale versus model-scale boards. The trusses were then fabricated using the metal plate connectors designed by Gutpa et al. (2005).

Table 3-1. MOE results for roof framing (southern yellow pine)

Scale	Sample Size	MOE (ksi)		Moisture Content	
		Avg.	COV	Avg.	COV
Full-scale 2×4	44	2020	0.195	15%	0.067
1/3-scale 2×4	82	2150	0.257	11%	0.059

The specific gravity of the truss framing members was also determined according to ASTM D2395 (ASTM 2006b), Method A – Volume by Measurement. A total of 65 samples were tested measuring 1 in. long by 0.5 in. thick by 1.17 in. wide. The specimens were placed in a laboratory oven and maintained at a temperature of 103° for more than four days. The specimens were then removed, their dimensions measured, and the weight recorded. For the dimensions, two measurements were taken and then averaged for each of the three directions. The specific gravity (*SG*) was then calculated according to Eqn. 3-3.

$$SG = \frac{KW}{Lwt} \tag{3-3}$$

where: *K* is a constant (27.68 for *W* in lbs and volume in in.^{3}); *W* is the weight (lbs); L, *w*, and *t* are the length, width, and thickness, respectively (in.). The average specific gravity of the SYP truss members was 0.620 with a coefficient of variation of 13.4%.

Truss stiffness

Once the trusses were fabricated, the six instrumented trusses were tested to measure individual truss stiffness (refer to Figure 3-2). The trusses were braced out-of-plane to prevent any sideways buckling while allowing them to move freely in the vertical direction. To be consistent with truss stiffness calculations by Gupta et al. (2005), all three top joints are loaded simultaneously. However, the proper equipment was not available to perform this loading. Therefore, the five fink trusses were loaded at the three top joints individually by a pneumatic actuator in 10 lb increments between 10 and 50 lbs. Deflections were measured at all three top joints simultaneously for each joint loaded with the actuator. Since the loaded system was within the linear-elastic region, superposition was used to determine the overall truss stiffness as well as the individual joint stiffness. The stiffness is calculated as the slope of the load-displacement curve for each joint. Table 3-2 and Table 3-3 provide the stiffness values for each of the top chord joints as well as the overall truss stiffness scaled to full-scale (model truss stiffness multiplied by three) for downward (gravity) loading and uplift loading, respectively.

A


B


C


D


E

Figure 3-2. Truss stiffness setup. A) Overall setup, B) Peak joint downward loading, C) Top chord joint downward loading, D) Peak joint uplift loading, and E) Top chord uplift loading

Table 3-2. Truss stiffness values for downward loading scaled to full-scale

Truss	Joint Stiffness (lbs/in)				Avg. MOE (ksi)	St. Dev. MOE (ksi)	COV MOE
	B	C	D	B, C, & D			
1[a]	2400	5190	1440	2460	NA	NA	NA
2	4080	3720	3660	4410	2186	423	0.194
3	3840	3870	4260	3990	1855	431	0.232
4	4890	5400	5640	5310	2254	595	0.264
5	4230	4230	4290	4260	1935	190	0.098
6	5640	4890	4980	5130	2073	544	0.262
Mean[b]	4540	4420	4570	4620			
St. Dev.[b]	730	710	760	570			
COV[b]	0.161	0.161	0.166	0.123			

Notes: (a) Gable end truss without sheathing. (b) Excludes gable end truss in calculations

Wall Framing

The same procedure was used to determine the MOE for the wall framing as for the SYP roof (ASTM 2004b) except No. 2 Grade Spruce-Pine-Fir (SPF) lumber was used. The moisture content was also recorded in a similar manner as for the SYP.

Table 3-4 presents the results from testing the SPF lumber. The variability in the full-scale and model-scale MOEs of the SPF is similar to that of the SYP. However, the SPF variability is larger than for the SYP, attributable to the fact that No. 2 grade SPF lumber was used as opposed to the No. 1 grade lumber used for the SYP. Similarly for the specific gravity measurements, the same procedure was used as for the SYP. 97 samples were used to arrive at an average specific gravity of 0.445 with a coefficient of variation of 12.2%.

Table 3-3. Truss stiffness values for uplift loading scaled to full-scale

Joint	Stiffness (lbs/in)				Avg. MOE (ksi)	St. Dev. MOE (ksi)	COV MOE
Truss	B	C	D	B, C, & D			
1[a]	1170	4260	1590	1740	NA	NA	NA
2	5040	4770	4860	4890	2186	423	0.194
3	3060	3300	3540	3780	1855	431	0.232
4	4560	5370	5790	5190	2254	595	0.264
5	5190	4650	4740	4860	1935	190	0.098
6	5430	5010	5220	5220	2073	544	0.262
Mean[b]	4660	4620	4830	4790			
St. Dev.[b]	950	790	830	590			
COV[b]	0.204	0.171	0.172	0.123			

Notes: (a) Gable end truss without sheathing. (b) Excludes gable end truss in calculations

Table 3-4. MOE results for wall framing (spruce-pine-fir)

Scale	Sample Size	MOE		Moisture Content	
		Avg. (ksi)	COV	Avg.	COV
Full-scale 2×4	47	1450	0.168	12%	0.114
1/3-scale 2×4	74	1550	0.318	11%	0.130

Sheathing Tests

For the sheathing, the flexural stiffness (*EI*) needs to be properly modeled to accurately represent load transfer in full-scale (*E* = MOE and *I* = moment of inertia). Since wind loads produce out-of-plane loading on the roof (and subsequently the sheathing), the sheathing needs to perform appropriately in the out-of-plane direction. For this reason, the flexural stiffness was determined to be the property of interest. The

flexural stiffness is scaled by $(EI)_p = S_E S_L^4 (EI)_m$ and if E is constant then this yields (for a 1/3 geometric scale): $(EI)_p = (1)(3^4)(EI)_m = 81(EI)_m$. Therefore, the target model stiffness is 1/81 times the target full-scale stiffness.

ASTM Standard D3043 (ASTM 2004a) outlines four procedures for determining the structural properties of structural panels subjected to flexure. For this test, Method B – Two-Point Flexure Test – was used to determine the MOE because it subjects a much larger portion of the specimen to the maximum applied moment than in the center-point flexure test (maximum moment is only at point of load application). The two-point flexure test for stiffness requires specimens sized so that the span is at least 48 times the nominal sheathing thickness for the principal direction of the panel parallel to the span. The test specimen is two inches longer than the span and two inches wide. Table 3-5 provides the details of the different materials tested.

Table 3-5. Sheathing MOE testing materials

Material ID	Material	Manufacturer	Purchase Location	Number of Specimens	Avg. Thickness (in.)	Avg. Width (in.)
OSB1	½" OSB	Langboard	Contractor Supply	36	0.500	2.045
OSB2	½" OSB	Langboard	Contractor Supply	58	0.492	2.021
OSB3	½" OSB	Georgia-Pacific	Lowes	36	0.478	2.016
OSB4	¼" OSB	Norbord	Lowes	35	0.240	2.006
Ply1	5.2mm Lauan Hardwood Plywood	N/A	Lowes	22	0.183	2.366
HW1	Basswood	N/A	Savannah, GA	9	0.187	0.987
HW2	Mahogany	N/A	Savannah, GA	3	0.188	0.983
HW3	Unknown hardwood	N/A	Savannah, GA	3	0.190	0.992

Based on ASTM D3043, the specimen size is 26 inches by 2 inches for testing the stiffness in the principal direction. The load points are placed at locations 6 inches from each support. An equal load is applied to each load point at a rate of 0.25 in./min as per Eqn. 4 in ASTM D3043. Deflections were measured at mid-span and just inside the two load points with linear potentiometers. Figure 3-3 describes the test setup visually. The average specimen bending stiffness (EI) is calculated using the slope of the load-deflection curve (ASTM D3043, Eqn. 5), shown in Eqn. 3-4.

$$EI = \left[\frac{(L - L_1)L_2^2}{32}\right]\left(\frac{P'}{\Delta}\right) \tag{3-4}$$

where: L is the span (24 in.), L_1 is the span between load points(12 in.), L_2 is the span between deflection measurement points(11.875 in.), and P'/Δ is the slope of the load deflection curve where deflection is mid-span relative to ends of span L_2.

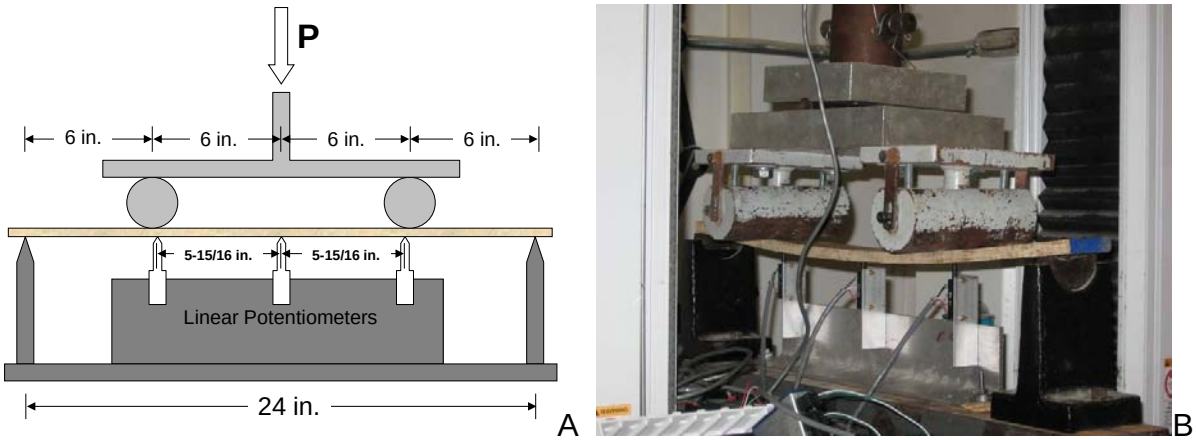

Figure 3-3. Sheathing testing setup. A) Schematic of test and B) Actual test

Table 3-6 provides the calculated slope of the load-deflection curves and the MOE. The slope of the load-deflection curves was calculated after removing the initial points and the ending points of the data set to remove any highly non-linear behavior due to initial loading and readings and when the load was removed. The first three OSB

samples tested were from two different manufacturers (OSB1 and OSB2 from Langboard and OSB3 from Georgia-Pacific). As can be seen, there is a large difference in the mean MOE between the two manufacturers. However, the two samples (OSB1 and OSB2) from Langboard are not statistically different (p-value = 0.71) and can therefore be combined. The MOE for the 0.25 in. thick OSB4 is also much lower than the other OSB (OSB1-3) specimens. The 0.25 in. thick OSB4 is less dense than the thicker 0.5 in. OSB and is not rated for use in structural applications. The plywood also has a much lower MOE than the OSB panels. The MOE values for the various hardwoods tended to be in the range of the full-scale OSB values.

Table 3-6. Results of MOE Sheathing Testing

Material ID		Slope of Load-Deflection (lb/in.)		Modulus of Elasticity (ksi)		
		Avg.	St. Dev.	Avg.	St. Dev.	COV
Full scale	OSB1	272.3	43.2	678.9	113.4	0.167
	OSB2	254.0	33.5	670.8	85.7	0.128
	OSB3	288.8	54.0	832.3	157.8	0.190
Model scale	OSB4	10.2	1.8	234.2	36.3	0.155
	Ply1	3.5	2.8	175.3	32.4	0.185
	HW1	6.9	0.32	568.8	42.4	0.075
	HW2	8.88	1.74	728.8	163.3	0.224
	HW3	10.6	1.2	828.1	82.4	0.100

Since the MOE is only part of the flexural stiffness, the moment of inertia is also needed to calculate the scaled stiffness. For the purpose of this analysis, a 12 in. wide strip of the full-scale sheathing is used resulting in a 4 in. wide strip for the 1/3-scale. Therefore, the average moment of inertia (accounting for their measured thickness in Table 3-5) of the OSB1 and OSB2 (full-scale) sheathing is 0.121 in.^{4} and is 0.109 in.^{4} for the OSB3 (full-scale), resulting in an average flexural stiffness of 81.7 k-in.^{2} and 90.9 k-in.^{2}, respectively.

Table 3-7 provides the scaled flexural stiffness of the proposed scale sheathing. A similarity error is also calculated based on Eqn. 2-29 to determine which proposed model sheathing matches the full-scale target stiffness. The similarity error has been calculated against both the OSB1 and OSB2 groups and the OSB3 group. As can be seen, the 0.25 in. OSB (OSB4 – model scale) has a small similarity error with both of the OSB groups and is selected as the scale sheathing to be used on the 1/3-scale building.

Table 3-7. Model scale sheathing stiffness and similarity error

Material ID	Mean MOE (ksi)	Mean *I* (in^4)	Mean *EI* ($k\text{-}in^2$)	Similarity Error	
				OSB 1 & 2	OSB 3
OSB4	234.2	0.00461	1.079	7.0%	-3.8%
Ply1	175.3	0.00204	0.358	-64.5%	-68.1%
HW1	568.8	0.00218	1.240	22.9%	10.5%
HW2	728.8	0.00222	1.614	60.0%	43.9%
HW3	828.1	0.00229	1.893	87.6%	68.7%

The specific gravity of the various sheathing materials was also tested. The same procedure was used as for the framing members with specimens measuring 1 in. by 1 in. Table 3-8 provides the details of the specific gravity tests.

Table 3-8. Specific gravity of OSB sheathing

Material ID	No. of Samples	SG	COV
OSB1	60	0.6458	7.8%
OSB2	60	0.6670	8.2%
OSB3	60	0.6797	7.8%
OSB4	58	0.6525	9.3%

Sheathing Fastener Selection

In selecting the sheathing attachment, several factors were considered. The ultimate objective of the one-third scale house is determining the structural load paths for wind uplift loads. Additionally, the model house cannot be taken to failure with any meaningful results, and so it was decided to ensure that the connections between the

sheathing and framing members did not fail, especially due to the point loads applied directly to the sheathing.

Several fasteners (two nails and three screws) were considered for the scaled sheathing attachment (Figure 3-4) – 18 gage pneumatic brad nail, 17 gage hand-driven brad nail, #6 metal screw, #6 wood screw, and #4 wood screw. The testing procedure used was a modified ASTM D1761 (ASTM 2006a). The test specimens (Figure 3-5) were constructed with a five inch long piece of the scaled SYP 2×4 framing members (scaled dimensions of 0.5 in. by 1.17 in.) and a two inch by five inch piece of the scaled OSB sheathing (0.25 in. thick). This modification to ASTM D1761 was used since the desired outcome was to have the sheathing remain attached to the framing members, as previously described. Therefore, the "system" was tested as a whole.

Figure 3-4. Scaled sheathing attachment trial fasteners

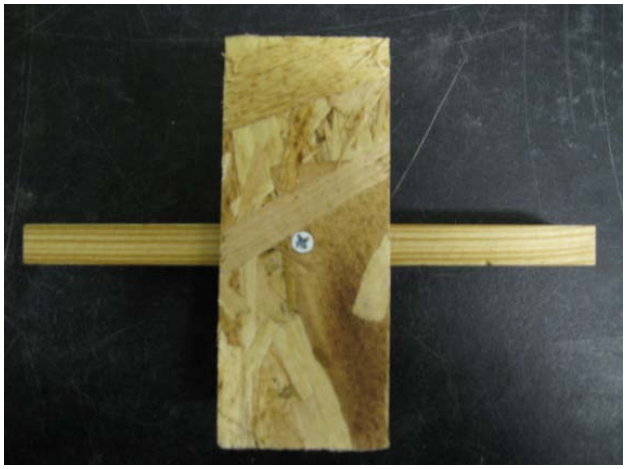
Figure 3-5. Typical scaled sheathing attachment test specimen

A 30 kN (6700 lbs) Instron universal testing machine (Model 3384) was used to load the specimens by pulling up on the edges of the sheathing (Figure 3-6) at a rate of 0.1 in./min. The load was recorded using a 300 lb tension/compression load cell (Model LRF350 by Futek).

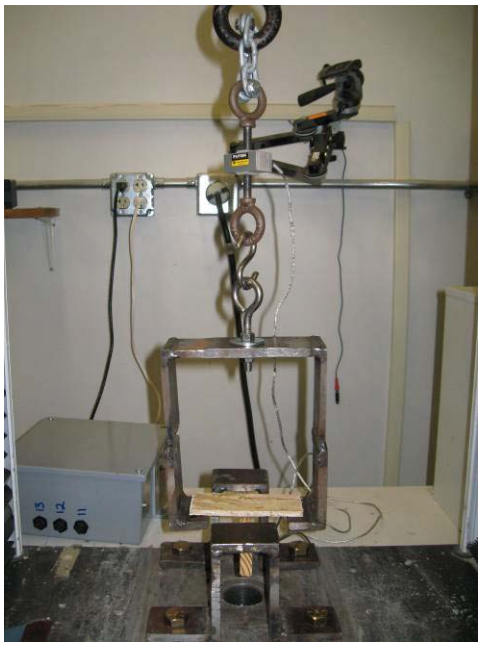

Figure 3-6. Sheathing attachment test setup

Table 3-9 provides the results of the testing, and Figure 3-7 shows the two dominant failure modes of the test specimens. The 18 gage pneumatically driven nails produced an average peak load of 29.8 lbs and all of the test specimens, except one, failed by the nail head pulling through the sheathing. The pneumatically driven nails have a head that is only slightly larger than the shank diameter resulting in nail head pull-through. The 17 gage hand driven brad nails were the closest match geometrically to an 8d common nail, and the average peak load was 19.7 lbs. The three different screws tested produced almost equivalent results – the average failure occurred near 77 lbs and in almost all individual tests the failure mode was sheathing fracture.

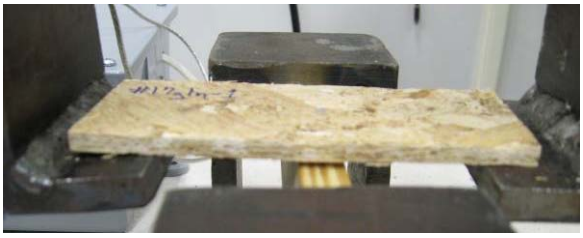
A

B

Figure 3-7. Failure modes of scaled sheathing attachment: A) Withdrawal and B) Sheathing fracture

Table 3-9. Scaled sheathing attachment test results

Fastener	Number Tested	Avg. Peak Load (lbs)	COV	Primary Failure Mode
18 gage pneumatic brad nail, 1 in. long	10	29.8	0.364	Nail pull-through
17 gage hand-driven brad nail, 1 in. long	10	19.7	0.607	Nail withdrawal
#6 metal screw, 1 in. long	10	77.9	0.315	Sheathing fracture
#6 wood screw, 1 in. long	9	73.8	0.210	Sheathing fracture
#4 wood screw, 0.75 in. long	10	78.9	0.246	Sheathing fracture

If the fastener loads are compared to full-scale values for a typical 8d common smooth shank nail (0.131 in. diameter, 2.5 in. long), the expected peak withdrawal value is 550 lbs based on Eqn. 3-5 (from NDS (AF&PA 2005a) Eqn. C11.2.3-1 without the factor of safety applied).

$$W = 6900G^{2.5}DL \tag{3-5}$$

where: *W* is the average withdrawal load (lbs); *G* is the specific gravity (0.620 for SYP used in this study); *D* is the nail diameter (in.); and *L* is the nail penetration into the framing member (2.0 in. for this study accounting for 0.5 in. thick sheathing). If we account for similitude between full and model scale, the full-scale load is reduced by a factor of 9 resulting in a 1/3-scale average withdrawal value of 61 lbs. Based on this result, neither of the nails tested meet the similitude requirements. All of the screws

tested exceeded 61 lbs; however, none of the screwed specimens failed by screw withdrawal or sheathing pull-through. In all cases, the sheathing fractured. Additionally, because of the failure mode for the nails (nail withdrawal from the framing member and nail pulling through the sheathing), it was decided to use the #4 wood screw since all of the screws tested performed equally well. The #4 screws were then used at four inches on center for attaching the sheathing to the walls and the roof.

1/3-Scale House Construction

The one-third scale trusses were constructed according to Gutpa et al. (2005). A completed truss with the construction jig is shown in Figure 3-8. As described by Gupta et al., the truss plate connectors consist of 30 gage sheet metal with 24-40 staples 0.25 in. in length. An example of the tension splice joint is shown in Figure 3-9.

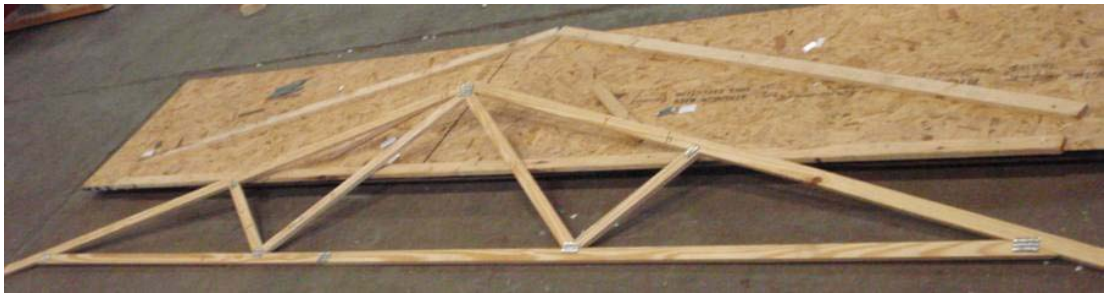

Figure 3-8. Completed 1/3-scale truss with construction jig

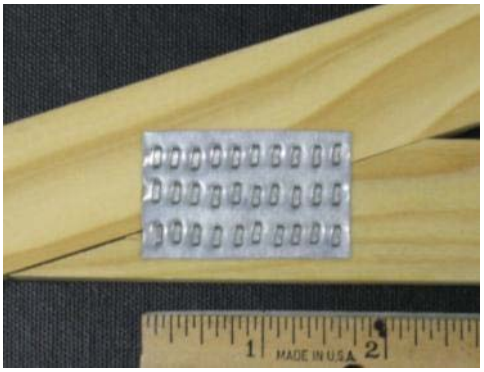

A


B

Figure 3-9. Examples of 1/3-scale metal plate connectors: A) heel and B) tension splice joint

In order to measure forces in the roof-to-wall connections, load cells were installed at eleven connections. For interior trusses, the arrangement is shown in Figure 3-10a, and for the gable end truss the load cell arrangement is shown in Figure 3-10b. Since the load cells resulted in an offset between the trusses and the wall, the remaining roof-to-wall connections needed a spacer to ensure all trusses were level with each other. The roof-to-wall connection for these trusses is shown in Figure 3-11 (note the metal strap over the truss to ensure that the truss would not fail at this connection). Nine load cells were also placed at wall-to-foundation connections, as shown in Figure 3-12. The house was then sheathed with the 0.25 in. thick OSB determined previously with 0.75 in. long #4 screws spaced at four inches on center. The completed one-third scale house is shown in Figure 3-13a. The overhangs were also sheathed on the underside as shown in Figure 3-13b.

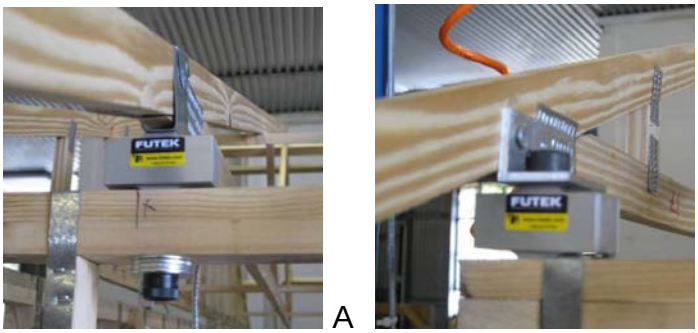

A B

Figure 3-10. Roof-to-wall connection load cell arrangements for A) interior trusses and B) gable end truss

Figure 3-11. Roof-to-wall connections without load cells

Figure 3-12. Instrumented wall-to-foundation connections

A

B

Figure 3-13. A) Completed 1/3-scale house and B) Sheathing fastened to underside of overhangs

Instrumentation

Figure 3-14 shows the overall instrumentation setup. The individual components are discussed in the following sections.

Data acquisition unit

A National Instruments CompactDAQ data acquisition unit recorded the sensors (load cells and pressure transducers) and controlled the pneumatic actuator using a laptop connected via USB running a LabVIEW data acquisition program. The load cells and most of the pressure transducers were connected to the CompactDAQ using a NI 9205 C series module. A NI 9465 C series module controlled the actuator, and a NI

9219 C series module was used for some of the pressure transducers. The data was recorded to ASCII files for processing by MATLAB.

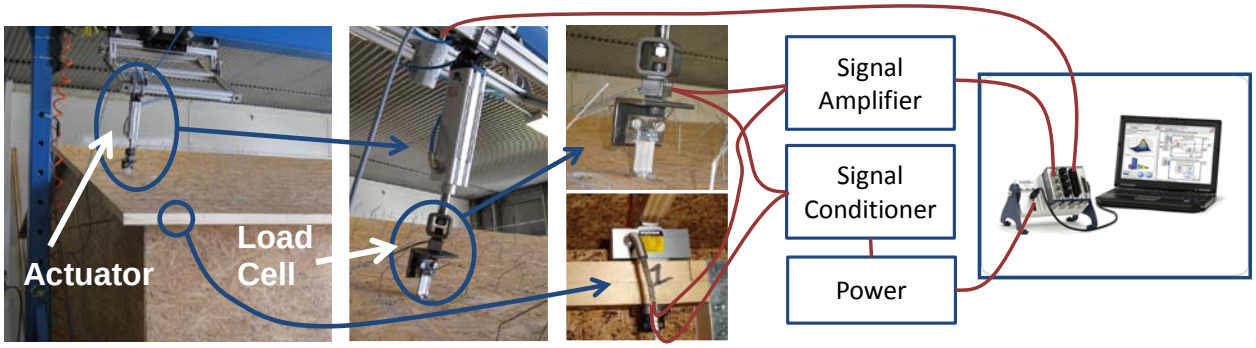

Figure 3-14. Instrumentation diagram

Load cells

Twenty load cells (reaction points) were installed in the model house (11 roof-to-wall and 9 wall-to-foundation connections, Figure 3-15). The load cells (Futek Advanced Sensor Technology, Inc. Model LRF350) had a capacity of ±300 lbs. Each load cell was connected to a signal conditioner and amplifier (Calex Model 6202-0334) to increase the accuracy of readings. The amplifier provided a conditioned 10 V power supply to the load cell, and the amplifier provided a gain of 334 to the load cell output. Because of the addition of the signal conditioner and amplifier, each load cell was recalibrated from its factory calibration by hanging weights from the load cell in 70-75 lb increments up to 300 lbs.

Pneumatic actuator

The loads were applied to a dense grid on the roof (Figure 3-16) by using a pneumatic actuator (Figure 3-17). The actuator was controlled with a regulator that was connected to the data acquisition unit and controlled with a LabVIEW program. A compressor provided the air supply to the regulator. The actuator applied the loads normal to the roof surface, and contained a load cell in series to record and act as a

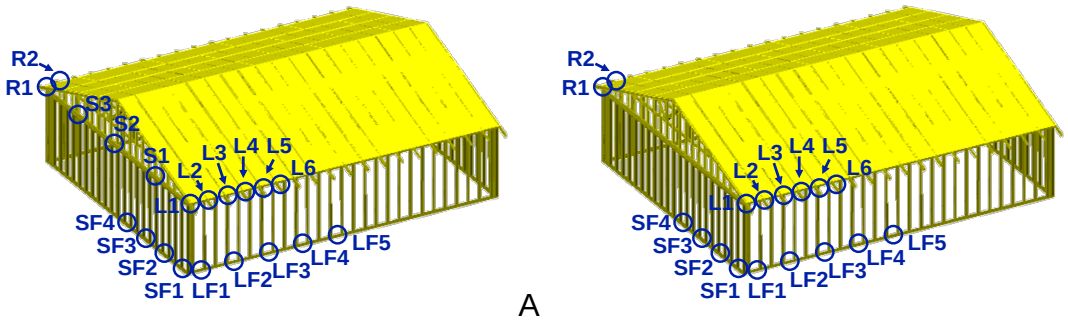

Figure 3-15. Load cell placement in 1/3-scale wood-frame building A) with gable end intermediate connections (S1-S3) and B) without intermediate gable end connections

feedback loop to maintain the desired load. For the influence coefficient testing, the loads were measured and recorded using a sampling rate of 50 Hz. The loads were applied in 10 lb increments from 10-50 lbs and held at each load step for 30 seconds to investigate the effects of the load magnitude on the influence coefficients (i.e., load path). According to the scaling laws, these loads correspond to full-scale point loads of 90-450 lbs. The equivalent pressures are determined by dividing the applied load by the tributary area of each load point (shown in Figure 3-16) with a maximum pressure of

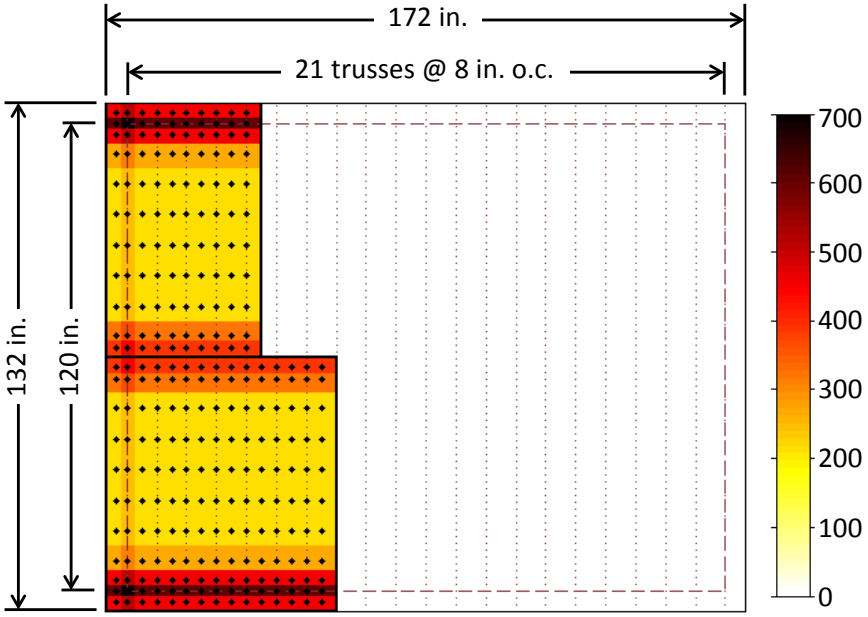

Figure 3-16. Influence coefficient load points with equivalent full-scale pressures in psf (using the equivalent full-scale point load of 450 lbs)

686 psf and minimum of 216 psf corresponding to tributary areas ranging from 0.66 ft^2 to 2.08 ft^2, respectively, for a 450 lb load. A typical actuator response is shown in Figure 3-18. The loads were applied as both uplift and gravity (downward) loads.

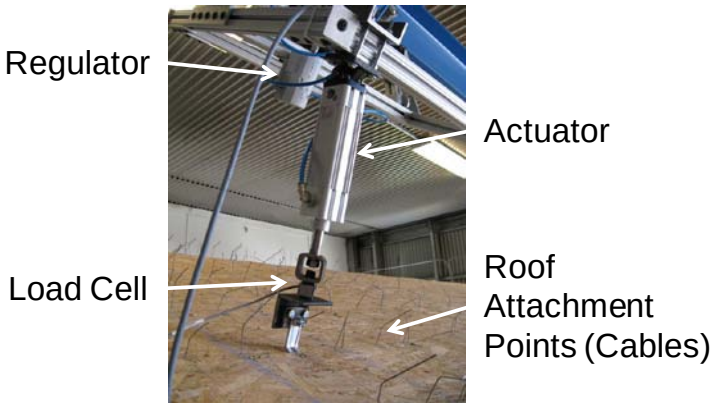

Figure 3-17. Pneumatic actuator for influence function load testing

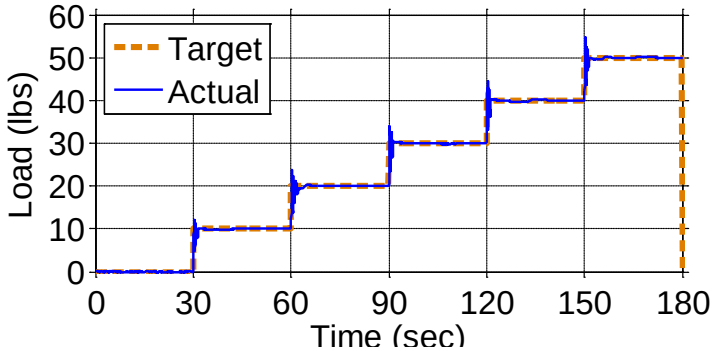

Figure 3-18. Typical actuator loading of influence function points

Pressure transducers

For the DAD validation tests, 25 pressure transducers (Omega, Model PX138) were installed on the roof of the 1/3rd-scale building. Four additional pressure transducers (Setra, Model 265) were mounted on two exterior walls to capture the static pressures. Finally, one pressure transducer (Dwyer, Model 616-20B) was mounted inside the structure to record internal pressure fluctuations. Figure 3-19 shows the locations of the pressure transducers along with the load cells for the DAD validation testing.

Influence Function Testing of Scale House

In order to provide a means of checking to see if the entire applied load was being measured by the load cells, the contour plots in Figure 3-20 were developed (see Appendix A for a detailed example of one point load). Figure 3-20 shows the contours for the summed reaction loads at the roof-to-wall connections normalized by the applied load. In other words, each of the 11 measured reaction loads at the roof to wall connections was added together for each application point on the roof (Figure 3-16). Then that total load is normalized by dividing by the applied load. Hence, if the normalized load is equal to one, then the entire applied load at that point was measured by all of the load cells at the roof-to-wall connections. If the normalized load is less than one, then not all of the applied load was measured by the load cells at the roof-to-wall connections. As can be seen, along the bottom and left side of the plots in Figure 3-20, the summation is close to unity. The right halves of the plots show a summation much less than unity due to the placement of the load cells, which were concentrated in the lower left corner and along the left edge of the house. Therefore, for these load points farther away from the actual load cells, much of the load was passing through points in the structure where there were no load cells placed. There is also a spot along the bottom of the plots which shows a normalized summation greater than unity. These spots are located over the eave and wall. When the loads are applied over the eave, a negative reaction load is measured at the opposite end of the truss. However, only two trusses were instrumented at both ends – the gable end truss and the first interior truss, meaning that the negative reaction loads likely on the other trusses was not measured producing a normalized summation greater than unity. Figure 3-20 provides reasonable evidence that the load cells were properly calibrated.

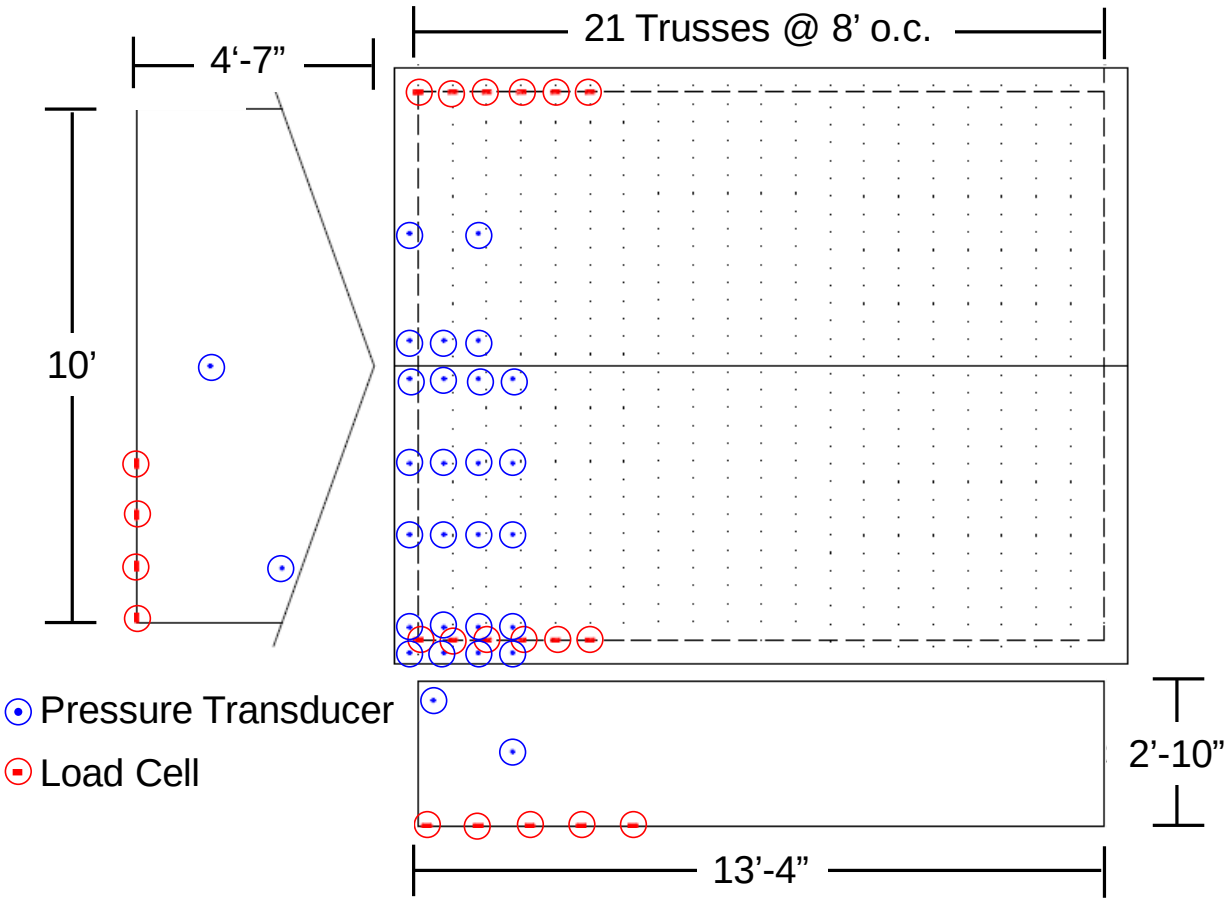

Figure 3-19. Pressure transducer and load cell arrangement for DAD validation testing

Figure 3-20 also provides a normalized summation (i.e., summation of all influence coefficient surfaces) of the measured loads at the wall-to-foundation loads. There is a notable difference between this plot and that for the roof-to-wall connections. The normalized summation is only unity right at the lower left corner of the house where the load cells were concentrated in the foundation. The contours maintain a fairly uniform spacing as the normalized load reduces. This sharp reduction in the normalized load is attributed to the walls acting as stiff, deep beams and effectively spreading the load more evenly into the foundation, including transferring load to reaction points that were not instrumented.

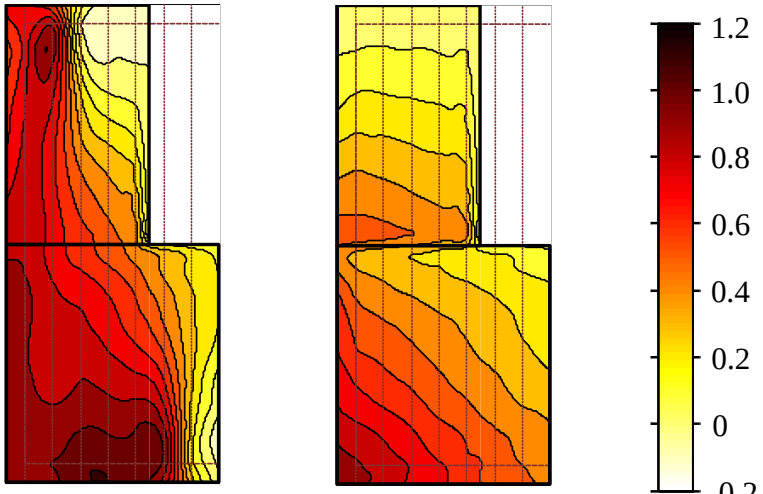

Figure 3-20. Summation of measured connection loads normalized by the applied load (uplift loads)

Wind Tunnel Testing

Wind tunnel testing was performed in the atmospheric boundary layer wind tunnel at Clemson University's Wind Load Test Facility (WLTF – now called the Wind Engineering and Structures Lab). The atmospheric boundary layer is the lowest part of the atmosphere that is affected by the frictional effects of the roughness of the earth surface. The open-return wind tunnel at the WLTF has cross-sectional dimensions of approximately 10 ft (3 m) wide by 6.5 ft (2 m) tall with a working section approximately 48 ft (14.6 m) long (Figure 3-21). Wind is generated by two 6 ft (1.8 m) diameter fans and then immediately passes through a settling chamber, contraction cone, and several screens and honeycombs before entering the test section with near uniform wind speed and minimal turbulence across the test section entrance. Trip plates and spires are set up at the entrance to the test section, which, in addition to the roughness elements arranged along the test section, create the atmospheric boundary layer (see Figure 3-22 for a schematic of the wind tunnel layout).

Figure 3-21. Clemson University wind tunnel test section for 1:50 suburban terrain

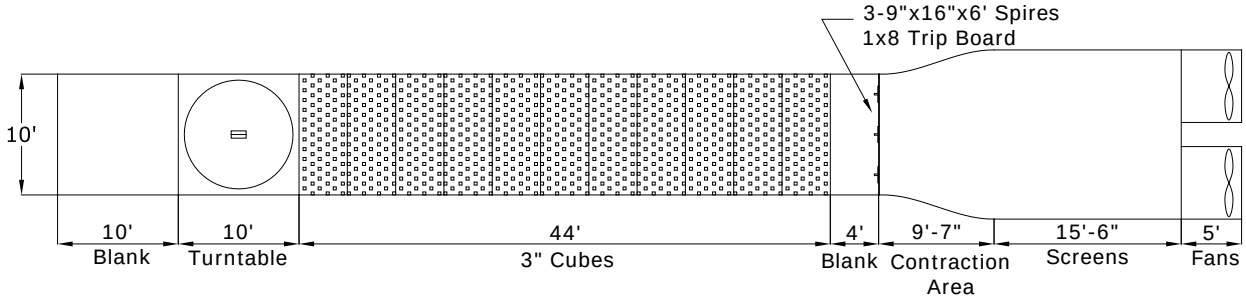

Figure 3-22. Wind tunnel arrangement for 1:50 suburban terrain

The velocity and turbulence intensity profiles are shown in Figure 3-23. Liu (2006) found that the roughness length of the WLTF 1:50 suburban terrain simulation was 0.72 ft. Figure 3-24 shows the power spectral density of the wind speed at an equivalent full-scale height of 33 ft. As can be seen, it matches the von Karman spectrum well (von Karman 1948; Simiu and Scanlan 1996). The mean wind speed, *U*, is 13.2 mph and the calculated length scale, L_x^u, is 83.2 ft at full-scale.

Pressure tap models are constructed from acrylic so as to be rigid. Metal taps 0.063 in. (1.6 mm) in outside diameter are glued into the acrylic and are connected to miniature electronic pressure scanners by 12 in. (300 mm) long vinyl tubes. The

Scanivalve® ZOC33 electronic pressure scanning modules have 64 channels each capable of scanning pressures up to 500 Hz, allowing for near simultaneous measurements of pressures on the model. A RAD3200 digital remote A/D converter base unit allows for up to eight of the ZOC33 modules to be connected at the same time allowing up to 512 channels to be used simultaneously allowing for closely spaced pressure measurements on a model.

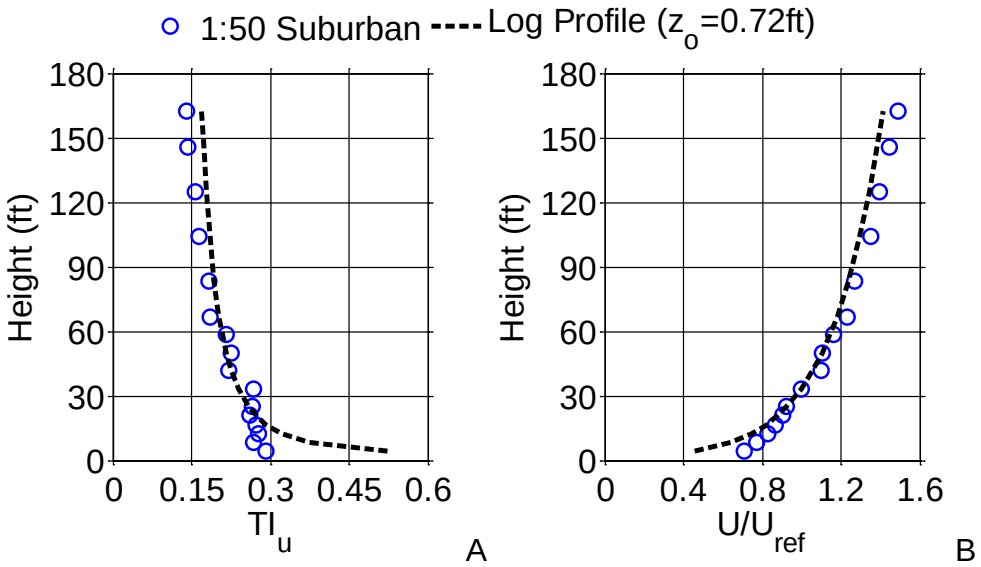

Figure 3-23. A) Turbulence intensity profile and B) Velocity profile for 1:50 suburban terrain in the WLTF

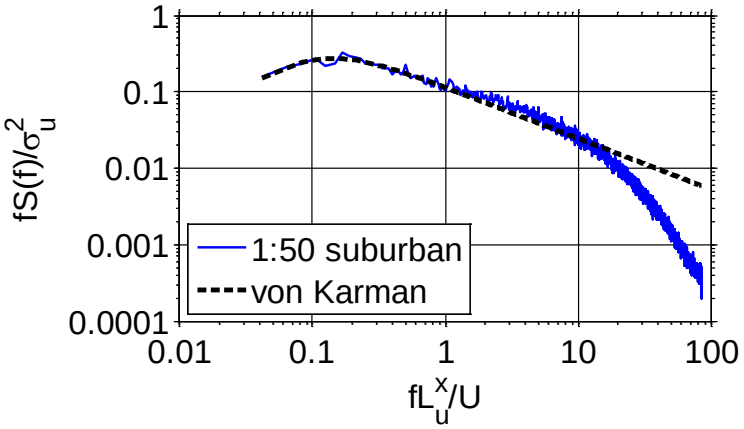

Figure 3-24. Power spectral density of WLTF wind speed at 33 ft full-scale in 1:50 suburban terrain

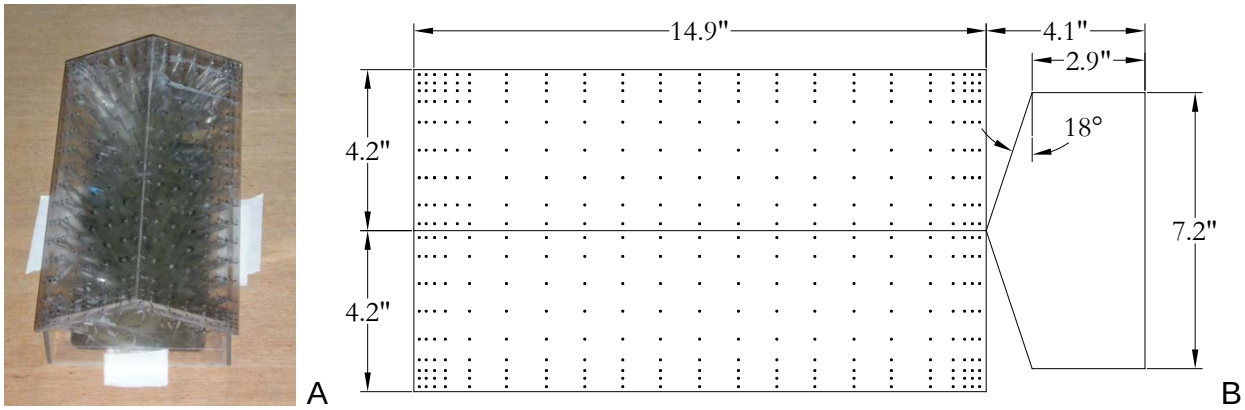

Figure 3-25. A) 1:50 scale wind tunnel model and B) Pressure tap layout and dimensions

The wind tunnel model for this project consisted of a simple gable roof structure with dimensions 7.2 in. (183 mm) by 14.4 in. (387 mm) in plan with a mean roof height of 3.3 in. (84 mm) and a roof slope of 18.4° (4 in 12) (Figure 3-25). The model has 387 pressure taps installed on the roof. Wind tunnel tests were performed at five wind directions: 0°, 45°, 90°, 135° and 180°, with eight repeats per azimuth. Pressure data was sampled at 300 Hz for 120 seconds and then digitally low-pass filtered at 150 Hz (using an eighth-order Butterworth filter).

Tubing System

A 12 in. (300 mm) long tubing system was used to connect each pressure tap to the pressure scanning modules. The tubing system consists of an 8 in. (200 mm) long, 0.054 in. (1.37 mm) internal diameter (ID) vinyl tube connected to the model, a 4 in. (100 mm) long, 0.034 in. (0.86 mm) ID vinyl tube connected to the pressure scanner, and a 0.40 in. (10 mm) long brass tube with a 0.054 in. (1.37 mm) ID connecting the two vinyl tubes.

The tubing system's frequency response was determined by comparing the direct (no tubing) measurement of a white noise signal with the measurement after passing

through the tubing system (Liu et al. 2009). The tubing response was determined up to 300 Hz as shown in , along with a sketch of the tubing system arrangement. The worst case dynamic amplification was less than +/- 10%. The dynamic amplification for each tap was removed by adjusting the signal in the frequency domain before analyzing the wind tunnel data.

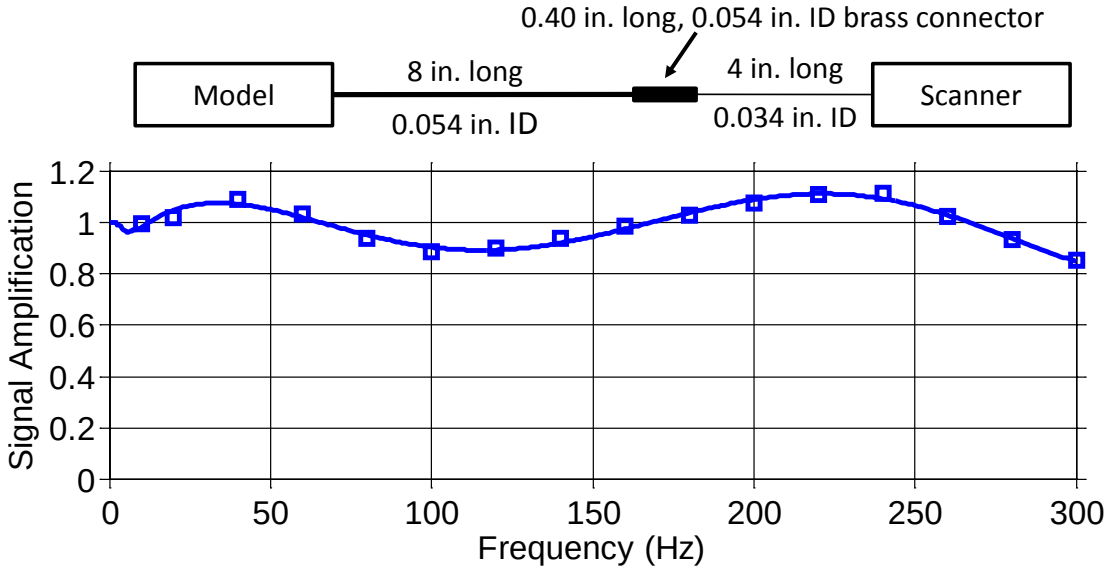

Figure 3-26. Frequency response and arrangement of pressure tubing system

Pressure Coefficient Referencing

Pressure coefficients are calculated from the individual tap's recorded pressure time histories. The pressure coefficients, C_p, are determined by Eqn. 3-6.

$$C_p = \frac{P_{tap}}{\bar{P}_{ref}} = \frac{P_{tap}}{0.5\rho\bar{V}_{ref}^2} \tag{3-6}$$

where: P_{tap} is the pressure difference between the model surface pressure measured at a given tap and the reference level static pressure at a given time; $\bar{P}_{ref}$ is the average reference dynamic pressure recorded at the pitot tube located directly above the model 12 in (300 mm) below the wind tunnel ceiling during a specified sampling time; ρ is the density of air; and $\bar{V}_{ref}$ is the mean velocity of air at the (reference) pitot tube during the

sample. Therefore, the pressure coefficients are referenced to the mean pressure (wind speed) at the pitot tube.

In order to compare results with the currently adopted methods given in ASCE 7-05 (ASCE 2006), the pressure coefficients need to be referenced to a 3-second wind gust at mean roof height (H) of the structure. The pressure coefficients are multiplied by a conversion factor to make this adjustment. This conversion factor, C_a, is calculated according to the Eqn. 3-7.

$$C_a = \frac{\bar{V}_{ref}^2}{V_{3sec,H}^2} \tag{3-7}$$

where: $V_{3sec,H}$ is the 3-second gust wind velocity at mean roof height of the structure which can be calculated by two different methods: (1) theoretical and (2) experimental. Both of these methods are described in detail by Liu (2006).

Wind Generator Testing

A wind generator was used to create wind flow around the 1/3-scale building during which pressure variations on the roof and structural reactions at critical locations were monitored. The wind generator consists of an 8-fan array of 4.5 ft diameter, vane-axial fans, hydraulically powered by four 700 hp marine diesel engines (Masters et al. 2008). The fans channeled air through a contraction area leading to a 10 ft by 10 ft exit. The generator was designed primarily for testing window and door panels (Masters et al. 2008) and does not re-create hurricane wind fluctuations.

For the wind generator testing, the 1/3-scale building was instrumented with pressure transducers and additional load cells as shown in Figure 3-19. The building was then placed between two 16 ft tall walls 18 ft downstream of the generator exit (Figure 3-27). A mean wind speed of 50 mph and a turbulence intensity of 6% were

used in the experiment. A 4-hole Cobra Probe (Serial #193), by Turbulent Flow Instrumentation, Inc., was used to verify the uniformity of the wind speed downwind of the contraction exit (with no model in place) with a sampling frequency of 10,000 Hz (more details provided in Mensah (2010)).

The model building was oriented for wind flow in three angles of attack – 0°, 45°, and 90° – with three 10-minute duration test runs each. Pressure and load measurements were simultaneously taken at a sampling rate of 200 Hz and low-pass filtered at 100 Hz. During the testing, the wind velocity at mean roof height and upwind of the model building was measured using the Cobra Probe.

Figure 3-27. 1/3-scale building downstream of wind generator

Finite Element Model for Dynamic Analysis

In order to investigate the effects of dynamic loads on a LFWS, a finite element (FE) analysis was performed using ADINA (Automatic Dynamic Incremental Nonlinear Analysis) (ADINA 2009). ADINA is a multiuse finite element analysis program for linear and nonlinear analysis of solids and structures as well as fluid-structure interaction, heat transfer, and computational fluid dynamics (CFD). An input file for each model used in the analysis, containing dimensions, material and section properties, boundary

conditions, component connections, loading, etc., was created rather than building the model through the graphical user interface (GUI), allowing changes to the model to be made easily and quickly. A spreadsheet was developed to build the input file, simplifying the entering of repetitive information.

Truss Model

The trusses were modeled with beam elements using an elastic, isotropic material. All truss joints are modeled as pinned connections. The truss members were modeled as southern yellow pine (SYP) with a modulus of elasticity of 2000 ksi and a specific gravity of 0.62 determined from testing, as reported previously, with simple supports at the ends. For the individual truss validations, out-of-plane buckling was prevented by a roller at all five top and bottom chord joints. The truss validation steps are discussed in Chapter 5.

Sheathing Model

The sheathing was modeled with shell elements representing 0.5 in. thick OSB. The shell elements were modeled using an elastic, isotropic material, with a modulus of elasticity of 800 ksi and a specific gravity of 0.652 determined from testing described previously. The sheathing joints found in actual wood roofs were not modeled, but rather a single “sheet” of sheathing was used for each side of the roof. Modeling individual 4 ft by 8 ft sheathing sheets is time consuming, and Cramer et al. (2000) and Martin (2010) have shown that for investigating load sharing and load paths in roofs, modeling individual joints is unnecessary. Martin (2010) provides a detailed explanation for why this is valid. The sheathing was offset from the centerline of the framing members by 2 in. to account for the physical distance between the centerlines of the

framing and sheathing. The sheathing was attached to the framing members through the use of “link” (nail) elements described in the next section.

Nail Model

A nail spacing of 12 in. o.c. was used to attach the roof sheathing to the framing members. Several types of “links” were investigated to model the sheathing-to-framing attachment. ADINA has a built in function (RIGIDLINK) to generate rigid links between two nodes. This command ensures that the distance between the two nodes remains constant and that the two nodes have the same rotations as the model deforms (ADINA 2009). The RIGIDLINK command was first used to model the individual nails, however, when testing the full roof model, the load sharing behavior was not as expected. An applied point load on the sheathing along a truss line resulted in influence coefficients greater than 1.5 when loaded inside the truss support. By replacing the rigid links with beam elements, the static influence functions were reasonable (as shown in Chapter 5). Therefore, instead of using the rigid links, beam elements were instead used to model the nail attachment. The properties of 8d common nails (0.131 in. diameter) were used as the geometric properties of the link elements.

21 Truss Roof Model

Once the individual trusses were validated, an entire 21-truss model was constructed. Sheathing was attached to the sides of the gable end trusses and meshed using ADINA’s free-form Delaunay meshing mode. The roof sheathing was meshed into 3 in. by 6 in. shell elements, and attached at 12 in. intervals to the top chords of the trusses with the nail link elements. Figure 3-28 shows the gable end sheathing mesh, and Figure 3-29 shows the entire roof model. No damping was provided in the FE model.

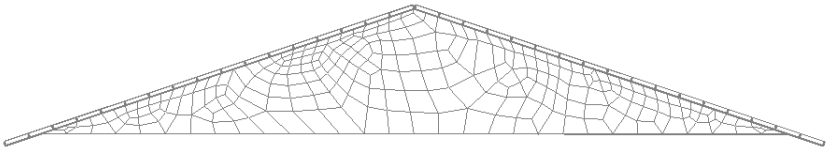

Figure 3-28. Gable end meshing

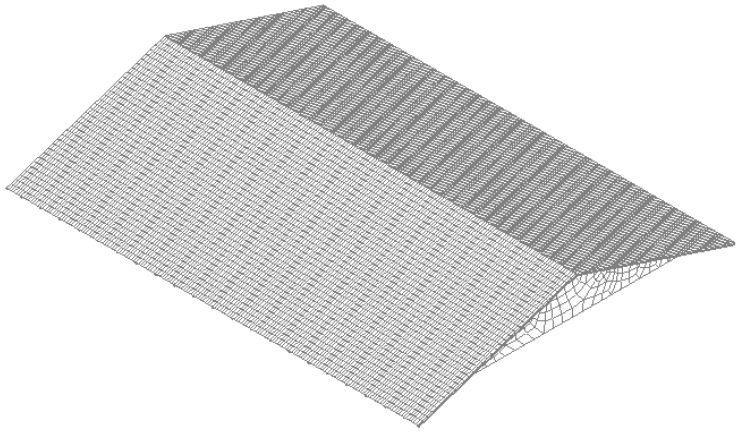

Figure 3-29. Full-scale 21-truss roof model

Dynamic Analysis Procedure

Impulse and Frequency Response Functions

Impulse and frequency response functions will be used to quantify the "dynamic" load paths in a residential LFWS, and therefore a brief description of the functions is presented below. For the ideal single input/single output system as shown in Figure 3-30, the output $y(t)$ (i.e., roof-to-wall connection load time history) is related to the input $x(t)$ (i.e., dynamic wind load time history) through the impulse response function $h(\tau)$. The output is given by the convolution integral, also known as Duhamel's integral (Tedesco et al. 1999) presented in Eqn. 3-8.

$$y(t) = \int_{-\infty}^{\infty} h(\tau)x(t-\tau)d\tau \tag{3-8}$$

The convolution integral provides a weighted linear summation (using superposition and weighted by the impulse response function $h(t)$) of the system at

each time step of the input, $x(t)$, and is therefore only valid for linear systems (Tedesco et al. 1999; Bendat and Piersol 2000). If the system is physically realizable, it cannot respond to an input until that input has been applied (Bendat and Piersol 2000). Therefore, the lower integration limit in Eqn. 3-8 is changed to zero.

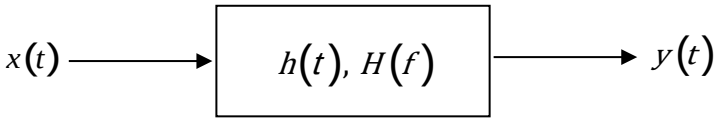

Figure 3-30. Ideal single input/single output system

The frequency response function, $H(f)$, is defined as the Fourier transform of the impulse response function (Bendat and Piersol 2000) given in Eqn. 3-9.

$$H(f) = \int_0^\infty h(\tau) e^{-j2\pi f t} d\tau \tag{3-9}$$

The frequency response function can be estimated from the spectral density functions (described in the next section) as shown in Eqn. 3-10.

$$\hat{H}(f) = \frac{\hat{G}_{xy}(f)}{\hat{G}_{xx}(f)} \tag{3-10}$$

where: $\hat{G}_{xy}(f)$ is an estimate of the cross-spectrum of the input and output, and $\hat{G}_{xx}(f)$ is an estimate of the autospectrum of the input.

Spectral Density Functions

The power spectral density (PSD) function (also called the autospectral density function or the autospectrum) is the Fourier transform of the autocorrelation function. The PSD is defined in Eqn. 3-11.

$$S_{xx}(f) = \int_{-\infty}^\infty R_{xx}(\tau) e^{-j2\pi f \tau} d\tau \tag{3-11}$$

where: $R_{xx}(\tau)$ is the autocorrelation function, $S_{xx}(f)$ represents the average power in x between $f \pm \Delta f/2$ divided by Δf.

For two different time histories, $x(t)$ and $y(t)$, the cross-spectral density (or cross-spectrum) is given by Eqn. 3-12.

$$S_{xy}(f) = \int_{-\infty}^{\infty} R_{xy}(\tau) e^{-j2\pi f\tau} d\tau \tag{3-12}$$

where: $R_{xy}(\tau)$ is the cross-correlation function.

The spectral density functions $S_{xx}(f)$ and $S_{xy}(f)$ are defined over both positive and negative frequencies and are called two-sided. It is more convenient to work with one-sided spectral density functions, $G(f)$, that only involve positive frequencies and are shown in Eqns. 3-13 and 3-14. Figure 3-31 provides a graphical representation of the difference between one-sided and two-sided spectral density functions.

$$\begin{aligned} G_{xx}(f) = 2S_{xx}(f) &= 2\int_{-\infty}^{\infty} R_{xx}(\tau) e^{-j2\pi f\tau} d\tau && f > 0 \\ &= S_{xx}(f) = \int_{-\infty}^{\infty} R_{xx}(\tau) e^{-j2\pi f\tau} d\tau && f = 0 \\ &= 0 && f < 0 \end{aligned} \tag{3-13}$$

$$\begin{aligned} G_{xy}(f) = 2S_{xy}(f) &= 2\int_{-\infty}^{\infty} R_{xy}(\tau) e^{-j2\pi f\tau} d\tau && f > 0 \\ &= S_{xy}(f) = \int_{-\infty}^{\infty} R_{xy}(\tau) e^{-j2\pi f\tau} d\tau && f = 0 \\ &= 0 && f < 0 \end{aligned} \tag{3-14}$$

The spectral density functions can also be defined by the Fourier transforms of the original data sets. If $x(t)$ and $y(t)$ are two distinct data records of length T with k number of records, the finite Fourier transforms are shown in Eqn. 3-15.

$$X_k(f,T) = \int_0^T x_k(t)e^{-j2\pi ft}dt$$

$$Y_k(f,T) = \int_0^T y_k(t)e^{-j2\pi ft}dt \qquad (3\text{-}15)$$

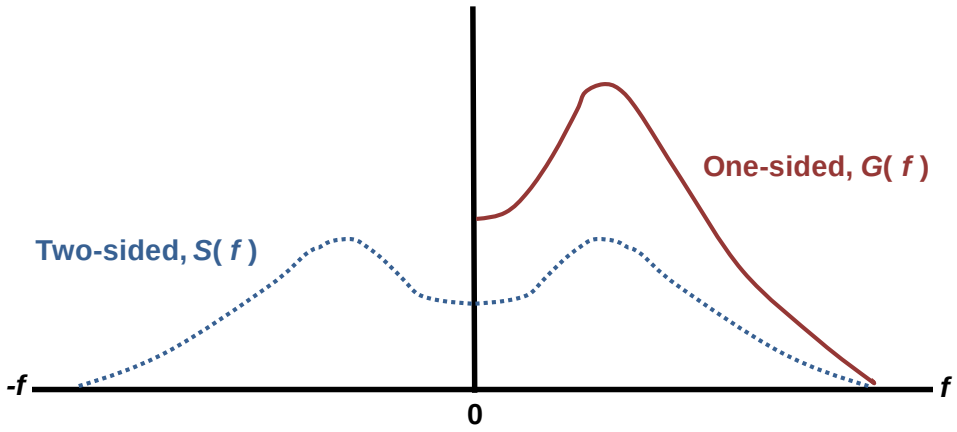

Figure 3-31. Comparison of one-sided and two-sided spectral density plots (after Bendat and Piersol 1993)

The two-sided cross-spectrum is then defined in Eqn. 3-16.

$$S_{xy}(f) = \lim_{T\to\infty}\frac{1}{T}E\left[X_k^*(f,T)Y_k(f,T)\right] \qquad (3\text{-}16)$$

where: $(\quad)^*$ is the complex conjugate, and $E[\quad]$ is the expected value operator and is an average over k number of records. In terms of the one-sided spectrum, Eqns. 3-17 and 3-18 provide the autospectrum and cross-spectrum, respectively.

$$G_{xx}(f) = \lim_{T\to\infty}\frac{2}{T}E\left[|X_k(f,T)|^2\right] \qquad (3\text{-}17)$$

$$G_{xy}(f) = \lim_{T\to\infty} \frac{2}{T} E\left[X_k^*(f,T)Y_k(f,T)\right] \tag{3-18}$$

For stationary data, the estimation of the spectral density functions is obtained by breaking the record into n_d records each of length T such that the total length of data analyzed is $n_d T$. The autospectral and cross-spectral density functions are then estimated by Eqns. 3-19 and 3-20, respectively.

$$\hat{G}_{xx}(f) = \frac{2}{n_d T}\sum_{k=1}^{n_d} |X_k(f,T)|^2 \tag{3-17}$$

$$\hat{G}_{xy}(f) = \frac{2}{n_d T}\sum_{k=1}^{n_d} X_k^*(f,T)Y_k(f,T) \tag{3-18}$$

Coherence Functions

The squared coherence function is a tool to estimate the correlation between two signals, $x(t)$ and $y(t)$, with respect to frequency and is given in Eqn. 3-19.

$$\gamma_{xy}^2(f) = \frac{\left|G_{xy}(f)\right|^2}{G_{xx}(f)G_{yy}(f)} \tag{3-19}$$

where: $0 \le \gamma_{xy}^2 \le 1$. The squared coherence function is similar to the square of the correlation coefficient in the time domain and provides a measure of the correlation between two signals in the frequency domain.

Since the FRFs will be estimated by using Eqn. 3-10, Bendat and Piersol (1993) note that this estimation will include both random and bias errors, which should be minimized. The coherence function is the mechanism to identify the presence of errors and can help to determine their origin and magnitude. If $x(t)$ and $y(t)$ are completely correlated, the coherence function will be unity. If the two signals are not related, the

coherence function will be zero. If the coherence function is between zero and one, one or more of the following reasons exist (Bendat and Piersol 2000):

- Extraneous noise is present in the measurements.
- The system is nonlinear between $x(t)$ and $y(t)$.
- $y(t)$ has other inputs contributing to its response beside just $x(t)$.

Analysis Details

For all of the power spectra analysis presented in this study, MATLAB (MathWorks 2008) was used to calculate the needed quantities. Use of the Fast Fourier Transform (FFT) was employed using Welch's method for calculating power spectra (Welch 1967; MathWorks 2008). A 1024-point FFT was used along with a Hanning window and 75% overlap. Built-in MATLAB commands were used in all instances.

CHAPTER 4
STATIC INFLUENCE COEFFICIENT RESULTS

Static Influence Coefficients

Influence coefficients (as described in Chapter 2) are the fraction of the applied load that is transferred through a given connection. Since the focus of this study is the investigation of load paths due to wind loading on wood roofs, only the vertical (uplift) influence coefficients were calculated for the instrumented connections. Various methods of using the influence coefficients were explored and used as a means of understanding the load paths in a residential LFWS. 2D influence lines as well as 3D influence surfaces were constructed. Four different sets of influence coefficients (and subsequently influence surfaces) were determined. The following describes each case, including the major differences among them the direction of loading (uplift or downward) and the instrumented connections (shown in Figure 4-1).

- *Case 1* – Uplift loads (tested 5/28-6/2/2009) with three intermediate gable end connections (S1-S3) between the bottom chord of the gable end truss and the gable end wall, 10-50 lb point loads in 10 lb increments
- *Case 2a* – Uplift loads (tested 10/30-11/12/2009) without the intermediate gable end connections (S1-S3), 10-50 lb point loads in 10 lb increments
- *Case 2b* – Uplift loads (tested 5/7-5/13/2010) without the intermediate gable end connections (S1-S3), 50 lb point loads
- *Case 3* – Downward loads (tested 7/27-7/31/2009) with three intermediate gable end connections (S1-S3) between the bottom chord of the gable end truss and the gable end wall, 10-50 lb point loads in 10 lb increments

The following section on the influence surfaces discusses the negligible effect of the magnitude of the applied load on the influence coefficients for the load range tested. For the influence lines reported here, only the 50 lb loads are used.

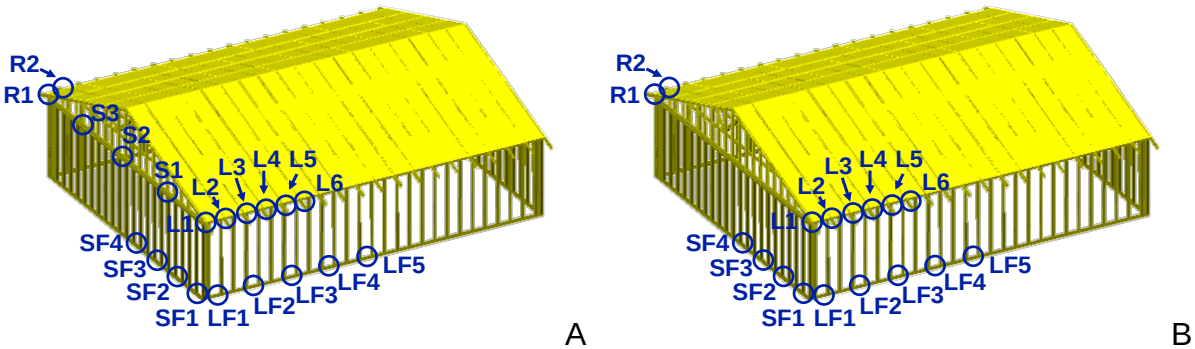

Figure 4-1. Load cell placement in 1/3-scale wood-frame building for A) Cases 1 and 3 and B) Case 2

Influence Lines Along Trusses

Influence lines were plotted for several roof-to-wall connections for loading along the truss. An analytical influence line for a single truss (without being part of a roof assembly) was calculated and is shown in Figure 4-2 where an interesting phenomenon is observed. At the center of the truss (at the peak joint), there is an offset in the influence line due to applying the load perpendicular to the top chord which has a corresponding vertical and horizontal component. By applying simple statics, the horizontal component adds or subtracts from the vertical forces (depending on which side of the peak the load is applied) resulting in the influence line as shown. This influence line is the same if a tributary width of sheathing is also attached to the top chords.

Figure 4-3 shows influence lines for the four cases. As Figure 4-3 shows, Case 1 and Case 3 are nearly identical in shape and magnitude for all of the connections. Therefore, within the range of testing the direction of loading (uplift or downward) has no effect on the influence coefficients. However, there is a difference between Case 2 and Cases 1 and 3 for the gable end truss (connections L1 and R1) and the first interior truss (connections L2 and R2). In Case 2a, the influence line tends to be more linear

than for Cases 1 and 3 as well as higher in magnitude, which makes sense because there are no intermediate load transfer connections to share the load. An influence coefficient of 1.0 for vertical loads would be expected at the reaction location, which does not occur in this experiment. Most likely this is due to load sharing by the sheathing, resulting in some of the load applied directly above the connection transferred to adjacent connections leading to a peak influence coefficient of less than unity.

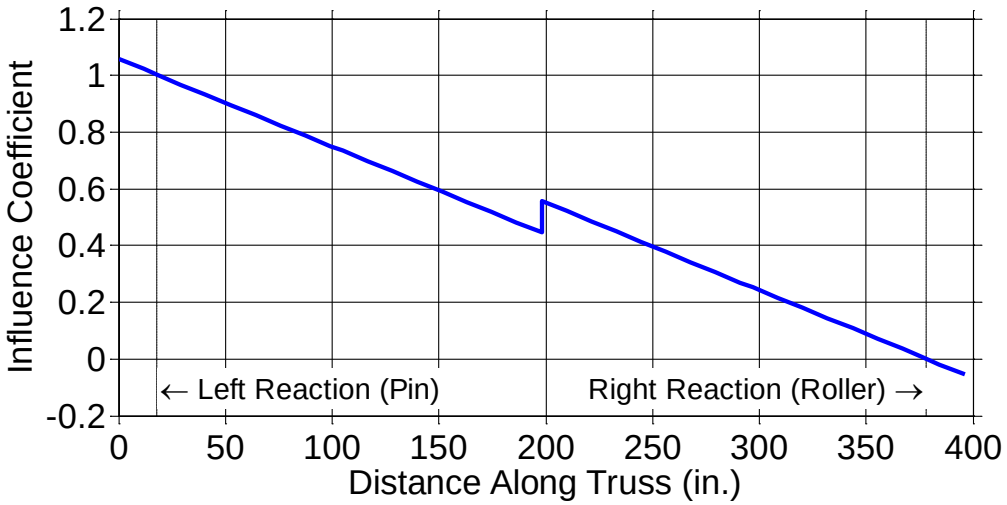

Figure 4-2. Theoretical influence line for the left reaction on a single truss (4 in 12 slope with point loads applied normal to top chord)

There is a pronounced difference between the influence lines for Cases 2a and 2b, for the gable end truss connections L1 and R1. The likely cause of the differences in influence surfaces is an alteration of the stiffnesses of the roof-to-wall connections that resulted in different load sharing among the gable end and first interior trusses. The effect of this changed structural system is obvious in Figure 4-4 which shows the influence lines for truss connections of the first interior truss (L2 and R2) while load is applied directly over the gable end truss. Substantially higher influence coefficients are observed for Truss 2 at both connections L2 and R2 for Case 2b over Case 2a

indicating that the load on the gable end truss is spread more to the second truss resulting in lower influence coefficients for connections L1 and R1 as seen in Figure 4-3.

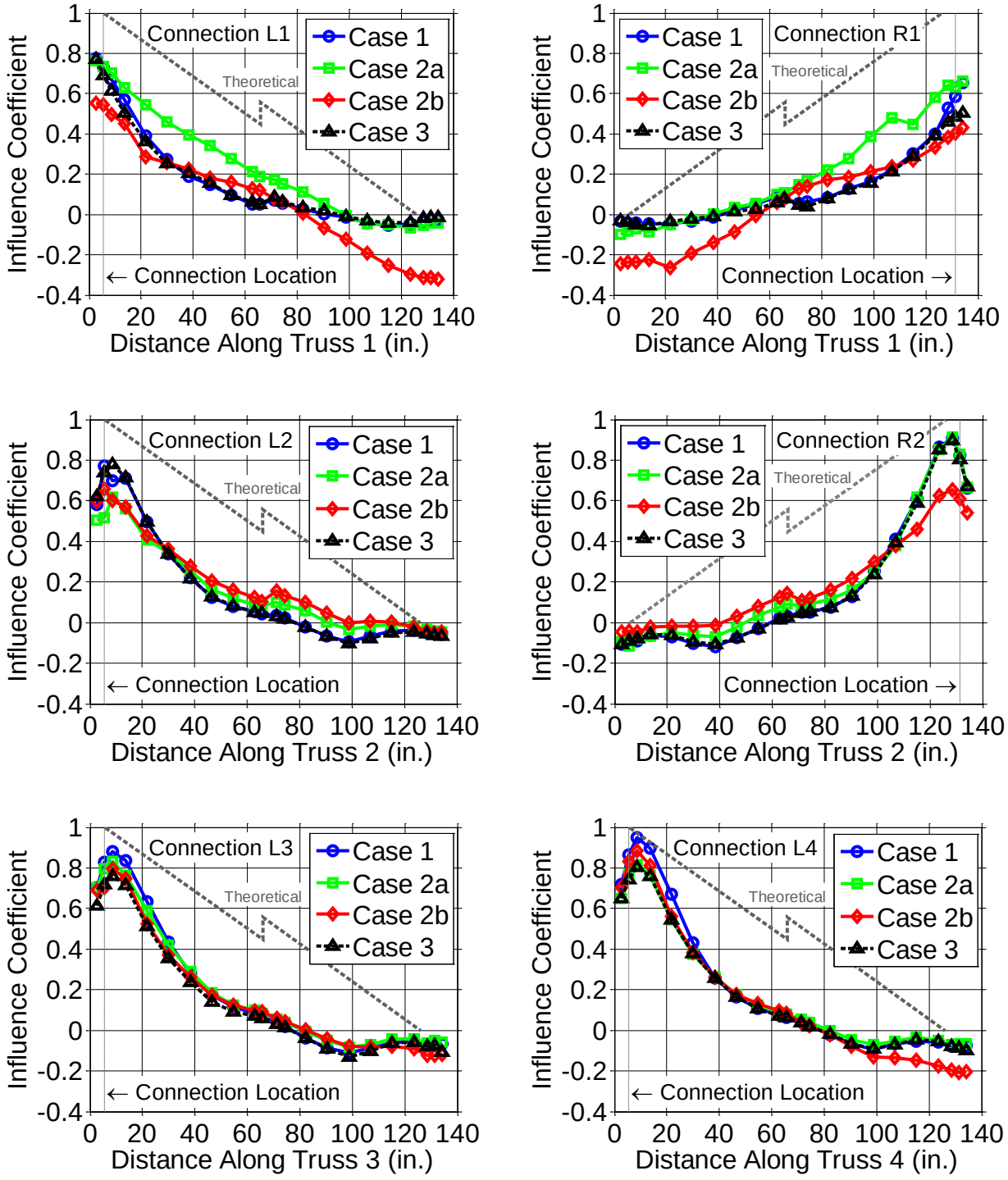

Figure 4-3. Influence lines for roof-to-wall connections

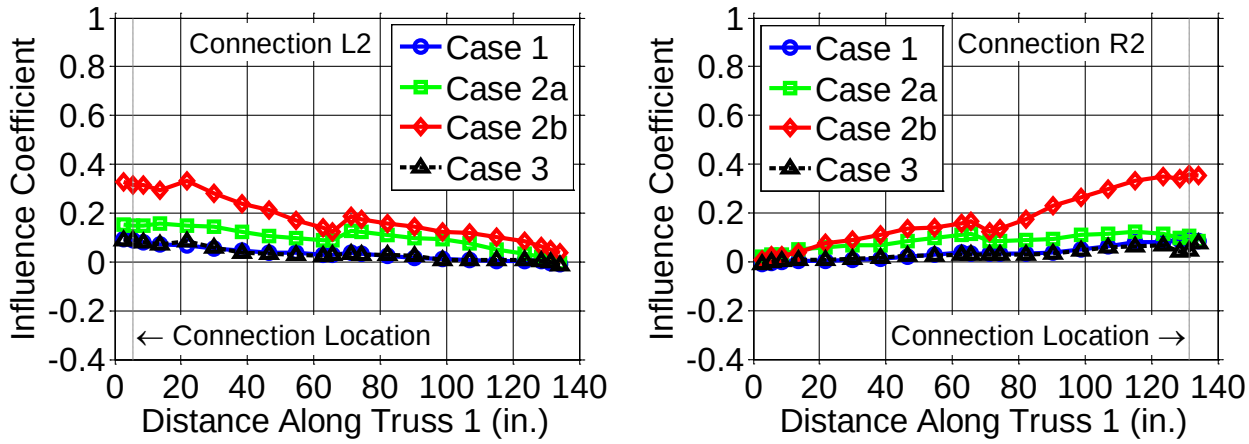

Figure 4-4. Influence lines for connections L2 and R2 when gable end truss is loaded

The influence coefficient testing for Case 2b was performed six months (May 2010) after testing was completed for Case 2a (November 2009). The influence coefficients for Case 2a were determined approximately five months before the wind generator test. The 1/3-scale model had to be moved via a forklift to the wind generator location, which occurred in March 2010 and the Case 2 influence coefficients were performed about a month later (May 2010) , after the model was returned to the laboratory. It appears that despite its sturdy steel base frame, the model building may have experienced some bumps during transport which laterally displaced the roof which was isolated from the walls (by load cells and wood spacers).

The change in stiffness could be due to wood fiber crushing at the load cell-to-top plate interface or a loosening of the truss-to-load cell connections (i.e., the steel strap). Another less likely possibility was that the stiffness changed due to temperature and relative humidity changes between the periods of the influence surface experiments, since the first test was conducted in November 2009 when the mean ambient temperature was about 15°F cooler than it was during the second testing (conducted in May 2010). The evidence in support of this latter possibility is weak because the

influence surfaces of all connections were not equally affected. As a result of this finding, for the remaining study the influence coefficient data used for Case 2 was determined from Case 2a (testing in November 2009).

Figure 4-5 shows the influence lines for roof-to-wall connections along the gable end walls. As expected, the maximum influence coefficients occur just above the connection. The peak influence coefficients are between 0.3 and 0.4 suggesting that the majority of the load is distributed either to other connections on the gable end truss or to the adjacent truss. For Cases 1 and 3, the gable end truss is supported at five locations (at both ends and at quarter points) acting as a four-span continuous beam. The plots in Figure 4-5 show that when the gable end truss is connected at discrete points between its end supports, a significant portion of the applied load on the roof is transferred through these intermediate connections. In his analytical FE analysis, Martin (2010) also observed this phenomenon when the gable end sheathing was continuous between the wall and the truss.

3-Dimensional Influence Surfaces

Influence surface contours provide a convenient way for observing the source of loads transferred to any connection. By applying point loads at multiple locations on the roof individually, the effect of load transfer can be determined. Appendix B contains the influence surfaces for all instrumented connections. Influence surfaces of two roof-to-wall connections are shown in Figure 4-6 and Figure 4-7 for increasing load magnitudes for Case 1. The influence surfaces in Figure 4-6 are typical for the connection points of interior trusses, and Figure 4-7 is typical of the gable end corner connection. The peak influence coefficients are centered above or near the connected point, and for the load range tested little change in the influence coefficients occurs with increasing load

signifying that the loading was kept within the linear-elastic range. As such, results presented later in this dissertation will be based on the influence coefficients calculated from the 50 lb applied point loads. Generally, the influence surfaces show that loads transferred to interior roof-to-wall connections, occur within the adjacent two trusses on either side of that connection point.

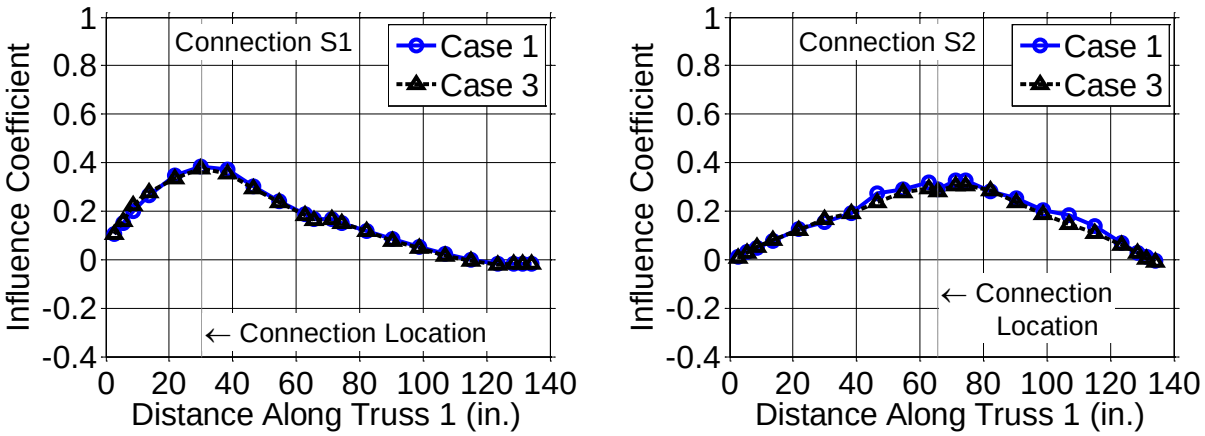

Figure 4-5. Influence lines for intermediate gable end roof-to-wall connections

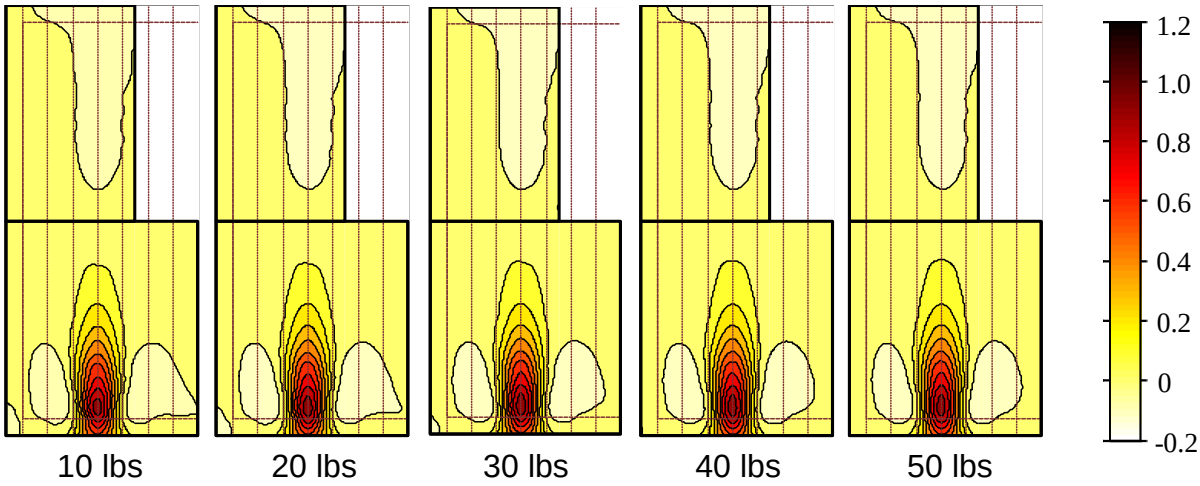

Figure 4-6. Influence surfaces for connection L4 (Case 1) for increasing load magnitudes

Figure 4-7 shows the influence surfaces for the corner roof-to-wall connection. As can be seen, the influence coefficients are largest (maximum of 0.86) when the applied load is over the eaves and decrease as the distance from the corner increases. Figure

4-8 shows the influence surfaces for wall-to-foundation connections. It is interesting to note that the influence surfaces are between about 0.1 and 0.2 for interior foundation connections (LF2 and LF4) likely due to the wall acting as a stiff, deep beam spreading the loads (even those applied right above the reaction point) more evenly across the foundation. The corner wall-to-foundation connections (LF1 and SF1) attract load from a larger roof area than the interior foundation connections as well as having influence coefficients that are a bit higher (up to more than 0.3 over 0.2 for interior connections). Additionally, the gable end foundation connections (SF1 and SF2) attract more load than the side wall connections (LF1 and LF2).

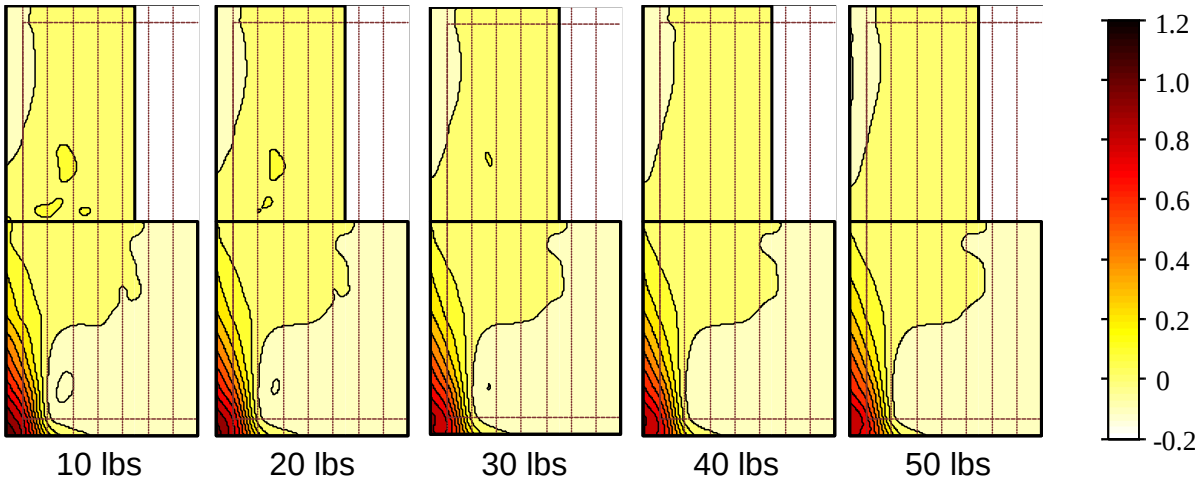

Figure 4-7. Influence surfaces for connection L1 (Case 1) for increasing load magnitudes

The influence surfaces shown have been for uplift loads only. The loads on the house were also applied in a downward direction (Case 3) to investigate the effects of the load direction. Figure 4-9 shows the gravity influence surfaces for connection L4 (compare with Figure 4-6). There is little difference between the plots, inferring that the influence surfaces for this house are equal for both uplift and downward applied loads on the roof.

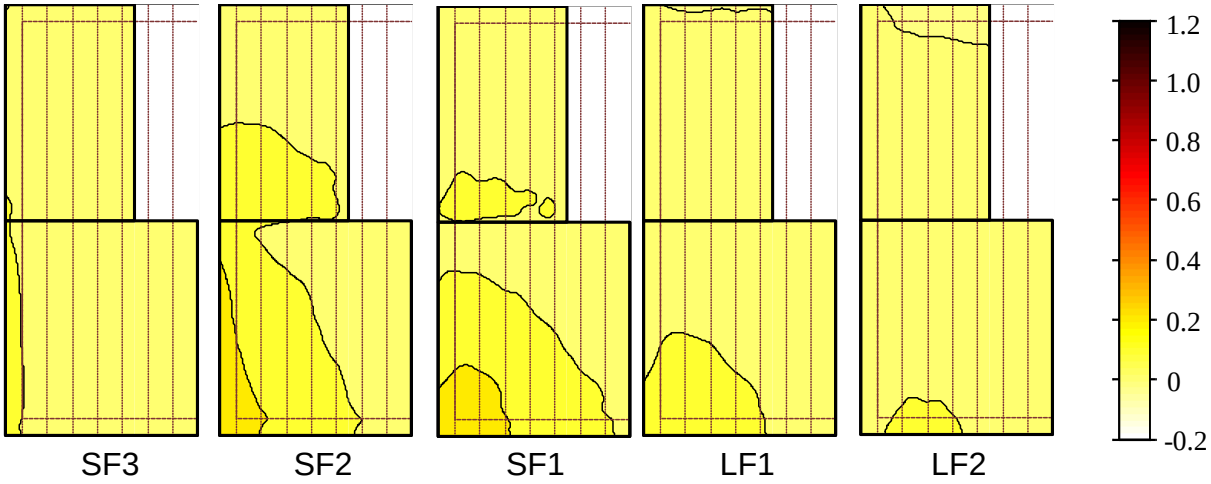

Figure 4-8. Influence surfaces for wall-to-foundation connections (Case 1)

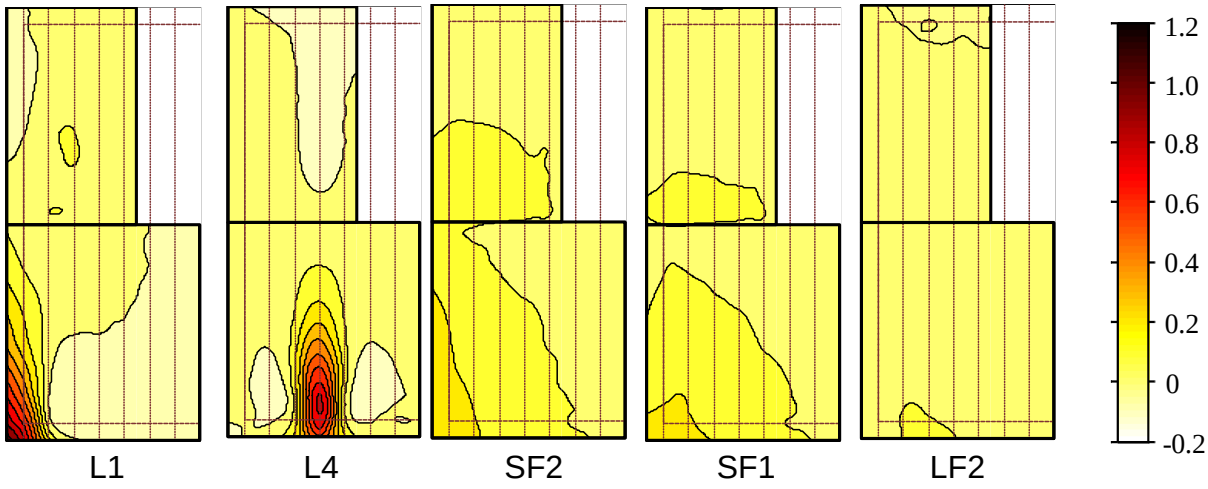

Figure 4-9. Influence surfaces for connections for Case 3 (gravity loading)

As a check of superposition assumptions, adjacent connection influence surfaces were summed to provide insight into the effect of two adjacent connections. Figure 4-10 through Figure 4-13 provide influence surface plots for several adjacent connections for Cases 1 and 2a.

As can be seen in Figure 4-10, the three intermediate gable end load cells (S1-S3) account for up to 70% of the applied load over the gable eave overhang and up to 30% of the load applied to the second interior truss. In contrast, the summation of the influence surfaces of the two gable end reaction connections (L1 and R1) accounts for

up to 8% of the load but concentrated over the cantilevered eave. When the influence surfaces of all five gable end truss connections (L1, S1-S3, and R1) are combined, it is seen that the gable end truss is influenced by a relatively large area of the roof with influence coefficients over 1.0. However when the influence surface of the first interior truss connections are included, the area of influence is only increased by one truss spacing (i.e., 24 in. full scale). The lack of symmetry in the influence functions is attributed to differences in truss stiffnesses and variations in the stiffness (specifically

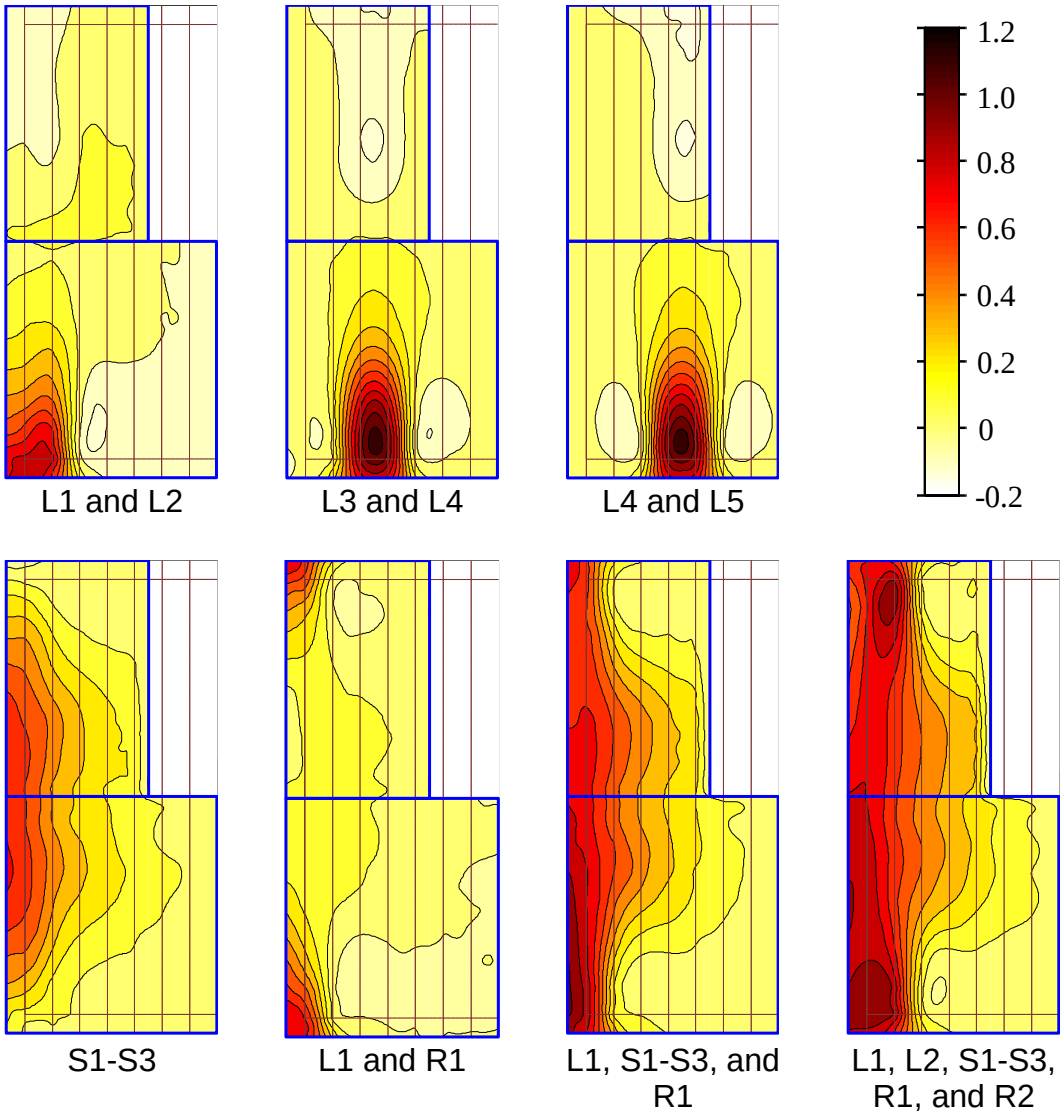

Figure 4-10. Influence surface summations for adjacent roof-to-wall connections (Case 1)

MOE values) within individual trusses. Additionally, the gable end truss is stiffer than the interior trusses due to the sheathing attached on one side.

Figure 4-11 shows the combined influence surfaces for wall-to-foundation connections for Case 1. The combined influence surfaces are reduced in magnitude from the roof-to-wall connections. One interesting feature made obvious by Figure 4-11 is that the gable end wall (SF1-SF4) transfers more load into the foundation than the side walls (LF1-LF4). Again, Martin (2010) observed a similar phenomenon.

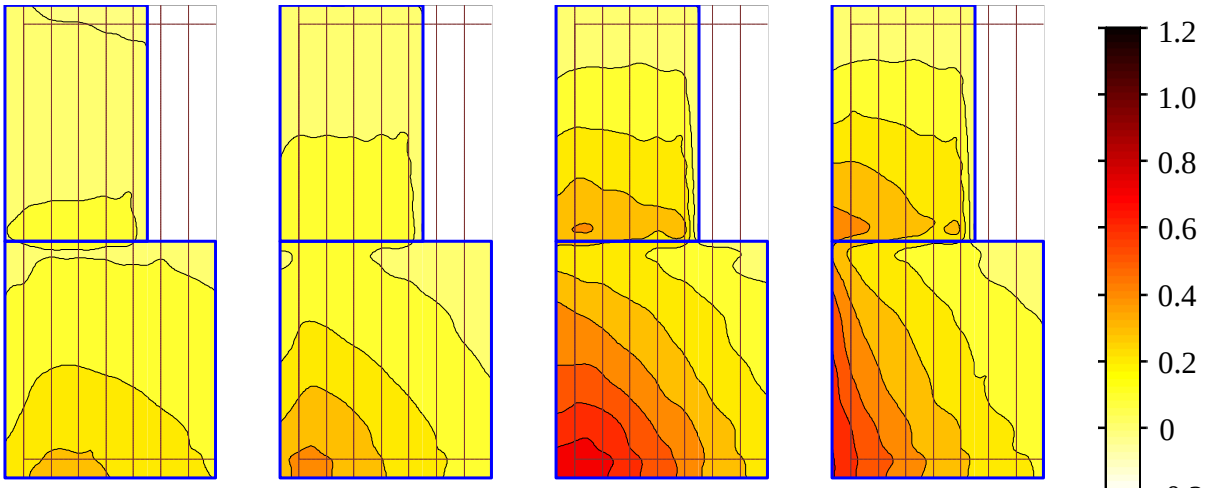

Figure 4-11. Influence surface summations for adjacent wall-to-foundation connections (Case 1)

Figure 4-12 shows combinations of roof-to-wall connections for Case 2a (without the intermediate gable end connections). By contrast with Figure 4-10, the gable end reactions (L1 and R1) in Case 2a are larger in magnitude with a larger influence area. Again, the contrast of having the intermediate gable end connections is pronounced between Case 1 and Case 2a. In Case 2a, the magnitude of the influence coefficients for the two end trusses (L1 and L2) are larger than those for Case 1 due to the lack of the intermediate connections. The significance of this result is that current analysis techniques generally do not account for this load transfer mechanism through the gable

end wall. Typically trusses are designed as a single span with simple supports at either end that transfer the entire load applied on the truss to the walls. The effect of intermediate connections between the gable end truss and wall reduces the loads at the truss end reactions significantly.

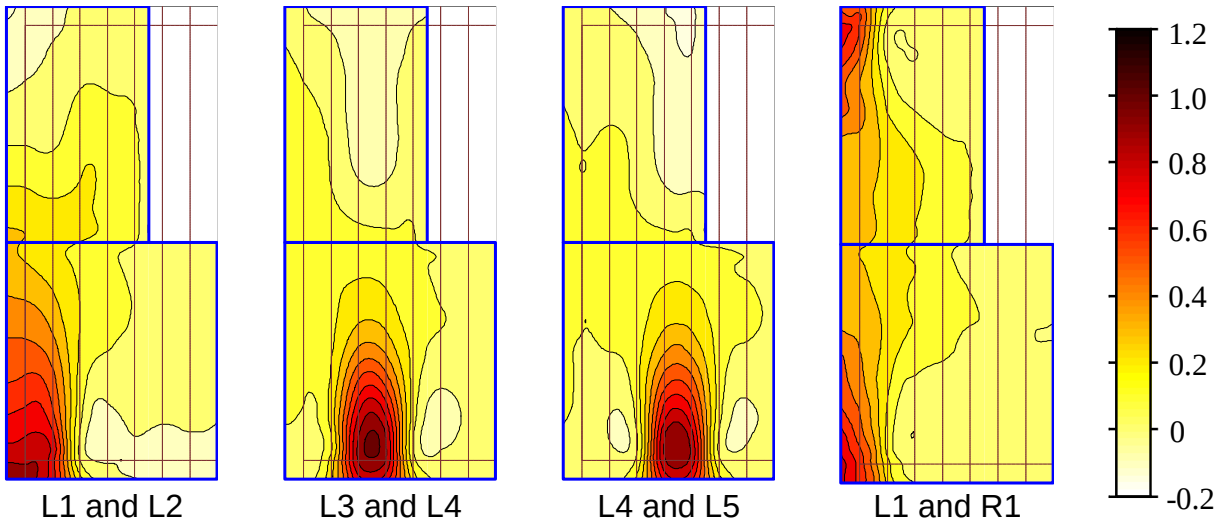

Figure 4-12. Influence surface summations for adjacent roof-to-wall connections (Case 2a)

Figure 4-13 shows the combined influence surfaces for wall-to-foundation connections for Case 2a. The gable end wall connections (SF1-SF4) transfer more of the load applied to the roof than the side wall (LF1-LF4) even though there are no intermediate connections between the gable end truss and the end wall. The load is most concentrated near the corner as in Case 1 but is slightly higher in magnitude in Case 2a. This finding again suggests that a significant portion of the load carried by the gable end wall is distributed into the end wall whenever intermediate connections are present.

Influence Coefficients for Line Loads

Since the loads were kept within the linear-elastic range of the roof system, the principle of superposition is valid (Wolfe and McCarthy 1989). Using this principle, the

individual point loads were superimposed to produce an equivalent line load. All of the line loads were applied parallel to the roof trusses (i.e., along the span). The effect of two line loads were calculated as follows: (1) a full-span load applied along the entire truss span and (b) a half-span load applied either on the left or right side of the ridge. The line loads were applied directly on each loaded truss as well as halfway between each truss on the sheathing. One additional line load was applied on the gable end overhang.

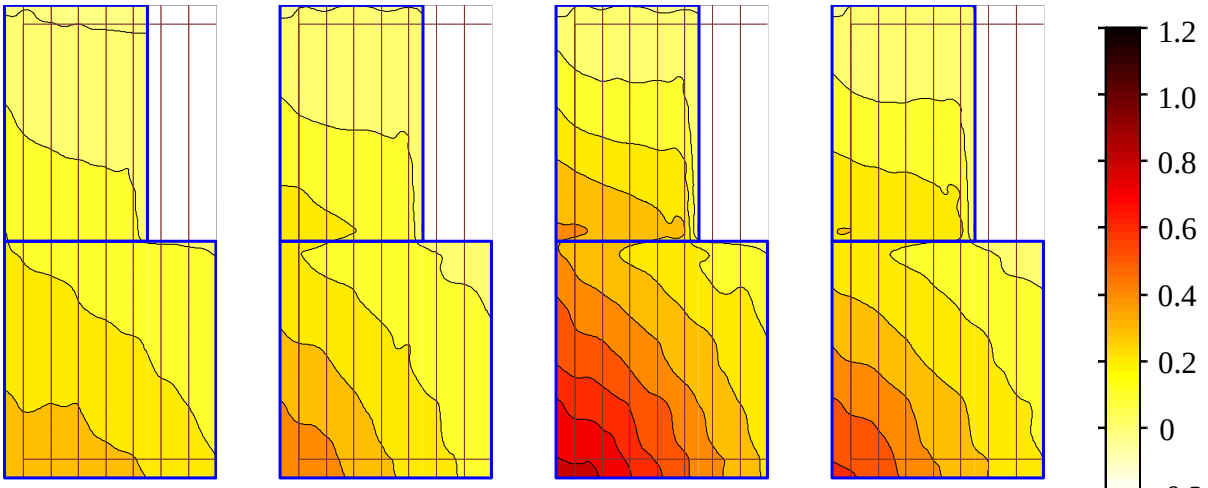

Figure 4-13. Influence surface summations for adjacent wall-to-foundation connections (Case 2a)

The influence coefficients for the line loading are defined as the load at the connection divided by the total applied line load. Therefore, if a connection has an influence coefficient of 0.25, then that connection bears 25% of the total applied line load. Influence coefficients for roof-to-wall connections are presented in Figure 4-14 for Case 1 and Figure 4-15 for Case 2a. The influence coefficients for the full-span loading are roughly half of those for the half-span loading. Also, when the load is applied directly on the sheathing halfway between the trusses, the influence coefficients for the two adjacent roof-to-wall connections are nearly equal, signifying that the load is equally

shared between these connections. The influence coefficients for connection L2 are consistently lower than for the other connections in both full span and half span line loading. When comparing individual truss stiffness values, this truss does not have the lowest values (Truss 3 has the lowest stiffness). The probable cause is the extra stiff gable end truss with the attached sheathing is much stiffer and thus attracts more of the

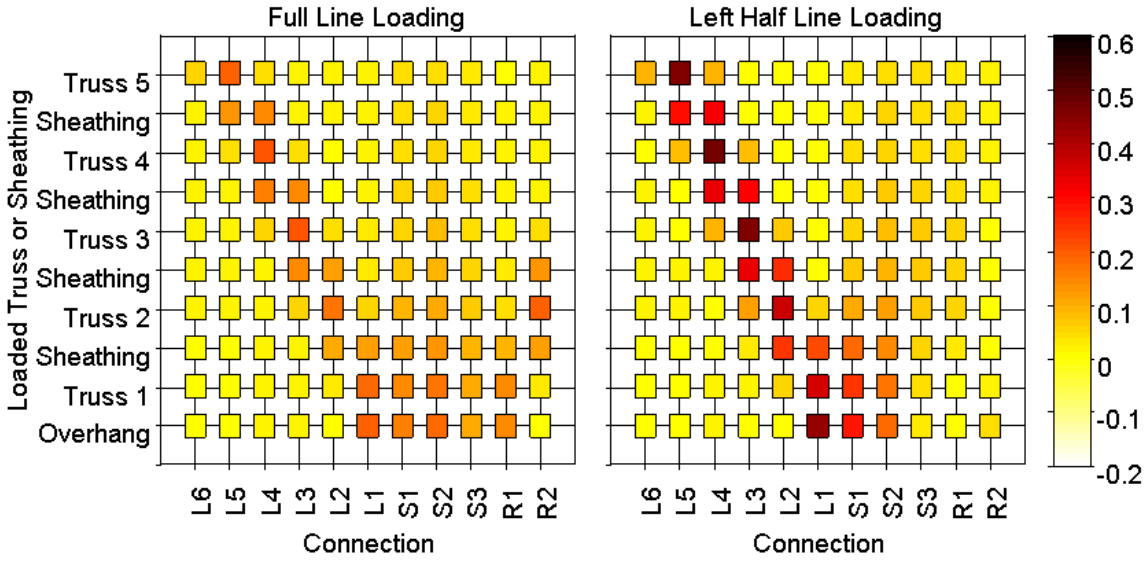

Figure 4-14. Roof-to-wall influence coefficients for full- and left half-line loading (Case 1)

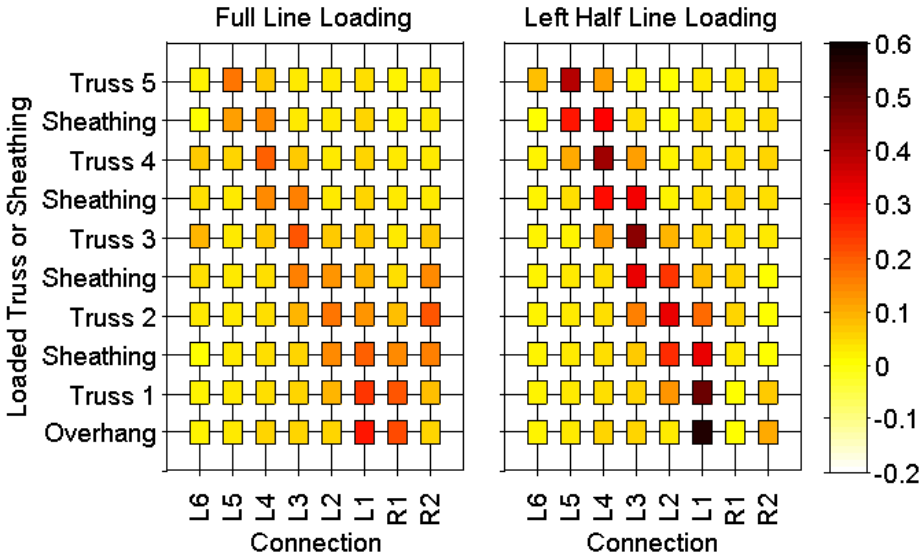

Figure 4-15. Roof-to-wall influence coefficients for full- and left half-line loading (Case 2a)

load from Truss 2. This same phenomenon was observed by Wolfe and McCarthy (1989) on their full-scale roof assemblies. By the time the load is applied to Truss 3, the gable end truss is sufficiently far that it does not attract as much of the load, causing Truss 3 to carry more load than Truss 2 when it is loaded.

In comparing these values to those obtained by Wolfe and McCarthy (1989), only Case 2a can be used, since they built a nine truss roof with no end walls. Figure 4-16 shows the influence coefficients obtained for a 3 in 12 slope roof to be compared to the present study with a 4 in 12 slope. The influence coefficients in Wolfe and McCarthy are provided as the sum of both truss reactions instead of a single truss reaction. Therefore, the coefficients presented in Figure 4-16 are divided by two, assuming a uniform distribution of loads along the trusses for direct comparison. A couple of differences are noted in Figure 4-16. First, connection L2 has the highest influence coefficient for the interior truss connections for the Wolfe and McCarthy roof than the model roof. This is most likely due to the Wolfe and McCarthy gable end truss not being

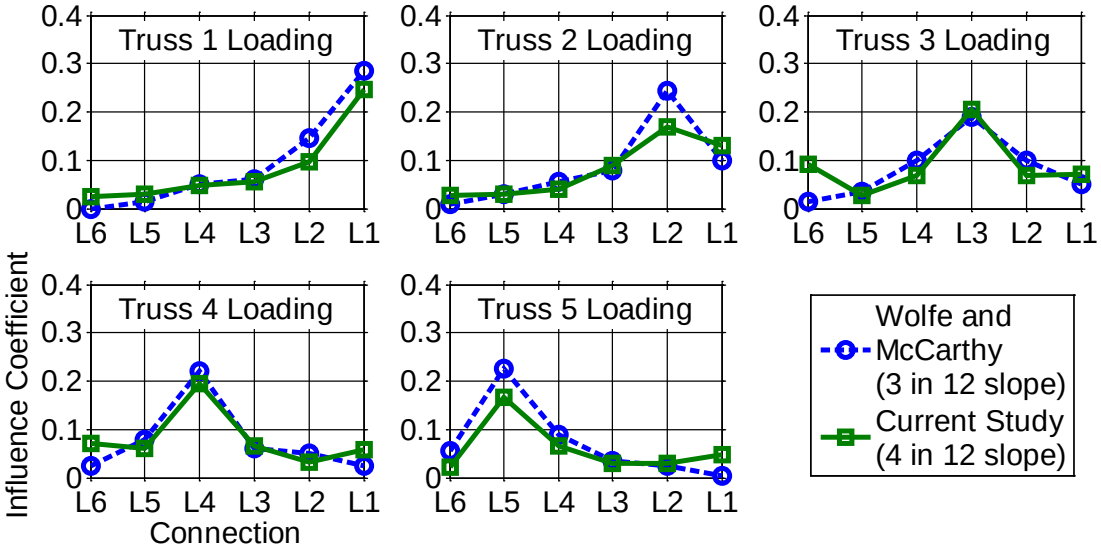

Figure 4-16. Comparison of influence coefficients from Wolfe and McCarthy (1989) with current study (Case 2a)

as stiff as in the current study since their gable end truss was an open web Fink truss (the same as all of the interior trusses) with no gable end sheathing. Another significant difference is that the gable end connection (L1) has a higher influence coefficient than the model roof. This is somewhat surprising since the full-scale roof did not have sheathing on the gable end truss and the model roof did. Therefore, it can be concluded that the gable end truss will always attract more load than the other trusses no matter how much stiffer it is than the other trusses.

DAD Validation

In order to validate the database-assisted design (DAD) method for a LFWS, the scale building was subjected to winds created by UF's wind generator. Pressures and loads were simultaneously measured on the structure.

Wind Generator Testing

Contour plots of peak pressure coefficients on the building roof from testing with the wind generator are shown in Figure 4-17. Wind pressures were normalized by the wind velocity measured by the Cobra Probe at the mean roof height. The time series of wall pressure coefficients at W1 and W3 (Figure 3-19) are assumed to be representative of the uniform pressure distributed along the bottom surface of the eave overhang. Vickery (2008) found that soffit pressures are nearly fully correlated with nearby wall pressures (average of 7% difference between their peak negative values). Therefore, the wall pressures were added to the roof pressure coefficient time series along the overhang regions to account for soffit pressures. Figure 4-18 shows contour plots of peak coefficients of total roof pressures, including eave pressures.

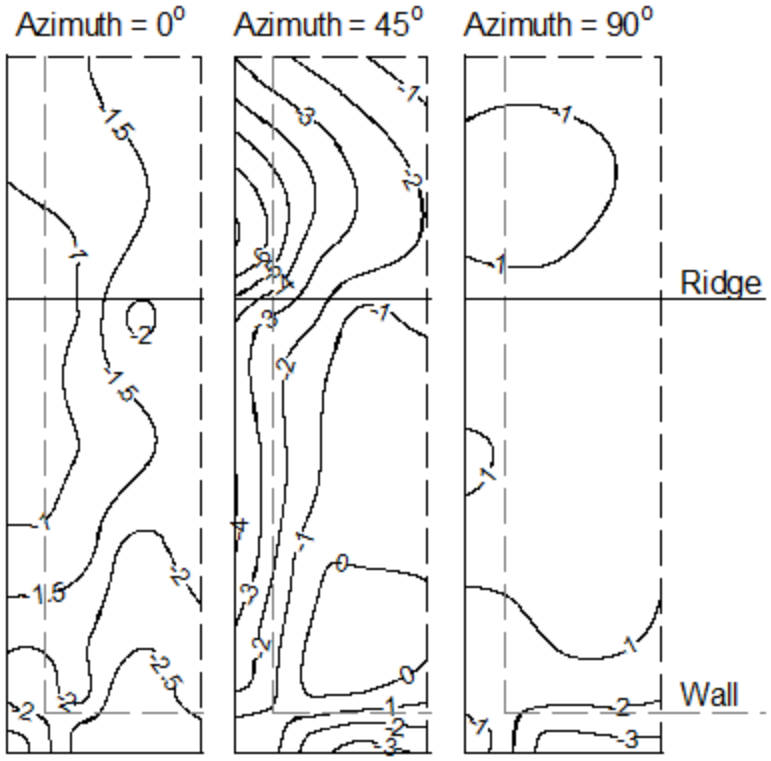

Figure 4-17. Contour plots of pressure coefficients measured on the roof of the 1/3-scale building

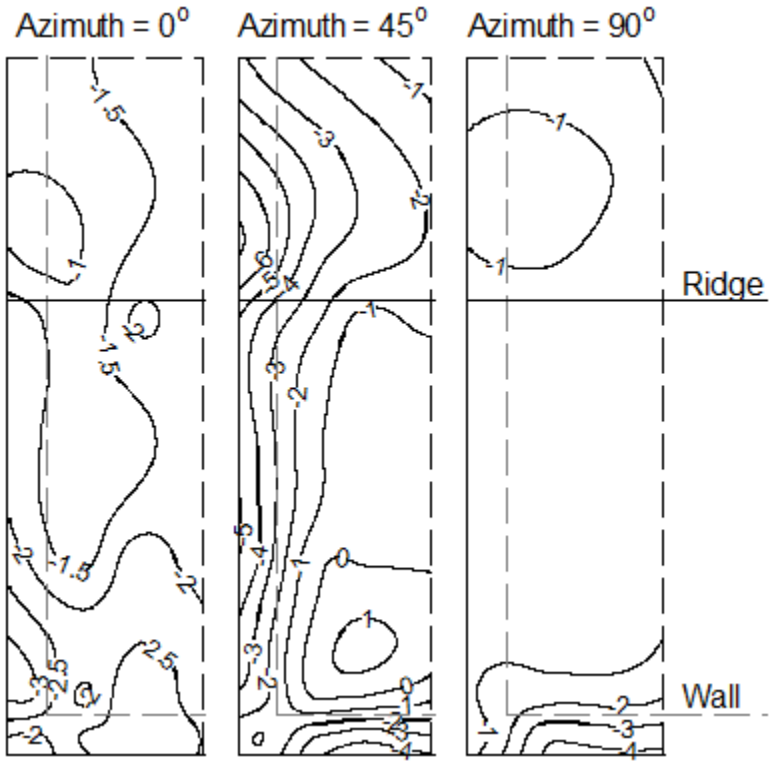

Figure 4-18. Contour plots of pressure coefficients measured on 1/3-scale building (including soffit pressures)

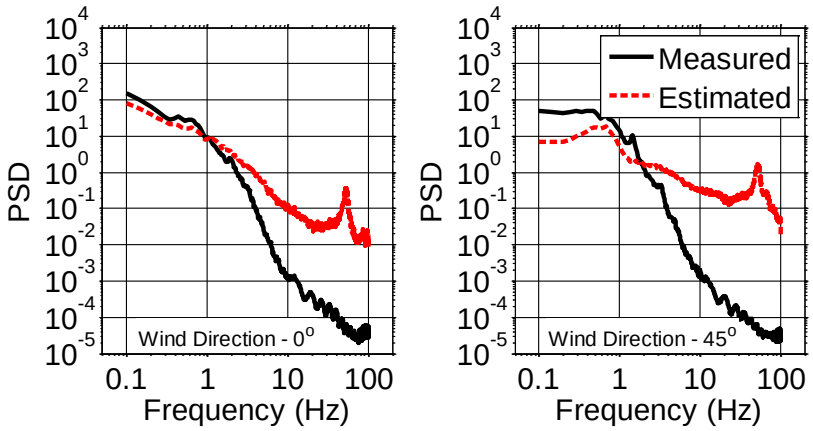

Figure 4-19. Power spectra of reaction load at connection L1 (model-scale)

DAD Validation Results

Structural reactions at the connections L1, L2, and L3 were estimated using the DAD methodology by analytically combining the influence coefficients with the two wind pressure time histories: (1) roof pressures only and (2) using the total pressure on the roof (from upper and lower soffit surfaces on overhang roof areas). Since the influence surfaces were significantly different between Case 2a and Case 2b (especially for connections L1 and L2 – the focus of the validation), with the major difference being that they were tested before and after the wind generator tests, it was decided to use the influence surfaces from the second set of tests (Case 2b) for the validation of the DAD methodology. Since the hypothesis is that the transfer of the building caused a change in stiffness values, using Case 2b for the validation methodology is reasonable.

Figure 4-19 shows typical power spectral densities (PSD) of the structural reactions measured and estimated using the DAD methodology for the combined pressures of the roof and soffit. Most of the energy falls within a low frequency range (0 to 5 Hz) with reasonable agreement between the PSDs of measured and estimated reactions. The spike observed in the estimated reactions (near a frequency of 55 Hz) was attributed to signal resonance in the tubing system since the spike was not seen in

the PSDs of the incident wind flow from the Cobra probe nor in the loads recorded by the load cells. The data was low-pass filtered at 5 Hz (using an eighth-order Butterworth filter) to generate the reaction time histories.

Figure 4-20 shows the first 60 seconds of a typical 10-minute time history (for clarity) of the experimentally measured reactions compared to the DAD-estimated reactions using only the roof pressures for L1 for wind azimuths 0° and 45°. Figure 4-21 shows the same time history for L1 including the effect of soffit pressures. (Additional time-histories for different directions and connection locations are provided in Appendix C). It is observed that without the inclusion of soffit pressures, the DAD method underestimated the measured reactions. However, there is generally a good agreement (especially for a wind direction of 0°) between the measured structural loads and reactions estimated when the soffit pressures are included. A comparison of the statistical values of the measured and estimated reactions using the combined pressures at connections L1, L2 and L3 is presented in Table 4-1.

There is reasonable agreement between the statistical values of measured and estimated (total) reactions, especially for gable end and first interior connections (L1 and L2), respectively. There is less agreement for the L3 connection because the limited distribution of the pressure taps did not completely cover the influence area of the L3 connection. In addition, the discrepancy between the measured and estimated reactions could be that the course geometric distribution of the pressure taps provides insufficient resolution to capture the spatial pressure distribution. Also, simplifying assumptions were made regarding the temporal variation and magnitude of the overhang pressures using two wall pressure taps (W1 and W3).

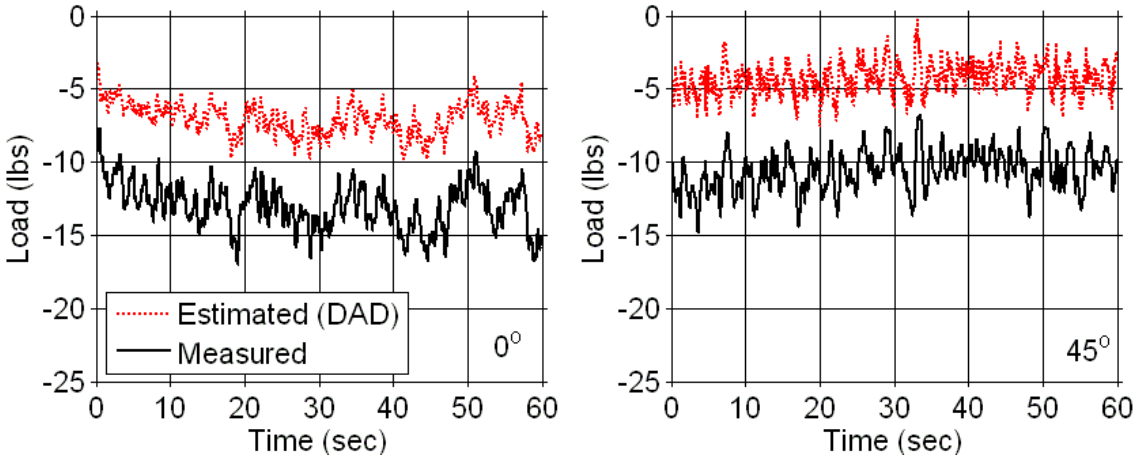

Figure 4-20. 60-second time histories of vertical reaction at L1 with only roof pressures on the 1/3-scale building

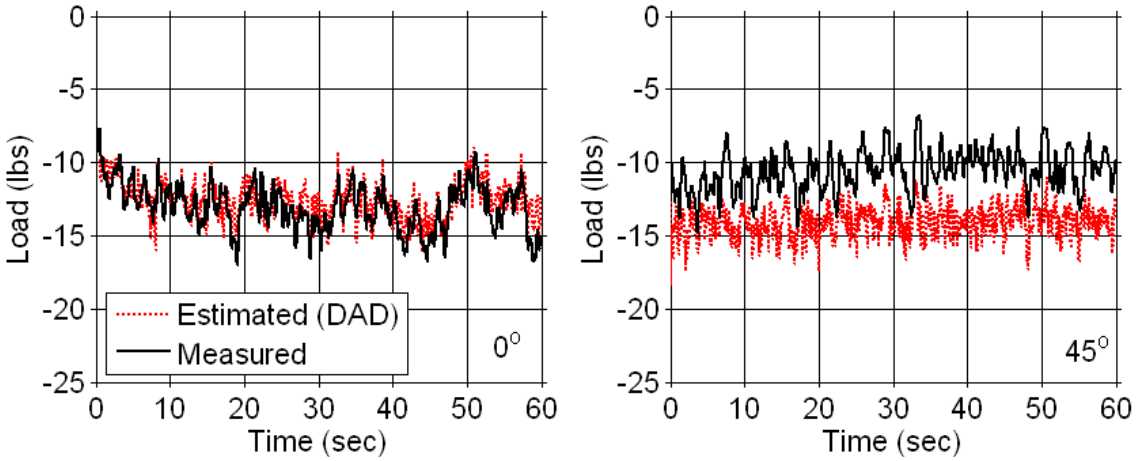

Figure 4-21. 60-second time histories of total vertical load at L1 including estimated soffit pressures on the 1/3-scale building

Table 4-1 includes results comparing the measured and estimated reactions when the model building was oriented at 90° to the wind. In all three cases there was poor agreement between measured and estimated reactions, both for peak and mean loads. This was somewhat expected due to the limitations in the experimental setup that prevented the wind flow from completely enveloping the structure, thus resulting in unnatural results (Mensah 2010). Figure 4-22 and Figure 4-23 provide the probability density functions (PDFs) of the connections L1-L3 for wind angles of 0° and 45°, respectively. In both of these figures, the measured loads are compared to the DAD-

estimated loads using the measured roof surface pressures combined with the respective influence coefficients. Additionally, a reverse lognormal distribution is fit to the data. There is reasonable agreement between the measured and estimated PDFs for connections L1 and L2 for a wind direction of 0°. However, less good agreement is observed for the 45° wind angle. It is believed that there was an insufficient number and low density of pressure taps to adequately capture the spatial pressure distribution as well as assumptions used in including the overhang pressures (Mensah 2010). However within the limitations of this study, the comparison of the DAD-based reactions versus directly measured reactions showed reasonable agreement leading to the conclusion that the DAD approach can predict structural reactions in a light-framed wood roof structure.

Table 4-1. Comparison of statistical values (in pounds) of DAD-estimated and measured vertical loads at L1, L2, and L3 in the 1/3-scale building

	Reaction		Peak	Mean	St. Dev.	Skewness	Kurtosis
0°	L1	Measured	-26.5	-15.3	3.04	-0.458	2.82
		DAD	-21.5	-12.9	1.99	-0.312	2.83
	L2	Measured	-22.2	-15.7	2.27	-0.211	2.35
		DAD	-23.3	-14.4	2.40	-0.242	2.69
	L3	Measured	-26.4	-18.6	2.37	0.056	3.09
		DAD	-18.6	-10.7	1.95	-0.131	2.71
45°	L1	Measured	-18.9	-12.1	1.88	-0.128	2.78
		DAD	-21.4	-15.2	1.46	0.063	3.00
	L2	Measured	-14.5	-9.9	1.23	-0.166	2.64
		DAD	-24.5	-17.1	1.89	-0.011	2.92
	L3	Measured	-17.0	-12.5	1.46	0.064	2.64
		DAD	-16.1	-10.8	1.37	-0.036	2.84
90°	L1	Measured	-4.3	1.9	1.67	-0.117	2.94
		DAD	-14.1	-2.0	2.38	0.241	3.25
	L2	Measured	-22.4	-9.0	1.71	-1.25	7.17
		DAD	-14.4	-2.9	2.42	0.189	3.35
	L3	Measured	-4.7	1.4	1.08	-0.282	4.32
		DAD	-11.4	-1.9	2.19	-0.049	3.12

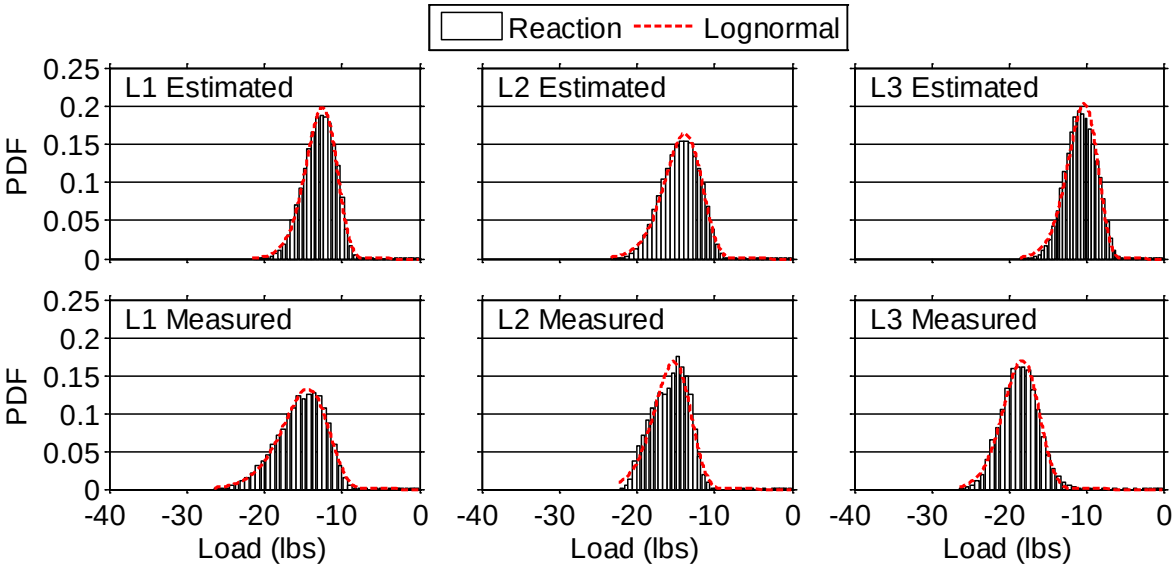

Figure 4-22. Probability density plots of reactions for DAD validation study (0°) in the 1/3-scale building

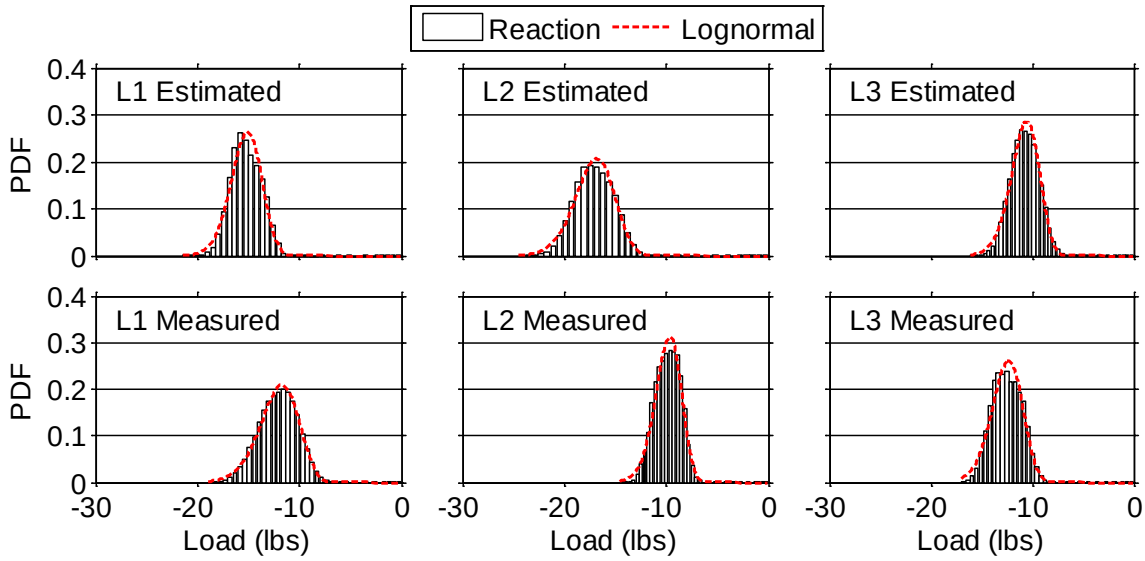

Figure 4-23. Probability density plots of reactions for DAD validation study (45°) in the 1/3-scale building

Wind Tunnel Results

Once the DAD validation was completed, the influence surfaces (Case 1 and Case 2a) were combined with the wind tunnel generated pressure coefficients to predict structural loads at the roof-to-wall and wall-to-foundation connections. Using the

pressure coefficients measured in the wind tunnel, realistic time histories of the connection loads are developed. The design wind speed used in the analysis is 130 mph (referenced to 3-sec gust, open terrain, at 33 ft elevation as per ASCE 7-05). The wind speed is converted to mean roof height and suburban terrain by multiplying by $\sqrt{0.7}$ which is the square root of K_z, the velocity pressure exposure coefficient from ASCE 7-05 for a structure with a mean roof height less than 15 ft.

DAD Results

For the results shown in this section, the influence surfaces for the left side were mirrored on the right side since the surfaces for the first two instrumented connections (R1 and R2) were similar to their opposite connections (L1 and L2). This allows a better comparison between the two sides as the wind angle changes.

Probability density functions of structural reactions

Figure 4-24 through Figure 4-27 show representative probability density functions (PDFs) for predicted roof-to-wall connections using the wind tunnel pressures for connections L1 and L4 for Case 1 and Case 2a. The best fit to the reaction time histories is a reverse 3-parameter lognormal distribution, which is the lognormal distribution mirrored about the vertical axis allowing the longer tail to trail to the left. The probability density function, $p(x)$, of the 3-parameter lognormal distribution is given by Eqn. 4-1.

$$p(x) = \frac{1}{(x-\theta)\sigma\sqrt{2\pi}} exp\left[-\frac{1}{2}\left(\frac{ln(x-\theta)-\mu}{\sigma}\right)^2\right] \quad (4\text{-}1)$$

where: θ is the location parameter, μ is the scale parameter, and σ is the shape parameter.

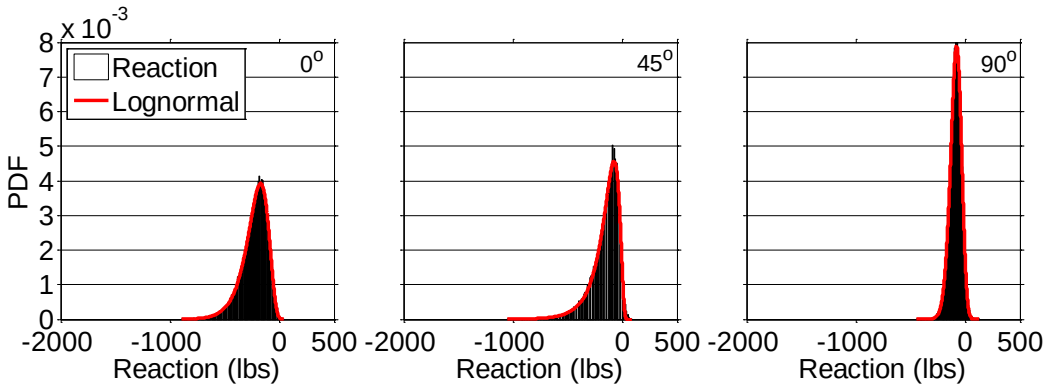

Figure 4-24. Probability density functions of a typical full-scale load at connection L1 (Case 1) with a reverse lognormal distribution

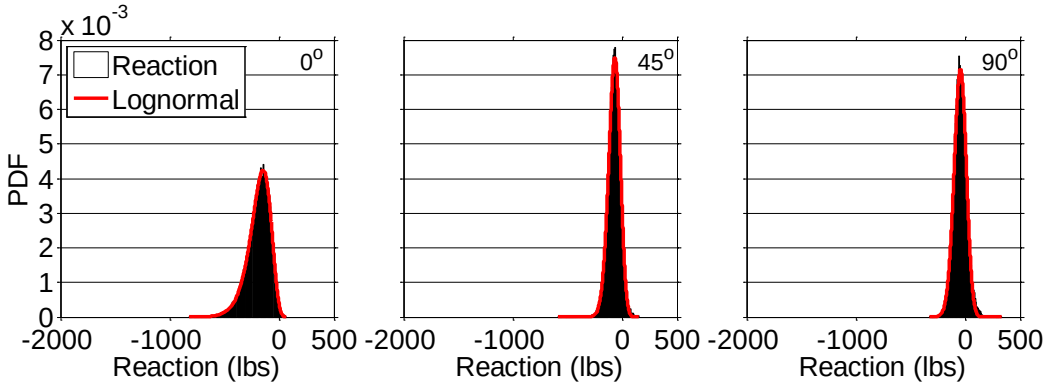

Figure 4-25. Probability density functions of a typical full-scale load at connection L4 (Case 1) with a reverse lognormal distribution

When the gable end intermediate connections are present (Case 1), the PDFs of the data are similar for the gable end connection (L1 – Figure 4-24) and the interior connections (L4 – Figure 4-25). The 45° wind direction between these two connections has the most pronounced difference. The largest difference comes from comparing Case 1 (Figure 4-24 and Figure 4-25) with Case 2a (Figure 4-26 and Figure 4-27). When the intermediate connections are removed, the corner connection (L1) has a significant increase in the spread of the load indicating higher mean and peak (absolute) values. Figure 4-26 shows a significantly larger spread of reactions obtained for the 0° and 45° wind azimuths over the 90° results for the gable end connection (L1) likely due to the high spatial and temporal fluctuations in the wind pressure distribution near the

reactions for these angles. Figure 4-27 includes the PDFs for an interior roof-to-wall connection (L4) showing that the spread of the data is larger for the 0° wind direction and then reduces with as the wind angle increases.

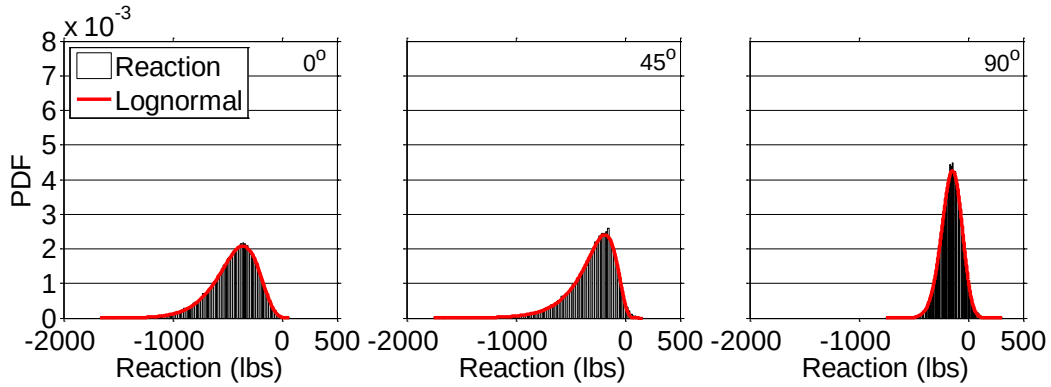

Figure 4-26. Probability density functions of a typical full-scale load at connection L1 (Case 2a) with a reverse lognormal distribution

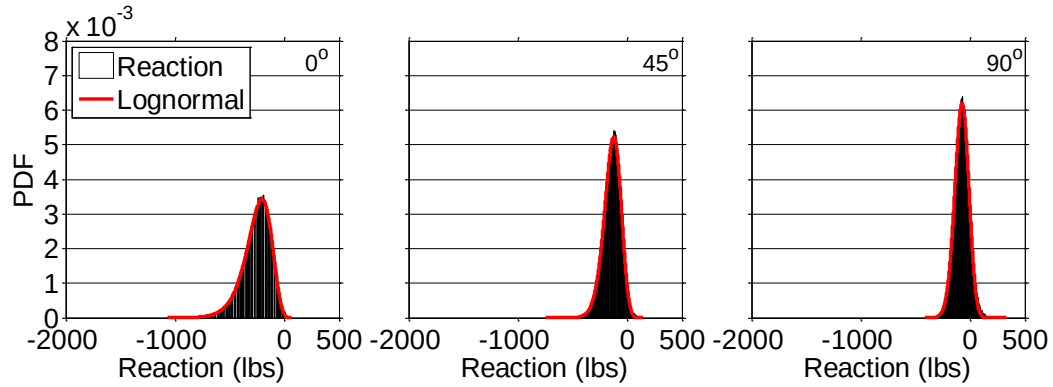

Figure 4-27. Probability density functions of a typical full-scale load at connection L4 (Case 2a) with a reverse lognormal distribution

Extreme value analysis

One of the most important values in the reaction load time histories is the peak (extreme) value. In order to establish a more stable statistical estimate of the extreme values, an extreme value (EV) Type I (Gumbel) distribution is fitted to the peak loads for each reaction based on the eight samples for each wind direction. The probability density function, $f(x)$, of the EV Type I (maximum) distribution is given by Eqn. 4-2 (NIST 2003).

$$f(x) = \frac{1}{\beta} exp\left[\frac{x-\mu}{\beta}\right] exp\left[-exp\left(\frac{x-\mu}{\beta}\right)\right] \quad (4\text{-}2)$$

The cumulative distribution function, $F(x)$, is represented by Eqn. 4-3.

$$F(x) = exp\left[-exp\left(-\frac{x-\mu}{\beta}\right)\right] \quad (4\text{-}3)$$

where: μ is the location parameter; and β is the scale parameter. These parameters are estimated using the Lieblein-BLUE (best linear unbiased estimator) method (Lieblein 1974).

The Lieblein-BLUE analysis method was developed for the maximum values of the Type I Extreme Value distribution, not minimum values. For this reason, each of the peak negative loads for the eight time histories for each connection and wind direction were multiplied by negative one (-1) to make them positive, maximum values. These values were then sorted in ascending order as shown in Eqn. 4-4.

$$x_1 \leq x_2 \leq \cdots \leq x_n \quad (4\text{-}4)$$

where: n is the sample size (8 for this study). The location parameter, μ, and the scale parameter, β, are then estimated by Eqn. 4-5.

$$\hat{\mu} = \sum_{i=1}^{n} a_i x_i \qquad \hat{\beta} = \sum_{i=1}^{n} b_i x_i \quad (4\text{-}5)$$

where: a_i and b_i are the BLUE numerical coefficients and are provided by Lieblein (1974). The mean (or expected value) and standard deviation of the EV Type I distribution can be calculated from the location and scale parameters (NIST 2003). The mean is calculated by Eqn. 4-6 and the standard deviation by Eqn. 4-7.

$$Mean = \mu + 0.5772\beta \quad (4\text{-}6)$$

$$St.Dev. = \frac{\beta\pi}{\sqrt{6}} \quad (4\text{-}7)$$

Expected peak reactions were estimated from the eight extreme values for each wind direction using the Lieblein-BLUE method (Lieblein 1974). The validity of using the extreme value (EV) Type I distribution for the peaks was confirmed by using the Anderson-Darling goodness-of-fit test (Stephens 1986). Using the distribution parameters estimated from the Lieblein-BLUE method, 95% of the peak reaction distributions fit the EV Type I distribution well (p-values > 0.25). Kasperski (2003) states that using the EV Type I distribution for peak reactions is conservative if not enough samples are available to determine with great accuracy the true distribution of the peaks.

Estimated peak and mean connection loads

The expected peak and mean reactions for the wind azimuths are presented in and . The highest load occurs at the gable end and structural loads reduce as the distance from the gable end increases. In Case 1 (with intermediate gable connections), the peak wall-to-foundation load occurring at SF2 is significantly higher than the peak roof-to-wall connection loads directly above it at S1 and L1 for 0° and 45° wind azimuths. It is interesting to note that the peak wall-to-foundation reaction occurs not at the corner but approximately 4.8 ft away (at full-scale) along the gable-end wall, when the bottom chord of the gable end truss is connected to the wall. However, in Case 2a (without intermediate gable connections), the gable end corner reaction (SF1) has the largest load for the foundation connections.

As shown in and , the critical (peak-enveloped) connection loads at most of the roof-to-wall connections and all the wall-to-foundation are observed at wind direction 0°. For Case 1 (with intermediate connections on the gable-end truss), an average of 70% of the total peak and mean loads on the gable end truss is transferred through the three intermediate connections (S1- S3) while truss end connections (L1 and R1) carry only 30%. However in Case 2a when the intermediate connections are removed, the total peak load carried by L1 and R1 increased by an average of 93% over Case 1 (with a mean load increase of 107%) while the total peak and mean loads carried by the entire gable end truss decreased by 41%. The total peak load carried by Truss 2 (L2 and R2) increased 51% from Case 1 to Case 2a with a mean load increase of 75%, while for truss 3 (L3 and R3) the peak load increase was only 28% with a mean load increase of 39%. The peak load increases for trusses 4 and 5 were 22% and 14%, respectively, with mean load increases of 39% and 35%.

At the wall-to-foundation connections, there were significant differences between connection loads for the two cases. For the left wall connections (LF1-LF5), the individual peak connection loads were on average 32% higher for Case 2a than for Case 1 with a similar 36% increase in the mean loads. For the end wall connections (SF1-SF4), the variation was much larger between connections (79% reduction to 13% increase) with an average reduction in the peak and mean values of 30-32%. As a whole (summing all wall-to-foundation connections on a given wall), the gable end wall (SF1-SF4) peak load was 13% less for Case 2a than for Case 1 with a mean reduction of 16%. On the other hand, the side wall peak and mean loads increased by 32% and 36%, respectively, when gable end truss intermediate connections were removed. In

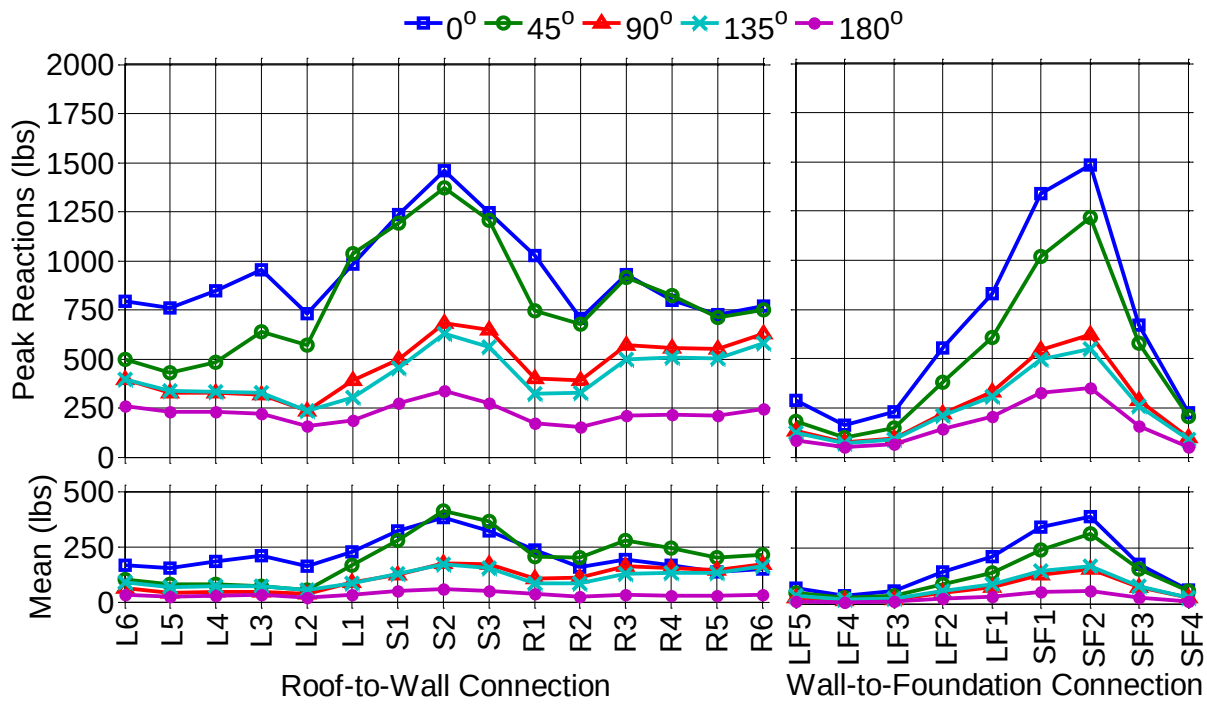

Figure 4-28. Expected peak and mean vertical reaction loads at full scale (Case 1)

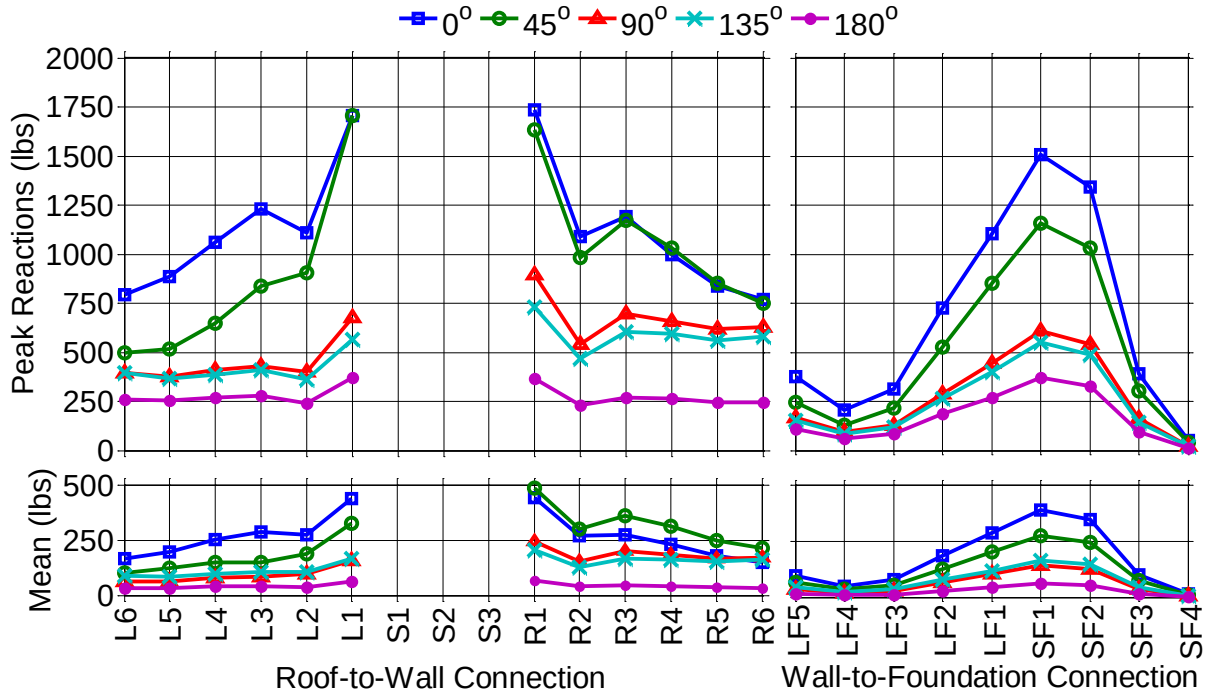

Figure 4-29. Expected peak and mean vertical reactions at full scale(Case 2)

both cases, the connections SF1 and SF2 experienced the highest peak loads at the foundation level. A similar observation is made at the side wall foundation connections

where higher peak loads are observed at connections LF1 and LF2 but reduce drastically at the other interior connections.

Covariance Integration and Load-Response Correlation Methods Results

As described in detail in Chapter 2, two other methods besides the DAD method are available for determining peak connection loads: the covariance integration (CI) method (Holmes and Best 1981) and the load-response-correlation (LRC) method (Kasperski 1992; Kasperski and Niemann 1992). The advantage of the CI and LRC methods is that they do not require the long-term storage of wind tunnel derived pressure coefficients that can be upwards of 20 GB or more in size. The CI and LRC methods require some basic statistical properties of the pressure coefficients that can be stored in less than 100 MB, more than two orders of magnitude less data.

This section provides a comparison between the DAD method and the CI and LRC methods to determine if they can successfully be used to predict the DAD estimated peak values necessary for design. Using the influence coefficients from Cases 1 and 2a, the eight wind tunnel samples per direction were analytically processed using the three methods for estimating the peak reactions (i.e., DAD, CI, and LRC methods) as described in detail in Chapter 2. Then, as described earlier, the eight peak responses for each wind direction were fit to an EV Type I distribution using the Lieblein-BLUE method (Lieblein 1974), and an expected (i.e., average) peak value was determined. Since the focus of this section is to compare the three methods, only the Case 2a (with no intermediate gable end connections) results are presented here. Similar graphs for Case 1 (with intermediate gable end connections) are presented in Appendix D.

The RMS values of the connections are presented in Figure 4-30 and Figure 4-31. The CI method tends to underestimate the DAD-derived RMS values; whereas, the LRC

method does not use the RMS values in its calculation procedures for the peak response. However, despite a difference in RMS values between the CI and DAD methods, the estimated peak values are similar.

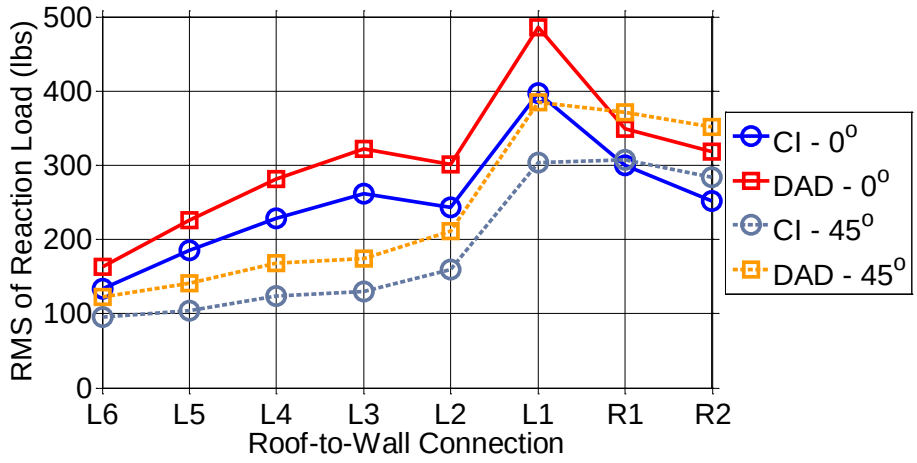

Figure 4-30. RMS values of full-scale roof-to-wall loads (Case 2a)

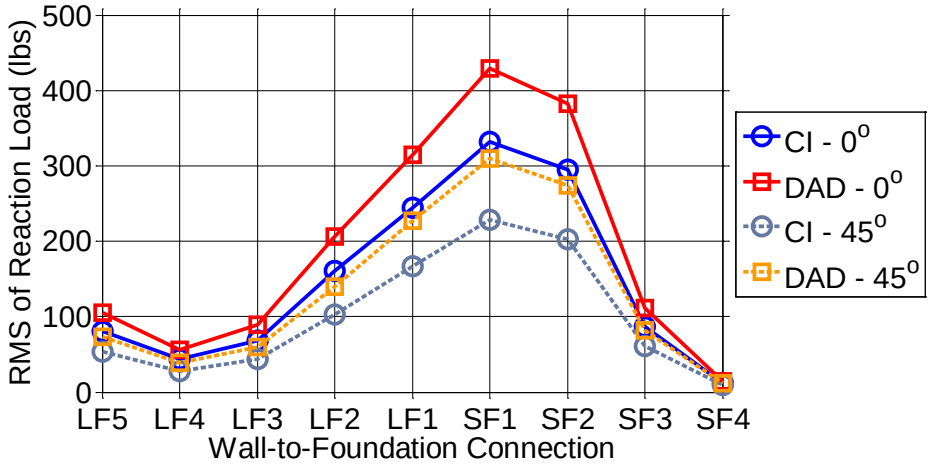

Figure 4-31. RMS values of full-scale wall-to-foundation loads (Case 2a)

Figure 4-32 and Figure 4-33 show the average values of the roof-to-wall and wall-to-foundation connections, respectively. As can be seen, the CI and the LRC method match almost perfectly the average connection values determined from the DAD analysis (< 2% difference).

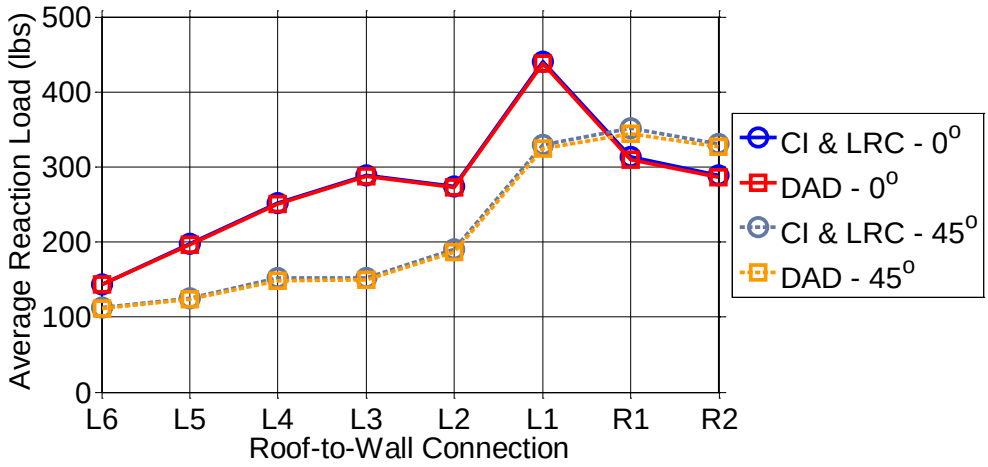

Figure 4-32. Average full-scale roof-to-wall connection loads (Case 2a)

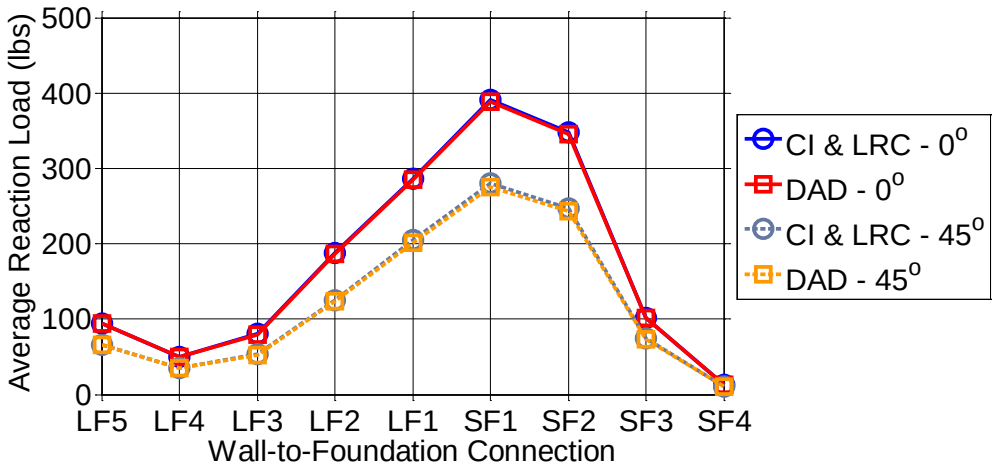

Figure 4-33. Average full-scale wall-to-foundation loads (Case 2a)

The peak negative (uplift) reaction loads are given in Figure 4-34 through Figure 4-36. As can be seen, the CI method tends to estimate the peak reactions well, especially for 0°, with some discrepancy for the 45° wind direction for the roof-to-wall connections. However, as seen in Figure 4-34, the LRC method underestimates the peak loads significantly using a recommended peak factor of 3.5 (Kasperski 1992). Through trial and error, a peak factor of 6.0 was found to produce much more agreeable results (Figure 4-35). Table 4-2 provides the percent difference of the CI and LRC methods compared to DAD. In general, the wall-to-foundation connection estimates are better than the roof-to-wall connections. The estimates for the 0° direction also tend to be

better than for 45°. The CI method has a large range (-25% to +23%) in estimating the peak reactions at the roof-to-wall connections with a mean of -2.3%. The LRC method has a smaller range (-18% to +4%) for the roof-to-wall connections. Both the CI and LRC methods are within the range of -6% to +9% for estimating the peak wall-to-foundation loads.

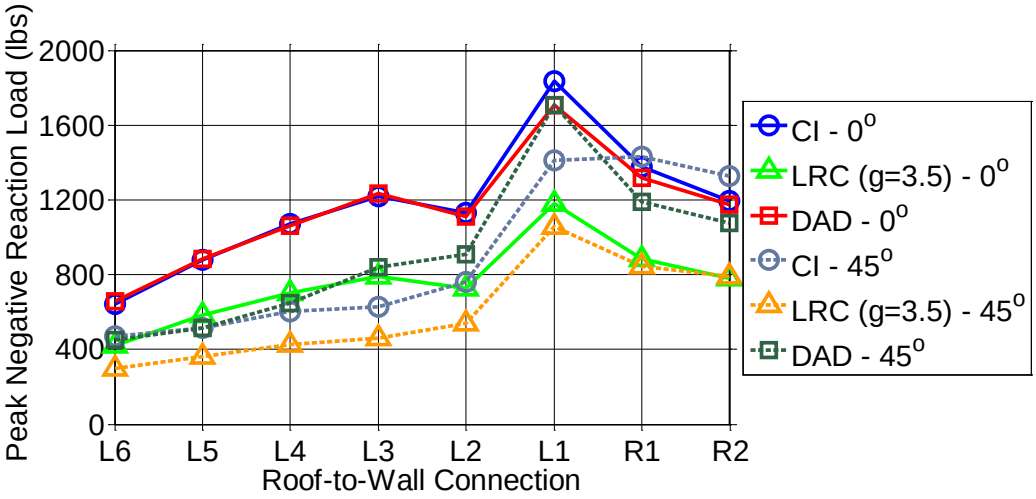

Figure 4-34. Peak negative full-scale roof-to-wall loads with a peak factor of 3.5 (Case 2a)

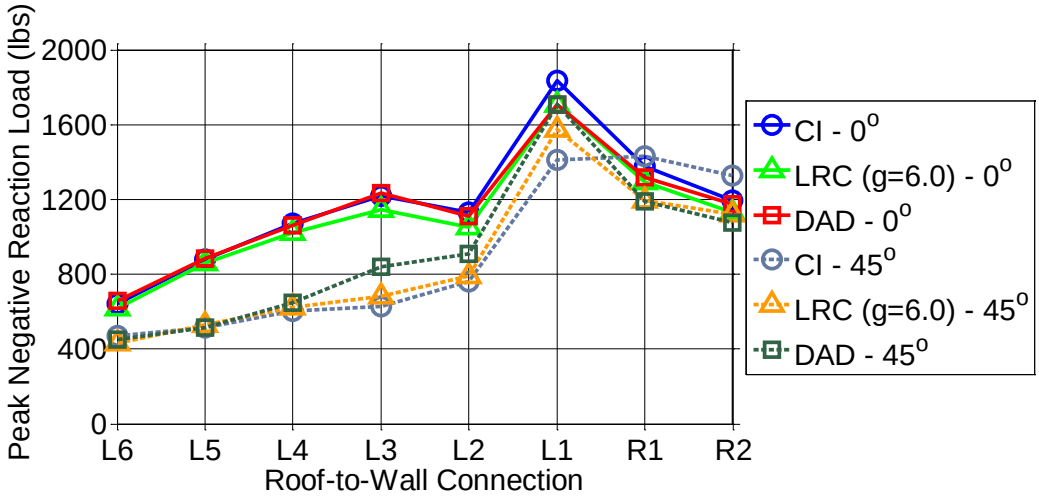

Figure 4-35. Peak negative full-scale roof-to-wall loads with a peak factor of 6.0 (Case 2a)

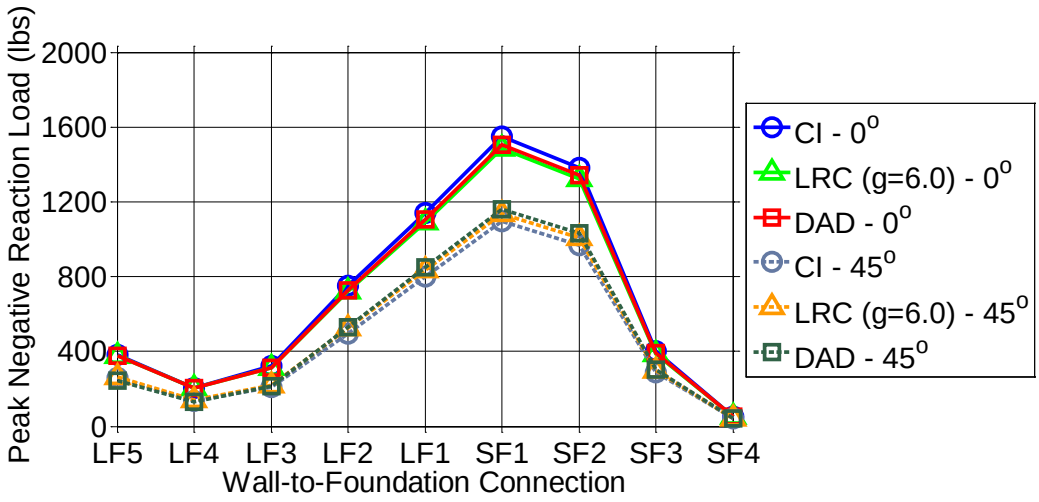

Figure 4-36. Peak negative full-scale wall-to-foundation loads (Case 2a)

Table 4-2. Percent difference of full-scale peak loads estimated by the CI and LRC methods compared to DAD*

Connection	Covariance Integration		Load-Response-Correlation	
	0°	45°	0°	45°
L6	-2.2%	3.6%	-5.5%	-5.0%
L5	-0.9%	0.0%	-3.1%	2.7%
L4	0.9%	-6.6%	-3.5%	-3.8%
L3	-0.9%	-25.3%	-7.1%	-18.5%
L2	2.0%	-16.2%	-5.3%	-13.0%
L1	7.5%	-17.3%	0.1%	-8.0%
R1	4.6%	20.0%	-1.9%	0.2%
R2	1.7%	23.4%	-3.9%	4.3%
Avg.	1.6%	-2.3%	-3.8%	-5.1%
LF5	0.7%	5.9%	-0.7%	8.1%
LF4	-0.8%	6.9%	-1.3%	9.1%
LF3	2.7%	-1.9%	-0.3%	2.8%
LF2	3.2%	-6.4%	-0.9%	-0.9%
LF1	3.2%	-5.7%	-1.3%	-2.1%
SF1	3.0%	-5.6%	-1.3%	-2.1%
SF2	2.8%	-6.1%	-1.5%	-2.3%
SF3	2.6%	-4.8%	-1.7%	-2.0%
SF4	3.3%	-0.2%	-2.0%	-0.3%
Avg.	2.3%	-2.0%	-1.2%	1.2%
Overall Avg.	2.0%	-2.1%	-2.4%	-1.8%

*Percent difference computed as [((CI or LRC)-DAD)/DAD]

A peak factor analysis was performed on the reaction time histories to compare with the LRC method peak factor of 6.0 that was found to match well with the DAD results. The peak factor, g, is determined according to Eqn. 4-8.

$$x_{max} = \bar{x} + g\sigma_x \tag{4-8}$$

where: x_{max} is the peak response of some process x; $\bar{x}$ is the mean response; and σ_x is the standard deviation. Eqn. 4-8 is rearranged to calculate the peak factor (Eqn. 4-9).

$$g = \frac{x_{max} - \bar{x}}{\sigma_x} \tag{4-9}$$

Two different peak factors were generated for each wind direction based on the time length used to determine the peak factors – 10 min. and 25 min. The 10-min. time length was chosen because it is a commonly used reference time in wind engineering. The 25-min. duration corresponds to the length of the full-scale time histories calculated using the reduced frequency relationship (ASCE 1999) yielding a full-scale sampling frequency of 24 Hz. Figure 4-37 through Figure 4-40 provide the peak factors for the 10-min. and 25-min. segments for Cases 1 and 2a, respectively. As the figures show, the peak factors are close to the 6.0 used previously. Peak factor curves for different averaging times (similar to gust factor curves) based on the 10- and 25-minute records are provided in Appendix E.

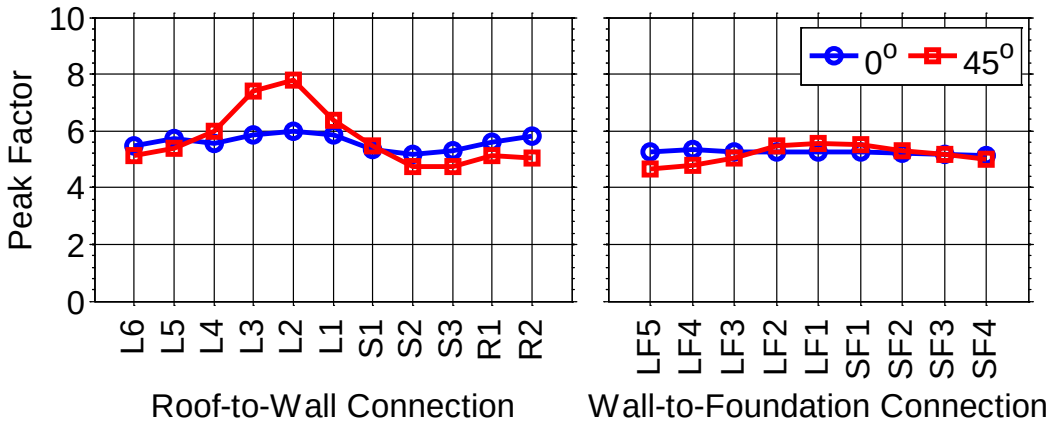

Figure 4-37. Calculated peak factors from full-scale DAD-derived connection time histories based on 10-minute record length (Case 1)

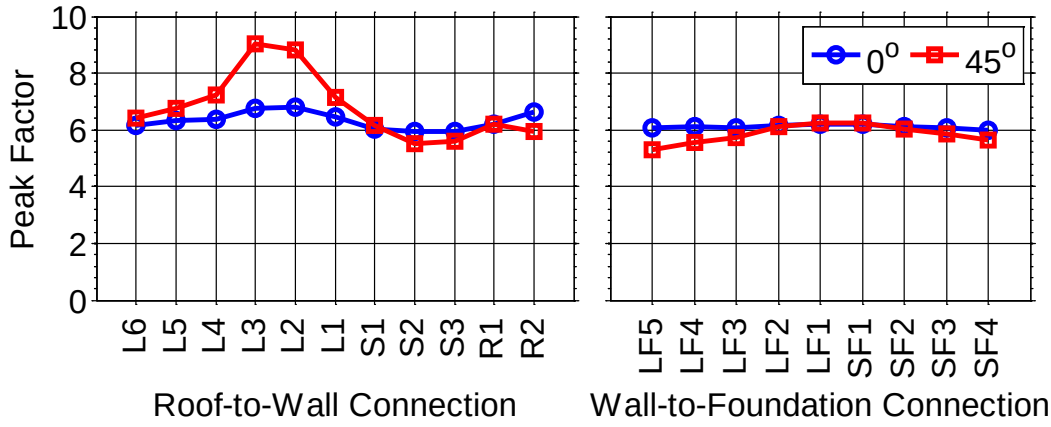

Figure 4-38. Calculated peak factors from full-scale DAD-derived connection time histories based on 10-minute record length (Case 1)

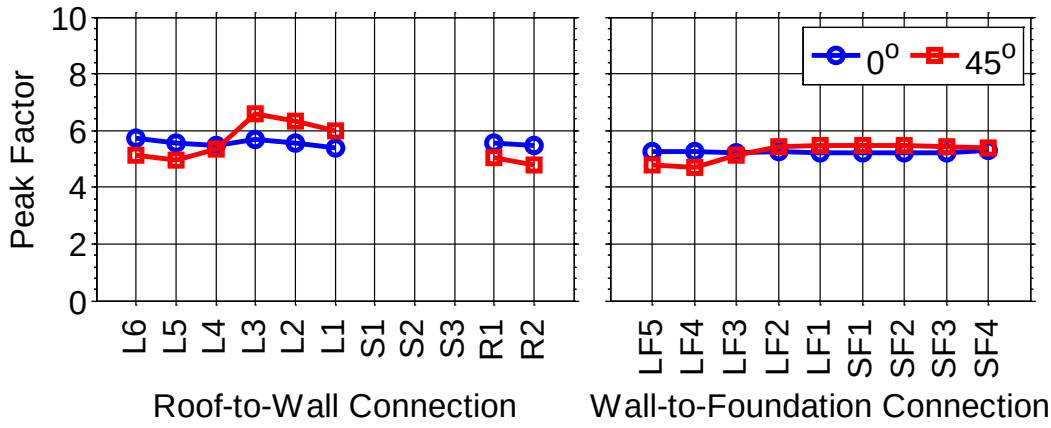

Figure 4-39. Calculated peak factors from full-scale DAD-derived connection time histories based on 10-minute record length (Case 2a)

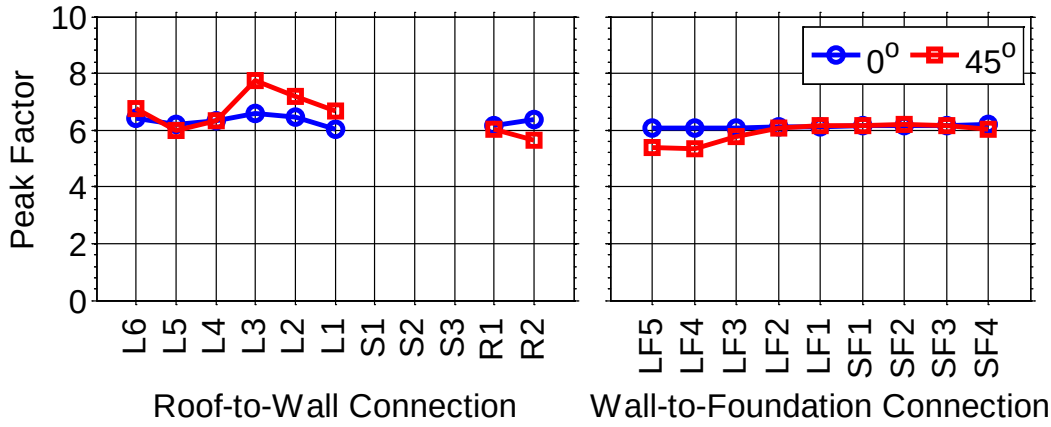

Figure 4-40. Calculated peak factors from full-scale DAD-derived connection time histories based on 25-minute record length (Case 2a)

Kasperski (2007) provides another method to determine an appropriate peak factor using the 80th-percentile value of the extreme value distributions of the peak reactions (presented and discussed in Chapter 2). Figure 4-41 and Figure 4-42 provide the peak factors determined from Eqn. 2-20 for Cases 1 and 2a, respectively. The peak factors developed using the Kasperski (2007) method are similar to those calculated based on the actual response time histories which are close to the value of 6.0 that was used earlier. Additionally, comparing the Kasperski model peak values to those in

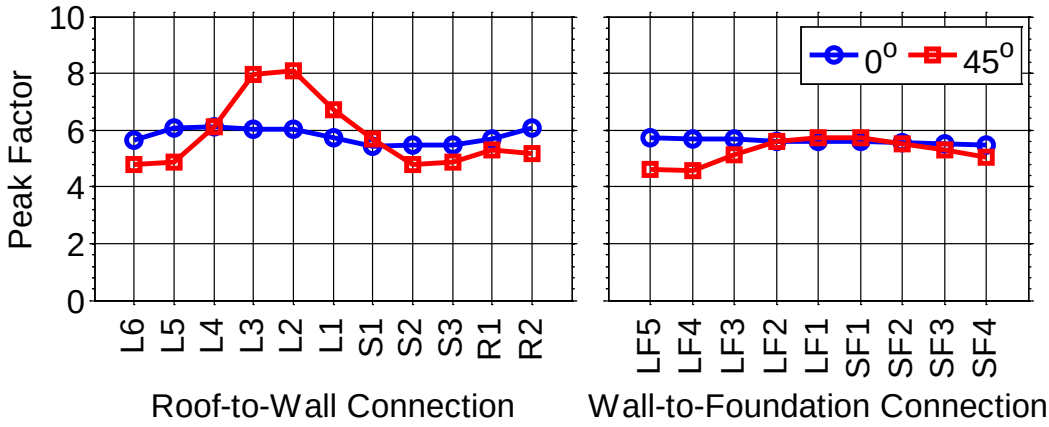

Figure 4-41. Peak factors determined using the Kasperski model for Case 1 (with intermediate gable end connections)

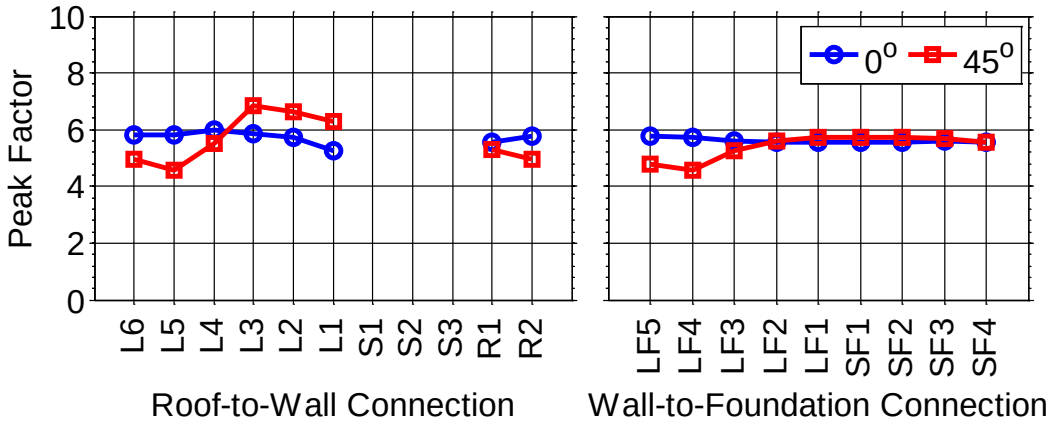

Figure 4-42. Peak factors determined using the Kasperski model for Case 2a (without intermediate gable end connections)

Figure 4-37 through Figure 4-40, the Kasperski model is a close match to the DAD-derived peak factors thus validating the analytical (Kasperski) model. Figure 4-43 and Figure 4-44 provide the peak reactions for the roof-to-wall and wall-to-foundation loads, respectively, using the calculated peak factors. Table 4-3 provides the percent difference between the DAD method and the LRC method using the Kasperski (2007) peak factor model.

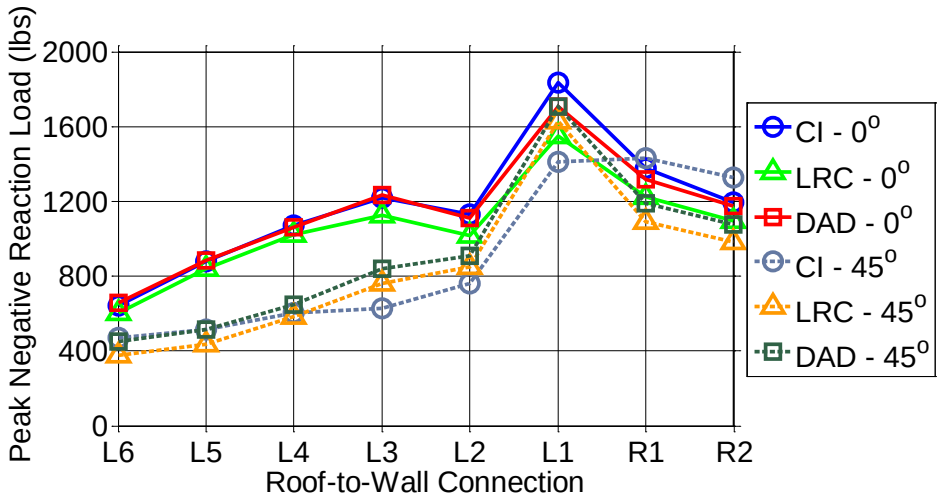

Figure 4-43. Peak negative full-scale roof-to-wall connection loads with adjusted peak factors based on the Kasperski model for Case 2a

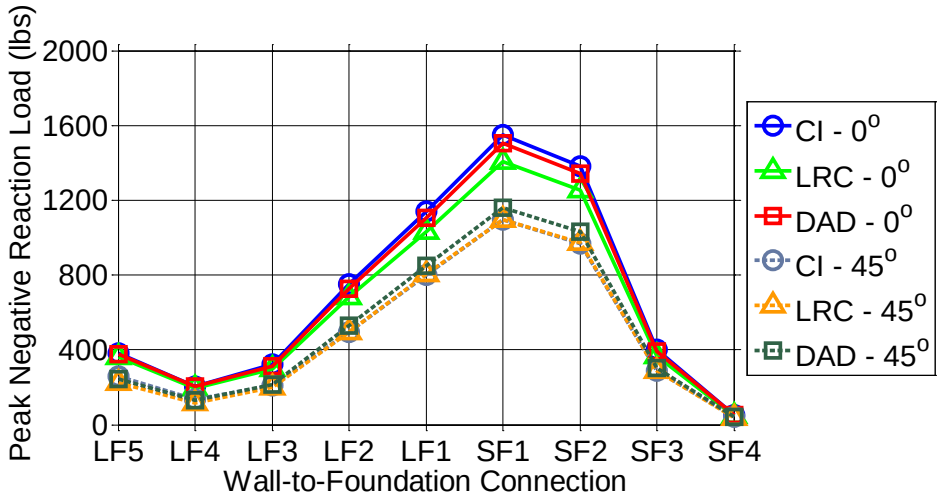

Figure 4-44. Peak negative full-scale wall-to-foundation connection loads with adjusted peak factors based on the Kasperski model for Case 2a

Table 4-3. Percent difference of full-scale peak loads estimated by the LRC method using the Kasperski peak factor model compared to DAD*

Connection	Case 1 (w/ gable connections)		Case 2a (w/o gable connections)	
	0°	45°	0°	45°
L6	-7.0%	-18.1%	-7.9%	-17.2%
L5	-3.5%	-20.1%	-5.4%	-15.9%
L4	-3.8%	-12.9%	-3.8%	-9.9%
L3	-8.7%	-10.4%	-8.7%	-9.5%
L2	-9.4%	-8.5%	-8.3%	-6.3%
L1	-8.9%	-4.9%	-9.2%	-4.7%
S1	-7.0%	-5.1%	--	--
S2	-4.5%	-7.7%	--	--
S3	-4.2%	-7.2%	--	--
R1	-6.4%	-9.9%	-7.2%	-8.3%
R2	-6.0%	-9.6%	-6.6%	-8.7%
Avg.	-6.3%	-10.4%	-7.2%	-10.1%
LF5	-4.7%	-9.8%	-3.5%	-8.2%
LF4	-5.9%	-12.8%	-4.9%	-10.3%
LF3	-4.7%	-8.3%	-5.0%	-6.9%
LF2	-6.6%	-6.9%	-6.4%	-6.0%
LF1	-7.1%	-6.0%	-6.6%	-5.6%
SF1	-6.9%	-5.8%	-6.5%	-5.6%
SF2	-6.4%	-5.7%	-6.7%	-5.6%
SF3	-6.1%	-6.1%	-6.8%	-5.7%
SF4	-5.6%	-6.6%	-7.6%	-5.8%
Avg.	-6.0%	-7.5%	-6.0%	-6.6%
Overall Avg.	-6.2%	-9.1%	-6.5%	-8.2%

*Percent difference computed as [(LRC-DAD)/DAD]

Comparison using Influence Coefficients vs. Tributary Areas

A comparison of the reaction loads (L1-L4) made with the DAD method was compared to using just the tributary width of the individual trusses. As described in Chapter 1, the tributary area analysis is a 2D analysis technique commonly used which determines design loads based on isolating individual components of a structural system and applying the loads to a “tributary” width or area of the component. For example, if roof trusses are spaced at 24 in. on center, an individual truss has a tributary width of 24 in. All design pressures that fall within this 24 in. width would be

applied to the truss and used for its design and to determine the required truss-to-wall connection load.

For the tributary analysis presented here, each of the pressure tap tributary areas that fell within the tributary width of an individual truss (24 in. for all trusses except gable end truss which has a 30 in. tributary width because of the overhang) were used to calculate the truss reaction time histories. To calculate the effect of each of the pressure taps, an influence line was developed for the truss reactions (described previously and shown in Figure 4-2) and applied to each of the roof taps. Figure 4-45 shows graphically how the tributary area analysis was used to develop the reaction time histories.

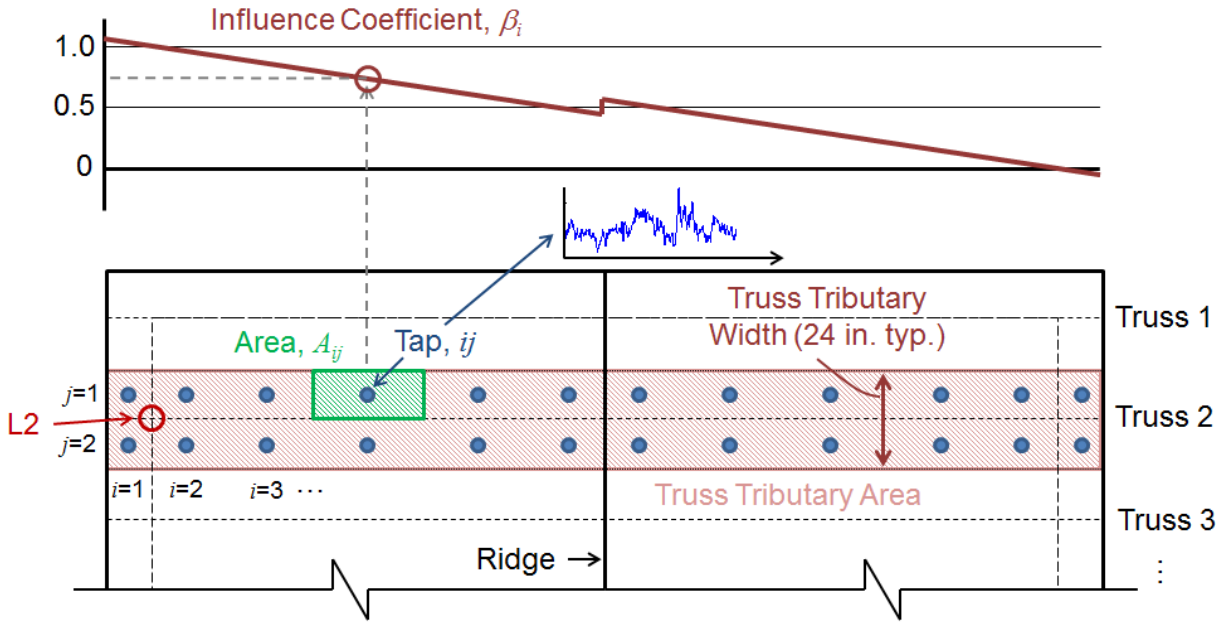

Figure 4-45. Example of tributary area (TA) analysis calculation (not to scale)

Figure 4-46 and Figure 4-47 show typical reaction time histories for four roof-to-wall connections (L1-L4) derived from both the DAD and tributary area methodologies for Case 1 (with intermediate gable end connections). As can be seen, the tributary

area time histories are consistently higher (more negative) with the mean and peak values. Figure 4-50 provides a comparison of the mean and expected peak values. The mean values of the tributary area reaction time histories are 55-130% higher than the mean DAD, whereas the expected peak values are 60-115% higher than the DAD peaks.

Figure 4-48 and Figure 4-49 show typical reaction time histories for four roof-to-wall connections (L1-L4) derived from both the DAD and tributary area methodologies for Case 2a (with no intermediate gable end connections). As can be seen, the mean and peak values of the tributary area time histories are much closer to the DAD derived values than in Case 1. However, significant differences still exist. Figure 4-50 provides a comparison of the mean and expected peak values. The mean values of the tributary area reaction time histories are 12-37% higher than the mean DAD, whereas the peak values are 19-47% higher than the DAD peaks.

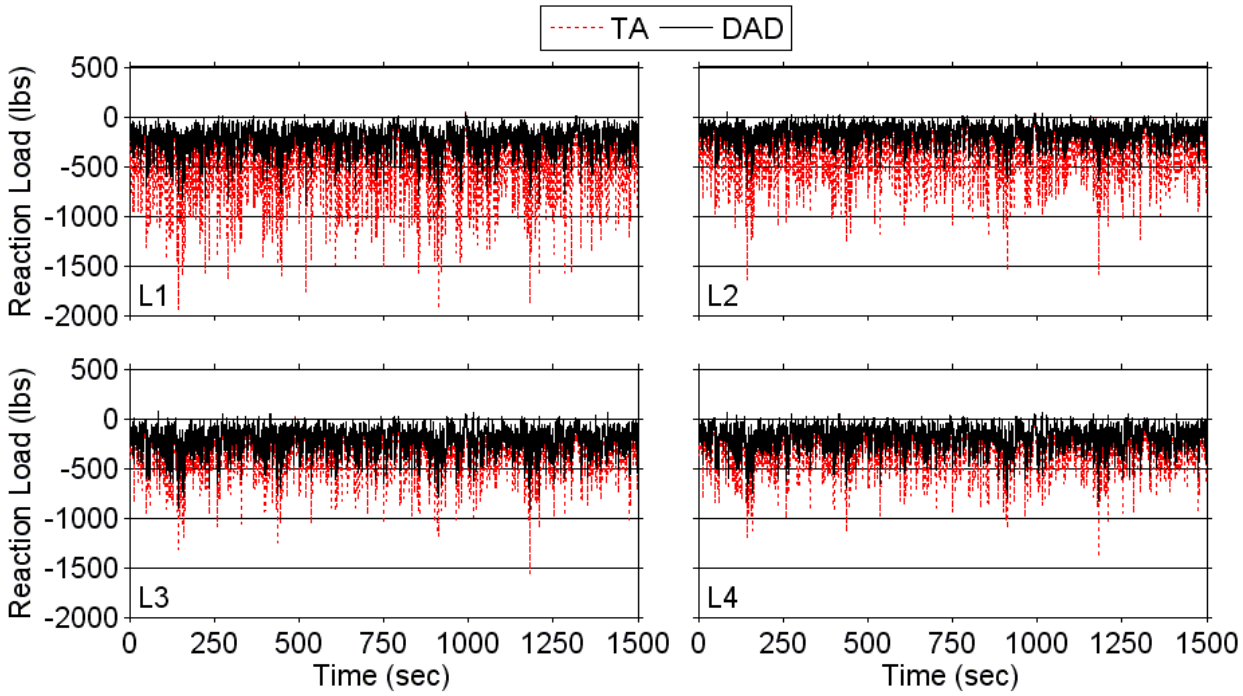

Figure 4-46. Typical tributary area and DAD-derived full-scale reaction time histories (Case 1 – 0°)

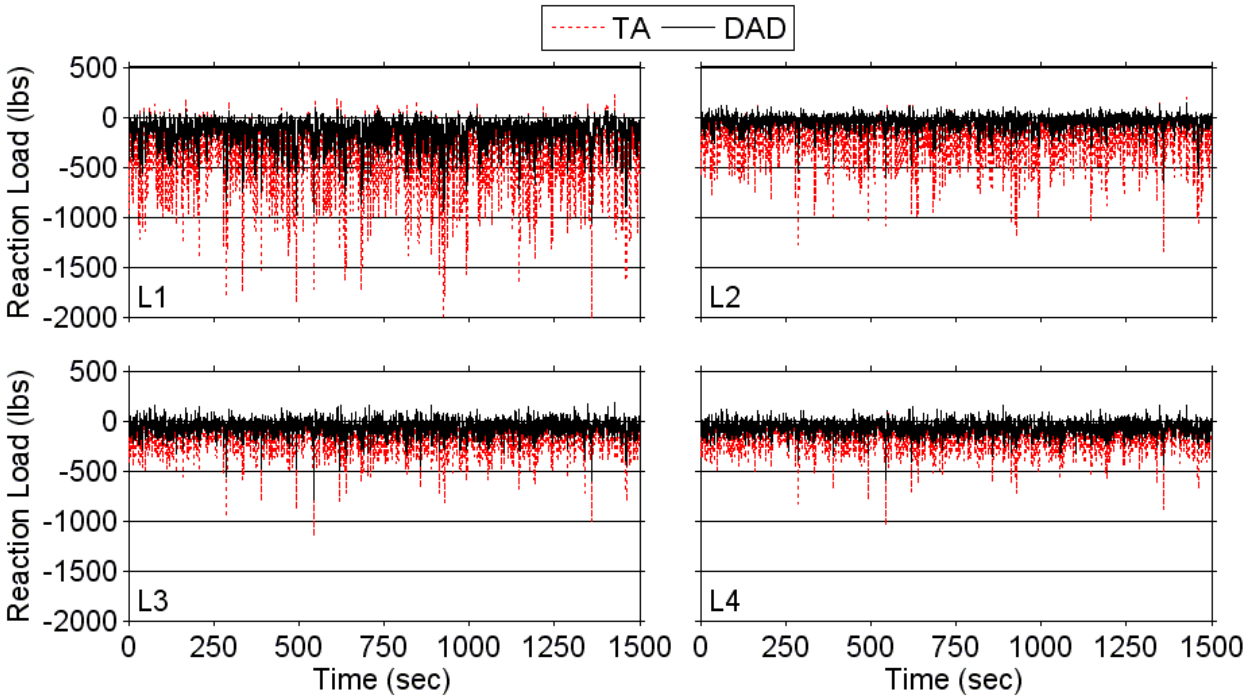

Figure 4-47. Typical tributary area and DAD-derived full-scale reaction time histories (Case 1 – 45°)

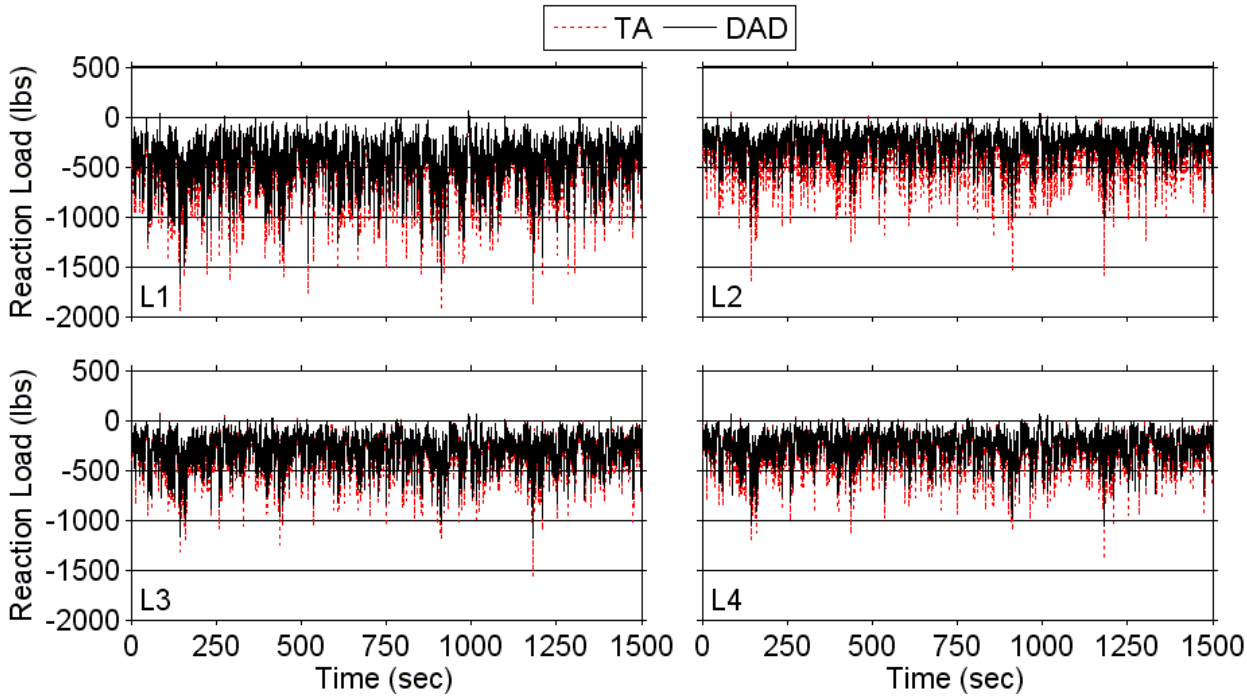

Figure 4-48. Typical tributary area and DAD-derived full-scale reaction time histories (Case 2a – 0°)

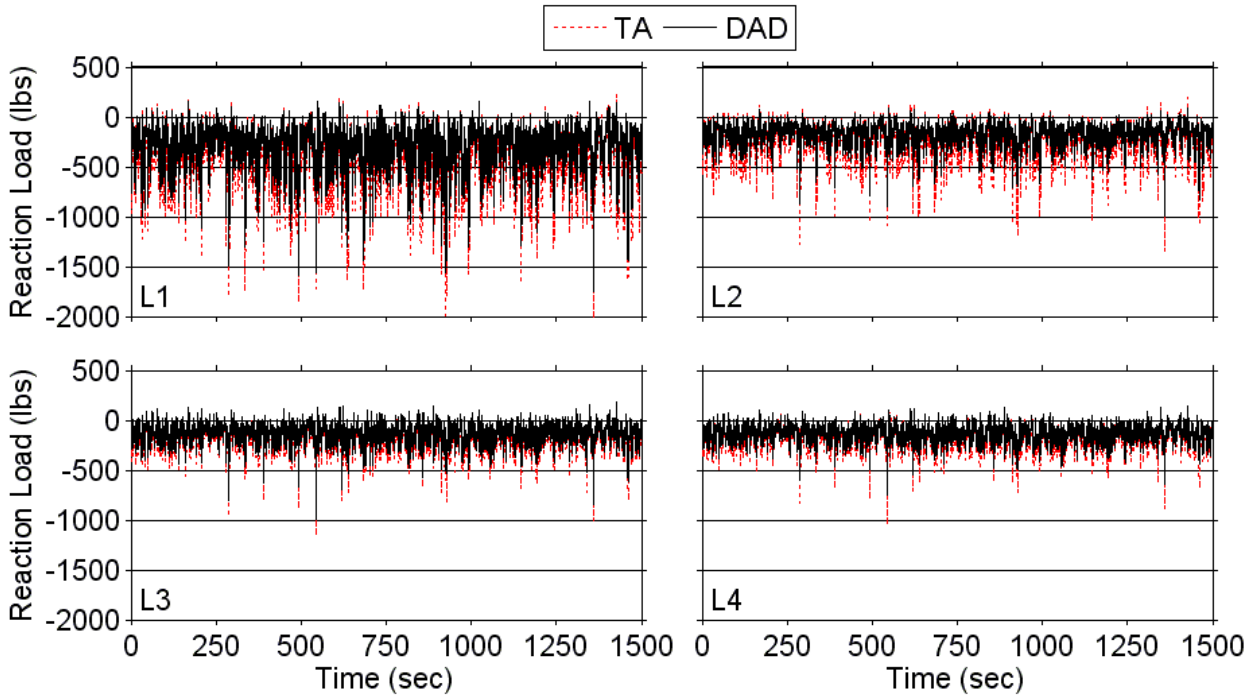

Figure 4-49. Typical tributary area and DAD-derived full-scale reaction time histories (Case 2a – 45°)

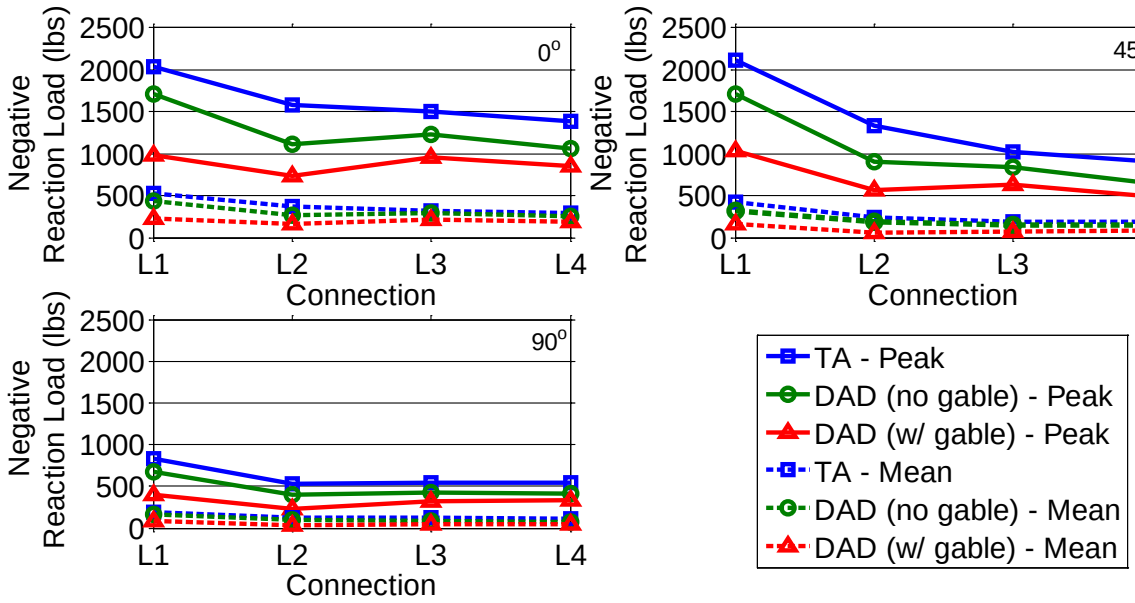

Figure 4-50. Expected peak and mean values of full-scale tributary area and DAD-derived reactions

Comparison of Peak Loads with Design Values

Since ASCE 7-05 (ASCE 2006) is the current wind loading standard reference in most of the building codes in the US, it is only appropriate to compare the estimated

peak values derived in this study with those of ASCE 7. The analytical procedure for both the main wind-force resisting system (MWFRS) and the components and cladding (C&C) provisions is used. The velocity pressure, q_z, used in both calculations is given by Eqn. 4-10.

$$q_z = 0.00256 K_z K_{zt} K_d V^2 I \tag{4-10}$$

where: q_z is given in lbs/ft^2 (psf); K_z is the velocity pressure exposure coefficient; K_{zt} is the topographic factor (=1.0); K_d is the wind directionality factor (=0.85); V is the design wind speed in mph at 33 ft elevation in open terrain (=130 mph); and I is the importance factor (=1.0).

To calculate the MWFRS design loads, two different procedures are provided in ASCE 7-05 for low-rise buildings: (1) the low-rise building provisions (ASCE 7-05 Section 6.5.12.2.2) with the design wind pressures determined according to Eqn. 4-11 and (2) the rigid buildings of all heights provisions (ASCE 7-05 Section 6.5.12.2.1) with the design wind pressures determined according to Eqn. 4-12.

$$p = q_h \left[\left(GC_{pf} \right) - \left(GC_{pi} \right) \right] \tag{4-11}$$

$$p = q_h G C_p - q_i \left(GC_{pi} \right) \tag{4-12}$$

where: p is the design wind pressure in psf; q_h is the velocity pressure evaluated at mean roof height, h; $\left(GC_{pf} \right)$ is the external pressure coefficient determined from Fig. 6-10 in ASCE 7-05; $\left(GC_{pi} \right)$ is the internal pressure coefficient; G is the gust effect factor (=0.85 for rigid buildings); C_p is the external pressure coefficient from Fig. 6-6 or 6-8 in ASCE 7-05; and q_i is the velocity pressure referenced either to mean roof height (q_h) or

the highest elevation on the building where an opening is located that could affect the positive internal pressure (q_z).

Since internal pressures were not recorded during the wind tunnel tests (only external roof pressures were measured), the internal pressures are not included in the ASCE 7-05 calculations. (Alternatively a constant internal pressure coefficient could have been used as included in ASCE 7-05: 0.18 or 0.55 for partially and fully enclosed buildings, respectively.) The design values were determined by using the tributary width of the trusses and using the wind pressure zone diagrams found in ASCE 7-05. For all trusses, only the roof pressures were used on the overhang (i.e., the higher overhang pressure coefficients were not used) because the wind tunnel pressure coefficients used in the DAD analysis were only for the roof and did not include overhang soffit pressures.

Figure 4-51 shows the ASCE 7 design loads for the roof-to-wall connections on the left side (L1-L6) with the DAD estimated peak negative (uplift) reactions for Case 1. Immediately one can see the discrepancy between the two design value curves for the MWFRS. The all heights method is significantly lower than the low-rise method due to a lower velocity exposure coefficient (K_z) and the use of the gust factor (G) which both serve to reduce the overall loads. As can be seen when intermediate gable end connections are present, the MWFRS design loads are higher than the DAD derived loads for the 45° wind direction. However for the 0° direction, the MWFRS loads do not adequately account for the DAD derived peak loads for four of the six connections shown. However, the MWFRS all-heights method underestimates the DAD-derived peak loads at all connections.

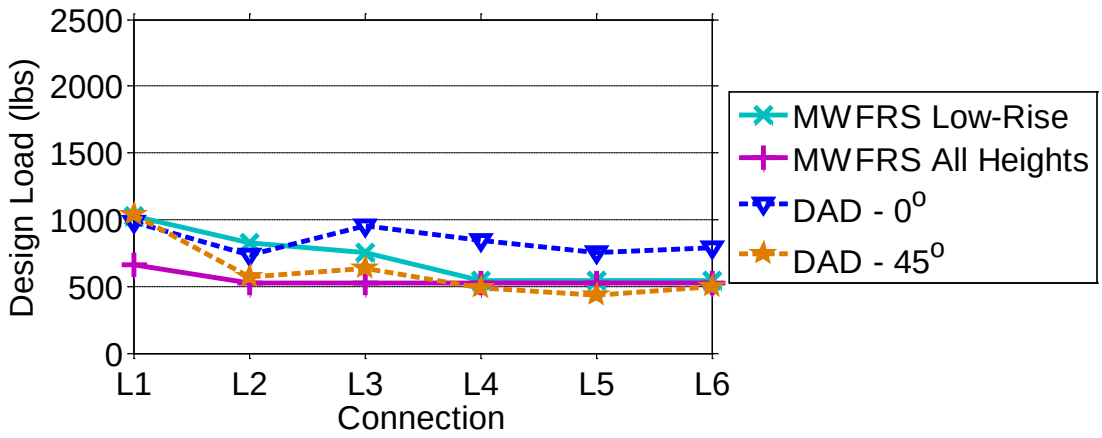

Figure 4-51. Comparison of ASCE 7-05 MWFRS design loads with DAD-estimated peak roof-to-wall connections (Case 1 – with intermediate gable end connections)

For Case 2a (without intermediate gable end connections), the design values are plotted against the DAD-derived peak loads in Figure 4-52. The MWFRS low-rise method matches closely with the DAD derived values for the 45° wind except for the gable end connection (L1). However, the DAD values are consistently higher than the MWRFS for the 0° wind direction.

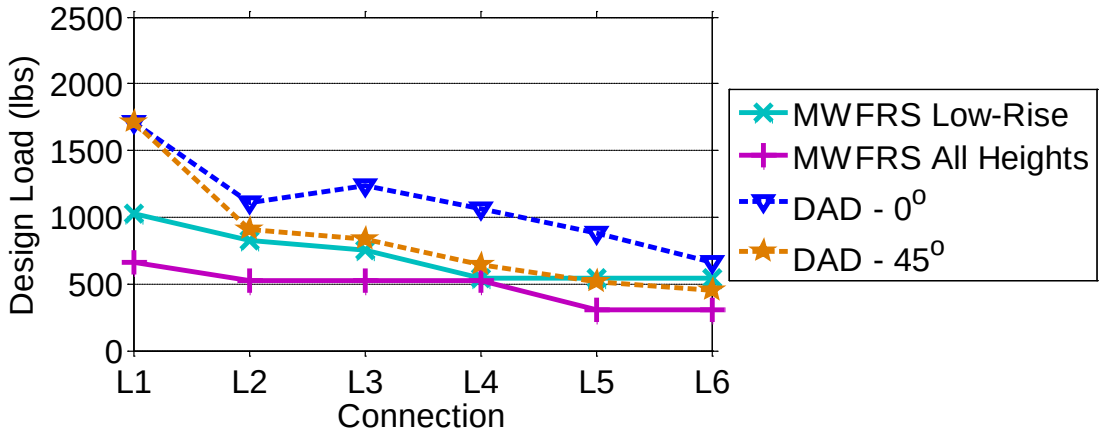

Figure 4-52. Comparison of ASCE 7-05 MWFRS design loads with DAD-estimated peak roof-to-wall connections (Case 2a – without intermediate gable end connections)

The C&C design pressures are determined from Eqn. 4-13 for low-rise buildings.

$$p = q_h[(GC_p) - (GC_{pi})] \tag{4-13}$$

where: (GC_p) is the external pressure coefficient determined from Figs. 6-11 through 6-16 in ASCE 7-05. The external pressure coefficient is dependent on the effective wind area (EWA) of the component being designed. The EWA is taken as the span length L times an effective width (i.e., tributary area) but not greater than the span times the span divided by 3 (i.e., $L^2/3$). For the building used in this study, the trusses span 30 ft so the effective wind area would be 300 ft^2 (i.e., 30^2/3). However, when the EWA exceeds 100 ft^2 the external pressure coefficients remain constant. Similarly, when the effective wind area is less than 10 ft^2 the external pressure coefficients remain constant. Thus, these two effective wind areas (10 and 100 ft^2) envelope the maximum and minimum external pressure coefficients applied to the roof for design loads (Figure 6-11C in ASCE 7-05).

The C&C design loads are shown in Figure 4-53 with the DAD-estimated peak loads. Using an effective wind area (EWA) of 100 ft^2 (as would be used if the entire truss was designed using the C&C provisions) is not adequate and underestimates the DAD-estimated peak reaction for a 0° wind angle by as much as 35% at connection L3 but only by 8% at the gable end. Conversely, if an EWA of 10 ft^2 is used, ASCE 7-05 overestimates the gable end (L1) peak load by 25% and underestimates the peak load at connection L3 by 19%. Even though the C&C loading underestimates the peak loads at various locations, it is a better prediction of the truss reaction loads than the MWFRS provisions. The use of the EWA is a point for debate since using the smallest EWA still produces design loads that underestimate the DAD-derived peak loads by as much as 19% while being overly conservative at the gable end.

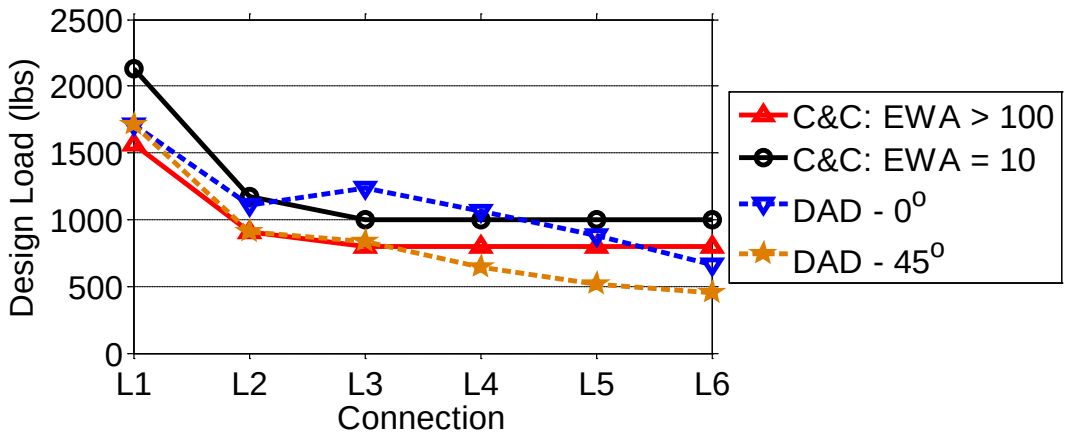

Figure 4-53. Comparison of ASCE 7-05 C&C design loads with DAD-estimated peak roof-to-wall connections (Case 2a – without intermediate gable end connections)

The *Wood Frame Construction Manual* (WFCM) (AF&PA 2001) and the accompanying guide for use with 130 mph design wind speed in exposure B (AF&PA 2006) provide prescriptive design guidelines for one- and two-family dwellings. Through the use of simple tables, these wood-framed, residential structures can be designed with little to no engineering background needed. Figure 4-54 and Figure 4-55 show the WFCM design uplift value for roof truss-to-wall connections for a 30 ft span with 24 in. truss spacing (Table 2.2A in the WFCM). A dead load of 0 psf was used to determine these values since only uplift loads are considered in the DAD analysis. The WFCM also states that for connections located more than six feet from any building corner, the tabulated uplift connection loads can be reduced by 25% (as is shown in Figure 4-54 and Figure 4-55 for connections L5 and L6). For Case 1, the WFCM design values are adequate and conservative. However when Case 2a is considered (Figure 4-55), the WFCM underestimates peak reaction force at the gable end significantly while providing an adequate design value at all other connections. One will notice that the WFCM design loads are larger than the ASCE 7-05 MWFRS loads at all connections. The

WFCM design uplift loads were based on the MWFRS loads in ASCE 7-98 (ASCE 1998) based on a worst case roof slope (20°) and including overhang and internal pressures (see Commentary to Table 2.2A in AF&PA 2001). Including the internal pressure and overhang pressures will increase the design loads over the ASCE 7 MWFRS loads. Therefore, if the internal and overhang pressure were included in the DAD-estimated peak values, the WFCM design loads would probably underestimate the peak loads at most of the connections.

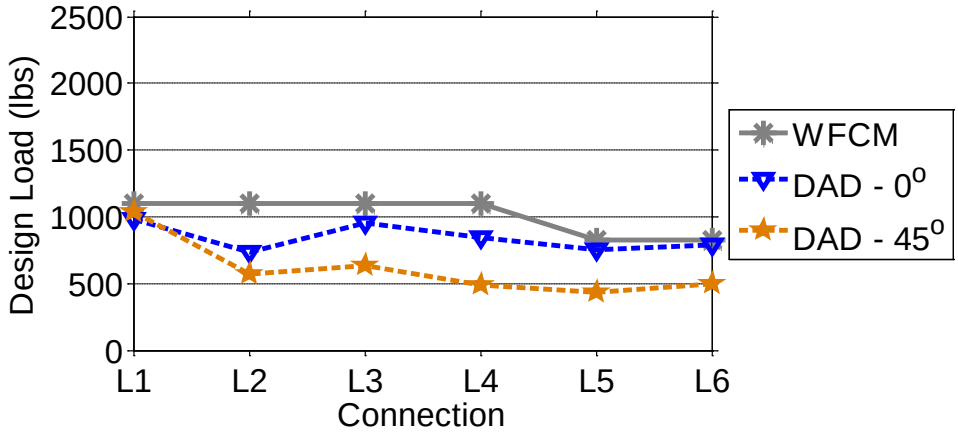

Figure 4-54. Comparison of the WFCM design loads with DAD-estimated peak roof-to-wall connections (Case 1 – with intermediate gable end connections)

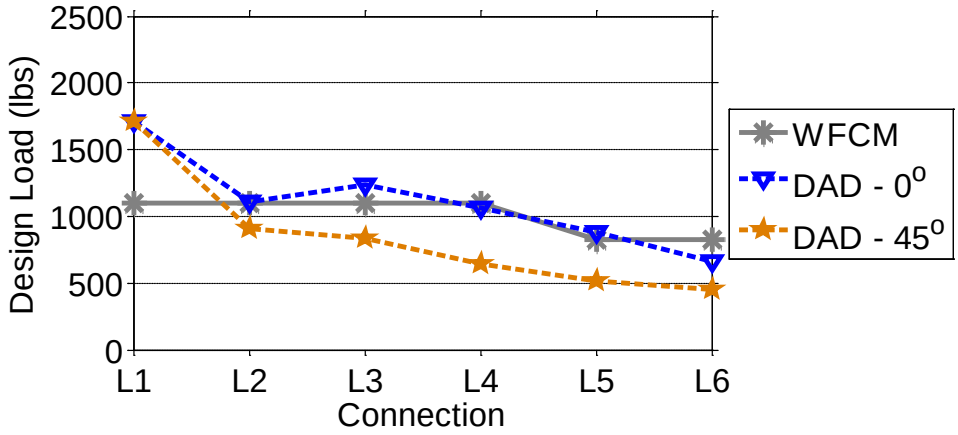

Figure 4-55. Comparison of the WFCM design loads with DAD-estimated peak roof-to-wall connections (Case 2a – without intermediate gable end connections)

The WFCM (AF&PA 2001) and its accompanying high wind region design guide (AF&PA 2006) also contain provisions to design foundation anchors (i.e., wall-to-foundation connections). Figure 4-56 and Figure 4-57 present the peak estimated wall-to-foundation loads compared to the WFCM design value for Cases 1 and 2a, respectively. Interestingly, the WFCM design guide for a 130 mph design wind speed in suburban terrain (AF&PA 2006) specifies that anchors can be spaced at 48 in. when a stem wall is used with the current building aspect ratio (length/width = 1.33), but for slab-on-grade foundations, the anchors must be spaced at 24 in. maximum. The influence functions developed were for foundation anchors spaced at 48 in. As can be seen by the plots in Figure 4-56 and Figure 4-57, the WFCM design load for the anchor bolts is conservative.

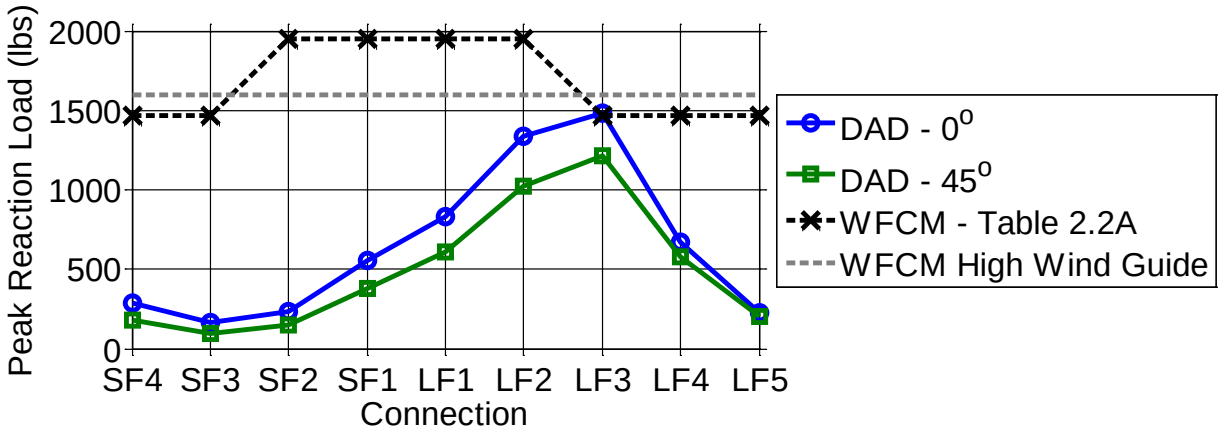

Figure 4-56. Comparison of DAD estimated wall-to-foundation peak loads with design values in the WFCM (Case 1 – with gable end intermediate connections)

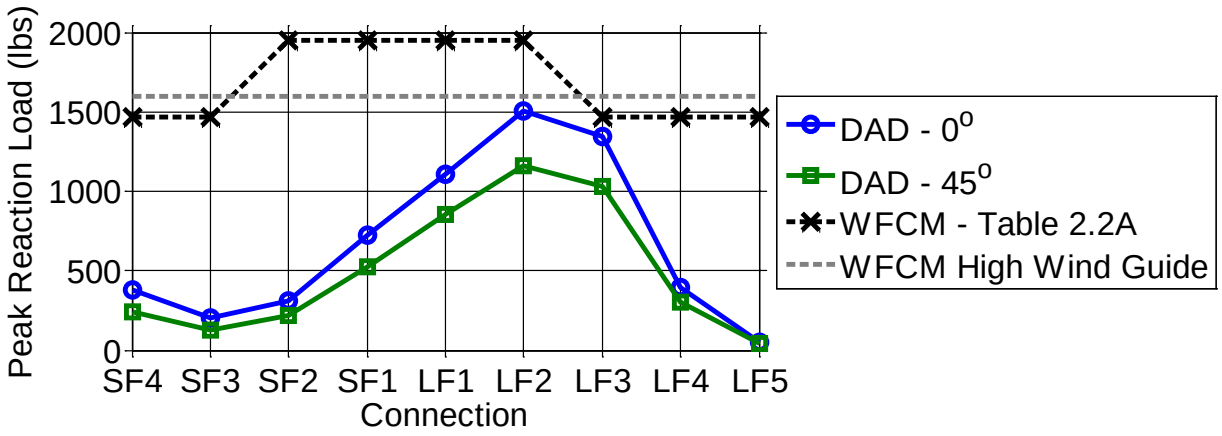

Figure 4-57. Comparison of DAD estimated wall-to-foundation peak loads with design values in the WFCM (Case 2a – without intermediate gable end connections)

CHAPTER 5
DYNAMIC INFLUENCE COEFFICIENT RESULTS

Introduction

As discussed in Chapter 1, the hypothesis of this research is that static influence functions do not accurately reflect the true wind load/structure interaction because they do not consider the correlations of the spatio-temporal wind fluctuations or the dynamic properties of the system. Therefore, a dynamic analysis was performed to determine the effects of dynamic loading on the roof to the roof-to-wall connection loads. The "dynamic influence function" will capture the structural dynamics characteristics of the structure and provide a better understanding of the load paths in these complex, non-engineered buildings, including the damping in the structure.

This chapter presents the results of a dynamic analysis on a full-scale wood-frame 21-truss roof assembly. A 3D finite element (FE) model of the roof was developed using ADINA as described in Chapter 3. The validity of this model was established in a step-by-step procedure as follows:

- Single truss validation comparing experimental results by Wolfe et al. (1986) to the FE truss model
- Analytically-derived influence surfaces comparing with the results presented in Chapter 4

In addition to the static validation, the ADINA frequency analysis was validated using a simply supported beam. A check of the dynamic similitude requirements presented in Chapter 2 for performing a dynamic analysis at a 1/3 scale is also presented. Once the FE roof model was validated, a frequency analysis was conducted on the full 21-truss roof model as well as various components to determine the vertical

fundamental frequencies and first modes of vibration. Lastly, a dynamic analysis was performed to evaluate the effect of dynamic loading on the roof-to-wall connections.

Finite Element Model Validation

In order to ensure that the finite element (FE) model was appropriate, a step-by-step validation procedure was undertaken. First, a single truss was evaluated and compared with the benchmark experimental work reported by Wolfe et al. (1986). Next, influence lines for a single truss were calculated. Finally, the entire 21-truss roof model was tested by applying point loads systematically to the roof and calculating the influence coefficients (and surfaces) for the truss reactions. Additionally, since the FE model was to be used in a dynamic analysis, the ADINA program was checked to ensure accuracy in its frequency analysis. Although the FE model was at full-scale, the accuracy of using the dynamic similitude requirements was also validated in case the actual 1/3-scale model is ever used for a dynamic analysis.

Single Truss Validation

The validation of the ADINA truss model was performed by comparing deflections with full-scale experimental models tested by Wolfe et al. (1986). They tested 42 individual Fink trusses with a span of 28 ft designed to be installed in a typical residential roof at 24 in. o.c. Constructed of No. 2 grade southern pine, half of the trusses had a roof slope of 3 in 12 and the other half 6 in 12. The truss members were carefully selected based on their individual modulus of elasticity (MOE) values. Three MOE groups were established – low (L), medium (M), and high (H) – and each truss was fabricated with members selected from the same group. Additionally, the trusses were braced to prevent out-of-plane deflection when loaded on the top chords with a uniformly distributed load.

The ADINA truss validation model consisted of nominal SYP 2×4s with a span of 28 ft and no overhang (Figure 5-1). The simply-supported truss was braced out of plane by rollers at the five top and bottom chord joints. Two roof slopes (3 in 12 and 6 in 12) were tested with the truss member MOE values matching those reported by Wolfe et al. (1986). The loading on the trusses was also the same as that used by Wolfe et al. – 55 lb/ft for the 3 in 12 slope and 66 lb/ft for the 6 in 12. The deflections are calculated as the average vertical deflection of the five top and bottom chord joints. Comparisons are also made with two other analytical models discussed in Chapter 2 (Li 1996; Martin 2010). Table 5-1 and Table 5-2 present the results for the 3 in 12 and 6 in 12 sloped trusses, respectively. The percent difference in deflections is calculated as the FE model minus the Wolfe study divided by the Wolfe study.

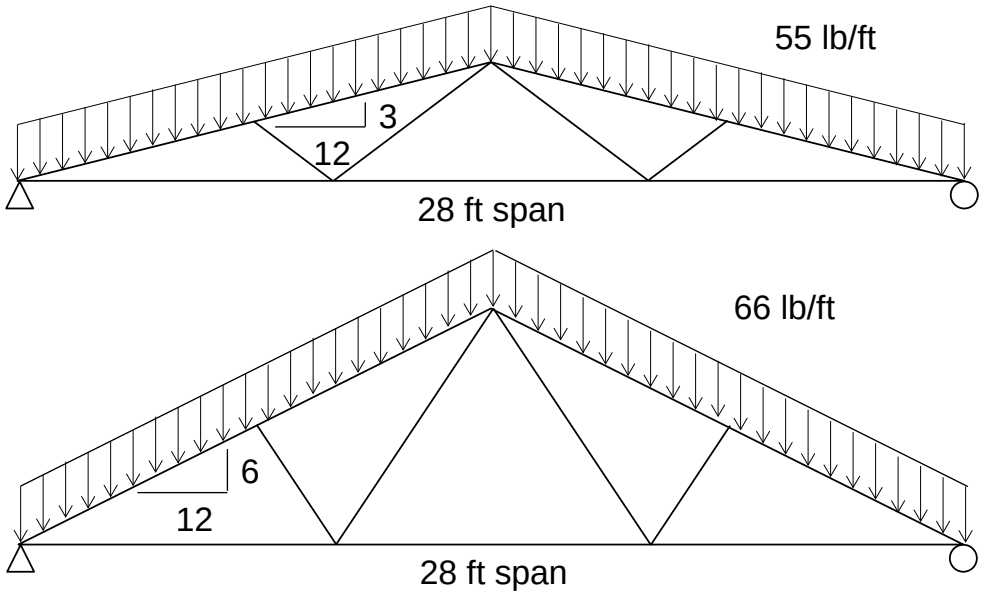

Figure 5-1. Trusses and loading used for ADINA full-scale truss model validation

Table 5-1 and Table 5-2 show that the analytical displacements match the experimental values within an average of 7% for the individual MOE categories and within an average of 3% for the 3 in 12 slope trusses and 6% for the 6 in 12. Although

the models developed by Li (1996) and Martin (2010) are slightly better at estimating the truss deflections, the ADINA model is also acceptable.

Table 5-1. Comparison of full-scale 3 in 12 sloped truss deflections (FE vs. full-scale)

Truss ID	Wolfe et al. (1986)	Present Study ADINA Model		Li (1996) ETABS Model		Martin (2010) SAP Model	
	Defl., in	Defl., in	% Diff	Defl., in	% Diff	Defl., in	% Diff
3L1	0.452	0.457	1.0%	--	1.5%	--	--
3L3	0.478	0.479	0.3%	--	1.9%	--	--
3L5	0.467	0.451	-3.4%	--	0%	--	--
3L7	0.440	0.432	-1.9%	--	2.3%	--	--
Avg.	0.456	0.455	-1.0%	--	1.3%	--	--
3M1	0.324	0.321	-0.8%	--	3.1%	--	--
3M3	0.343	0.323	-5.9%	--	-2.6%	--	--
3M5	0.293	0.316	7.8%	--	11.9%	--	--
3M7	0.330	0.313	-5.0%	--	-1.5%	--	--
Avg.	0.318	0.318	-1.3%	--	2.2%	--	--
3H2	0.266	0.234	-11.9%	--	-6.8%	--	--
3H4	0.247	0.248	0.5%	--	6.9%	--	--
3H6	0.287	0.267	-6.8%	--	-2.4%	--	--
3H7	0.274	0.258	-5.9%	--	-0.7%	--	--
Avg.	0.267	0.252	-6.2%	--	-1.1%	--	--

Table 5-2. Comparison of full-scale 6 in 12 sloped truss deflections (FE vs. full-scale)

Truss ID	Wolfe et al. (1986)	Present Study ADINA Model		Li (1996) ETABS Model		Martin (2010) SAP Model	
	Defl., in	Defl., in	% Diff	Defl., in	% Diff	Defl., in	% Diff
6L2	0.172	0.176	2.2%	0.179	4.1%	0.179	3.9%
6L3	0.180	0.178	-1.0%	0.186	3.0%	0.186	3.3%
6L5	0.194	0.169	-13.1%	0.176	-9.3%	0.176	-9.3%
6L7	0.198	0.172	-13.2%	0.175	-11.6%	0.175	-11.6%
Avg.	0.186	0.174	-6.7%	0.179	-3.8%	0.179	-3.7%
6M1	0.123	0.112	-9.0%	0.121	-1.6%	0.118	-4.1%
6M2	0.136	0.119	-12.2%	0.129	-5.1%	0.127	-6.6%
6M4	0.121	0.120	-1.1%	0.127	5.0%	0.126	4.1%
6M7	0.117	0.124	6.2%	0.133	13.7%	0.132	12.8%
Avg.	0.124	0.119	-4.4%	0.128	3.2%	0.126	1.6%
6H1	0.107	0.091	-15.0%	0.099	-7.5%	0.094	-12.1%
6H2	0.107	0.095	-11.4%	0.101	-5.6%	0.097	-9.3%
6H6	0.086	0.096	12.0%	0.104	20.9%	0.101	17.4%
6H7	0.107	0.096	-10.3%	0.104	-2.8%	0.102	-4.7%
Avg.	0.102	0.094	-7.1%	0.102	0.0%	0.099	-2.9%

Single Truss Influence Line

Once the single truss model was validated, an influence line for vertical reactions at the heel joint was generated for a single 4 in 12 sloped roof truss with an 18 in. overhang on both sides. This truss was braced out of plane in the same manner as the trusses used for the model validation. Figure 5-2 shows the influence line for this truss (which is the same as the theoretical influence line developed in Chapter 4) where an interesting phenomenon is observed. At the mid-point of the truss (at the peak joint), there is an offset in the influence line due to applying the load perpendicular to the top chord which has a vertical and horizontal component. By applying simple statics, the horizontal component adds or subtracts from the vertical forces (depending on which side of the peak the load is applied) resulting in the influence line as shown.

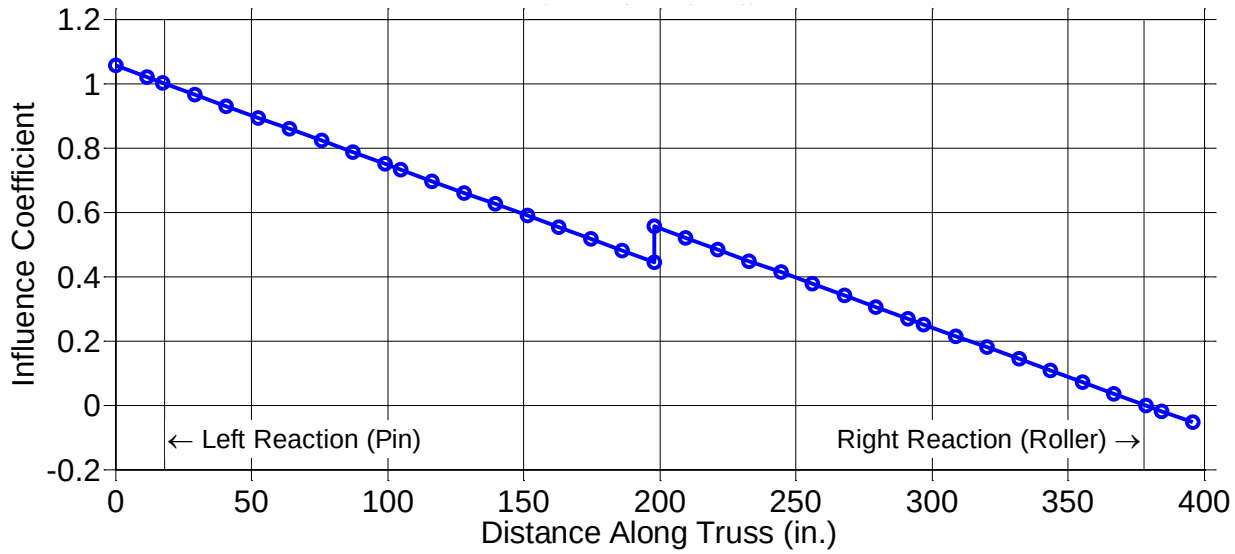

Figure 5-2. Analytical influence line for the left reaction on a single truss (4 in 12 slope with point loads applied normal to top chord)

Frequency Analysis Validation

Since the frequency response of a structure is essential when applying dynamic loads, a validation of ADINA's frequency analysis was conducted using an 8 ft long 2×4 member, modeled using 48 beam elements. The MOE of the beam was taken as 2000

ksi and the specific gravity as 0.55. Tedesco et al. (1999) provides an equation for estimating the fundamental frequencies of a simply supported beam (Eqn. 5-1).

$$\omega_n = \left(\frac{n\pi}{L}\right)^2 \sqrt{\frac{EI}{\rho A}} \tag{5-1}$$

where: ω_n is the fundamental frequency of the *n*-th mode; L is the span; E is the modulus of elasticity; I is the moment of inertia; ρ is the density of the material; and A is the cross-sectional area of the beam. Table 5-3 provides the first three fundamental frequencies of the simply supported beam using the ADINA model and Eqn. 5-1. As can be seen, ADINA calculates nearly identical frequencies.

Table 5-3. ADINA frequency analysis check

Mode	Theoretical Frequency (Hz)	ADINA Frequency (Hz)
1	33.95	33.93
2	135.8	135.5
3	305.5	304.0

An additional check on ADINA's frequency analysis procedure was conducted using shell elements for the sheathing. For this check, a 24 in. long by 48 in. wide by 0.5 in. thick piece of sheathing was modeled using 64 8-node shell elements. The MOE of the sheathing was taken as 832 ksi and the specific gravity as 0.68. The sheathing was simply supported along the 48 in. long sides. Treating the sheathing as a simply supported beam with a 24 in. span, the first fundamental frequency was calculated as 45.01 Hz using Eqn. 5-1, while ADINA calculated 45.51 Hz. The higher fundamental frequencies did not match between Eqn. 5-1 and ADINA due to the higher mode shapes of the sheathing being different from the higher mode shapes of a beam. However, the frequency analysis check showed that ADINA does properly calculate the fundamental frequencies of both beams and shell elements.

Scaled Frequency Analysis Validation

Since the experimental model was at a 1 to 3 geometric scale, the validity of using the dynamic similitude equations (Harris and Sabnis 1999) presented in Chapter 2 was investigated. A single 4 in 12 sloped roof truss with a span of 30 ft at full-scale was modeled at both full-scale and at 1/3-scale. The modulus of elasticity was the same in both cases. For a 1/3 geometric scale, the similitude requirements show that the density of the scaled structure materials needs to be three times that at full-scale. Therefore, a density at full-scale of 5.801E-8 kip-s^2/in^4 was used for the full-scale truss members (corresponding to a specific gravity of 0.62) and the corresponding density for the 1/3-scale model was 1.7404E-7 kip-s^2/in^4. Both of the trusses were braced out-of-plane at all truss joints to force only vertical deflections and frequencies.

Dynamic similitude also states that the frequency scaling is proportional to the inverse of the square root of the geometric scale (i.e., $1/\sqrt{3}$ for the current study). Table 5-4 shows the first five fundamental frequencies for the roof trusses at both full and model scale along with the adjustment of the model scale frequencies by the $1/\sqrt{3}$ multiplier. As can be seen, the corrected model-scale frequencies are nearly identical to the full-scale frequencies, thus validating the dynamic similitude requirements.

Table 5-4. Dynamic similitude requirements validation

Mode	Full-Scale Frequency (Hz)	Model-Scale Frequency (Hz)	
		Measured	Measured × $1/\sqrt{3}$
1	11.96	20.73	11.97
2	13.00	22.54	13.01
3	17.27	29.91	17.27
4	18.18	31.49	18.18
5	18.75	32.55	18.79

Static Influence Coefficients

In addition to validating the single truss model, once the entire 21-truss roof was assembled, the static influence surfaces for roof-to-wall connections were calculated. These were determined by a similar manner as the experimental model by applying point loads at various locations on the roof and measuring the reaction loads. Figure 5-3 shows the influence surfaces for various roof-to-wall connections in the FE model. The plots show that the influence surfaces are similar to those derived experimentally and presented in Chapter 4. There are some slight differences, namely that the concentrated influence area extends further along the truss and even continues past the ridge. However, the lateral spread of the concentrated influence area is similar to the experimental surfaces. The more concentrated portion near the ridge is most likely due to the effect of loading the sheathing directly at the ridge and the influence coefficient increases as shown previously in Figure 5-2 for a single loaded truss. The 1/3-scale building was not loaded right at the ridge so this phenomenon was not captured.

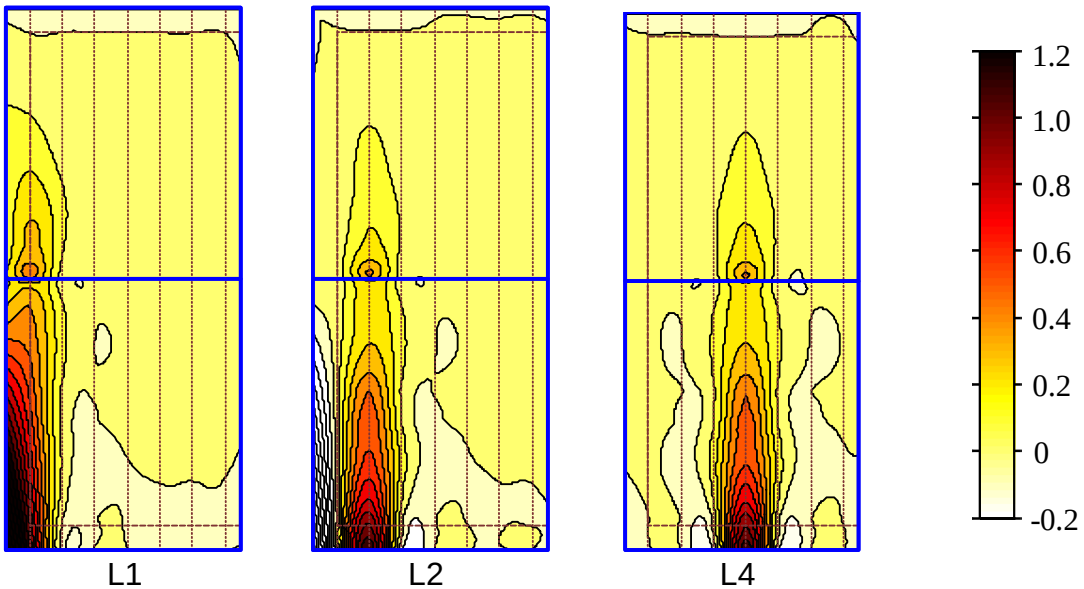

Figure 5-3. Influence surfaces for the full-scale finite element model

Fundamental Frequency Analysis

The above studies established the validity of the static behavior of the FE model. This section presents the results of the experiments examining the dynamic behavior of the 3D truss system. The fundamental (or natural) frequencies were investigated for various components in a wood-framed roof. Loading a structure at or near its natural frequency of vibration produces resonance where the structure is able to absorb more energy than if loaded at frequencies far from the resonant frequency causing the vibrations to amplify, sometimes drastically, and can cause the structure to collapse. The hypothesis being tested is that the roof structure is sufficiently flexible to be excited by wind loading causing dynamic amplification, thus changing the influence coefficients. Since this investigation is just looking at wind loading on the roof, only the vertical natural frequencies were investigated. Others (Foliente and Zacher 1994; Camelo 2003) have determined the lateral fundamental frequencies of wood-framed buildings, discussed previously in Chapter 2. However, the author was unable to find a single study that determined the vertical frequencies of wood-framed roofs or roof sheathing. In order to ensure that only vertical frequencies are calculated, all of the systems investigated were braced out-of-plane to force only vertical and longitudinal movement.

For dynamic analysis, it is important that the mass of the system is modeled correctly. Thus, 2 psf was added to the structure to account for the roofing material (i.e., asphalt shingles and felt underlayment) (Breyer et al. 2007). Appendix F shows the calculation of the additional mass added to the sheathing using a weighted specific gravity.

The vertical natural frequencies of six individual components or sub-assemblies were investigated using ADINA:

- Single 4 ft by 8 ft piece of OSB sheathing supported at 24 in. o.c. by simple supports spanning the 4 ft dimension. The addition of asphalt shingles was also investigated.
- Single 4 ft by 8 ft piece of OSB sheathing supported at 24 in. o.c. by SYP 2×4s with the link elements (simulating nails) spaced at 12 in. o.c. The framing members were simply supported at each end. The addition of asphalt shingles was also investigated.
- Single fink truss with no sheathing attached.
- Single fink truss with 24 in. wide strip of OSB roof sheathing attached using the link elements spaced at 24 in. o.c. The addition of asphalt shingles was also investigated.
- Sheathed gable end truss.

Table 5-5 provides the fundamental vertical frequencies as well as the first mode of vibration for the various components. The natural frequency of the wood structure (without the added weight of roofing) was 10.3 Hz, compared to 8.6 Hz when the roofing material weight was added. These natural frequencies for vertical displacement of the structure exceed the natural frequencies for lateral displacements reported in Chapter 2. Figure 5-4 shows the first mode of vibration for the entire 21-truss roof assembly.

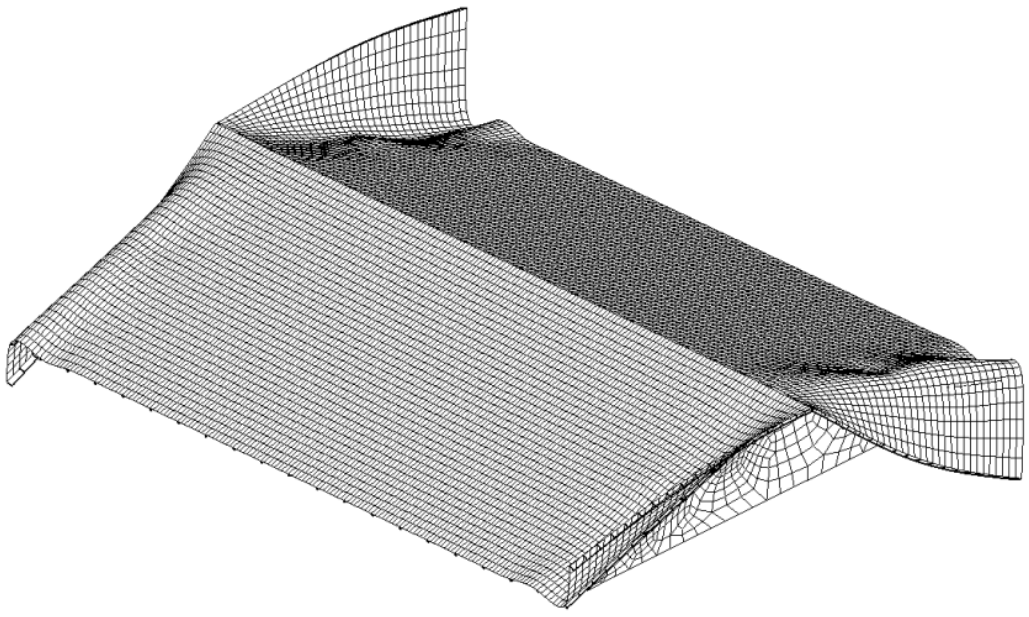

Figure 5-4. First vertical mode of vibration for the full-scale 21-truss roof assembly

Table 5-5. Fundamental frequencies and mode shapes for various full-scale wood-framed roof components

Configuration	Frequency (Hz)	First Mode Shape
Sheathing without 2×4 support	44.8	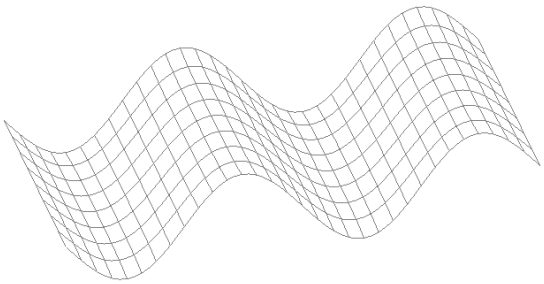
Sheathing without 2×4 support + shingles	30.6	
Sheathing with 2×4 support	45.5	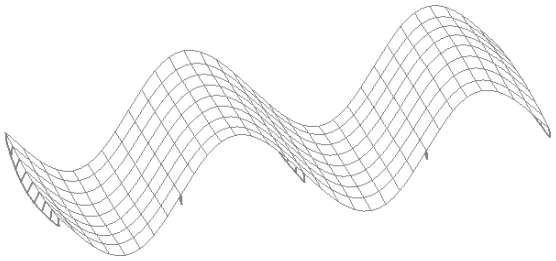
Sheathing with 2×4 support + shingles	31.2	
Single truss	18.2	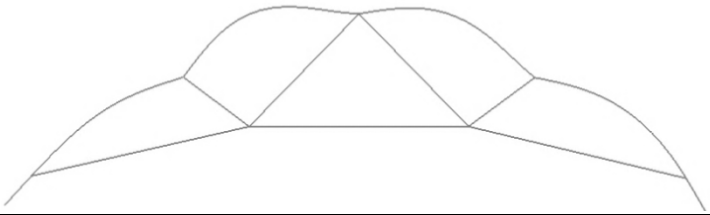
Single truss with sheathing	13.6	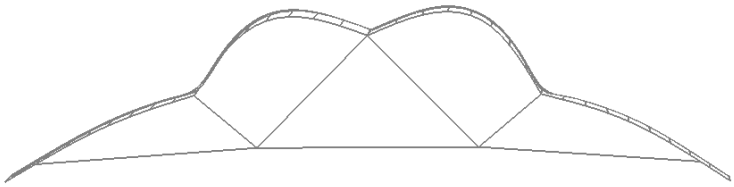
Single truss with sheathing + shingles	10.3	
Sheathed gable end truss	20.2	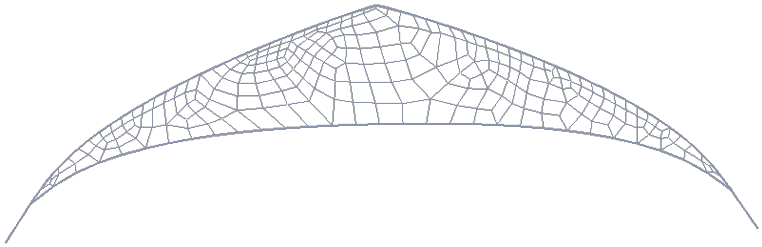

When compared with the dominant frequencies in natural wind flows (0 to 2 Hz), shown earlier in Figure 2-13, the fundamental frequencies for all fundamental vibration modes are larger (by a factor of 10). Figure 5-5 shows a normalized PSD of this

stationary record with a mean speed of 67.8 mph and an integral length scale of approximately 650 ft. The power spectral density (PSD) of wind speed was obtained during a full-scale wind-storm event recorded by the Florida Coastal Monitoring Program (FCMP) in 2005 in Bella Chase, Louisiana, during Hurricane Katrina. The data is a stationary record from a 10 m (33 ft) tower in open terrain. Appendix G provides more details of this wind speed time history with aerial photographs showing the location and surrounding terrain.

It is clear in Figure 5-5 that most of the power in this natural wind flow occurs at frequencies below 1 Hz and most of the energy falls below about 0.5 Hz. Therefore, given the high natural frequencies of the typical wood-framed roof, they would not be excited by the low-frequency energy contained in natural winds. The next section confirms this fact.

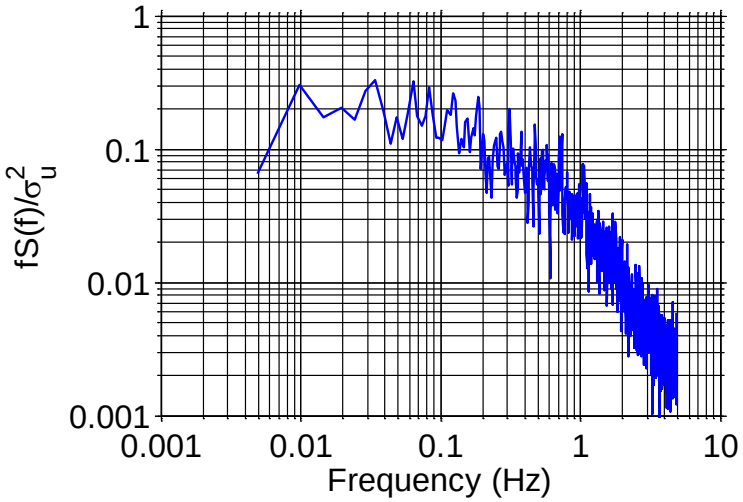

Figure 5-5. Power spectral density of wind speed time history recorded during Hurricane Katrina (2005)

Dynamic Loading

Sinusoidal loading was applied to the roof in various locations. Two different loading conditions were considered for the dynamic loads: (1) a 100 lb force oscillating

at 8.6 Hz, corresponding to the first vertical fundamental frequency of the roof structure; and (2) a summation of six low frequency sine waves with characteristics shown in Table 5-6 to create a “randomized” test signal. The first 25 seconds of the total applied low frequency load is shown in Figure 5-6. Both of the loadings considered were applied for approximately 100 seconds each with a sampling frequency of 100 Hz. The oscillating loads were placed at nine different locations on the roof as shown in Figure 5-7. For the discussion presented here, only figures for points P2c and P3a are presented. For each of these load points, the reactions measured at connections L1, L2, and R1 are presented.

Table 5-6. Parameters for low frequency load applied to the wood-framed roof FE model

Sine Function No.	Frequency (Hz)	Amplitude (lbs)	Phase Angle (deg.)
1	1.0	100	0°
2	0.9	80	65°
3	0.75	60	330°
4	0.45	40	205°
5	0.6	20	50°
6	0.25	50	75°

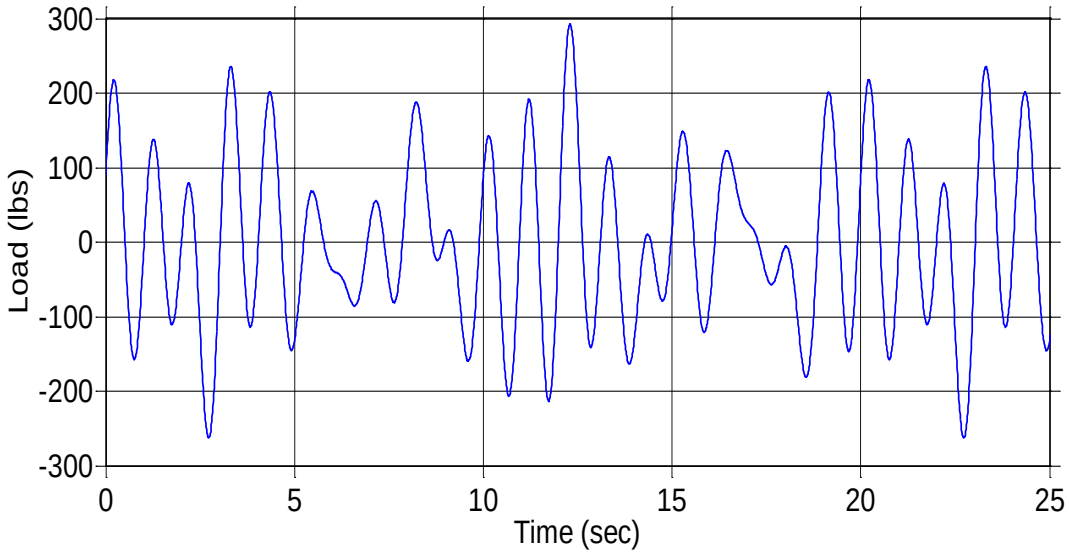

Figure 5-6. Low frequency loading time history (first 25 seconds)

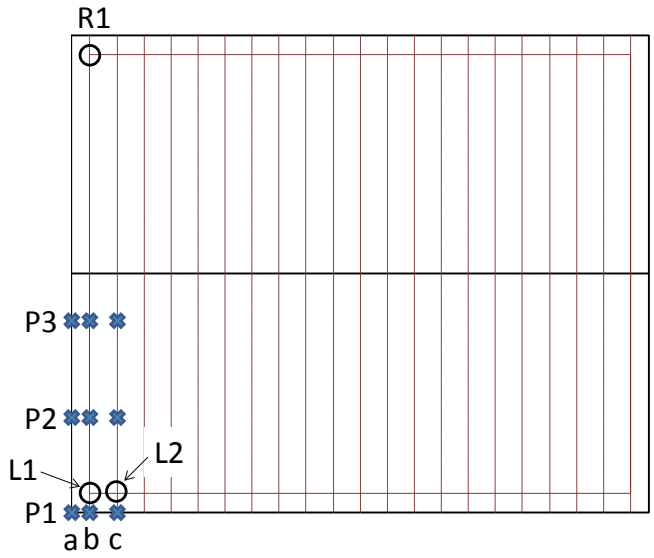

Figure 5-7. Location of roof-to-wall connections and roof loading points for dynamic analysis

Fundamental Frequency Loading

To illustrate the effect of loading the structure at its natural frequency, the FE model was loaded in several locations with a sinusoidal load with a frequency of 8.6 Hz. First, the squared coherence function was calculated and is shown in Figure 5-8 and Figure 5-9 (details of the calculation procedure are provided in Chapter 3). The nearly identical coherence functions show that the input load and the reaction load are strongly correlated near a frequency of 8.6 Hz. However, this is not a dominant frequency of natural wind. Figure 5-10 and Figure 5-11 show the frequency response functions which for resonance frequency loading causes a dramatic gain in the reaction load at 8.6 Hz. These gains are manifest in the time histories of the recorded load versus the applied load in Figure 5-12 and Figure 5-13, where the measured load is much larger than the applied load (±100 lbs sine wave). Table 5-7 reports the ratio of the peak measured connection load to the input signal for all nine load points. The dynamic amplification is quite severe in some instances with all of the ratios larger than unity. Even though no damping was accounted for in the model (producing larger reaction

forces), the resonance loading was performed to show the difference in how the structure reacts when loaded near or at the fundamental frequency versus when it is loaded by frequencies found in natural wind flow.

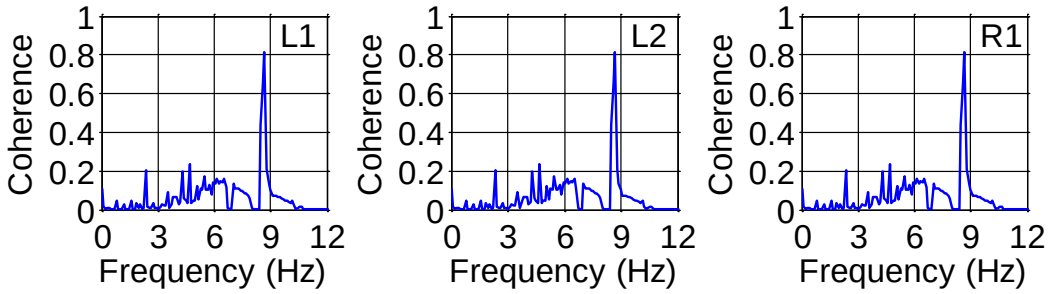

Figure 5-8. Coherence functions for resonance loading at P2c

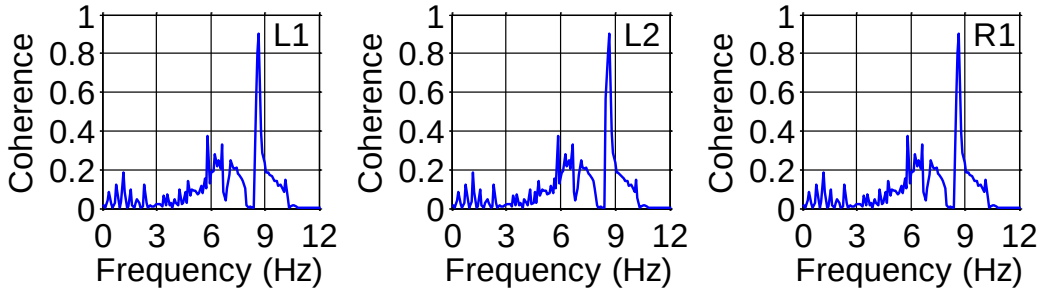

Figure 5-9. Coherence functions for resonance loading at P3a

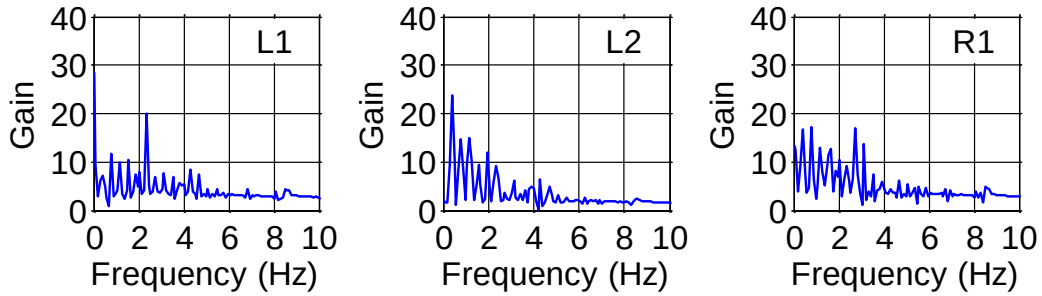

Figure 5-10. Frequency response functions for resonance loading at P2c

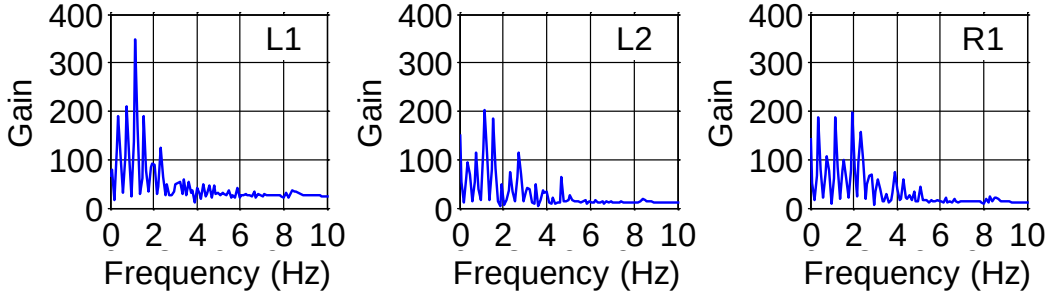

Figure 5-11. Frequency response functions for resonance loading at P3a

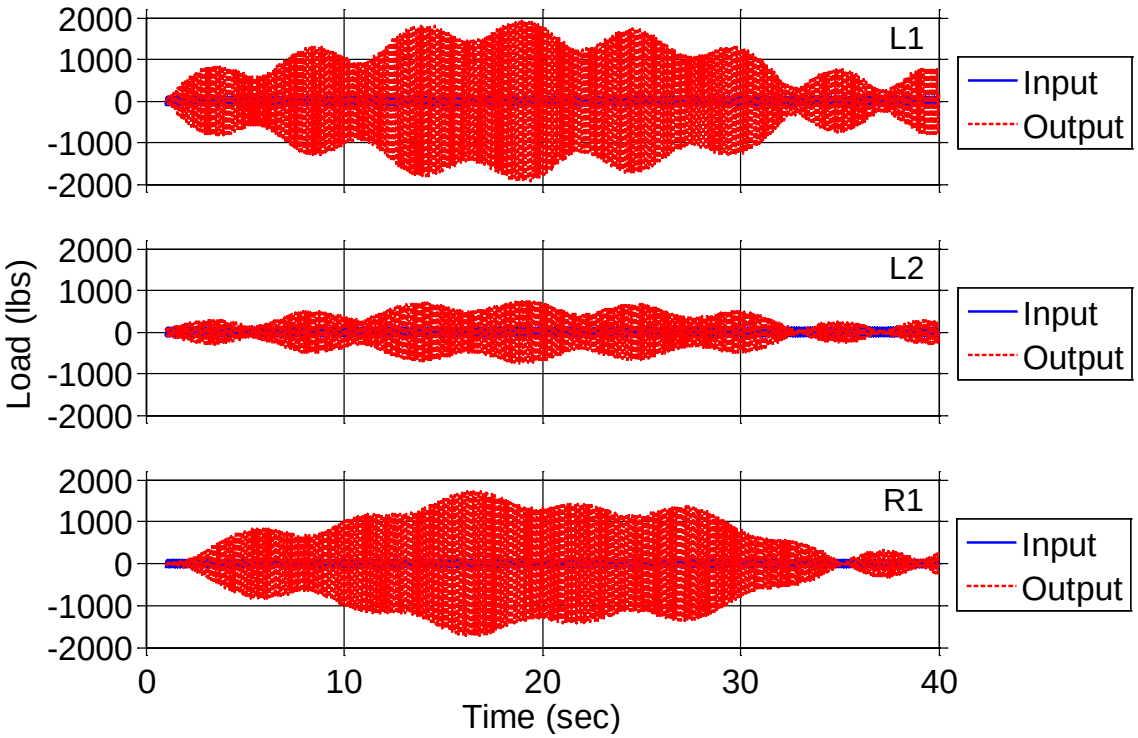

Figure 5-12. Time histories of applied load and reaction loads for resonance loading at P2c

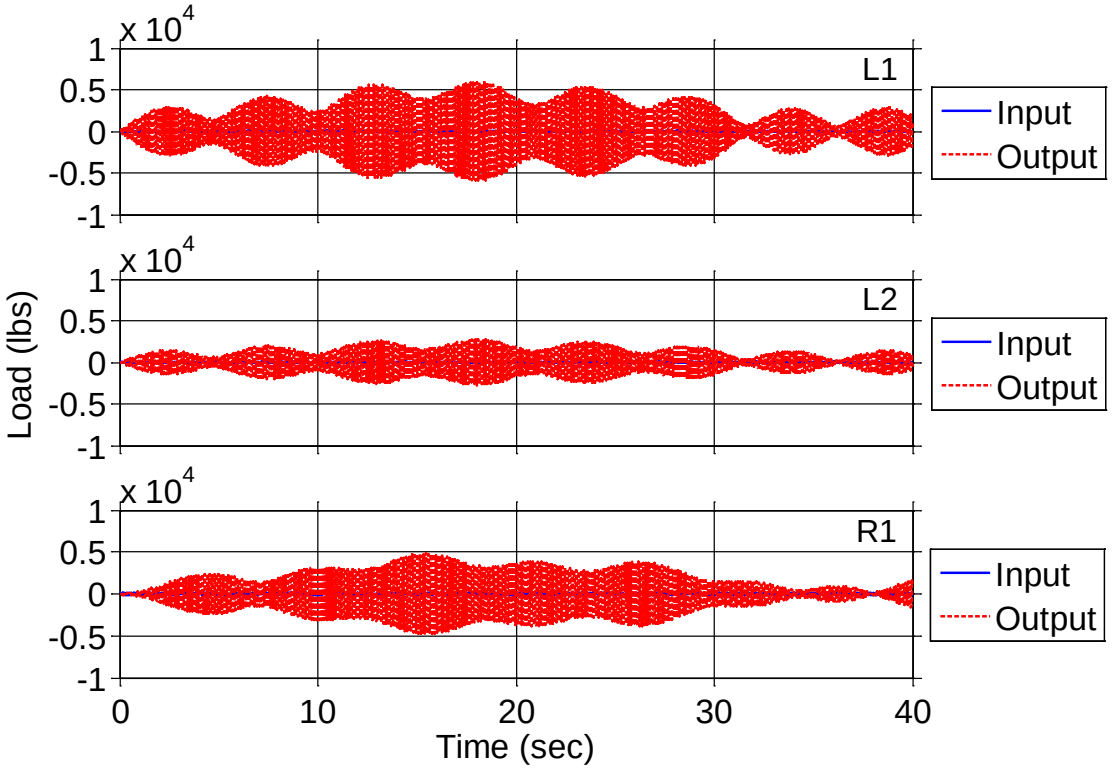

Figure 5-13. Time histories of applied load and reaction loads for resonance loading at P3a

Table 5-7. Ratio of peak roof-to-wall connection loads to peak input load for resonant frequency loading

Loaded Point	L1	L2	R1
P1a	199.4	87.1	192.0
P2a	148.5	64.5	136.6
P3a	60.0	27.5	48.0
P1b	3.6	1.2	2.8
P2b	8.0	4.0	9.4
P3b	9.6	4.5	11.4
P1c	10.1	5.4	9.0
P2c	19.2	7.5	17.3
P3c	6.4	2.2	3.7

Low Frequency Loading

For the low-frequency loading, the squared coherence functions shown in Figure 5-14 and Figure 5-15 were calculated, which show that the input signal and the reaction load are only correlated in the low frequencies as expected. The FRFs were also calculated and are shown in Figure 5-16 and Figure 5-17. The magnitudes of these FRFs are low with a maximum of only 1.0 for R1 when the load is applied at P1. The time histories are shown in Figure 5-18 and Figure 5-19. As shown, the reaction load follows the input signal almost exactly. The difference in these time histories from those shown in Figure 5-12 and Figure 5-13 also provide further evidence that the structure is not excited in the frequency range of natural wind. Therefore, the current assumption that a wood-framed residential building is a rigid structure appears to be valid. The ratios of the peak measured connection load to the input signal for all nine load points are presented in Table 5-8, where almost all of the values are less than one. These ratios are nearly equal to the influence coefficients for the static loading, further solidifying that the dynamic loading at natural (low) wind frequencies does not alter the load path form the static loading.

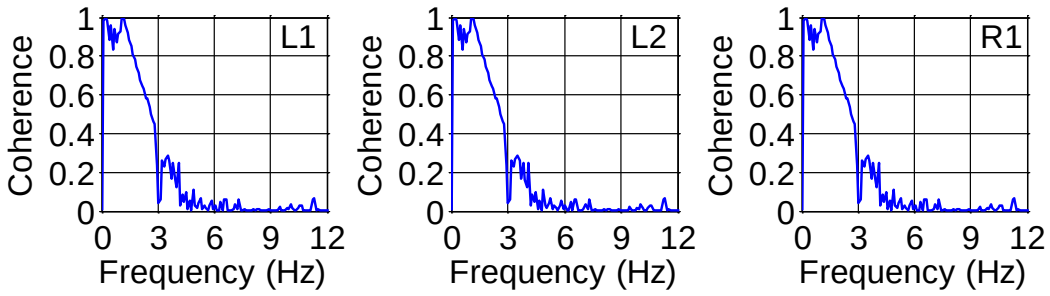

Figure 5-14. Coherence functions for low-frequency loading at P2c

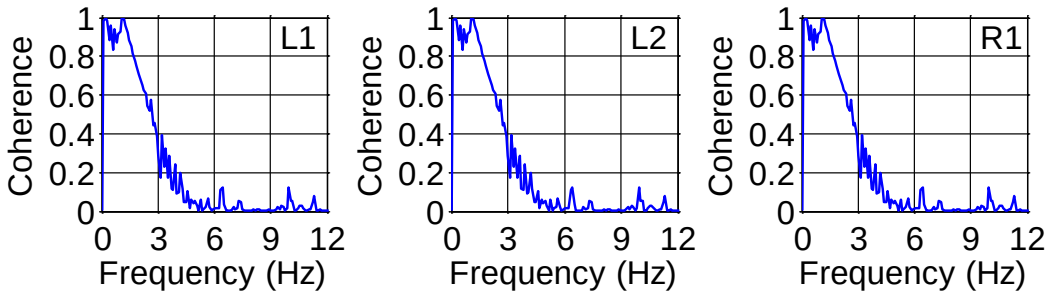

Figure 5-15. Coherence functions for low-frequency loading at P3a

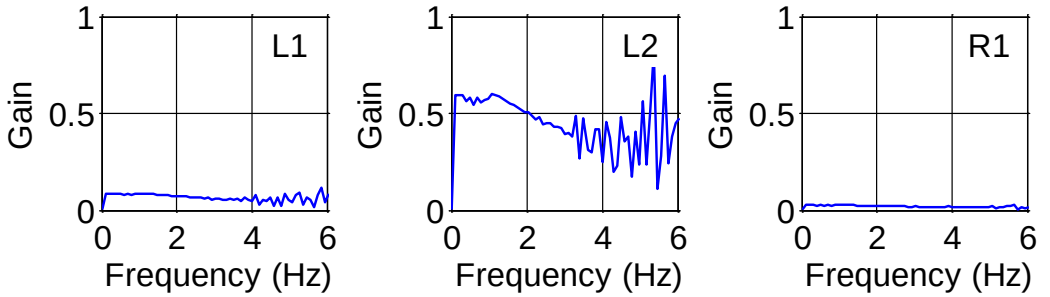

Figure 5-16. Frequency response functions for low-frequency loading at P2c

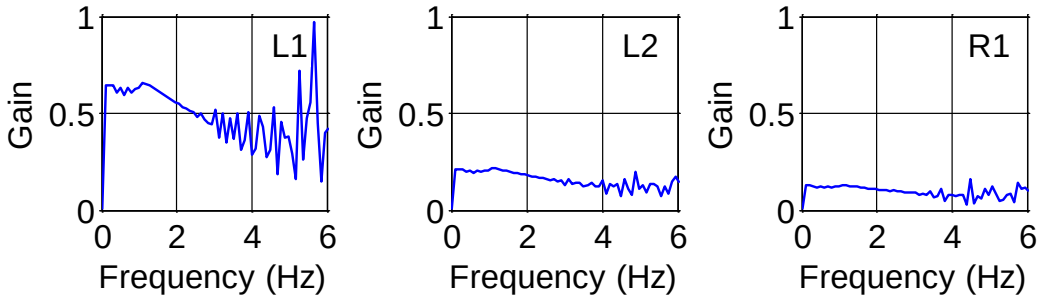

Figure 5-17. Frequency response functions for low-frequency loading at P3a

Discussion and Limitations of Finite Element Model

Despite the above results, the FE model presented here has several limitations. First, the nail “links” used did not provide the best representation of the full-scale connection. The “RIGIDLINK” command in ADINA would provide a much better

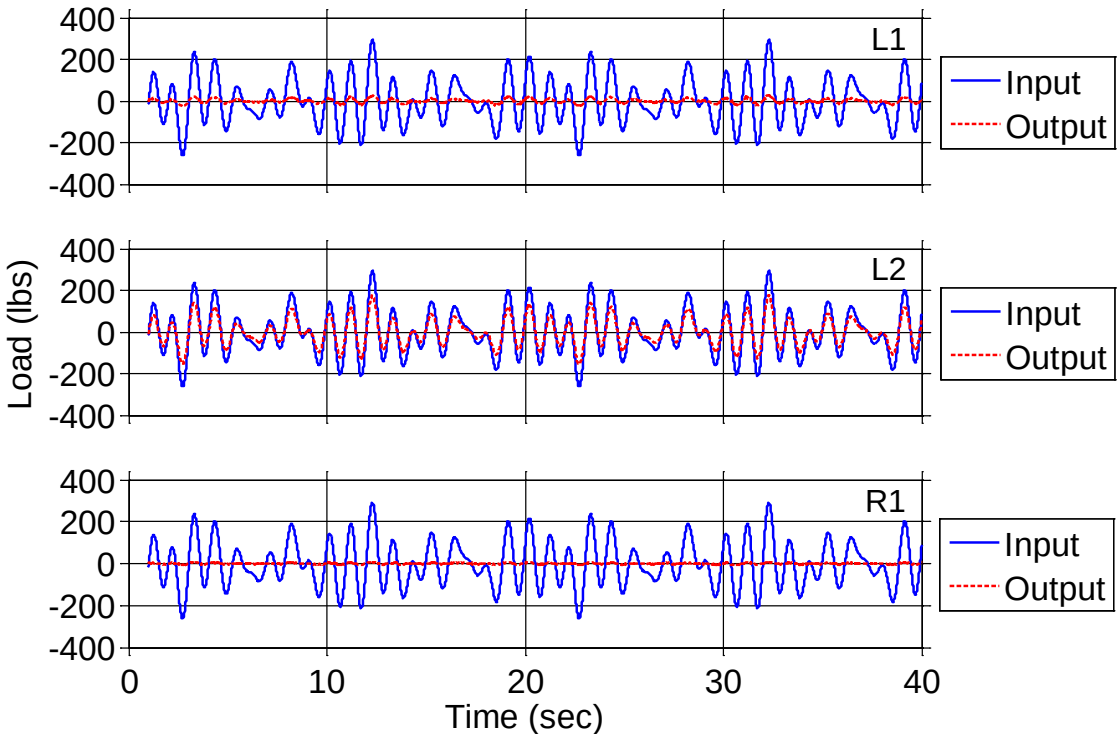

Figure 5-18. Time histories of applied load and reaction loads for resonance loading at P2c

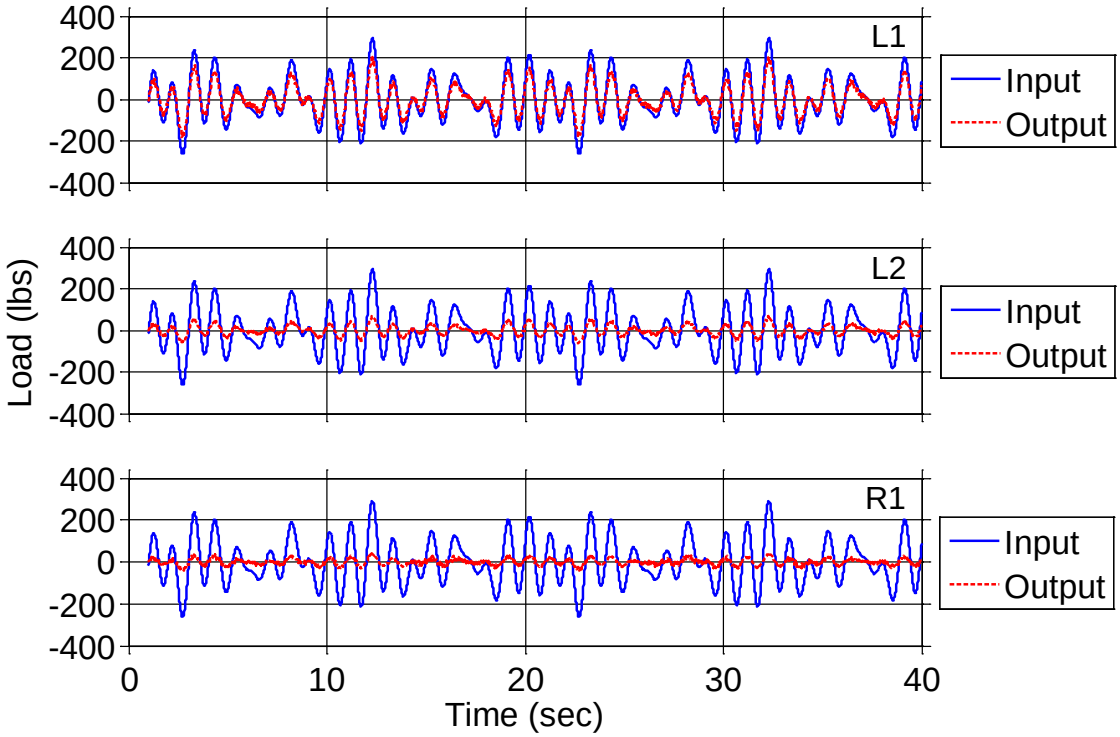

Figure 5-19. Time histories of applied load and reaction loads for resonance loading at P3a

Table 5-8. Ratio of peak roof-to-wall connection loads to peak input load for low-frequency loading

Loaded Point	L1	L2	R1
P1a	1.78	1.09	0.12
P2a	1.25	0.67	0.14
P3a	0.62	0.23	0.14
P1b	0.91	0.01	0.02
P2b	0.68	0.03	0.08
P3b	0.49	0.04	0.23
P1c	0.04	0.96	0.01
P2c	0.09	0.54	0.03
P3c	0.13	0.33	0.11

representation of a full-scale connection in this FE model. The RIGIDLINK command maintains a constant distance between the two nodes as well as ensuring that the rotations at the two nodes are the same (ADINA 2009). Since in an actual sheathing-to-truss/rafter connection, the nail is not allowed to buckle since it is restrained by the embedment in the truss/rafter. In the FE model, only the centerlines of the truss chords and the sheathing were modeled, so a two inch offset was imposed between the truss chords and the sheathing. The beam elements used did not provide the rigidity at this connection that was necessary to more accurately represent the physical conditions.

Initially, the rigid links were used, but when applying static point loads the calculated influence coefficients were unrealistic (i.e., extremely high and highly concentrated around the point of load application). For this reason, less stiff beam elements were used which provided more realistic influence coefficients. In retrospect, a possible reason for this discrepancy with the rigid links is that the loads were applied as point loads directly at the “nail” locations. If the load was applied as a pressure centered at the “nail,” the results may have been better for the static influence coefficients.

Based on the dynamic loading analysis, the wood roof structure has vertical fundamental frequencies that are far higher than the fundamental frequencies of natural wind. Use of the rigid links would only serve to increase the fundamental frequencies of the structure even more. For example, for the full 4 ft by 8 ft roof sheathing panel supported on 2x4s at 24 in. on center, the fundamental frequency increases from 45.5 Hz with the beam links to 74.7 Hz when the rigid links are used. Table 5-9 provides a tabulated summary of the influence of using the rigid links for the nail connections. A full reanalysis of the 21-truss roof model was deemed unnecessary since the fundamental vertical frequency would only increase by using the rigid links. This further validates that low-rise, wood-framed roofs are not excited by natural wind loads.

Table 5-9. Vertical fundamental frequency analysis comparison using "beam" versus "rigid" links for nail connections

Configuration	Frequency (Hz)		First Mode Shape (RIGIDLINK)
	Beam link	Rigid link	
Sheathing with 2×4 support	45.5	74.7	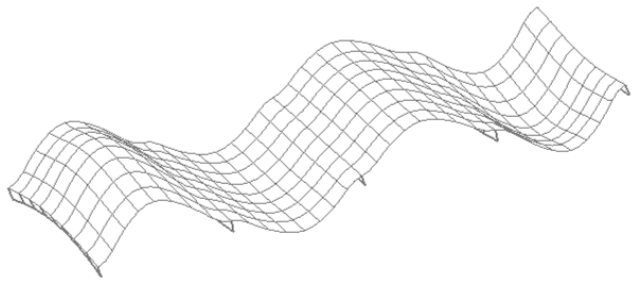
Sheathing with 2×4 support + shingles	31.2	51.4	
Single truss with sheathing	13.6	20.8	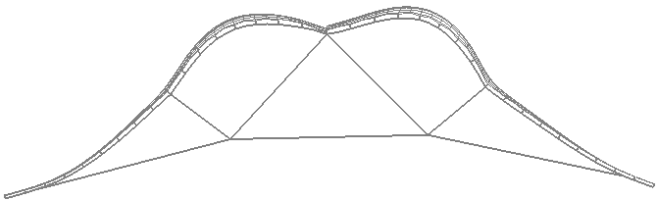
Single truss with sheathing + shingles	10.3	16.8	

CHAPTER 6
DISCUSSION OF RESULTS

1/3-Scale Wood-Framed Building

To the author's knowledge, this study utilizing a 1/3-scale wood-framed building is the first time a 3D full structural model of a light-framed structure was fabricated and instrumented to investigate structural load paths due to wind uplift loads. Using appropriate structural similitude requirements, the scale structure was found to accurately reproduce the response of a full-scale structure. However, several issues with model scale wood structures were manifest during the construction and testing.

First, the influence of moisture content on the behavior of the structure can be significant. Moisture content in wood is well known to change its structural behavior. The constructed model was kept in an open laboratory building and was subject to the changes in humidity and temperature fluctuations of the local climate. Moisture measurements were made during the testing of the modulus of elasticity of the framing members and sheathing but none were taken after construction of the building. The temperature and humidity were also not recorded.

Another issue with scaled wood models is properly scaling the connections so that they provide comparable stiffness values to the full-scale connections. A further issue that also occurs with full-scale modeling is that the presence of the load cells needed to measure structural loads alters the connection stiffness. This model had metal strap connectors at the roof-to-wall connections, in contrast to the majority of residential homes where roof trusses are toe-nailed to the top wall plates. Sufficient time should be devoted to ensuring that this connection is not overly stiff or not stiff enough that load paths are altered significantly. The sheathing attachment is also an important

consideration. In this study, screws were used instead of nails to ensure that the sheathing remained attached to the framing members. The screw attachment may be somewhat unrealistic but this compromise was necessary for experimental purposes.

Another issue that was considered is that with scaled wood structures performance at ultimate load (i.e., at failure) cannot be modeled with any meaningful results. The structure must remain within the linear elastic range, eliminating any inferences on performance at failure. Because the same wood is used at model scale as at full scale, the model scale wood has the same grain size and imperfections as the full-scale members. There are also fewer growth rings within the cross-sectional area of the scaled members. All of these associated topics contribute to rendering the model structure less reliable in determining the failure modes and mechanisms of full-scale, wood-framed structures.

Influence Coefficients

The influence coefficients reported in Chapter 4 provide much insight into the load transfer and load paths in wood-framed roofs. Similar observations were made with the 1/3-scale house and the full-scale roof assembly built and tested by Wolfe and McCarthy (1989). The principle of superposition was found to be valid for the static influence coefficients and the line loads developed in this manner compared well with those results found in Wolfe and McCarthy (1989). Additionally, the influence surfaces did not change with increasing magnitude of the applied load, indicating that the structure remains within the linear elastic range and the static influence coefficients are valid. Wolfe and McCarthy (1989) also concluded the same and noted that not until the roof began to experience damage did the influence coefficients begin to change.

As both the 2D influence lines and 3D influence surfaces show, when intermediate gable end connections exist between the end truss and wall, a large portion of the load (upwards of 70%) applied to the gable end truss is transferred through these connections. In addition, the total load carried by the gable end truss when these intermediate connections exist increased by 70%. In most residential LFWS, the gable end wall sheathing is continuous with the end truss. Therefore, a continuous connection can be expected to cause a similar load distribution to when the intermediate connections are present. This load path is not anticipated by any current design guidelines. Beyond the WFCM guide (AF&PA 2006), which states that these connections must resist the uplift and lateral loads provided by the truss designer, there are no other guidelines available. This is the first time experimental results have shown this gable end load path to occur.

At the wall-to-foundation connections, the influence surfaces showed that the gable end wall carries a higher percentage of the roof uplift forces than the side wall whether or not the gable end truss is connected intermittently with the top of the end wall. For the case when the gable end truss is not connected to the end wall, this signifies a different load path exists than may be typically assumed. The loads transferred into the side walls are then partially transferred into the end wall around the corner where the two walls are rigidly connected. The reason for this phenomenon may be partly explained by the following. The gable end wall is loaded at the corner almost as a point load (more realistically a distributed line load acting at the corner along the height of the wall) placing the end wall in bending across multiple supports (i.e., as a continuous deep beam). The side walls directly below the roof-to-wall connections (i.e.,

truss reactions) are loaded only vertically (more like an axial load) resulting in a lower stiffness than the end wall loaded in bending. Thus, the stiffer end wall attracts more load away from less stiff (side wall) elements.

Database-Assisted Design Method

The wind generator testing was used to validate the DAD methodology for predicting structural loads, as it produced good agreement between the measured and DAD-predicted connection loads. This result affirmed the validity of the DAD method for designing LFWS subjected to spatio-temporal variations in wind pressures. With some additional post-processing, the influence coefficients developed in this study, along with the wind pressure database can be added to the existing NIST database for evaluating wind loads on residential buildings. It is suggested that the next step to validate the results will be to investigate the reasonableness of the existing influence coefficients developed at NIST to these experimentally derived influence surfaces. Any differences in predicted wind load reactions can be traced to non-conservative uncertainties in the existing ASCE 7 wind design procedures for low-rise building systems.

When the influence surfaces are combined with the wind tunnel pressure coefficients using the DAD methodology (Figure 4-28 and Figure 4-29), it is observed that the gable end truss carries the most load compared with all other roof trusses. It would be expected that the load (both mean and peak) would decrease to a certain point (maybe 2 or 3 trusses from the end truss) and then be approximately equal, especially for the 0° and 45° wind azimuths, since the gable end truss is stiffer than the other trusses and attracts more load. However, the second truss (connections L2 and R2) has consistently lower peak and mean loads than the third truss (connections L3 and R3). Comparing individual truss stiffness values presented in Chapter 3, the

second truss is stiffer than the third truss. The probable cause of the decrease in load carried by the second truss is that the extra stiff gable end truss with the attached sheathing is much stiffer and thus attracts more of the load. However, the third truss is not as affected by the gable end truss and therefore carries more load than the second truss.

The roof-to-wall connections modeled in this experimental study consisted of metal straps wrapping over the top of the trusses and fastened to the wall. In most of the older existing residential LFWS, less-stiff toe-nail connections are prevalent. If all of the roof-to-wall connections in the structure were toe-nailed, the influence coefficients (or surfaces) should be similar to that of using the straps. However, using equivalent full-scale point loads of 450 lbs (as was used in this study for reporting the influence coefficients) would most likely fail some of the toe-nailed connections as this exceeds the mean capacities reported in the literature (e.g., 341 lbs for two 16d nails and 442 lbs for three 16d nails in southern yellow pine wood, as reported by Shanmugam et al. (2009)). This effect of using such a large point load to determine the influence coefficients is countered by the fact that little change in the influence coefficients occurred when smaller magnitude loads were applied, so the influence surface would be the same for a smaller load (e.g., equivalent 90 lb full-scale load).

With the DAD method validated, the possibilities for improving design are significant. As long as the influence functions are accurate, or at least reasonable, and wind tunnel pressure coefficients are available for a given roof geometry, the peak roof-to-wall and wall-to-foundation connections can be estimated with reasonable accuracy. This method provides a more comprehensive and robust manner to determine the peak

design values rather than relying on prescriptive and simplified wind load design values. The software and database assembled by NIST (Main and Fritz 2006) can be used along with the influence coefficients generated in this project to provide a comprehensive study of the effects of wind loads on residential LFWS.

DAD Predictions vs. CI and LRC Methods

This study has shown that in addition to the DAD method, two existing methods – the covariance integration (CI) method (Holmes and Best 1981) and the load-response-correlation (LRC) method (Kasperski and Niemann 1992) – can also be used for estimating peak reaction loads for design purposes were compared with the DAD method. All three methods provide results that are in close agreement in mean loads, although the CI and LRC methods generally underestimate the peak uplift loads (by up to 25%) at several roof-to-wall and wall-to-foundation connections. These discrepancies are traced to one underlying assumptions in the derivation of the CI and LRC methods that the structural reactions have a Gaussian distribution. However, a comparison of PDFs shown in Figure 6-1 indicates that the best fit distribution of the structural reactions is the reverse 3-parameter lognormal distribution. These results confirm earlier findings of the non-Gaussian distribution of structural reactions determined by Whalen et al. (2002) for steel, portal-framed buildings.

This departure from normality is most likely the reason that the CI and LRC methods do not match the DAD method more closely, especially for the roof-to-wall connections. The reverse lognormal distribution has a tail that extends further to the left and thus encapsulates a larger number of more extreme values. Therefore, the peak estimates would be further from the mean than those assuming a Gaussian distribution. With this in mind, a modification of the CI or LRC methods is needed to account for a

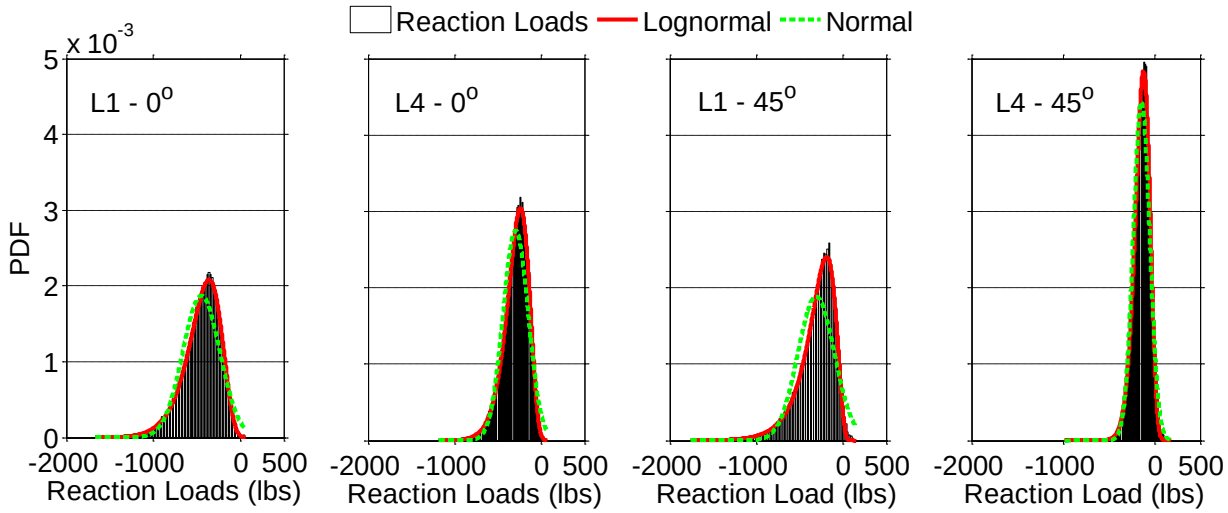

Figure 6-1. Full-scale roof-to-wall reaction time history PDF plots

non-Gaussian distribution before they can be used for estimating peak uplift reactions in residential LFWS connections.

A further comparison of the LRC method was made using an adjusted peak factor model developed by Kasperski (2007) where it was found that the estimated peak reactions still underestimate the DAD derived peak reactions. Again, the assumption of a Gaussian distribution was used for the reaction time histories, even though he assumed an EV Type I distribution for the peak reactions, which is a conservative approach with limited data sets (Kasperski 2003; Kasperski 2007). The modification of either the CI or LRC methods will probably require the selection of a more appropriate connection load distribution and a method for implementing it into the methodologies.

The advantage to using either the CI or LRC methods over the DAD method is the amount of data storage space and processing time. The CI and LRC methods require substantially reduced data storage by two orders of magnitude (i.e., 20 GB for the DAD vs. 100-200 MB for the CI and LRC methods) leading to reduced computational time and computer power. This reduction is possible because the CI and LRC methods use

post-processed wind tunnel data (including mean, standard deviations, RMS, and cross-correlations of pressure coefficients) rather than the need for wind tunnel time histories. The DAD method is a powerful tool to provide time-varying connection time histories. However, for design purposes, the important values are the expected peak forces. The CI and LRC methods would provide these necessary peak forces if appropriate distributions were utilized.

DAD vs. Tributary Area Analysis

When the DAD derived connection loads using the measured influence surfaces are compared with those assuming a simple tributary width of a truss, the tributary area always overestimates the loads. This overestimation is due to higher influence coefficients along the length of the truss when it is loaded as a single 2D component compared to when the composite 3D action is included (Figure 4-3). However, when the intermediate gable end connections are removed (Case 2a), the discrepancy between values is reduced significantly. The mean connection loads determined by the tributary area method are 55-130% higher than for the DAD estimated mean values, when the intermediate gable end connections are present (Case 1). The peak values are in the similar range (60-115% higher), which is a significant overestimation of connection loads. Such overdesign may increase the size and cost of metal plate connectors and installation costs, when a smaller connector may be adequate. When the bottom chord of the gable end truss in not connected to the gable wall (Case 2a), the mean connection loads predicted by the tributary area method are a more reasonable 12-37% higher with the peak load estimates 19-47% higher than those predicted by the DAD.

Design Load Comparison

ASCE 7-05

This research identified several important items pertaining to the design loads prescribed in ASCE 7-05 (ASCE 2006) and in the WFCM guide for high wind regions (AF&PA 2006). Firstly, there is ambiguity in ASCE 7-05 with respect to the definition of main wind force resisting system (MWFRS) components as opposed to components and cladding (C&C) members. Section C6.2 in the Commentary (ASCE 2006) states that roof trusses are part of the MWFRS when they receive loading from cladding and transfer overall loads to the structure. It also states clearly that long-span roof trusses are to be designed for MWFRS loads, implying that the truss reactions are also designed to resist MWFRS loads. The confusion is that the commentary also states that roof trusses can be considered a component (and thus designed according to the C&C loading) when they "receive wind loads directly."

The analysis presented in Chapter 4 shows that the estimated peak loads derived from the DAD method are consistently and significantly greater than the MWFRS loads when gable end intermediate connections are not present, and for certain wind directions some peak loads are greater than the MWFRS loads when the intermediate connections are present. The discrepancy between the low-rise and all heights method is another important issue to discuss. The MWFRS low-rise building design method results in design loads that are 56% larger than the all heights methods (conversely, the all heights method is 36% lower than the low-rise method) for the gable end and first interior truss reactions (L1 and L2) for the low-rise structure used in this study. For connections L5 and L6 the discrepancy is even larger with the low-rise method design load being 77% larger than the all heights method (conversely, the all heights method is

43% lower than the low-rise method). The reason for this large discrepancy is that the all heights method uses a lower velocity exposure coefficient (K_z = 0.57) compared to the velocity exposure coefficient (K_z = 0.7) used for the low-rise method. Additionally, the all heights method multiplies the external pressure coefficients (C_p) by a gust factor (G) of 0.85, whereas the low-rise method accounts for the gust factor in the external pressure coefficients (GC_p). Together, these two factors produce lower loads using the all heights method and provide another example of the risk inconsistency within the wind load provisions of ASCE 7.

The non-conservative nature of the MWFRS (both low-rise and all heights methods) for roof-to-wall connections is alarming, and as shown in Figure 4-51 and Figure 4-52, the C&C loading tends to capture the enveloped peak reaction loads at roof-to-wall connections better than the MWFRS provisions. However, the method for calculating the correct effective wind area (EWA) is still a matter of debate. Using the EWA as prescribed ($L^2/3$) yields C&C design values that are up to 35% less than the DAD-estimated peak loads. (In fact, the $L^2/3$ criteria for EWA is not based on any engineering calculations or data, but rather it was selected by the ASCE 7 wind effects committee (Cook 2010).) When using the smallest EWA (=10 ft^2), the C&C design loads overestimate the gable end truss reactions by 25% but still underestimate some interior truss reactions by up to 19%. An attempt was made to calculate an appropriate EWA based on the DAD-estimated peak reactions, but it was unsuccessful. One reason that calculating an appropriate EWA based on the external pressure coefficient (GC_p) charts in ASCE 7-05 is that this assumes that the GC_p values are assumed to be correct for a light-frame structural system. Additionally, the roof zones are assumed to

be adequate in size and location. Additional work is needed to verify that the GC_p values and roof zones provided in ASCE 7-05 are appropriate for use with light-frame, wood systems. Until such a validation is available, the results of this study present a convincing argument for determining wind loads on roof-to-wall connections using only the C&C design provisions rather than for MWFRS loading. The real issue, however, is to establish a reasonable design value for MWFRS design or eliminate it entirely for low-rise, wood-framed structures.

The greater issue with the underestimation of the peak roof-to-wall connection loads is the development of the ASCE 7-05 MWFRS loads using pseudo-pressure coefficients (GC_p) developed by Stathopoulos (1979). These pseudo-pressure coefficients include influence coefficients that are based on a simple, steel portal-framed building (Stathopoulos 1979; ASCE 2006) with the frames spaced at 25 ft on center (as discussed in detail in Chapter 2). The influence coefficients for a wood-framed building differ significantly from the steel buildings due to a much closer truss spacing (typically 24 in.), shorter spans, and a more variable building material. Figure 6-2 provides a visual depiction of the differences in the structural framing methods for the large steel, portal-framed building versus that of a light-frame, wood system making it obvious that influence coefficients will differ (possibly drastically) between the two building types. Although, the ASCE 7-05 commentary states that the GC_p values have been validated for other low-rise structures, no reference in the public domain is available. It is unclear what building types were used and no experimental data was provided. As Simiu and Stathopoulos (1997) suggested before, it is strongly recommended that the existing design pressure coefficients in ASCE 7-05 be validated in a robust manner possibly

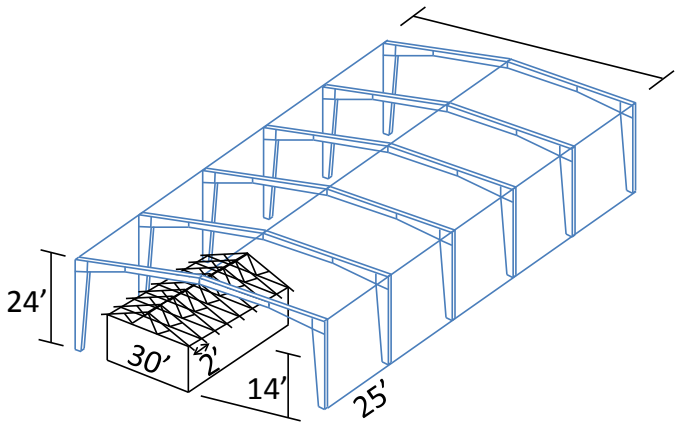

Figure 6-2. Structural framing systems for steel portal-frame buildings vs. light-frame wood buildings

using a DAD methodology as outlined in this work further adopted to determine appropriate GC_p values for residential LFWS.

While this study used only two wind directions to arrive at the conclusions, this is not considered a big limitation for determining the extent of ASCE 7-05 underestimation. Since the wind directions chosen already have high wind loads, the effect of using additional wind directions may serve to widen the discrepancy between the ASCE 7 values and the realistic uplift loads (i.e., the enveloped loads will not be reduced). More research is needed to ensure that the peak loads presented in this research are in fact the actual peak loads experienced by the connections.

Wood Frame Construction Manual (WFCM)

The WFCM (AF&PA 2001) provides prescriptive, tabulated design loads for almost all connections in residential LFWS. As shown previously in Figure 4-54 and Figure 4-55, the WFCM design loads reasonably predict the DAD-derived peak uplift forces except for the gable end truss reaction (L1) when the intermediate gable end connections are not present. However, caution is needed in interpreting this to mean that the WFCM is better than ASCE 7. The Commentary to the WFCM states that the

tabulated uplift values provided were derived based on the MWFRS method (whether the low-rise or all heights method is used in unclear) in ASCE 7-98 (ASCE 1998) and includes overhang pressures (assuming 24 in. overhangs) and internal pressures. The DAD-estimated peak loads presented in this study do not account for overhang or internal pressures (i.e., only external roof pressures used) which would only increase the peak values. Thus, the WFCM design loads would probably underestimate the peak loads at most of the roof-to-wall connections, just as the ASCE 7 MWFRS loads do not adequately predict the peak uplift forces experienced by these connections. In contrast, the WFCM design value for wall-to-foundation loads is larger than all the DAD-derived peak values leading to a conservative design value.

Dynamic Loading

The ADINA FE model developed for this investigation provided a reasonable model of the static influence coefficients developed experimentally. The truss model used compared well to the previous full-scale trusses tested as well as other analytical models. With this validation performed, the dynamic loads and frequency analysis was conducted.

The frequency analysis showed that the fundamental vertical frequencies of the entire roof and the individual components ranged from 8.6 Hz to over 40 Hz, well above the dominant frequencies in natural wind flows that are in the range of 0 to 1 Hz. The magnitudes of model frequencies strongly suggest that the roof of a LWFS will not be excited near resonance by the wind. As a result, the hypothesis that dynamic wind loading on the roof causes different structural load paths to occur is rejected. The dynamic analysis using loading frequencies less than 1 Hz showed that the static influence coefficients were equal to those derived from the dynamic loads. The

frequency response functions showed no gain in the connection loads when the applied load had a frequency less than 1 Hz. Therefore, dynamic loading on wood-framed roofs is not important, and the concept of using quasi-static loading is validated. It is believed that more flexible roofing systems, like standing seam metal roofing, may be more easily excited by natural wind loading since its natural frequency may be lower than for the stiff LFWS system and start to approach the frequencies observed in natural winds. The fundamental frequency of this system is unknown but further investigation might be warranted.

CHAPTER 7
CONCLUSIONS AND RECOMMENDATIONS

Summary

The research presented in this dissertation focuses on understanding the fundamental structural load paths in residential, low-rise, light-framed, wood construction. Through the use of an instrumented 1/3-scale structural model and analytical models of a rectangular, gable-roofed building various aspects of the structural load paths were considered. Influence coefficients (and ultimately 3D influence surfaces) were developed for uplift wind loads for various roof-to-wall and wall-to-foundation connections. These static influence surfaces were then combined with wind tunnel generated pressure coefficients using a database-assisted design (DAD) framework to develop connection (or reaction) time histories due to wind loading. The DAD method was validated by subjecting the 1/3-scale structure to winds generated by a wind generator at the University of Florida and simultaneously measuring roof and wall pressures along with connection forces.

The DAD method was compared against two previously developed methods for determining the mean and peak connection loads that can then be used in design – namely the covariance integration (CI) and load-response-correlation (LRC) methods. These two methods predict the mean loads within 2% of the DAD derived mean loads. However, the CI and LRC methods tend to predict lower peak loads than the DAD method. Both the CI and LRC methods assume the connection time histories are normally distributed, when in fact they are non-Gaussian and are more similar to a reverse lognormal distribution.

A critical (and unexpected) finding is that the ASCE 7-05 method to calculate truss reaction loads (i.e., the main wind force resisting system – MWFRS) significantly underestimates the actual peak forces experienced by the truss-to-wall connections. However, it was shown that the components and cladding (C&C) approach provides a reasonable estimation of the peak connection loads for interior trusses. This study concludes that the design of truss-to-wall connections in LFWS should follow the C&C design procedure and not the MWFRS procedure but that one needs to use caution in selecting the effective wind area (EWA) for designing with the C&C provisions. Additionally, the Wood Frame Construction Manual (WFCM) provides a conservative estimation of the wall-to-foundation loads.

A finite element (FE) model of a full-scale, wood-framed roof was developed to investigate the effects of dynamic loading on the roof. After validating the FE model by comparing reactions from experimental data and from previous research, a fundamental frequency analysis of the FE model was performed. It was found that the vertical natural frequencies of vibration for the entire roof as well as individual components are well above the dominant fundamental frequencies of natural wind, and so low-frequency dynamic winds do not produce dynamic amplification in the structure. The study confirms that static influence coefficients can be used along with the DAD method to predict the dynamic nature of various inter-component connection forces.

Limitations of this Study

Several limitations and cautions are provided below for this study.

- Only a simple, rectangular, gable roof building was investigated. Extrapolating some of the conclusions to more complicated building models and roof geometries is cautioned.

- The test building lacks window or door openings in the exterior walls which will alter some of the structural load paths (Martin 2010).

- The sheathing to framing connections (i.e., nails) were overly designed (using screws) to prevent premature pullout failure of the connection due to the applied point loads.

- The structure was only loaded in the linear elastic range, and therefore any inferences about failure modes are unwarranted.

- No internal walls or gypsum board sheathing was used which contribute to additional load sharing and distribution, further altering load paths through the structure.

Conclusions

Several conclusions can be drawn from this research on structural load paths in low-rise, wood-frame structures using a simple, rectangular, gable roof building.

Scaled Wood-Framed Structures

- A geometrically-similar 1/3-scale wood-framed structure can be used to determine/evaluate the load paths of a full-scale light-frame, wood structure (LFWS).

Influence Coefficients

- Static influence coefficients (and subsequent influence surfaces) capture the load path (distribution) on wood-framed roofs loaded by wind.

- The direction of loading (i.e., upward or downward) on a wood-framed roof has little effect on the influence coefficients and subsequently on the load paths.

- The principle of superposition is valid for loading a roof within the linear-elastic range of the materials.

- The effect of load magnitude on the influence coefficients and load paths is minimal within the linear-elastic range of the materials.

Load Paths

- Due to the stiffness provided by the attached sheathing, the gable end truss carries more load than the other roof trusses regardless of how it is connected to the walls (i.e., only at the truss end reactions or additionally at intermediate points with the gable end wall). When intermediate truss-to-end wall connections are present along the bottom chord of the gable end truss, the uplift loads on the gable end truss reactions are reduced significantly (up to 60%). The significance of this

finding is that smaller truss-to-wall connectors could be used resulting in a lower cost of construction, as long as the intermediate connectors are capable of resisting uplift forces.

- The gable end wall has higher influence coefficients than the side wall at the wall-to-foundation connections, corresponding to higher loads in the end wall regardless of whether intermediate connections exist between the bottom of the gable truss and the top of the end wall.

Database-Assisted Design (DAD)

- The database-assisted design (DAD) methodology appears to be applicable to wood-framed structures for determining structural load paths, as it provided reasonable agreement between measured connection loads and DAD-derived connection loads on the 1/3-scale building.

- The covariance integration (CI) and load-response-correlation (LRC) methods can accurately predict the mean structural loads in inter-component connections. In contrast, neither method adequately predicts the peak connection loads due to the fact that they both incorrectly assume that the reaction time histories are normally distributed. From the DAD method, results show that the roof-to-wall and wall-to-foundation connection time histories do not follow a normal distribution, rather the tail of the distributions is much longer that the normal distribution effectively pushing the peak connection loads to higher values. The CI and LRC methods need to be refined to include non-Gaussian structural response load distributions. The application of the CI and LRC methods will be limited for most structures (including LFWS and steel, portal-framed buildings) until this can be achieved.

- A distinct advantage of the CI and LRC methods is that they require substantially reduced data storage by two orders of magnitude (i.e., 20 GB for the DAD vs. 100-200 MB for the CI and LRC methods) leading to reduced computational time and computer power. This reduction is possible because the CI and LRC methods use post-processed wind tunnel data (including mean, standard deviations, RMS, and cross-correlations of pressure coefficients) rather than the need for wind tunnel time histories.

Dynamic Loading

- A wood-framed roof and its components all appear to have natural frequencies of vibration well above the dominant frequencies found in natural winds, even extreme hurricane winds, so resonance of the structure and dynamic amplification are not possibilities. Therefore, the quasi-steady theory used for determining design loads on low-rise LFWS seems to be valid, and static influence coefficients can be used to accurately predict the load paths and dynamic connection load time histories.

Design Provisions

- For low-rise buildings, the ASCE 7-05 main wind force resisting system (MWFRS) loads can be calculated using either the low-rise or all heights method which yield drastically different roof-to-wall design loads for the building used in this study. In fact, the all heights method produces design loads that are up to 44% lower than the low-rise method for the same connections.

- The design loads for truss-to-wall connections developed using ASCE 7-05 MWFRS loads (using both the low-rise and all heights methods) underestimate the peak connection loads as determined by the DAD methodology. The DAD-predicted results show better agreement with ASCE 7-05 component and cladding (C&C) loads for roof-to-wall connections, although for some connections the C&C design loads still underestimate the DAD-derived peak reaction loads. Further studies with additional wind directions and different building shapes are needed to provide a more reliable data set than this simple rectangular, gable roof building.

- When the effective wind area (EWA) definition for ASCE 7-05 C&C loading (i.e., $L^2/3$) is used for calculating roof truss reactions, the design values are non-conservative. However, when using the maximum C&C external pressure coefficients (i.e., smallest EWA), the C&C design loads still underestimate some interior connection loads by as much as 19% while overestimating the gable end truss reactions by 25%. Therefore, this research suggests that the EWA definition in ASCE 7 is non-conservative and risk inconsistent.

- The design uplift loads prescribed in the *Wood Frame Construction Manual* (WFCM) appear to adequately capture the peak loads at wall-to-foundation connections as estimated using the DAD methodology. However, the WFCM methodologies for roof-to-wall connections seem to closely match the ASCE 7 MWFRS loads.

- The risk inconsistencies in ASCE 7-05 and the WFCM most likely derive from inappropriate structural influence coefficients (i.e., incorrect load path) that were assumed in determining the external pressure coefficients in ASCE 7-05. The influence coefficients for light-frame, wood structures presented in this study are starkly different from those used to develop the design pressure coefficients in ASCE 7-05, which utilized a steel, portal frame. This is another example of the risk inconsistency in ASCE 7.

Recommendations for Future Work

Based on the research performed, several areas for improving upon and extending this work are presented.

- The evaluation of influence coefficients at incremental failure steps (e.g., removal of one or more roof sheathing panels) should be performed to investigate how the

post-failure structural load paths may change in the remaining intact structure. An important part of that study would be to conduct tests on a full-scale structure which would provide realistic behavior of the full-scale failure mechanisms.

- The effect of wall and door openings on structural load paths should be investigated. This initial model was a simplified rectangular shape without openings. The effect of jack trusses and door beams to collect and distribute loads can have significant impact in concentrating the wall-to-foundation loads. Additionally, the next step of the investigation should also evaluate the effect of geometrically complex roof shapes, such as intersecting gables and hips. The results have shown that significant variation in truss stiffness affects load paths, with stiffer elements attracting a greater proportion of the load. Potentially such real structural variations can cause further increases in connection loads than is shown for the simple structure.

- Combined loading on the gable end truss should be investigated in a future study as this study focused on vertical uplift loads. The combined effect of lateral wind loading and the roof overhang pressures on the gable end truss, in conjunction with the roof loads, may increase the loads on its connections.

- A design guide for the intermediate connections between the bottom chords of the gable end truss and the end wall for uplift loads should be developed. Currently, no such guideline exists, and with significant load transfer through these connections, recommendations are needed. There are existing guidelines to provide out-of-plane bracing for the lateral loads (IBHS 2010) which may be useful in developing uplift resistance recommendations.

- A logical extension of this influence surface study will be to investigate the structural load paths in a single roof panel. By studying the influence surfaces for nail withdrawal it may yield new knowledge on the load sharing capability of sheathing. Sheathing failure contributes to extensive progressive failures of roof systems and subsequent water ingress. Structural models of these systems, which comprise the overwhelming majority of existing residential roofs, will be helpful in retrofitting existing roofs and designing better new roofs.

- More analysis (i.e., data) is needed in order to compare the ASCE 7-05 design values for roof-to-wall connections. Instrumented wood-framed structures are needed to provide actual time histories of the connection forces experienced during extreme wind events. With a sufficiently large database of actual recorded structural forces, the risk inconsistencies in the wind load standards can be addressed. Additionally, the data from instrumented full-scale structures will provide indisputable validation of the DAD methodology providing a robust manner to evaluate the structural load paths and connection forces in any structural system.

- An investigation is needed to determine the appropriate effective wind area (EWA) for use with the components and cladding (C&C). The current use of the square of

the span divided by three (i.e., $L^2/3$) for the EWA has no engineering basis. Developing an appropriate EWA could help to mitigate some of the damages experienced in extreme wind events.

- Since the external pressure coefficients (GC_p) provided in ASCE 7-05 are weighted with influence coefficients developed for steel, portal frames spaced 25 ft apart (Figure 2-2), validation of the GC_p values is needed for stick-built, wood construction with starkly different influence coefficients (e.g., Figure 4-7). This can be accomplished by combining the influence coefficients for the roof-to-wall connections with the wind tunnel-derived pressure coefficients to provide weighted (or "pseudo") pressure coefficients and then comparing with those in ASCE 7-05. Verifying that the GC_p values in ASCE 7-05 are valid for typical LFWS is an important step towards providing risk consistent wind design standards.

- Due to the high fundamental frequencies of wood roofs, dynamic influence coefficients do not provide any insight into the load distribution from wind loads. However, their application in seismic loading should be explored. Since the fundamental frequencies of wood structures fall within the typical dominant frequencies in earthquakes, dynamic influence functions could provide insight into load paths excited during a seismic event. The application of the DAD methodology using dynamic influence functions to seismic loading has the potential to be a valuable tool in the movement towards performance-based design.

APPENDIX A
EXAMPLE OF LOAD CELL CHECK IN 1/3-SCALE BUILDING

A check of the load cells was performed to ensure that the applied load was adequately being recorded by the load cells installed in the 1/3-scale building. A contour plot is shown in Chapter 3 of the summation of the normalized loads. This section will detail the calculation of one of these points for both the roof-to-wall connections and the wall-to-foundation connections. The load point is located near the gable end corner where the load cells are concentrated. Therefore, most of the load, if not all of it, should be recorded by the installed load cells and not be spread to connections were load cells were not installed.

Figure A-1and Figure A-2 provide the load cell check for the roof-to-wall and wall-to-foundation connections, respectively. As can be seen, the roof-to-wall connections capture nearly the entire vertical load (97%) applied to the roof. The wall-to-foundation connections do not capture as much of the load (86%). However, this can be explained by the fact that the wall-to-foundation loads are spread out much more evenly as is shown the influence surface plots in Chapter 4. As such, it is reasonable that the wall-to-foundation load cells installed would not capture as much of the load as the roof-to-wall load cells. This check confirms that the installed load cells are working properly.

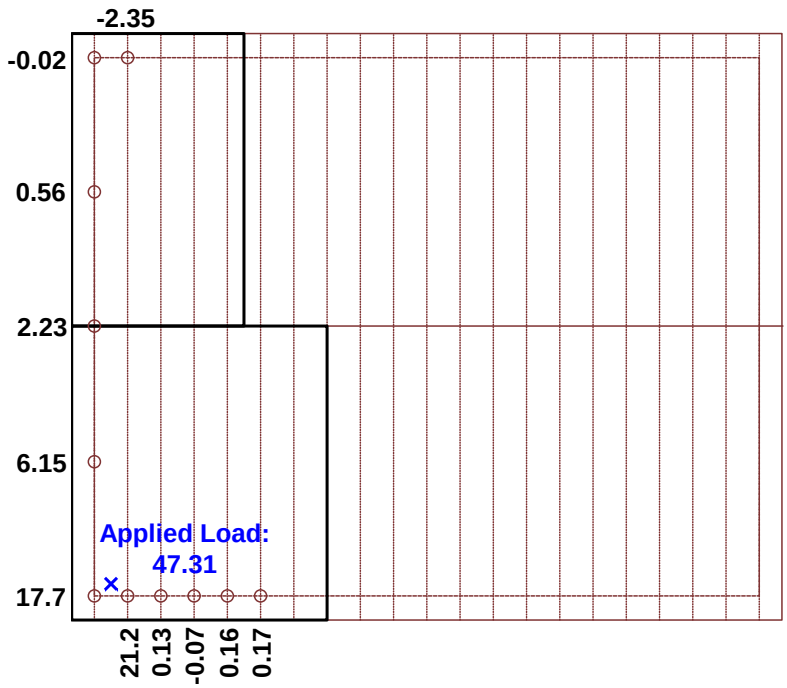

Load summation = 45.90 lbs

Applied load = 47.31 lbs

97% of applied load measured at roof-to-wall connections

Figure A-1. Roof-to-wall connection load cell check

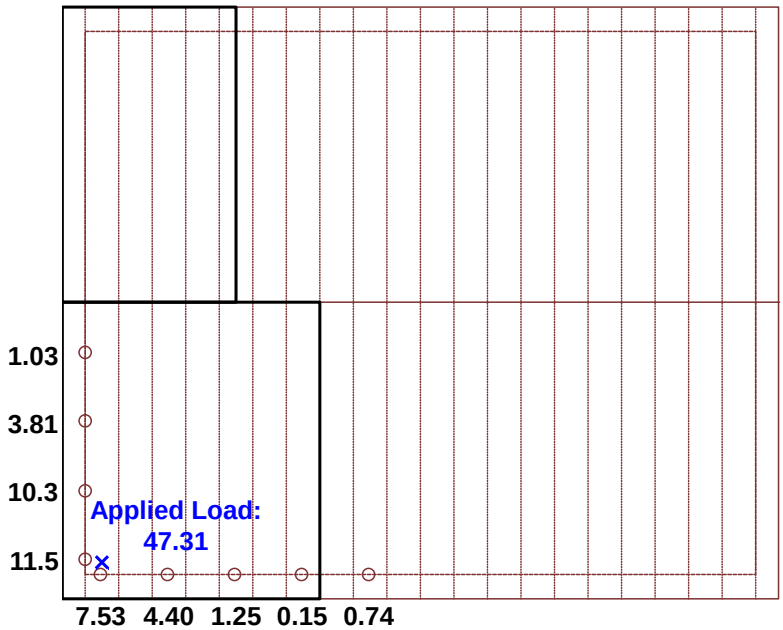

Load summation = 40.75 lbs

Applied load = 47.31 lbs

86% of applied load measured at wall-to-foundation connections

Figure A-2. Wall-to-foundation connection load cell check

APPENDIX B
INFLUENCE SURFACE PLOTS FOR ALL CONNECTIONS

The 3D influence surface plots presented in Chapter 4 are also contained in this appendix, where all of the instrumented connections are presented for both load case 1 and load case 2a. Figure B-1 shows the location of the connections for both of these cases. Figure B-3 and Figure B-4 provide the influence surfaces for Case 1 and Case 2a, respectively. Only the contours for a load magnitude of 50 lbs are shown as the surfaces are nearly identical for the other load tested (Chapter 4). The scale for the contour plots is provided in Figure B-2 with the contour spacing set at 0.1.

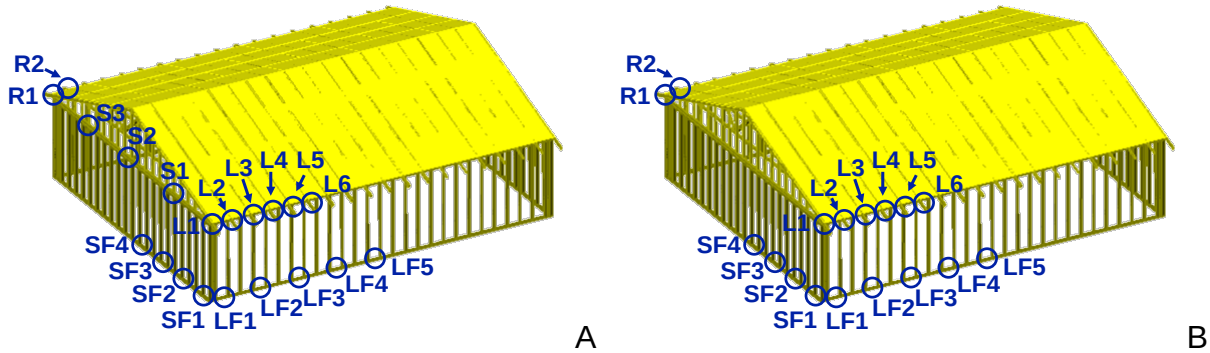

Figure B-1. Location of instrumented connections for A) Case 1 and B) Case 2a

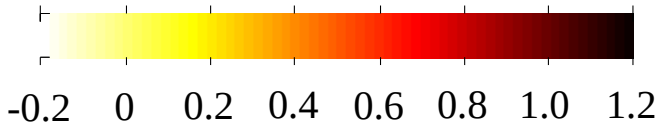

Figure B-2. Influence surfaces contour labels

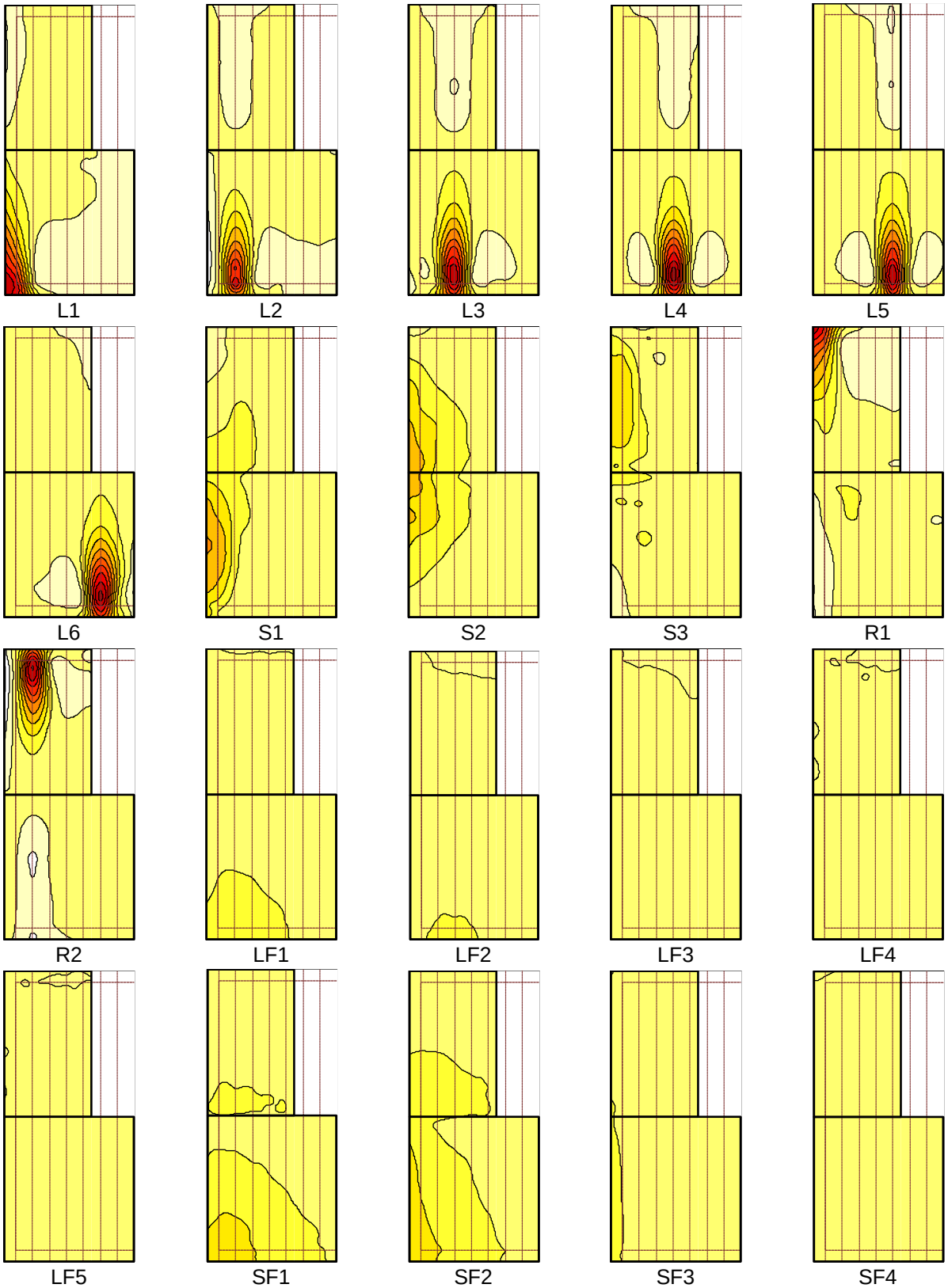

Figure B-3. Influence surfaces for Case 1

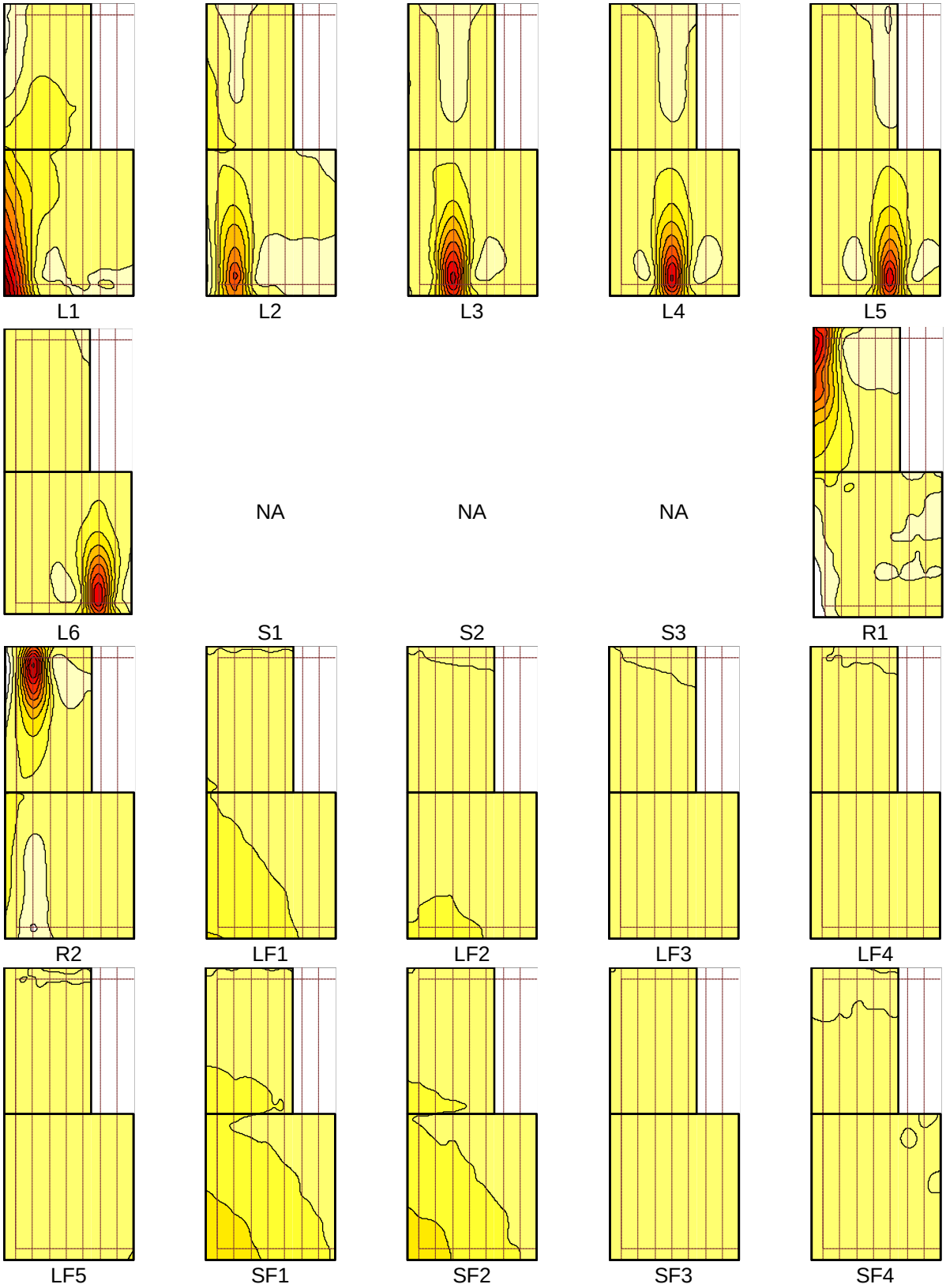

Figure B-4. Influence surfaces for Case 2a

APPENDIX C
TIME HISTORY PLOTS FOR DAD VALIDATION

The following figures provide the first 60 second time histories of the measured versus DAD-estimated truss reaction loads at connections L1, L2, and L3. The time histories include the soffit pressures measured with wall taps (Chapter 4).

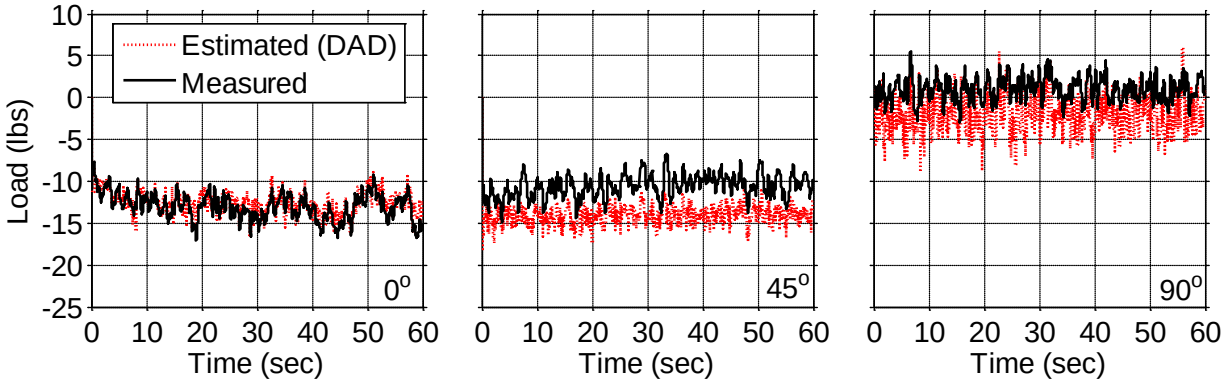

Figure C-1. 60-second time histories of total vertical load at L1 on the 1/3-scale building

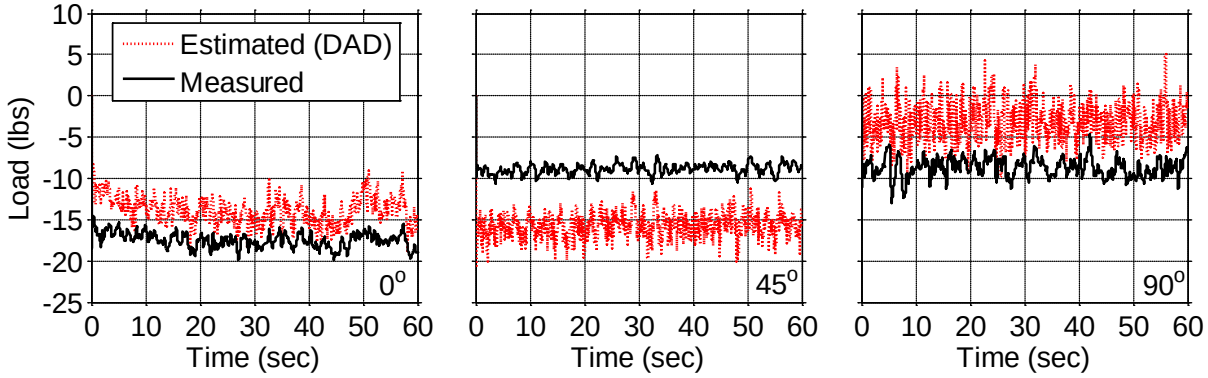

Figure C-2. 60-second time histories of total vertical load at L2 on the 1/3-scale building

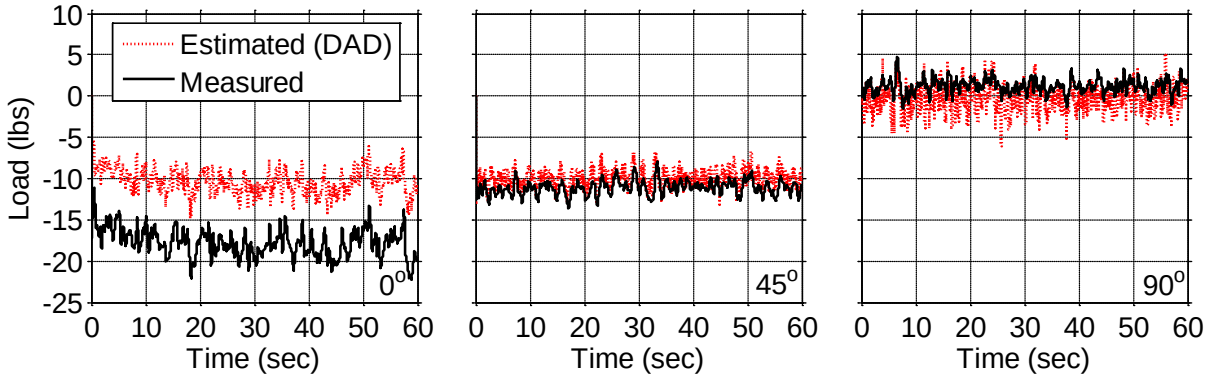

Figure C-3. 60-second time histories of total vertical load at L3 on the 1/3-scale building

APPENDIX D
COMPARISON OF DAD WITH CI AND LRC METHODS

Chapter 4 provides comparison figures between the estimated peak connection loads for the DAD, CI, and LRC methods for Case 2a. This appendix provides the same figures for Case 1 as well as the tabulated data used to generate the figures. The same conclusions can be made for Case 1 as for Case 2a (Chapter 4).

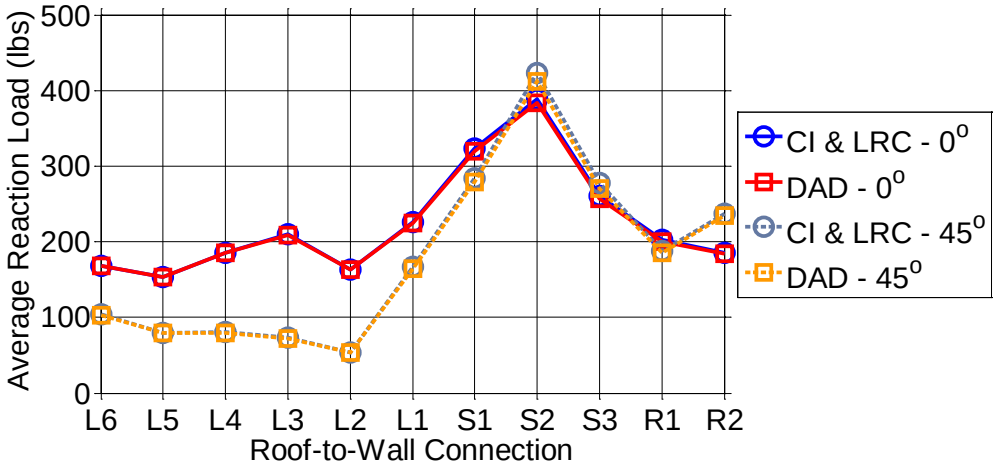

Figure D-1. Average full-scale roof-to-wall connection loads (Case 1)

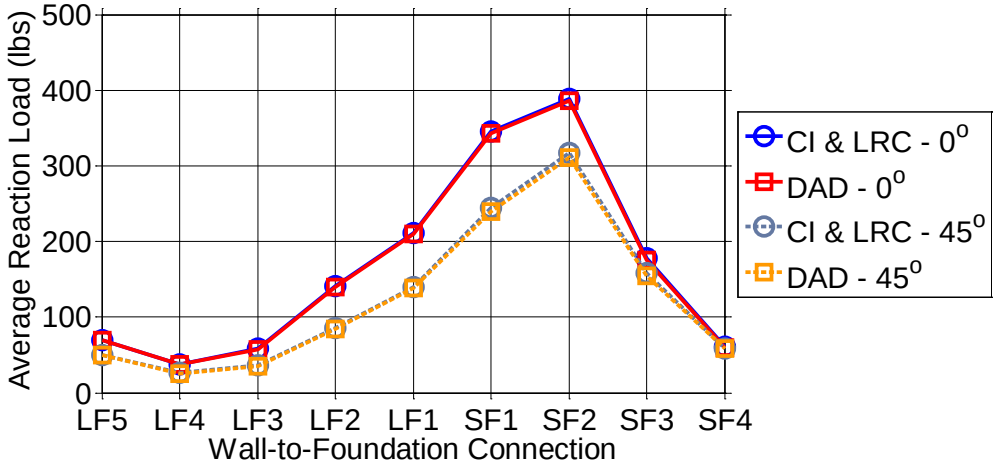

Figure D-2. Average full-scale wall-to-foundation connection loads (Case 1)

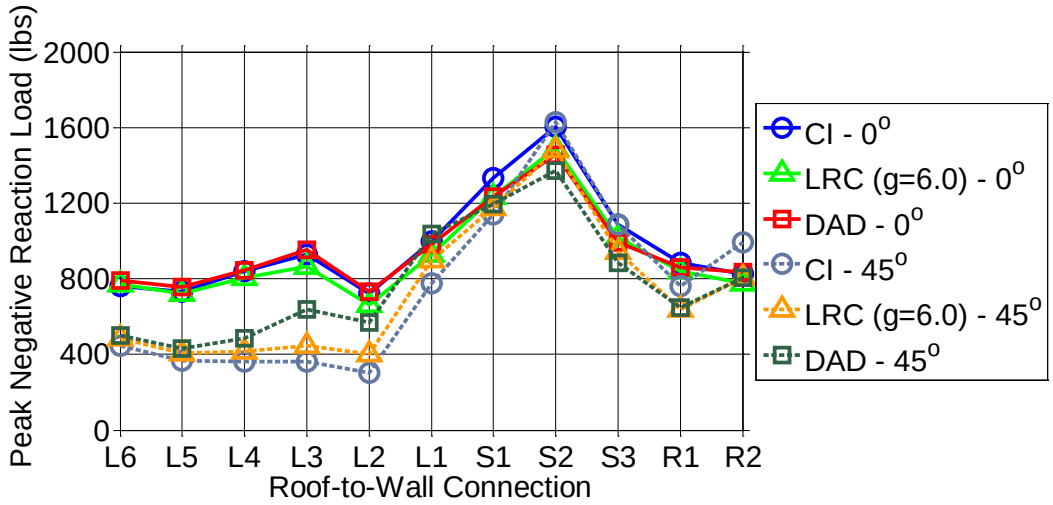

Figure D-3. Peak negative full-scale roof-to-wall loads with peak factor of 6.0 (Case 1)

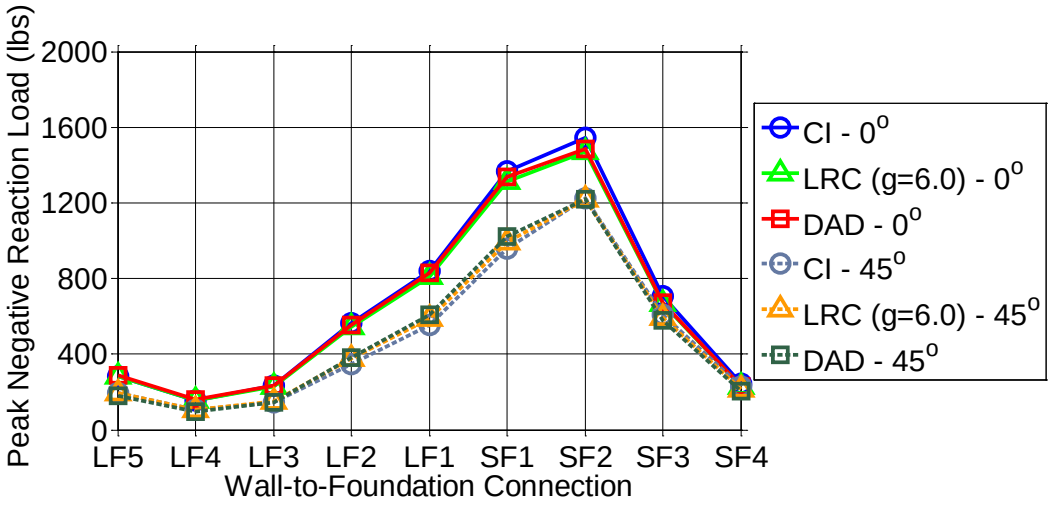

Figure D-4. Peak negative full-scale wall-to-foundation loads with peak factor of 6.0 (Case 1)

Table D-1. Comparison of DAD-derived full-scale connection loads with LRC and CI methods using a peak factor (GF) of 6.0 for Case 1

	DAD Average (lbs)		DAD Peak (lbs)		CI & LRC Average (lbs)		% Diff with DAD		CI Peak (lbs)		% Diff with DAD		LRC Peak (lbs)		% Diff with DAD	
	0°	45°	0°	45°	0°	45°	0°	45°	0°	45°	0°	45°	0°	45°	0°	45°
L6	-168	-103	-793	-500	-168	-104	0.2	0.6	-759	-444	-4.3	-11.1	-772	-486	-2.7	-2.8
L5	-153	-79	-757	-431	-153	-80	0.3	1.0	-731	-365	-3.4	-15.2	-722	-405	-4.7	-6.1
L4	-185	-80	-847	-484	-186	-81	0.3	1.4	-840	-363	-0.8	-24.9	-804	-414	-5.1	-14.3
L3	-209	-72	-955	-636	-210	-73	0.2	1.3	-931	-360	-2.5	-43.4	-866	-447	-9.3	-29.7
L2	-164	-53	-733	-571	-164	-53	-0.1	-0.4	-724	-304	-1.2	-46.8	-662	-400	-9.7	-29.9
L1	-224	-164	-983	-1038	-226	-167	0.5	1.4	-999	-777	1.6	-25.1	-928	-899	-5.6	-13.5
S1	-320	-279	-1234	-1193	-323	-284	0.9	1.9	-1334	-1140	8.1	-4.4	-1233	-1177	0.0	-1.4
S2	-383	-412	-1458	-1372	-389	-423	1.5	2.5	-1603	-1630	9.9	18.8	-1491	-1483	2.3	8.1
S3	-256	-270	-995	-886	-261	-278	1.7	2.9	-1084	-1087	9.0	22.7	-1017	-946	2.3	6.7
R1	-200	-185	-861	-650	-202	-188	0.8	1.7	-886	-763	2.9	17.5	-840	-636	-2.5	-2.1
R2	-184	-234	-833	-804	-185	-237	0.8	1.1	-826	-995	-0.9	23.8	-777	-806	-6.7	0.2
LF4	-37	-26	-161	-98	-37	-26	0.1	0.4	-156	-104	-2.7	5.3	-157	-105	-1.9	6.5
LF3	-58	-36	-232	-147	-58	-36	0.4	1.2	-235	-143	1.5	-2.8	-230	-152	-0.7	3.3
LF2	-140	-85	-553	-382	-141	-86	0.5	1.4	-563	-345	1.8	-9.6	-544	-375	-1.6	-1.7
LF1	-210	-138	-828	-607	-212	-140	0.6	1.6	-841	-555	1.5	-8.6	-809	-590	-2.4	-2.9
SF1	-343	-240	-1340	-1021	-345	-244	0.7	1.8	-1367	-956	2.1	-6.4	-1312	-995	-2.1	-2.6
SF2	-386	-311	-1484	-1218	-389	-317	0.9	1.9	-1543	-1226	4.0	0.6	-1470	-1219	-0.9	0.1
SF3	-176	-155	-671	-579	-178	-158	1.0	2.0	-708	-609	5.5	5.2	-670	-593	-0.2	2.4
SF4	-60	-58	-227	-204	-61	-59	0.9	1.8	-245	-227	7.6	11.0	-230	-216	1.0	5.7
						Avg.	0.6%	1.4%		Avg.	1.9%	-4.2%		Avg.	-2.6%	-3.3%

Table D-2. Comparison of DAD-derived full-scale connection loads with LRC and CI methods using a peak factor (GF) of 6.0 for Case 2a

	DAD		DAD		CI & LRC		% Diff with		CI		% Diff with		LRC		% Diff with	
	Average (lbs)		Peak (lbs)		Average (lbs)		DAD		Peak (lbs)		DAD		Peak (lbs)		DAD	
	0°	45°	0°	45°	0°	45°	0°	45°	0°	45°	0°	45°	0°	45°	0°	45°
L6	-143	-111	-657	-453	-144	-113	0.5	1.3	-643	-469	-2.2	3.6	-621	-431	-5.5	-5.0
L5	-197	-123	-885	-516	-198	-125	0.5	1.4	-878	-516	-0.9	0.0	-858	-530	-3.1	2.7
L4	-250	-149	-1061	-647	-252	-152	0.6	1.8	-1070	-605	0.9	-6.6	-1023	-623	-3.5	-3.8
L3	-288	-150	-1232	-838	-289	-152	0.5	1.9	-1221	-627	-0.9	-25.3	-1145	-684	-7.1	-18.5
L2	-272	-187	-1110	-907	-274	-190	0.7	1.8	-1132	-760	2.0	-16.2	-1050	-789	-5.3	-13.0
L1	-437	-324	-1707	-1708	-440	-329	0.6	1.6	-1835	-1413	7.5	-17.3	-1708	-1572	0.1	-8.0
R1	-309	-344	-1318	-1192	-313	-352	1.3	2.2	-1379	-1430	4.6	20.0	-1293	-1194	-1.9	0.2
R2	-286	-326	-1175	-1077	-288	-331	0.9	1.4	-1194	-1328	1.7	23.4	-1129	-1123	-3.9	4.3
LF5	-94	-66	-377	-244	-94	-66	0.4	1.0	-380	-259	0.7	5.9	-375	-264	-0.7	8.1
LF4	-50	-35	-206	-128	-50	-35	0.3	0.9	-204	-137	-0.8	6.9	-203	-140	-1.3	9.1
LF3	-80	-53	-314	-215	-80	-54	0.5	1.4	-322	-210	2.7	-1.9	-313	-221	-0.3	2.8
LF2	-186	-123	-726	-528	-187	-125	0.5	1.4	-749	-494	3.2	-6.4	-720	-523	-0.9	-0.9
LF1	-285	-201	-1106	-851	-287	-205	0.6	1.6	-1141	-802	3.2	-5.7	-1092	-833	-1.3	-2.1
SF1	-388	-275	-1506	-1160	-391	-280	0.7	1.8	-1551	-1095	3.0	-5.6	-1486	-1136	-1.3	-2.1
SF2	-346	-243	-1344	-1033	-348	-247	0.6	1.7	-1382	-970	2.8	-6.1	-1323	-1009	-1.5	-2.3
SF3	-101	-73	-393	-304	-102	-74	0.7	1.7	-404	-290	2.6	-4.8	-386	-299	-1.7	-2.0
SF4	-13	-10	-52	-42	-13	-11	0.9	2.0	-54	-42	3.3	-0.2	-51	-42	-2.0	-0.3
						Avg.	0.6	1.6		Avg.	2.0	-2.1		Avg.	-2.4	-1.8

Table D-3. Comparison of DAD-derived full-scale connection loads with LRC and CI methods using calculated peak factors (GF) using the Kasperski method for Case 1

	DAD		DAD		CI & LRC		% Diff with		CI		% Diff with		LRC		% Diff with	
	Average (lbs)		Peak (lbs)		Average (lbs)		DAD		Peak (lbs)		DAD		Peak (lbs)		DAD	
	0°	45°	0°	45°	0°	45°	0°	45°	0°	45°	0°	45°	0°	45°	0°	45°
L6	-168	-103	-793	-500	-168	-104	0.2	0.6	-759	-444	-4.3	-11.1	-737	-409	-7.0	-18.1
L5	-153	-79	-757	-431	-153	-80	0.3	1.0	-731	-365	-3.4	-15.2	-731	-344	-3.5	-20.1
L4	-185	-80	-847	-484	-186	-81	0.3	1.4	-840	-363	-0.8	-24.9	-815	-421	-3.8	-12.9
L3	-209	-72	-955	-636	-210	-73	0.2	1.3	-931	-360	-2.5	-43.4	-872	-570	-8.7	-10.4
L2	-164	-53	-733	-571	-164	-53	-0.1	-0.4	-724	-304	-1.2	-46.8	-664	-523	-9.4	-8.5
L1	-69	-50	-983	-1038	-226	-167	0.5	1.4	-999	-777	1.6	-25.1	-896	-988	-8.9	-4.9
S1	-37	-26	-1234	-1193	-323	-284	0.9	1.9	-1334	-1140	8.1	-4.4	-1148	-1132	-7.0	-5.1
S2	-58	-36	-1458	-1372	-389	-423	1.5	2.5	-1603	-1630	9.9	18.8	-1392	-1266	-4.5	-7.7
S3	-140	-85	-995	-886	-261	-278	1.7	2.9	-1084	-1087	9.0	22.7	-953	-823	-4.2	-7.2
R1	-210	-138	-861	-650	-202	-188	0.8	1.7	-886	-763	2.9	17.5	-806	-585	-6.4	-9.9
R2	-343	-240	-833	-804	-185	-237	0.8	1.1	-826	-995	-0.9	23.8	-783	-726	-6.0	-9.6
LF4	-386	-311	-161	-98	-37	-26	0.1	0.4	-156	-104	-2.7	5.3	-272	-162	-4.7	-9.8
LF3	-176	-155	-232	-147	-58	-36	0.4	1.2	-235	-143	1.5	-2.8	-151	-86	-5.9	-12.8
LF2	-60	-58	-553	-382	-141	-86	0.5	1.4	-563	-345	1.8	-9.6	-221	-135	-4.7	-8.3
LF1	-224	-164	-828	-607	-212	-140	0.6	1.6	-841	-555	1.5	-8.6	-517	-355	-6.6	-6.9
SF1	-320	-279	-1340	-1021	-345	-244	0.7	1.8	-1367	-956	2.1	-6.4	-770	-571	-7.1	-6.0
SF2	-383	-412	-1484	-1218	-389	-317	0.9	1.9	-1543	-1226	4.0	0.6	-1247	-962	-6.9	-5.8
SF3	-256	-270	-671	-579	-178	-158	1.0	2.0	-708	-609	5.5	5.2	-1388	-1149	-6.4	-5.7
SF4	-200	-185	-227	-204	-61	-59	0.9	1.8	-245	-227	7.6	11.0	-630	-543	-6.1	-6.1
						Avg.	0.6%	1.4%		Avg.	1.9%	-4.2%		Avg.	-6.2%	-9.1%

Table D-4. Comparison of DAD-derived full-scale connection loads with LRC and CI methods using calculated peak factors (GF) using the Kasperski method for Case 2a

	DAD		DAD		CI & LRC		% Diff with		CI		% Diff with		LRC		% Diff with	
	Average (lbs)		Peak (lbs)		Average (lbs)		DAD		Peak (lbs)		DAD		Peak (lbs)		DAD	
	0°	45°	0°	45°	0°	45°	0°	45°	0°	45°	0°	45°	0°	45°	0°	45°
L6	-143	-111	-657	-453	-144	-113	0.5	1.3	-643	-469	-2.2	3.6	-605	-375	-7.9	-17.2
L5	-197	-123	-885	-516	-198	-125	0.5	1.4	-878	-516	-0.9	0.0	-838	-434	-5.4	-15.9
L4	-250	-149	-1061	-647	-252	-152	0.6	1.8	-1070	-605	0.9	-6.6	-1020	-583	-3.8	-9.9
L3	-288	-150	-1232	-838	-289	-152	0.5	1.9	-1221	-627	-0.9	-25.3	-1125	-759	-8.7	-9.5
L2	-272	-187	-1110	-907	-274	-190	0.7	1.8	-1132	-760	2.0	-16.2	-1017	-850	-8.3	-6.3
L1	-437	-324	-1707	-1708	-440	-329	0.6	1.6	-1835	-1413	7.5	-17.3	-1549	-1628	-9.2	-4.7
R1	-309	-344	-1318	-1192	-313	-352	1.3	2.2	-1379	-1430	4.6	20.0	-1223	-1093	-7.2	-8.3
R2	-286	-326	-1175	-1077	-288	-331	0.9	1.4	-1194	-1328	1.7	23.4	-1096	-983	-6.6	-8.7
LF5	-94	-66	-377	-244	-94	-66	0.4	1.0	-380	-259	0.7	5.9	-364	-224	-3.5	-8.2
LF4	-50	-35	-206	-128	-50	-35	0.3	0.9	-204	-137	-0.8	6.9	-196	-115	-4.9	-10.3
LF3	-80	-53	-314	-215	-80	-54	0.5	1.4	-322	-210	2.7	-1.9	-298	-200	-5.0	-6.9
LF2	-186	-123	-726	-528	-187	-125	0.5	1.4	-749	-494	3.2	-6.4	-680	-497	-6.4	-6.0
LF1	-285	-201	-1106	-851	-287	-205	0.6	1.6	-1141	-802	3.2	-5.7	-1033	-804	-6.6	-5.6
SF1	-388	-275	-1506	-1160	-391	-280	0.7	1.8	-1551	-1095	3.0	-5.6	-1408	-1095	-6.5	-5.6
SF2	-346	-243	-1344	-1033	-348	-247	0.6	1.7	-1382	-970	2.8	-6.1	-1254	-975	-6.7	-5.6
SF3	-101	-73	-393	-304	-102	-74	0.7	1.7	-404	-290	2.6	-4.8	-366	-287	-6.8	-5.7
SF4	-13	-10	-52	-42	-13	-11	0.9	2.0	-54	-42	3.3	-0.2	-48	-39	-7.6	-5.8
						Avg.	0.6	1.6		Avg.	2.0	-2.1		Avg.	-6.5%	-8.2%

APPENDIX E
PEAK FACTOR CURVES OF CONNECTION LOAD TIME HISTORIES

The peak factors of the full-scale connection time histories are presented in Chapter 4. This appendix provides peak factor curves (similar to gust factor curves) for both Case 1 (with gable end intermediate connections) and Case 2a (without gable end intermediate connections). The peak factors reported in Chapter 4 are the instantaneous peak factors corresponding to an averaging time of 0.05 seconds in the peak factor curves presented here and in Table E-1 and Table E-2. Table E-3 provides the peak factors using the Kasperski (2007) model.

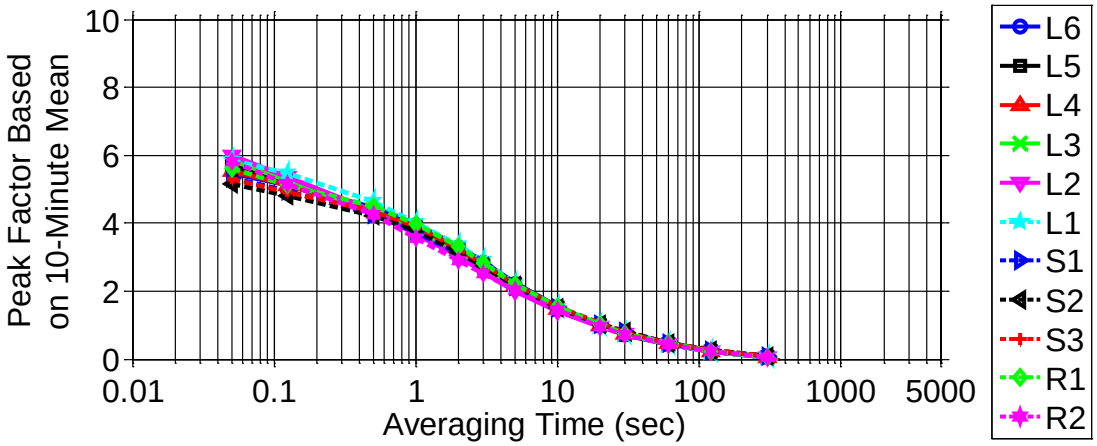

Figure E-1. Peak factors for full-scale reaction loads based on 10-min. mean (0° - Case 1 - with gable end intermediate connections)

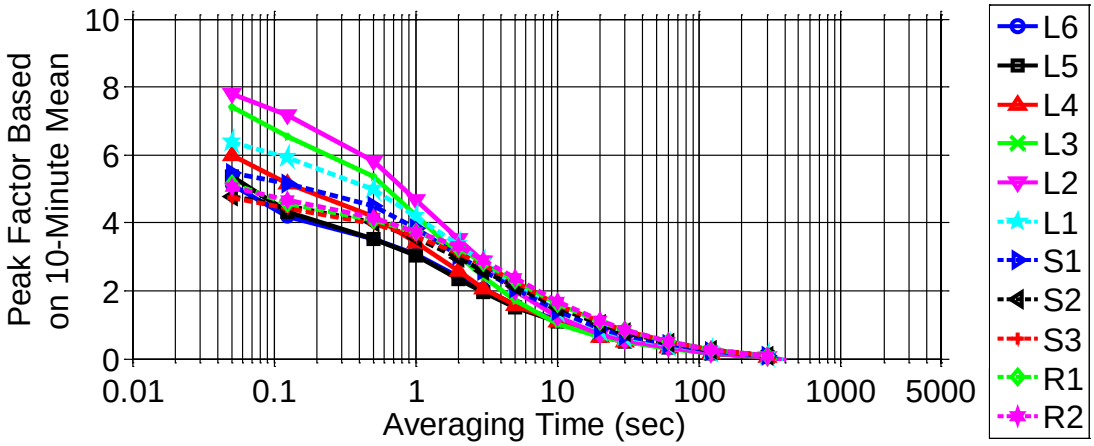

Figure E-2. Peak factors for full-scale reaction loads based on 10-min. mean (45° - Case 1 - with gable end intermediate connections)

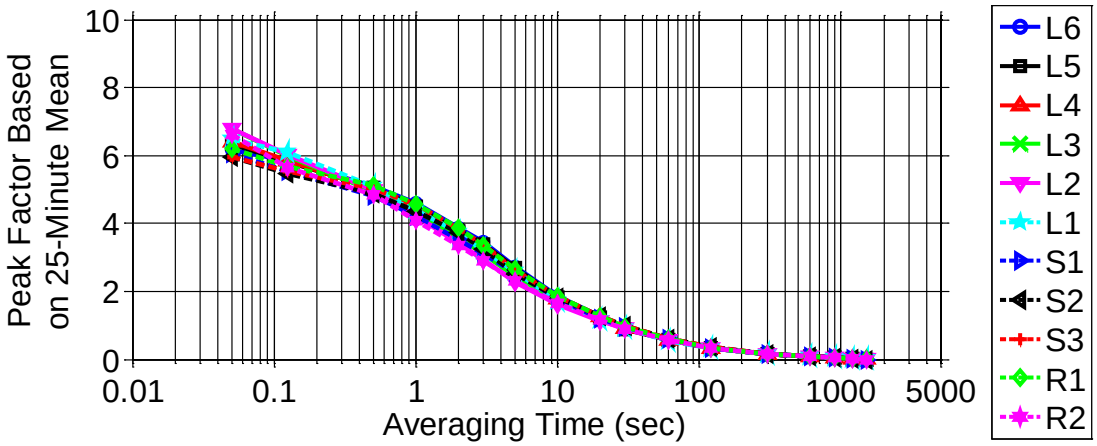

Figure E-3. Peak factors for full-scale reaction loads based on 25-min. mean (0° - Case 1- with gable end intermediate connections)

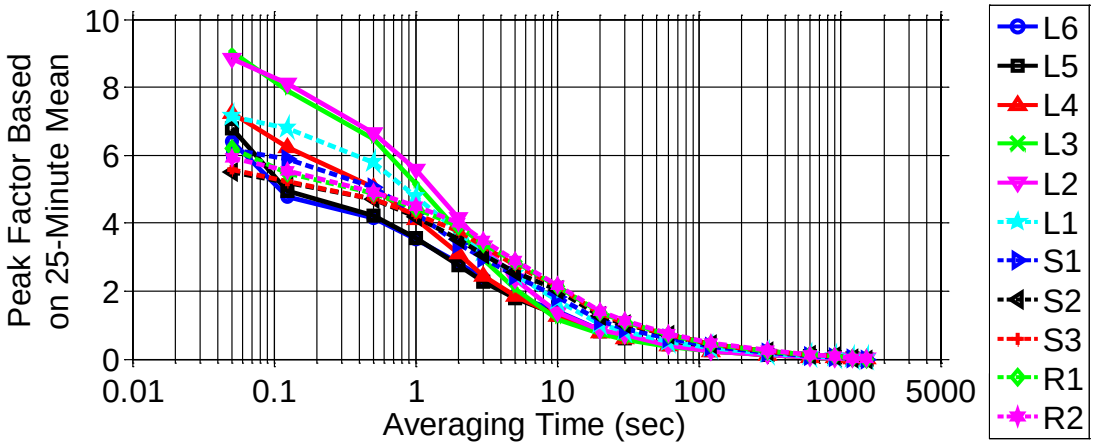

Figure E-4. Peak factors for full-scale reaction loads based on 25-min. mean (45° - Case 1- with gable end intermediate connections)

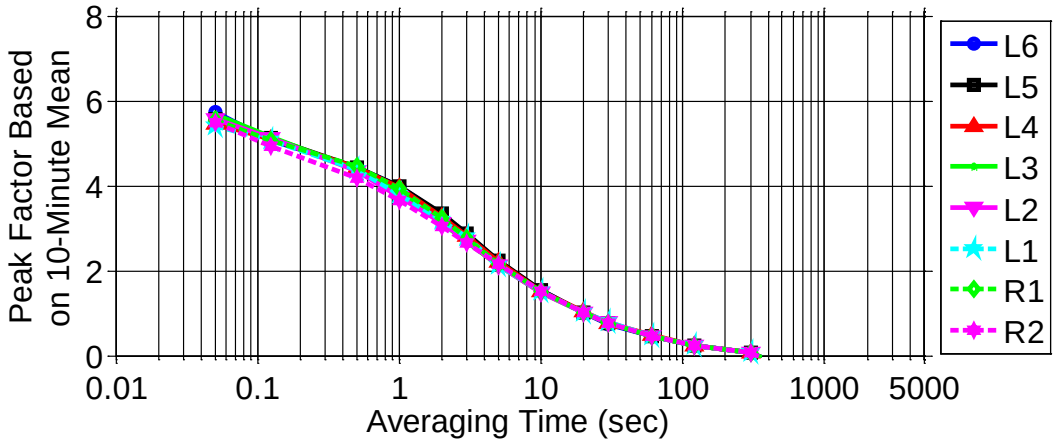

Figure E-5. Peak factors for full-scale reaction loads based on 10-min. mean (0° - Case 2a - without gable end intermediate connections)

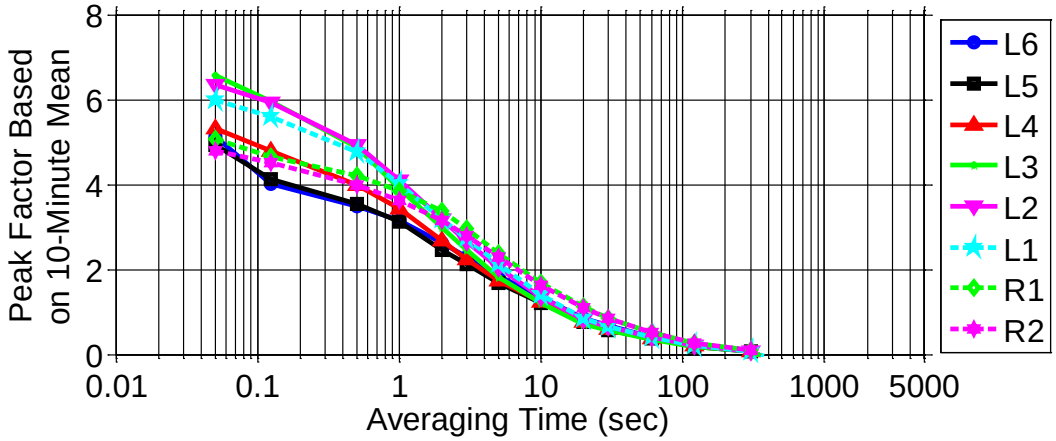

Figure E-6. Peak factors for full-scale reaction loads based on 10-min. mean (45° - Case 2a - without gable end intermediate connections)

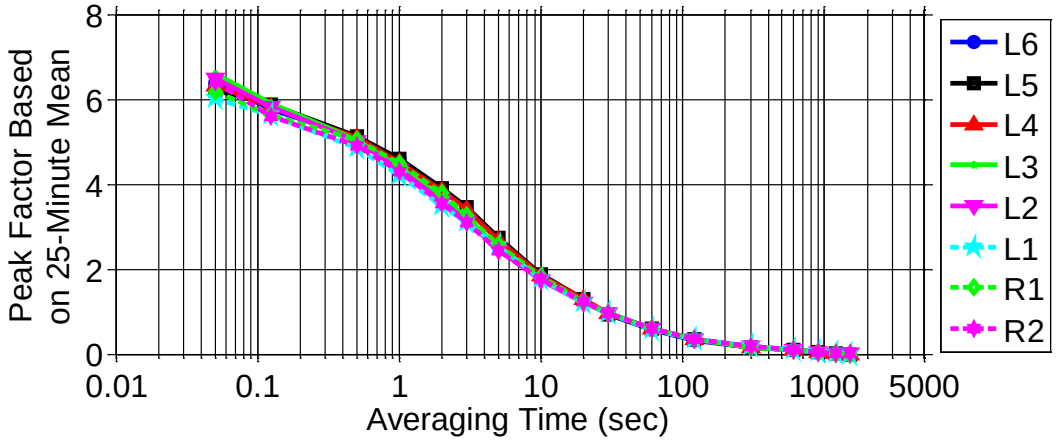

Figure E-7. Peak factors for full-scale reaction loads based on 25-min. mean (0° - Case 2a - without gable end intermediate connections)

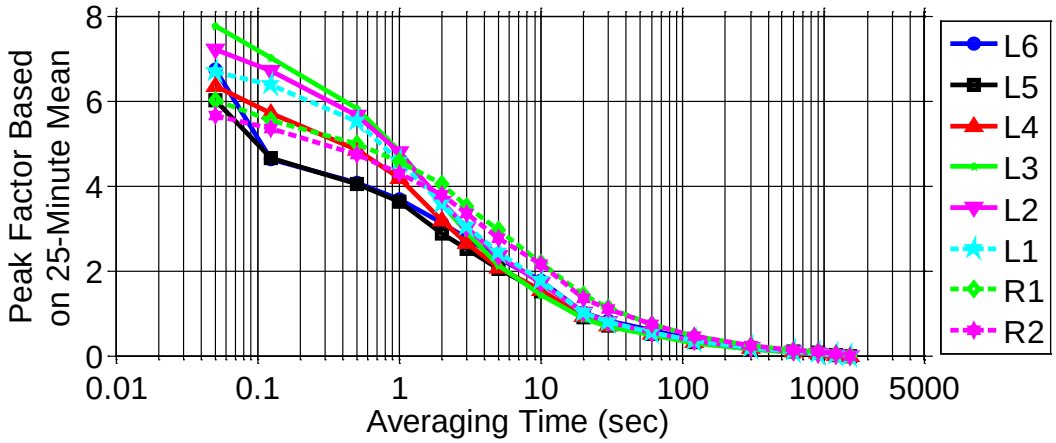

Figure E-8. Peak factors for full-scale reaction loads based on 25-min. mean (45° - Case 2a - without gable end intermediate connections)

Table E-1. Instantaneous peak factors for 10-minute full-scale record lengths

Connection	Case 1 (w/ gable connections)		Case 2a (w/o gable connections)	
	0°	45°	0°	45°
L6	5.47	5.11	5.73	5.14
L5	5.71	5.37	5.56	4.94
L4	5.54	5.99	5.46	5.33
L3	5.86	7.41	5.68	6.58
L2	5.98	7.80	5.57	6.35
L1	5.85	6.36	5.40	5.97
S1	5.33	5.47	--	--
S2	5.17	4.76	--	--
S3	5.29	4.74	--	--
R1	5.59	5.15	5.55	5.06
R2	5.80	5.05	5.47	4.80
LF5	5.27	4.67	5.24	4.77
LF4	5.33	4.79	5.27	4.68
LF3	5.25	5.06	5.21	5.13
LF2	5.27	5.48	5.24	5.42
LF1	5.27	5.57	5.23	5.46
SF1	5.24	5.51	5.23	5.46
SF2	5.20	5.29	5.23	5.48
SF3	5.17	5.17	5.23	5.44
SF4	5.15	5.00	5.30	5.38

Table E-2. Instantaneous peak factors for 25-minute full-scale record lengths

Connection	Case 1 (w/ gable connections)		Case 2a (w/o gable connections)	
	0°	45°	0°	45°
L6	6.15	6.40	6.41	6.74
L5	6.34	6.78	6.22	6.00
L4	6.39	7.24	6.31	6.34
L3	6.78	9.03	6.60	7.76
L2	6.80	8.83	6.47	7.21
L1	6.48	7.13	6.02	6.67
S1	6.05	6.16	--	--
S2	5.96	5.50	--	--
S3	5.96	5.59	--	--
R1	6.19	6.21	6.19	6.03
R2	6.62	5.93	6.39	5.65
LF5	6.07	5.31	6.08	5.38
LF4	6.10	5.55	6.09	5.33
LF3	6.08	5.74	6.06	5.79
LF2	6.14	6.13	6.10	6.08
LF1	6.20	6.24	6.13	6.18
SF1	6.19	6.23	6.14	6.18
SF2	6.12	6.04	6.15	6.20
SF3	6.08	5.87	6.17	6.17
SF4	5.99	5.64	6.19	6.05

Table E-3. Peak factors determined using the Kasperski method

Connection	Case 1 (w/ gable connections)		Case 2a (w/o gable connections)	
	0°	45°	0°	45°
L6	5.66	4.80	5.80	4.95
L5	6.09	4.88	5.82	4.57
L4	6.11	6.12	5.98	5.50
L3	6.05	7.97	5.86	6.85
L2	6.03	8.11	5.74	6.61
L1	5.73	6.73	5.25	6.27
S1	5.44	5.70	--	--
S2	5.46	4.78	--	--
S3	5.49	4.89	--	--
R1	5.68	5.32	5.57	5.29
R2	6.06	5.16	5.77	4.94
LF5	5.72	4.61	5.77	4.78
LF4	5.69	4.55	5.71	4.58
LF3	5.68	5.12	5.62	5.25
LF2	5.59	5.59	5.55	5.60
LF1	5.61	5.75	5.56	5.72
SF1	5.59	5.74	5.57	5.71
SF2	5.55	5.53	5.57	5.73
SF3	5.52	5.32	5.58	5.70
SF4	5.47	5.04	5.54	5.55

APPENDIX F
CALCULATION OF ASPHALT SHINGLE MASS FOR FE ANALYSIS

The addition of asphalt shingles and roofing on a wood-framed roof changes the mass of the system, which in turn changes its dynamic characteristics. The following describes the calculation procedure to add the mass of the roofing to the roof sheathing used in the FE analysis presented in Chapter 5.

The specific gravity of the OSB sheathing used in the FE analysis is 0.675 corresponding to a density of 0.02439 lbs/in.^{3}. Breyer et al. (2007) provide a typical value of asphalt shingles to be 2.0 psf and approximately 0.25 in. thick.

The density of shingles is:

$$\rho_s = \frac{2lbs/ft^2}{(144\ in.^2/ft^2)(0.25\ in.)} = 0.05556\frac{lbs}{in.^3}$$

Since the density of water is 0.03613 lbs/in.^{3}, the specific gravity of the shingles is:

$$SG = \frac{0.05556}{0.03613} = 1.54$$

Adding the unit weight per area of the shingles to that of the OSB, the combined unit weight is:

$$w_{combined} = (0.05556lbs/in.^3)(0.25in.) + (0.02439lbs/in.^3)(0.5in.) = 0.02609\frac{lbs}{in.^2}$$

The weighted specific gravity of the shingles with the OSB sheathing is:

$$SG_{weighted} = \frac{(0.02609lbs/in.^2)(1/0.5in.)}{0.03613lbs/in.^3} = 1.445$$

The mass density needed for input into the FE model is the combined density divided by gravity:

$$\rho_{m,combined} = \frac{(0.02609lbs/in.^2)(1/0.5in.)}{386.1in./s^2} = 1.3521 \times 10^{-4}\frac{lbs - s^2}{in.^4}$$

APPENDIX G
DETAILS OF FULL-SCALE WIND SPEED TIME HISTORY

The full-scale data used in Chapter 5 to illustrate the power spectral density of an actual wind speed time history was obtained by the Florida Coastal Monitoring Program (FCMP) during Hurricane Katrina in 2005 in Belle Chasse, Louisiana, at 33 ft elevation in open terrain. Figure G-1 shows the location of the tower (T1), and Figure G-2 provides an aerial photograph of the surrounding terrain. Table G-1 provides some of the specifics about the wind speed time history.

Table G-1. Hurricane Katrina tower T1 summary

Sampling Frequency (Hz)	10
Length of Record (sec)	900
Mean Longitudinal Wind Speed (mph)	67.8
Std of Longitudinal Wind Speed (mph)	10.8
Longitudinal Turbulence Intensity	0.16
Roughness Length Estimate (ft)	0.003
Correlation Time (sec)	6.57
Integral Length Scale, L_u^x (ft)	650

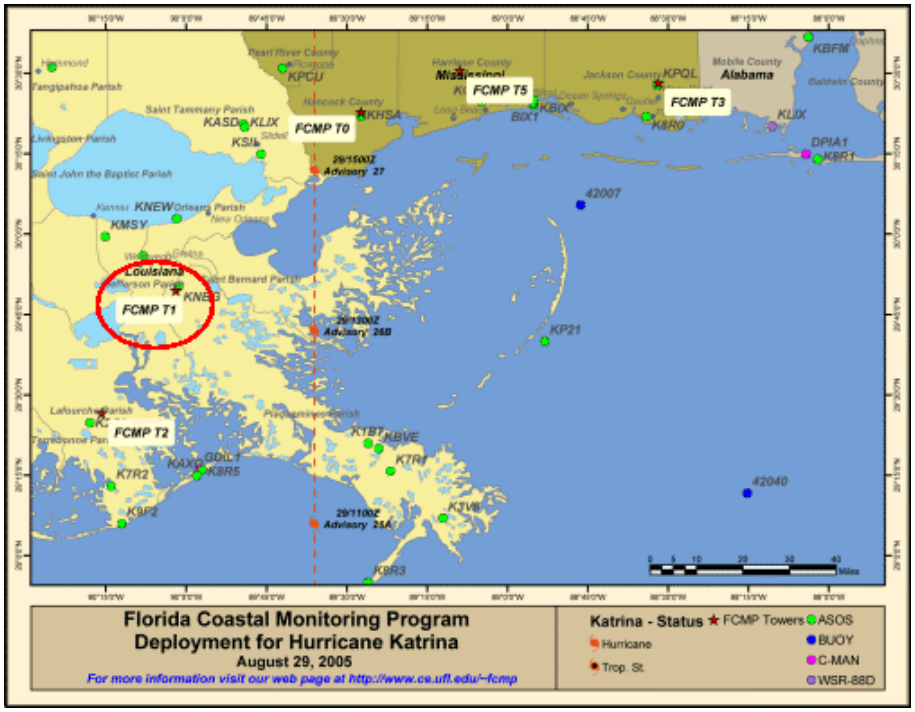

Figure G-1. Location of FCMP tower T1 during passage of Hurricane Katrina in 2005

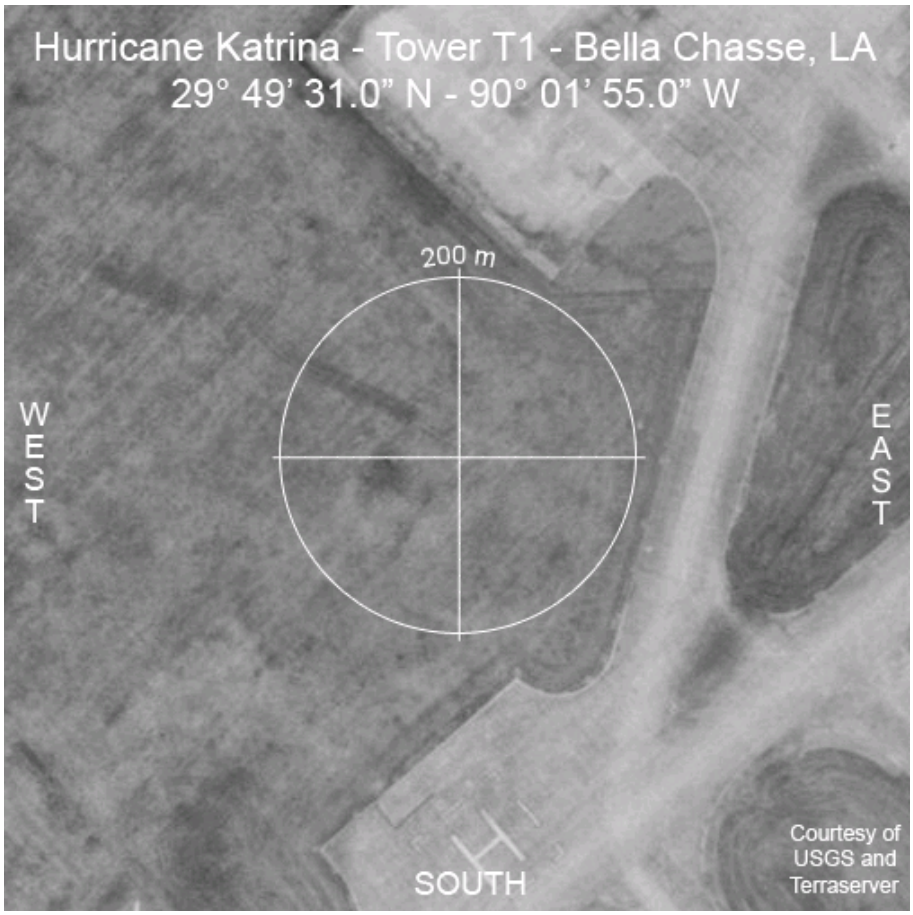

Figure G-2. Terrain around FCMP tower T1 during Hurricane Katrina in 2005

LIST OF REFERENCES

Adams, A. D. (1989). "Structural Framing Considerations for Wind Resistance of Buildings." Jamaican Institute of Engineers Seminar on Effects of "Hurricane Gilbert" on Buildings and Engineering Facilities in Jamaica, Jamaican Institute of Engineers, Jamaica.

ADINA. (2009). *ADINA User Interface Command Reference Manual Volume I: ADINA Solids & Structures Model Definition*, ADINA R & D, Inc., Watertown, MA.

AF&PA. (2001). *Wood Frame Construction Manual for One- and Two-Family Dwellings (ANSI/AF&PA WFCM-2001)*, American Forest and Paper Association, Washington, D.C.

AF&PA. (2005a). *National Design Specification for Wood Construction (NDS)*, American Forest and Paper Association, Washington, D.C.

AF&PA. (2005b). *Special Design Provisions for Wind and Seismic (SDPWS)*, American Forest and Paper Association, Washington, D.C.

AF&PA. (2006). *Guide to Wood Construction in High Wind Areas for One- and Two-Family Dwellings - 130 mph Exposure B Wind Zone*, American Forest and Paper Association, Washington, D.C.

Allen, D. E. (1989). "Hurricane Gilbert: Building Damage in Jamaica." Jamaican Institute of Engineers Seminar on Effects of "Hurricane Gilbert" on Buildings and Engineering Facilities in Jamaica, Jamaican Institute of Engineers, Jamaica.

ASCE. (1998). *Minimum Design Loads for Buildings and Other Structures (ASCE/SEI Standard 7-98)*, American Society of Civil Engineers, Reston, VA.

ASCE. (1999). *ASCE Manuals and Reports on Engineering Practice No. 67 - Wind Tunnel Studies of Buildings and Structures*, American Society of Civil Engineers, Reston, VA.

ASCE. (2006). *Minimum Design Loads for Buildings and Other Structures (ASCE/SEI Standard 7-05)*, American Society of Civil Engineers, Reston, VA.

ASTM. (2004a). "D 3043-00 Standard Test Methods for Structural Panels in Flexure." Annual Book of ASTM Standards, American Society for Testing and Materials, 427-439.

ASTM. (2004b). "D 4761-02a Standard Test Methods for Mechanical Properties of Lumber and Wood-Base Structural Material." Annual Book of ASTM Standards, American Society for Testing and Materials, 535-544.

ASTM. (2006a). "D 1761-06 Standard Test Methods for Mechanical Fasteners in Wood." Annual Book of ASTM Standards, American Society for Testing and Materials, 267-277.

ASTM. (2006b). "D 2395-02 Standard Test Methods for Specific Gravity of Wood and Wood-Based Materials." Annual Book of ASTM Standards, American Society for Testing and Materials, 342-349.

Banks, D., and Meroney, R. N. (2001). "The applicability of quasi-steady theory to pressure statistics beneath roof-top vortices." *Journal of Wind Engineering and Industrial Aerodynamics*, 89(6), 569-598.

Batts, M. E., Russell, L. R., and Simiu, E. (1980). "Hurricane Wind Speeds in the United States." *Journal of the Structural Division*, 106(10), 2001-2016.

Bendat, J. S., and Piersol, A. G. (1993). *Engineering Applications of Correlation and Spectral Analysis*, John Wiley & Sons, Inc., New York.

Bendat, J. S., and Piersol, A. G. (2000). *Random Data: Analysis & Measurement Procedures*, Wiley-Interscience.

Breyer, D. E., Fridley, K. J., Cobeen, K. E., and Pollock, D. G. (2007). *Design of Wood Structures - ASD/LRFD*, McGraw-Hill, New York.

Buckingham, E. (1914). "On Physically Similar Systems; Illustrations of the Use of Dimensional Equations." *Physics Review*, IV(4), 345-376.

Bulleit, W. M., and Liu, W.-F. (1995). "First-order reliability analysis of wood structural systems." *Journal of Structural Engineering*, 121(3), 517-529.

Camelo, V. (2003). "Dynamic Characteristics of Woodframe Buildings," Ph.D. Dissertation, California Institute of Technology, Pasadena, CA.

Cartwright, D. E., and Longuet-Higgins, M. S. (1956). "The statistical distribution of the maxima of a random function." *Proceedings of the Royal Society of London. Series A-Mathematical and Physical Sciences*, 237, 212-232.

Cheng, J. (2004). "Testing and analysis of the toe-nailed connection in the residential roof-to-wall system." *Forest Products Journal*, 54(4), 58-65.

Coffman, B. F., Main, J. A., Duthinh, D., and Simiu, E. (2010). "Wind effects on low-rise metal buildings: Database-assisted design versus ASCE 7-05 standard estimates." *Journal of Structural Engineering*, 136(6), 744-748.

Collins, M., Kasal, B., Paevere, P., and Foliente, G. C. (2005a). "Three-dimensional model of light frame wood buildings. I: Model description." *Journal of Structural Engineering*, 131(4), 676-683.

Collins, M., Kasal, B., Paevere, P., and Foliente, G. C. (2005b). "Three-dimensional model of light frame wood buildings. II: Experimental investigation and validation of analytical model." *Journal of Structural Engineering*, 131(4), 684-692.

Cook, R. A. (2010). "Personal Communication." University of Florida, Gainesville, FL.

Cramer, S. M., Drozdek, J. M., and Wolfe, R. W. (2000). "Load sharing effects in light-frame wood-truss assemblies." *Journal of Structural Engineering*, 126(12), 1388-1394.

Cramer, S. M., and Wolfe, R. W. (1989). "Load-distribution model for light-frame wood roof assemblies." *Journal of Structural Engineering*, 115(10), 2603-2616.

Crandell, J. H., Kenney, T. M., and Rosowsky, D. V. (2006). "Residential Building Loads - Review and Roadmap for Future Progress." American Society of Civil Engineers, Reston, VA.

Crandell, J. H., and Kochkin, V. (2003). "Common engineering issues in conventional construction." *Wood Design Focus*, 13(3), 13-23.

Cunningham, T. P., Jr. (1993). "Roof Sheathing Fastening Schedules for Wind Uplift." APA Report T92-28. APA - The Engineered Wood Association, Tacoma, WA.

Dao, T. N., and van de Lindt, J. W. (2008). "New Roof Sheathing Nail Model for use in FE Applications." *Journal of Structural Engineering*, 134(10), 1668-1674.

Datin, P. L., and Prevatt, D. O. (2007). "Wind Uplift Reactions at Roof-to-Wall Connections of Wood-Framed Gable Roof Assembly." 12th International Conference on Wind Engineering, Australasian Wind Engineering Society, Cairns, Australia.

Datin, P. L., and Prevatt, D. O. (2009). "Equivalent Roof Panel Wind Loading for Full-Scale Sheathing Testing." 11th Americas Conference on Wind Engineering (11ACWE), American Association of Wind Engineering, San Juan, Puerto Rico.

Datin, P. L., Prevatt, D. O., and Pang, W. (2010). "Wind Uplift Capacity of Residential Wood Roof Sheathing Panels Retrofitted with Insulating Foam Adhesive." *Journal of Architectural Engineering*, In Press.

Davenport, A. G. (1964). "Note on the distribution of the largest value of a random function with application to gust loading." *Proceedings of the Institution of Civil Engineers*, 28, 187-196.

Davenport, A. G. (1995). "How can we simplify and generalize wind loads?" *Journal of Wind Engineering and Industrial Aerodynamics*, 54-55, 657-669.

Davenport, A. G. (2002). "Past, present and future of wind engineering." *Journal of Wind Engineering and Industrial Aerodynamics*, 90(12-15), 1371-1380.

Dikkers, R. D., Marshall, R. D., and Thom, H. C. S. (1970). "Hurricane Camille - August 1969: A Survey of Structural Damage Along the Mississippi Gulf Coast." National Bureau of Standards.

Dixon, C. R., and Prevatt, D. O. "What do we learn from wind uplift tests of roof systems." *Structural Engineering Institute's 2010 Structures Congress joint with the North American Steel Construction Conference*, Orlando, FL.

Doudak, G., McClure, G., Smith, I., Hu, L., and Stathopoulos, T. (2005). "Monitoring structural response of a wooden light-frame industrial shed building to environmental loads." *Journal of Structural Engineering*, 131(5), 794-805.

Eaton, K. J., and Mayne, J. R. (1975). "Measurement of Wind Pressures on Two-story Houses at Aylesbury." *Journal of Wind Engineering and Industrial Aerodynamics*, 1(1), 67-109.

Ellingwood, B. R., Rosowsky, D. V., Li, Y., and Kim, J. H. (2004). "Fragility assessment of light-frame wood construction subjected to wind and earthquake hazards." *Journal of Structural Engineering*, 130(12), 1921-1930.

Ellingwood, B. R., van de Lindt, J. W., Gromala, D. S., Rosowsky, D. V., Gupta, R., and Pryor, S. E. (2006). "Performance-Based Engineering for Light-Frame Wood Construction in the United States: Status and Challenges." Proc. of the 2006 World Conference on Timber Engineering, Portland, OR.

Ewins, D. J. (1984). *Modal Testing: Theory and Practice*, Research Studies Press Ltd., Letchworth, Hertfordshire, England.

FEMA. (1992). "Building Performance: Hurricane Andrew in Florida - Observations, Recommendations, and Technical Guidance." Federal Emergency Management Agency.

FEMA. (1993). "Building Performance: Hurricane Iniki in Hawaii - Observations, Recommendations, and Technical Guidance." Federal Emergency Management Agency.

FEMA. (1999). "Building Performance Assessment Report: Oklahoma and Kansas Midwest Tornadoes of May 3, 1999: Observations, Recommendations, and Technical Guidance." FEMA 342, Federal Emergency Management Agency.

FEMA. (2005a). "Mitigation Assessment Team Report: Hurricane Charley in Florida - Observations, Recommendations, and Technical Guidance." FEMA 488, Federal Emergency Management Agency.

FEMA. (2005b). "Mitigation Assessment Team Report: Hurricane Ivan in Alabama and Florida - Observations, Recommendations, and Technical Guidance." FEMA 489, Federal Emergency Management Agency.

FEMA. (2005c). "Summary Report on Building Performance: 2004 Hurricane Season." FEMA 490, Federal Emergency Management Agency.

FEMA. (2006). "Hurricane Katrina in the Gulf Coast: Mitigation Assessment Team Report - Building Performance Observations, Recommendations, and Technical Guidance." FEMA 549, Federal Emergency Management Agency.

Ferry Borges, J., and Castanheta, M. (1971). *Structural Safety*, LNEC, Lisbon, Portugal.

Foliente, G. C. (1994). "Modeling and Analysis of Timber Structures Under Seismic Loads." Proceedings of a research needs workshop; analysis, design and testing of timber structures under seismic loads, G. C. Foliente, ed., University of California Forest Products Society, Richmond, CA, 87-109.

Foliente, G. C. (1997). "Timber Structures in Seismic Regions: General Overview and Research Needs." Earthquake Performance and Safety of Timber Structures, G. C. Foliente, ed., 2-23.

Foliente, G. C., and Zacher, E. G. (1994). "Performance Tests of Timber Structural Systems Under Seismic Loads." Proceedings of a research needs workshop; analysis, design and testing of timber structures under seismic loads, G. C. Foliente, ed., University of California Forest Products Society, Richmond, CA, 21-86.

Gad, E. F., Chandler, A. M., and Duffield, C. F. (2001). "Modal analysis of steel-framed residential structures for application to seismic design." *JVC/Journal of Vibration and Control*, 7(1), 91-111.

Garcia, R. A. (2008). "Wave and surge loading on light-frame wood structures," MS Thesis, Colorado State University, Fort Collins, CO.

Gupta, R. (2005). "System behavior of wood truss assemblies." *Progress in Structural Engineering and Materials*, 7(4), 183-193.

Gupta, R., and Limkatanyoo, P. (2008). "Practical approach to designing wood roof truss assemblies." *Practice Periodical on Structural Design and Construction*, 13(3), 135-146.

Gupta, R., Miller, T. H., and Dung, D.-R. (2004). "Practical solution to wood truss assembly design problems." *Practice Periodical on Structural Design and Construction*, 9(1), 54-60.

Gupta, R., Miller, T. H., and Kittel, M. R. (2005). "Small-scale modeling of metal-plate-connected wood truss joints." *Journal of Testing and Evaluation*, 33(3), 139-149.

Gurley, K., Davis Jr, R. H., Ferrera, S.-P., Burton, J., Masters, F., Reinhold, T., and Abdullah, M. (2006). "Post 2004 Hurricane field survey - An evaluation of the relative performance of the standard building code and the Florida building code." ASCE Structures Congress 2006, American Society of Civil Engineers, Reston, VA 20191-4400, United States, St. Louis, MO, United States, 8.

Gurley, K., Masters, F., Prevatt, D., and Reinhold, T. (2005). "Hurricane Data Collection: FCMP Deployments During the 2004 Atlantic Hurricane Season." 10th Americas Conference on Wind Engineering, American Association of Wind Engineers, Baton Rouge, LA.

Harris, H. G., and Sabnis, G. M. (1999). *Structural Modeling and Experimental Techniques*, CRC Press, Boca Raton, FL.

Hibbeler, R. C. (2002). *Structural Analysis*, Prentice Hall, Upper Saddle River, NJ.

Hill, K., Datin, P., Prevatt, D. O., Gurley, K., and Kopp, G. A. (2009a). "A Case for Standardized Dynamic Wind Uplift Pressure Test for Wood Roof Structural Systems." 11th Americas Conference on Wind Engineering (11ACWE), American Association of Wind Engineering, San Juan, Puerto Rico.

Hill, K. M., Datin, P. L., and Prevatt, D. O. (2009b). "Revisiting Wind Uplift Testing of Wood Roof Sheathing - Interpretation of Static and Dynamic Test Results." Hurricane Hugo 20th Anniversary Symposium on Building Safer Communities - Improving Disaster Resilience, Applied Technology Council (ATC), Charleston, SC.

Ho, T. C. E., Surry, D., and Davenport, A. G. (1991). "Variability of low building wind loads due to surroundings." *Journal of Wind Engineering and Industrial Aerodynamics*, 38(2-3), 297-310.

Ho, T. C. E., Surry, D., and Davenport, A. G. (1992). "Low building wind load variability with application to codes." *Journal of Wind Engineering and Industrial Aerodynamics*, 43(pt 3), 1787-1798.

Holmes, J. D., and Best, R. J. (1981). "An approach to the determination of wind load effects on low-rise buildings." *Journal of Wind Engineering and Industrial Aerodynamics*, 7(3), 273-287.

HUD. (2000). "Residential Structural Design Guide: 2000 Edition." U.S. Department of Housing and Urban Development, Office of Policy Development and Research, Washington, D.C.

IBHS. (2010). "High Winds - Gable End Bracing." Institute for Business and Home Safety, Accessed September 2010 at disastersafety.org.

Jang, S., Lu, L.-W., Sadek, F., and Simiu, E. (2002). "Database-assisted wind load capacity estimates for low-rise steel frames." *Journal of Structural Engineering*, 128(12), 1594-1603.

Kareem, A. (1985). "Structural Performance and Wind Speed-Damage Correlation in Hurricane Alicia." *Journal of Structural Engineering*, 111(12), 2596-2610.

Kasal, B., Collins, M. S., Paevere, P., and Foliente, G. C. (2004). "Design models of light frame wood buildings under lateral loads." *Journal of Structural Engineering*, 130(8), 1263-1271.

Kasal, B., Leichti, R. J., and Itani, R. Y. (1994). "Nonlinear finite-element model of complete light-frame wood structures." *Journal of Structural Engineering*, 120(1), 100-119.

Kasperski, M. (1992). "Extreme wind load distributions for linear and nonlinear design." *Engineering Structures*, 14(1), 27-34.

Kasperski, M. (2003). "Specification of the design wind load based on wind tunnel experiments." *Journal of Wind Engineering and Industrial Aerodynamics*, 91(4), 527-541.

Kasperski, M. (2007). "A consistent model for the codification of wind loads." *Journal of Wind Engineering and Industrial Aerodynamics*, 95(9-11), 1114-1124.

Kasperski, M., and Niemann, H. J. (1992). "The L.R.C. (load-response-correlation) Method - A General Method of Estimating Unfavourable Wind Load Distributions for Linear and Non-linear Structural Behaviour." *Journal of Wind Engineering and Industrial Aerodynamics*, 43(pt 3), 1753-1763.

Kittel, M. R. (1997). "Small-Scale Modeling of Metal-Plate Connected Wood Truss Joints," M.S., Oregon State University, Corvallis, OR.

Kopp, G. A., Morrison, M. J., Iizumi, E., and Henderson, D. (2008). "The 'Three Little Pigs' Project: Integration of wind tunnel model scale tests and full-scale laboratory tests." The 3rd International Symposium on Wind Effects on Buildings and Urban Environment (ISWE3), Tokyo, Japan.

Lee, J. J., and Hong, J. P. (2002). "Study on half-scale model test for light-frame shear wall." *Journal of Wood Science*, 48(4), 302-308.

Leicester, R. H., and Hawkins, B. T. (1983). "Large Models of Low Rise Buildings Loaded by the Natural Wind." *Journal of Wind Engineering and Industrial Aerodynamics*, 13(1-3), 289-300.

Levitan, M. L., and Mehta, K. C. (1992a). "Texas Tech field experiments for wind loads part 1. Building and pressure measuring system." *Journal of Wind Engineering and Industrial Aerodynamics*, 43(pt 3), 1565-1576.

Levitan, M. L., and Mehta, K. C. (1992b). "Texas Tech field experiments for wind loads part II. Meteorological instrumentation and terrain parameters." *Journal of Wind Engineering and Industrial Aerodynamics*, 43(pt 3), 1577-1588.

Li, Z. (1996). "A Practical Approach to Model the Behavior of a Metal-Plate-Connected Wood Truss System," M.S., Oregon State University, Corvallis, OR.

Li, Z., Gupta, R., and Miller, T. H. (1998). "Practical approach to modeling of wood truss roof assemblies." *Practice Periodical on Structural Design and Construction*, 3(3), 119-124.

Lieblein, J. (1974). "Efficient Methods of Extreme-Value Methodology." National Bureau of Standards, Washington, D.C.

Limkatanyoo, P. (2003). "System Behavior of Three-Dimensional Wood Truss Assemblies," M.S. Thesis, Oregon State University, Corvallis, OR.

Liu, W.-F., and Bulleit, W. M. (1995). "Overload behavior of sheathed lumber systems." *Journal of Structural Engineering*, 121(7), 1110-1118.

Liu, Z. (2006). "Field Measurements and Wind Tunnel Simulation of Hurricane Wind Loads on Single Family Dwellings," Ph.D. Dissertation, Clemson University, Clemson, SC.

Liu, Z., Prevatt, D. O., Aponte-Bermudez, L. D., Gurley, K. R., Reinhold, T. A., and Akins, R. E. (2009). "Field measurement and wind tunnel simulation of hurricane wind loads on a single family dwelling." *Engineering Structures*, 31(10), 2265-2274.

Main, J. A., and Fritz, W. P. (2006). "Database-Assisted Design for Wind: Concepts, Software, and Examples for Rigid and Flexible Buildings." National Institute of Science and Technology, Gaithersburg, MD.

Mani, S. (1997). "Influence Functions for Evaluating Design Loads on Roof-Truss to Wall Connections in Low-Rise Buildings," M.S. Thesis, Clemson University, Clemson, SC.

Martin, K. G. (2010). "Evaluation of system effects and structural load paths in a wood-framed structure," MS Thesis, Oregon State University, Corvallis, Or.

Masters, F., Gurley, K., and Prevatt, D. O. (2008). "Full-Scale Simulation of Turbulent Wind-Driven Rain Effects on Fenestration and Wall Systems." 3rd International Symposium on Wind Effects on Buildings and Urban Environment, Tokyo, Japan.

Masters, F. J. (2004). "Measurement, Modeling and Simulation of Ground-Level Tropical Cyclone Winds," Ph.D. Dissertation, University of Florida, Gainesville, FL.

MathWorks. (2008). "MATLAB - The Language of Technical Computing." Ver. 7.7.0.471 (R2008b). The Mathworks, Inc., Natick, MA

McCutcheon, W. J. (1977). "Method for Predicting the Stiffness of Wood-Joist Floor Systems with Partial Composite Action." FPL-RP-289, Forest Products Laboratory, Madison, WI.

Mensah, A. F. (2010). "Determination of Wind Uplift Forces using Database-Assisted Design (DAD) Approach for Light Framed Wood Structures," MS Thesis, University of Florida, Gainesville, FL.

Mizzell, D. P. (1994). "Wind Resistance of Sheathing for Residential Roofs," MS Thesis, Clemson University, Clemson, SC.

Morrison, M. J., and Kopp, G. A. (2009). "Application of Realistic Wind Loads to the Roof of a Full-Scale, Wood-Frame House." 11th Americas Conference on Wind Engineering (11ACWE), American Association of Wind Engineering, San Juan, Puerto Rico.

Morrison, M. J., and Kopp, G. A. "Performance of toe-nailed connections under realistic wind loading." *Structural Engineering Institute's 2010 Structures Congress joint with the North American Steel Construction Conference*, Orlando, FL.

Murphy, G. (1950). *Similitude in Engineering*, John Wiley & Sons, Inc., New York.

NHC/NOAA. (2010). "The Saffir-Simpson Hurricane Wind Scale." National Hurricane Center, National Weather Service, NOAA, Available at www.nhc.noaa.gov/aboutsshws.shtml.

NIST. (2003). "NIST/SEMATECH e-Handbook of Statistical Methods." National Institute of Standards and Technology. Retrieved March 8, 2007, from http://www.itl.nist.gov/div898/handbook/.

NSB. (2007). "Hurricane Warning: The Critical Need for a National Hurricane Research Initiative." National Science Board of the National Science Foundation, Arlington, VA.

Paevere, P. J., Foliente, G. C., and Kasal, B. (2003). "Load-sharing and redistribution in a one-story woodframe building." *Journal of Structural Engineering*, 129(9), 1275-1284.

Patton-Mallory, M., Gutkowski, R. M., and Soltis, L. A. (1984). "Racking Performance of Light-Frame Walls Sheathed on Two Sides " *FPL-RP-448*, USDA Forest Service.

Pielke, R. A., Gratz, J., Landsea, C. W., Collins, D., Saunders, M. A., and Musulin, R. (2008). "Normalized hurricane damage in the United States: 1900-2005." *Natural Hazards Review*, 9(1), 29-42.

Pinelli, J. P., Gurley, K. R., Subramanian, C. S., Hamid, S. S., and Pita, G. L. (2008). "Validation of a probabilistic model for hurricane insurance loss projections in Florida." *Reliability Engineering and System Safety*, 93(12), 1896-1905.

Porterfield, M. L., and Jones, N. P. (2001). "The development of a field measurement instrumentation system for low-rise construction." *Wind and Structures, An International Journal*, 4(3), 247-260.

Reed, T. D., Rosowsky, D. V., and Schiff, S. D. (1997). "Uplift capacity of light-frame rafter to top plate connections." *Journal of Architectural Engineering*, 3(4), 156-163.

Rigato, A., Chang, P., and Simiu, E. (2001). "Database-assisted design, standardization, and wind direction effects." *Journal of Structural Engineering*, 127(8), 855-860.

Riley, M. A., and Sadek, F. (2003). "Experimental Testing of Roof to Wall Connections in Wood Frame Houses." National Institute of Standards and Technology, Gaithersburg, MD.

Rosowsky, D. V., Reed, T. D., and Tyner, K. G. (1998). "Establishing uplift design values for metal connectors in light-frame construction." *Journal of Testing & Evaluation*, 26(5), 426-433.

Saffir, H. S. (1971). "Hurricane wind and storm surge." *The Military Engineer*, 423, 4-5.

Scoville, E. (2005). "Investigation of the Response of Low-Rise Wood-Frame Roof-Wall Systems under Combined Uplift and In-Plane Shear Loads," PhD Dissertation, Clemson University, Clemson, SC.

Shanmugam, B., Nielson, B. G., and Prevatt, D. O. (2009). "Statistical and analytical models for roof components in existing light-framed wood structures." *Engineering Structures*, 31(11), 2607-2616.

Simiu, E., Sadek, F., Whalen, T. M., Jang, S., Lu, L.-W., Diniz, S. M. C., Grazini, A., and Riley, M. A. (2003). "Achieving safer and more economical buildings through database-assisted, reliability-based design for wind." *Journal of Wind Engineering and Industrial Aerodynamics*, 91(12-15), 1587-1611.

Simiu, E., and Scanlan, R. H. (1996). *Wind Effects on Structures - Fundamentals and Applications to Design*, John Wiley & Sons, Inc., New York.

Simiu, E., and Stathopoulos, T. (1997). "Codification of wind loads on buildings using bluff body aerodynamics and climatological data bases." *Journal of Wind Engineering and Industrial Aerodynamics*, 69-71, 497-506.

Simpson, R. H. (1974). "The hurricane disaster potential scale." *Weatherwise*, 27, 169 & 186.

Sparks, P. R. (1990). "Performance of structures in Hurricane Hugo 1989. The Carolinas." *NIST Special Publication*(796), 445-457.

Sparks, P. R. (1991). "Hurricane Hugo in perspective." NIST Special Publication 820, National Institute of Standards & Technology, 29-37.

Stathopoulos, T. (1979). "Turbulent Wind Action on Low Rise Buildings," PhD Dissertation, University of Western Ontario, London, Ontario, Canada.

Stephens, M. A. (1986). "Tests Based on EDF Statistics." Goodness-of-Fit Techniques, R. B. D'Agostino and M. A. Stephens, eds., Marcel Dekker, Inc., New York.

Suzuki, S., Fujino, E., and Kawai, M. (1996). "Experimental modal analyses for full-scale house." Proceedings of the International Wood Engineering Conference, V. K. A. Gopu, ed., New Orleans, LA, 164-169.

Tedesco, J. W., McDougal, W. G., and Ross, C. A. (1999). *Structural Dynamics - Theory and Applications*, Addison Wesley, Menlow Park, CA.

Thampi, H., Dayal, V., and Sarkar, P. P. (2010). "Finite element modeling of interaction of tornado with a low-rise timber building." Fifth International Symposium on Computational Wind Engineering (CWE2010), Chapel Hill, NC.

Touliatos, P. G., Tsakanika, E. P., and Carydis, P. G. (1991). "On the Greek experience concerning the structural behaviour of timber constructions in seismic zones." Proceedings of a Workshop on Full-scale Behavior of Wood-Framed Buildings in Earthquakes and High Winds, Watford, United Kingdon.

Uematsu, Y., and Isyumov, N. (1999). "Wind pressures acting on low-rise buildings." *Journal of Wind Engineering and Industrial Aerodynamics*, 82(1), 1-25.

US Census Bureau. (2003). "Census of population and housing (2000)." US Dept. of Commerce, Economics and Statistics Administration, Washington, D.C.

US Census Bureau. (2007). "2007 Population Estimates." US Dept. of Commerce, Economics and Statistics Administration, Washington, D.C., Accessed 9/16/2009 from factfinder.census.gov.

van de Lindt, J. W., and Dao, T. N. (2009). "Performance-Based Wind Engineering for Wood-Frame Buildings." *Journal of Structural Engineering*, 135(2), 169-177.

van de Lindt, J. W., Graettinger, A., Gupta, R., Skaggs, T., Pryor, S., and Fridley, K. (2007). "Performance of Woodframe Structures During Hurricane Katrina." *Journal of Performance of Constructed Facilities*, 21(2), 108-116.

Vickery, P. J. (2008). "Component and cladding wind loads for soffits." *Journal of Structural Engineering*, 134(5), 846-853.

von Karman, T. (1948). "Progress in the statistical theory of turbulence." *Proceedings of the National Academy of Sciences*, 34(11), 530-539.

Welch, P. D. (1967). "The Use of Fast Fourier Transform for the Estimation of Power Spectra: A Method Based on Time Averaging Over Short, Modified Periodograms." *IEEE Transactions on Audio and Electroacoustics*, AU15(2), 70-73.

Whalen, T., Simiu, E., Harris, G., Lin, J., and Surry, D. (1998). "The use of aerodynamic databases for the effective estimation of wind effects in main wind-force resisting systems: application to low buildings." *Journal of Wind Engineering and Industrial Aerodynamics*, 77-78, 685-693.

Whalen, T. M., Sadek, F., and Simiu, E. (2002). "Database-assisted design for wind: Basic concepts and software development." *Journal of Wind Engineering and Industrial Aerodynamics*, 90(11), 1349-1368.

Whalen, T. M., Shah, V., and Yang, J.-S. (2000). "A Pilot Project For Computer-Based Design of Low-Rise Buildings for Wind Loads - The WiLDE-LRS User's Manual." Purdue University, West Lafayette, IN.

Wolfe, R. W. (1990). "Performance of Light-Frame Redundant Assemblies." Proceedings of the 1990 International Wood Engineering Conference, Tokyo, Japan, 124-131.

Wolfe, R. W., and LaBissoniere, T. (1991). "Structural Performance of Light-Frame Roof Assemblies II. Conventional Truss Assemblies." FPL-RP-499, Forest Products Laboratory, Madison, WI.

Wolfe, R. W., and McCarthy, M. (1989). "Structural Performance of Light-Frame Roof Assemblies I. Truss Assemblies With High Truss Stiffness Variability." FPL-RP-492, Forest Products Laboratory, Madison, WI.

Wolfe, R. W., Percival, D. H., and Moody, R. C. (1986). "Strength and Stiffness of Light-Frame Sloped Trusses." FPL-RP-471, Forest Products Laboratory, Madison, WI.

Zisis, I., and Stathopoulos, T. (2009). "Wind-induced cladding and structural loads on low-wood building." *Journal of Structural Engineering*, 135(4), 437-447.

Zisis, I., Stathopoulos, T., Smith, I., Galal, K., and Doudak, G. (2009). "Wind-Induced Structural Attenuation in Low-Rise Wood Buildings." 11th Americas Conference on Wind Engineering (11ACWE), American Association of Wind Engineering, San Juan, Puerto Rico.

BIOGRAPHICAL SKETCH

Peter L. Datin was born in 1980 in Bryan, Texas, to Dennis and Colette Datin while his father worked on his doctorate in agricultural engineering at Texas A&M University. He grew up on a small farm as the oldest of eight children just outside of Guthrie, Oklahoma, where he graduated from Guthrie High School. Peter attended Oklahoma State University and earned a degree in civil engineering in 2005. He then pursued graduate studies at Clemson University in South Carolina where he was a graduate research assistant at the Wind Load Test Facility conducting wind tunnel studies on low-rise residential buildings. He graduated with a master's degree in civil engineering with an emphasis in structures from Clemson in 2007. Peter then started his doctoral studies at the University of Florida continuing research in wind loading on low-rise, wood-framed residential buildings. He received his Ph.D. from the University of Florida in the fall of 2010. Outside of his graduate studies, Peter enjoys spending time with his wife, Angie, and their three children: Joshua, Emily, and Jessica.